

Thermal and Non-Thermal Processes
of Simple Molecules on
Model Interstellar Ices

Demian Marchione

Submitted for the degree of Doctor of Philosophy

Heriot-Watt University

School of Engineering and Physical Sciences

October 2015

The copyright in this thesis is owned by the author. Any quotation from the thesis or use of any of the information contained in it must acknowledge this thesis as the source of the quotation or information.

ABSTRACT

Thin film growth and desorption behaviour of simple molecules have been studied by means of surface science techniques, such as mass spectrometry and reflection-absorption infrared spectroscopy (RAIRS), in order to understand the physico-chemical processes and intermolecular interactions in model interstellar ices. The systems of interest comprise a silica surface, representing the bare grains in the interstellar medium, and films of water (H_2O), methanol (CH_3OH), diethyl ether ($(\text{CH}_3\text{CH}_2)_2\text{O}$) and benzene (C_6H_6). While H_2O and CH_3OH are key components of the icy mantles, $(\text{CH}_3\text{CH}_2)_2\text{O}$ and C_6H_6 are found in lower abundances being two products, among many, of the rich chemistry occurring in these environments.

Temperature programmed desorption and IR signatures of pure solid H_2O , CH_3OH , and $(\text{CH}_3\text{CH}_2)_2\text{O}$ adsorbed on amorphous silica were compared as a function of surface coverage and temperature. H_2O and $(\text{CH}_3\text{CH}_2)_2\text{O}$ display opposite behaviours, consistent with two-dimensional island formation and wetting of the amorphous silica surface respectively. CH_3OH , being intermediate between the two species, exhibited aspects of both behaviours. Temperature programmed RAIRS has revealed evidence for thermal activation of diffusion of H_2O over the amorphous silica surface between 40 K and 60 K, and of CH_3OH between 20 K and 40 K, while no conclusive evidence was found for such with $(\text{CH}_3\text{CH}_2)_2\text{O}$.

Experiments have been performed to study the thermal desorption and the IR features of C_6H_6 on CH_3OH and $(\text{CH}_3\text{CH}_2)_2\text{O}$ solids in comparison to those on a solid H_2O substrate at 110 K. The results give a clear picture of the C_6H_6 film growth from low to high coverages. *Ab initio* quantum chemical calculations highlight the key interactions between the two species for each system, $\text{C}_6\text{H}_6/\text{H}_2\text{O}$, $\text{C}_6\text{H}_6/\text{CH}_3\text{OH}$ and $\text{C}_6\text{H}_6/(\text{CH}_3\text{CH}_2)_2\text{O}$, in support of the interpretation of the data.

Building on this basis, 250 eV electron irradiation of C_6H_6 on thick ices of H_2O , or CH_3OH , or $(\text{CH}_3\text{CH}_2)_2\text{O}$ was investigated to demonstrate the crucial role of hydrogen-bonding in propagating electronic excitation to the solid-vacuum interface where C_6H_6 desorption can occur. Competitive electron-induced chemistry in the form of molecular hydrogen (H_2) formation was also observed. The electron beam used in these experiments is inelastically scattered by the molecules in the solid ices forming a similar flux of electrons to that associated to cosmic rays. Conclusions related to the impact of these observations on the early phase of icy interstellar grain chemistry are discussed.

ACKNOWLEDGMENTS

The author would like to acknowledge the use of the EPSRC UK National Service for Computational Chemistry Software (NSCCS) at Imperial College London in carrying out this work.

The work presented in this thesis is based on the help and guidance of many people. Gratitude to Prof. Martin McCoustra who encouraged me towards optimistic attitudes despite experimental difficulties. It is undeniable that his indications and many stimulating discussions have played a major role to both unveil and drive, in the “right” direction I would say, the experiments here presented. Always open to welcome new interpretations and ideas he has granted a unique opportunity to develop awareness and attitude to pursue scientific research.

The rest of the group, made of current and former members, has also been of invaluable assistance. Jerome, Mark, Ali, and even John, from miles away, have been enthusiastic to teach me what they knew about UHV equipment. Special gratitude should also be expressed to my friend Alex, who has read this thesis an endless number of times providing me with excellent suggestions.

Thanks to the entire LASSIE network, that embedded the perfect mix of exquisite quality science and friendly environment.

All the work here presented would not have come to light without the professionalism of the staff, Mary, Iain, and Alan in a special way, who have contributed to build a cheerful atmosphere on daily basis.

Also thanks to everyone in the ground floor of WP building, especially those who, like Cassandra, were bothered by many questions on English grammar or software.

Least, but most important, immense gratitude to Lucille who kept me going when I ran out of energy.

Contents

1	The Interstellar Medium	1
1.1	Introduction	2
1.2	A Historical Perspective	4
1.3	Molecular Clouds	6
1.3.1	Gas Phase Chemistry in Molecular Clouds	10
1.3.2	Dust in the ISM	13
1.3.3	Evidence for PAHs in the ISM	19
1.4	Grain Processes	22
1.4.1	Dust-catalysed Chemistry	22
1.4.2	Laboratory Studies of Desorption from Icy Mimics	24
1.5	Astrochemical models	29
1.6	Thesis Outline	33
	Bibliography	34
2	Methods	43
2.1	Introduction	44
2.2	From Theory to Vacuum Techniques	45
2.3	Ultrahigh Vacuum Chambers	49
2.4	The Beam Rig	49
2.4.1	Instrumentation	50
2.4.2	Sample Mounting	52
2.4.3	Substrate Heating and Temperature Control	54
2.4.4	Line-of-sight Detection	56
2.4.5	Thin Film Deposition	58
2.5	The Ice Rig	63
2.5.1	Instrumentation	63
2.5.2	Sample Mounting and Cryogenic System	65
2.5.3	Glass Gas Lines	67
2.6	From Metal Substrates to Grain Analogues	68
2.7	Experimental Techniques	71
2.7.1	Temperature Programmed Desorption	71

2.7.2	Reflection-Absorption Infrared Spectroscopy	74
2.8	Computational Chemistry	79
2.8.1	Hartree-Fock Method	79
2.8.2	MP2-CCSDT Methods	81
2.8.3	Towards Statistical Large Systems	84
	Bibliography	86
3	Adsorption of Small Molecules on Amorphous Silica	92
3.1	Introduction	93
3.2	TPD	93
3.2.1	Experimental Procedure	95
3.2.2	TPD: Results and Discussion	95
3.2.3	Comparison of TPD Traces	122
3.3	RAIRS	127
3.3.1	RAIRS: Results and Discussion	127
3.3.2	TP-RAIRS: Results and Discussion	135
3.4	Conclusions	141
	Bibliography	142
4	Benzene on Methanol and Diethyl Ether	147
4.1	Introduction	148
4.2	Experimental Section	148
4.3	Benzene on Methanol	149
4.3.1	TPD of Benzene on Methanol	150
4.3.2	RAIRS of Benzene on Methanol	160
4.4	Benzene on Diethyl Ether	166
4.4.1	TPD of Benzene on Diethyl Ether	168
4.4.2	RAIRS of Benzene on Diethyl Ether	171
4.5	Computational Studies on Model Systems	173
4.6	Conclusions and Comparison with ASW	179
	Bibliography	183
5	Electron Irradiation of Benzene on Water, Methanol and Diethyl Ether	187
5.1	Introduction	188
5.1.1	Previous Studies: Electron Induced Processes	188
5.2	Experimental Procedures	191
5.3	Electron Irradiation of Benzene Adsorbed on ASW	192
5.3.1	Discussion	198
5.4	Irradiation of Benzene Adsorbed on Methanol and on Diethyl Ether	206

5.4.1	Results and Discussion	206
5.4.2	Electron-induced Chemistry: H ₂ Formation	211
5.4.3	EPD <i>versus</i> EIC	216
5.5	Astrophysical Implications and Conclusions	220
	Bibliography	224
6	Conclusions and Outlook	230
6.1	Introduction	231
6.2	Overall Conclusions and Future Work	231
	Bibliography	241

List of Tables

1.1	<i>Components of the ISM and their physical properties. ¹ Note that the density is referred to H₂ in molecular clouds and to atomic H in the other cases.</i>	3
1.2	<i>Gas-phase reactions in astrochemistry.</i>	11
2.1	<i>Grades of vacuum and relative pressure ranges. Note that the pressure between the Earth and the Moon is 10⁻⁷ - 10⁻⁸ mbar and interplanetary space is less than 10⁻¹⁴ mbar</i>	46
2.2	<i>Table reporting number of collisions and time for a monolayer to form at different background pressures in the chamber.</i>	46
3.1	<i>Table listing the values of maxima, full width at half heights, and areas obtained from the fit of peak A and B of the CH₃OH TPD traces in the 1 L - 10 L range. Note that the smoothed curves (16 point adjacent-averaging method) for the 1 L and 2 L traces were used for the fits instead of the experimental traces. The area is reported in % as ratio with respect to the area of the cumulative peak.</i>	99
3.2	<i>Table reporting the calculated desorption energy of bulk amorphous CH₃OH by LEA and using CKS. Exposures are of: 20 L, 50 L, 100 L, 200 L, and 500 L. In the latter case both an ideal zeroth-order desorption and more realistic fractional kinetics were taken into account.</i>	102
3.3	<i>Table listing the estimated number of adsorbed molecules and film thickness for each exposure. Note that for the lowest coverages the monolayer is not yet complete and the thickness reported aside is an average.</i>	104
3.4	<i>Table reporting the range of E(θ) found for peak A of 1L, 2 L, 5 L, and 10 L CH₃OH on SiO₂.</i>	107
3.5	<i>Table reporting the calculated desorption energy of amorphous bulk (CH₃CH₂)₂O from SiO₂ by LEA and using CKS. The range of exposures is: 500 L - 5000 L.</i>	114
3.6	<i>Table listing the estimated number of adsorbed molecules and film thickness for each exposure of (CH₃CH₂)₂O from SiO₂. Note that for the lowest coverages the monolayer is not yet complete yet and the thickness reported should be regarded as average.</i>	115

3.7	Table reporting the calculated desorption energy (E_d) for H_2O , CH_3OH , and $(CH_3CH_2)_2O$ on SiO_2 . When available literature values for bulk desorption and for the second layer are reported below the results of this work. Note that H_2O has no defined transition from monolayer to multilayer; desorption energy of amorphous H_2O was assigned to the low coverages and desorption energy of crystalline H_2O was assigned to the high coverages taking the values estimated in previous works [28, 38]	124
3.8	List of vibrational modes of CH_3OH multilayer (500 L) adsorbed on amorphous SiO_2 at 20 K and 105 K and on HOPG at 97 K and 130 K for comparison [21]. Note that there could be contributions to the higher frequency region from the asymmetric A' and A'' CH_3 bendings at 2956 cm^{-1} and 2908 cm^{-1} respectively.	130
3.9	List of vibrational modes of multilayer $(CH_3CH_2)_2O$ (500 L) adsorbed on amorphous SiO_2 at 20 K and 110 K.	133
4.1	List of vibrational modes of C_6H_6 multilayer adsorbed on amorphous CH_3OH at 110 K. The superscript \dagger indicates that frequency assignment was obtained by the RAIR spectrum subtracted with the CH_3OH single beam.	161
4.2	Table listing the estimated number of adsorbed C_6H_6 molecules on a thick CH_3OH ice. C_6H_6 film thickness for each exposure is also reported. Note that for the lowest coverages the monolayer is not yet complete yet and the thickness reported should be regarded as average.	162
4.3	List of vibrational modes of 200 L of $(CH_3CH_2)_2O$ multilayer adsorbed on steel at 107 K.	167
4.4	Binding energy calculated for the, C_6H_6/H_2O , and C_6H_6/CH_3OH and $C_6H_6/(CH_3CH_2)_2O$ dimers at different levels of theory and vibrational shifts for the CC aromatic stretching mode with respect to the isolated C_6H_6 . MP2/TZ is the BSSE corrected binding energy obtained with a single point at MP2/TZ following the optimisation with aug-cc-pVDZ basis set. Corr. is the BSSE corrected binding energy obtained adding the $\Delta CCSD(T)$ at the MP2/TZ energy. Literature values are reported when available. Experimentally determined E_d values and $\Delta\bar{\nu}_{CC}$ ranges are also reported. Note that the E_d indicated for C_6H_6 on $(CH_3CH_2)_2O$ was determined for $(CH_3CH_2)_2O$ on C_6H_6 and does not represent the desorption energy of the inverted analogous system. It should be regarded as merely indicative. Experimental $\Delta\bar{\nu}_{CC}$ were obtained by comparing the C_6H_6 bulk IR feature at $\sim 1475\text{ cm}^{-1}$ with the 0.1 L spectrum on CH_3OH and $(CH_3CH_2)_2O$ in the same frequency region, and with 1 L of C_6H_6 on H_2O taken from [12].	177

4.5	<i>Table summarising the experimentally determined film growth and energetic of C_6H_6 for the binary layered systems: C_6H_6/H_2O, C_6H_6/CH_3OH and $C_6H_6/(CH_3CH_2)_2O$. The E_d value indicated in brackets was determined for $(CH_3CH_2)_2O$ on C_6H_6 and does not represent the desorption energy of the inverted analogous system. It should be regarded as merely indicative.</i>	181
5.1	<i>Table reporting: electron fluxes, decay constants and EPD cross-sections of C_6H_6 on ASW for each H_2O dose for the first series of experiments.</i>	195
5.2	<i>Table summarising the results for the fast EPD process from all the series of experiments investigating the effect of the H_2O thickness underlying 5 L of C_6H_6 on the non-thermal desorption of the adsorbate. C_6H_6 cross-sections are reported for each H_2O dose.</i>	196
5.3	<i>List of cross-section values derived from the fits of the experimental EPD traces: C_6H_6 on CI, on poly-CI H_2O film (see Figure 5.7) and on c-ASW. In the latter case, the values are reported as average from the experiments probing the effect of ASW film thickness, see Figure 5.2. The subscript under the cross-section indicates the deposition temperature of H_2O vapour.</i>	203
5.4	<i>Table listing the masses found by thermally desorbing 1 L C_6H_6 on 250 L of CH_3OH after exposing the ice to 250 eV electron irradiation for for ~ 700 seconds. The assignment was assumed to be the same as reported by Kaiser [20].</i>	212
5.5	<i>Table summarising the results from all the series of electron irradiation experiments. The errors reported for the EIC values are obtained from the propagation of the error on the current and on the decay constant. Although not directly determined, the second component of the C_6H_6 EPD cross-section from CH_3OH and $(CH_3CH_2)_2O$ can be assumed $\sim 10^{-17}$ cm², as estimated from electron irradiation of multilayer C_6H_6 [2]. Note that X and X' can both be: H (D) atoms or CH_3 and/or CH_3CH_2 groups. For the C_6H_6/c-ASW experiments D_2O was employed for the EIC traces, while H_2O was used for the EPD decays. In the latter case, literature values [1] are also reported.</i>	218

List of Figures

1.1	<i>An optical image of the famous molecular cloud Barnard 68 (B68). It is about 500 light years from Earth, towards the Ophiunchus constellation, available at: http://apod.nasa.gov/apod/ap141214.html.</i>	5
1.2	<i>This image represents the sky area of the B68 presented in six different wavelengths, clockwise from the blue to the near-infrared spectral region. It is evident that the obscuration caused by the cloud declines with increasing wavelength. Courtesy of ESO.</i>	5
1.3	<i>This image represents the sky region of the B68 presented in IR false-color. The yellow area would be dark when detecting visible light, while it is more transparent to less energetic photons. Courtesy of ESO.</i>	6
1.4	<i>Image of the molecular cloud in Taurus. NASA astronomy picture of the day, 25/04/2009.</i>	7
1.5	<i>Adaption of extinction curve reported in [38]. Three cases of a mean extinction law. Solid lines are obtained by fitting theoretical calculations and dashed line from the fitting of observational data. It is evident the common shape and feature at $4.60 \mu\text{m}^{-1}$ (217.5 nm).</i>	14
1.6	<i>Top row reports the dark-field scanning transmission electron microscopy (STEM) images of the cross-section of the crater. composite element distribution maps shows the heterogeneous distribution of Mg-Si-Fe (central row) and the O-S (bottom row) in four candidates of probable interstellar origin. Scale bars indicate 100 nm. Pt and C refer to Focused Ion Beam deposited protective masks Image taken from [39]</i>	15
1.7	<i>SWS spectrum of NGC 7538 URS9 adapted from [50]. The IR signatures, discussed in the text, of the main ice component are indicated and the water features are highlighted in red.</i>	17
1.8	<i>Optical depth spectrum of W33A from 4 to 5 μm. The dashed curve is a laboratory spectrum of a $\text{H}_2\text{O}:\text{NH}_3$ mixture 100:9 ice at 50 K scaled conveniently to highlight the combination mode of water in the observed spectrum. Image taken from [55]</i>	18

1.9	<i>Optical depth spectrum of W33A from 8 to 11 μm after further manipulation. In dotted curve the laboratory spectrum for $\text{H}_2\text{O}:\text{NH}_3$ mixture 100:9 ice at 50 K and dot-dashed curve for $\text{H}_2\text{O}:\text{CH}_3\text{OH}:\text{CO}_2$ (1.25:12:1.0) ice at 70 K. Image taken from [55]</i>	19
1.10	<i>Some Polycyclic Aromatic hydrocarbons and the fullerene C_{60}.</i>	20
1.11	<i>PAH emission features in the SWS spectrum of the Orion Bar PDR. Assignments in terms of C-H and C-C stretches are indicated. Image taken from [16, 61].</i>	20
1.12	<i>The absorption spectrum of (a), six neutral PAHs compared with the spectrum produced by the same PAHs in (b), the cationic form (anthracene, tetracene, 1, 2-benzanthracene, chrysene, pyrene, and coronene. Image taken from [63].</i>	21
1.13	<i>A cartoon summarising the complex physiochemical processes occurring on the interstellar dust [74].</i>	24
2.1	<i>Beam Rig: main chamber at the right and molecular beam source at the left.</i>	49
2.2	<i>General schematic highlighting the pump locations in the Beam Rig.</i>	51
2.3	<i>Schematic of the experimental level in the UHV chamber.</i>	52
2.4	<i>Pictures and schematic of the substrate and its mounting in the UHV chamber. Please note that in the upper photograph some components are not shown.</i>	53
2.5	<i>Schematic and picture of the sample manipulator in the Beam Rig.</i>	54
2.6	<i>Empirical calibration curve for K-type thermocouple in the Beam Rig. Coefficients are: $k = (261.38 \pm 0.10)\text{K}$, $C_1 = (108.03 \pm 0.36)\text{KV}^{-1}$, $C_2 = (-9.18 \pm 0.98)\text{KV}^{-2}$, $C_3 = (-0.40 \pm 1.2)\text{KV}^{-3}$, $C_4 = (-2.6 \pm 2.2)\text{KV}^{-4}$, $C_5 = (7.90 \pm 0.94)\text{KV}^{-5}$, $C_6 = (2.1 \pm 1.3)\text{KV}^{-6}$.</i>	55
2.7	<i>Tests of TPD profiles aimed at identifying and investigating the desorption from different areas of the sample mounting.</i>	57
2.8	<i>Final arrangement for tantalum wires supporting the disc to minimise and isolate desorption from the wires themselves.</i>	57
2.9	<i>Schematic of the gas manifolds used for background deposition (in violet).</i>	59
2.10	<i>Schematic of the molecular beam apparatus adjacent to the chamber.</i>	60
2.11	<i>Picture of the Knudsen cell from Chell as shown in its website (http://www.-chell.co.uk/product_details/vacuum-products/kcell).</i>	62
2.12	<i>Pictures of the left and right side of the Ice Rig.</i>	63
2.13	<i>Schematic of the experimental level and the pumping for the Ice Rig.</i>	64
2.14	<i>Temperature control system schematic. The inset at the bottom shows a detailed representation of the sample mounting.</i>	66
2.15	<i>Picture (a) and schematic (b) of the glass gas line.</i>	67

2.16	<i>On the left: cluster model of terminal silanol groups at the amorphous SiO₂ surface. The H atoms connected to the Si atoms are a simplification for the surrounding O-Si-O network. On the right: 100 × 100 μm AFM image taken from [5] of amorphous silica (~ 100 nm) deposited on the stainless steel substrate. The apparent curve in the film is an experimental artefact.</i>	70
2.17	<i>Some examples of TPD profiles.</i>	73
2.18	<i>Cartoon representing the relative phase of the electric field vector (\vec{E}) for a parallel polarisation (a) and for a perpendicular polarisation (b) before and after the reflection from the surface. \vec{v} is the propagation vector and \vec{n} is the normal to the plane. Adapted from [53].</i>	74
2.19	<i>Phase change ($\Delta\phi$) following the reflection on the metal surface as function of the incidence angle (θ) for a polarised light parallel (a) or perpendicular (b) to the plane of incidence. Image adapted from [53].</i>	75
2.20	<i>Cartoon of the complexed CO on a metal surface. On the left side the electric dipole of the molecule cancels out with the image dipole at the interface. On the right the molecular and image dipoles re-enforce and IR absorption will be further enhanced.</i>	76
2.21	<i>Schematic of a Michelson interferometer. The sample is just before the detector.</i>	77
2.22	<i>Schematic of a dispersive IR spectrometer. A monochromator is located in between the sample and the detector.</i>	78
3.1	<i>TPD traces for desorption of 1 L to 500 L of CH₃OH on SiO₂. Low coverages are reported in the upper row panels and high coverages are displayed in the lower row. In the subplot labelled (I) both peak A and B can be observed. Peak A is assigned to the desorption of physisorbed CH₃OH on the SiO₂ surface. In the low exposures regime (upper row panel) peak B is assigned to the formation of a second CH₃OH layer. The subplot labelled (II) shows the fitting functions for these two features clarifying their growth behaviour. The subplots (III) and (IV) display the peaks B and C. The former is consistent with bulk amorphous CH₃OH for exposures larger than 10 L. Peak C is consistent with bulk crystalline CH₃OH.</i>	96
3.2	<i>Leading edge analysis for the kinetic order of desorption of bulk amorphous CH₃OH on SiO₂. At low temperatures the order is zero, but it becomes fractional, 0.21 - 0.3, as higher temperatures are taken into account. In conclusion, the average desorption order is fractional, 0.2 ± 0.1.</i>	101
3.3	<i>Plot of $(\ln(r_d) - x \ln(\theta_{rel}))$ against $1/T$ for the multilayer desorption of 200 and 500 L of CH₃OH from SiO₂. The red line shows the fit to the experimental data points, which are reported in black open circles.</i>	102

3.4	<i>TPD traces for desorption of CH₃OH on SiO₂ in open circles and CKS fits in red (ideal case, $x = 0$) and blue (fractional order). Coverages are of 20 L, 50 L, 100 L, 200 L, and 500 L in the order of increasing signal.</i>	104
3.5	<i>TPD traces for desorption of 100 L, 200 L and 500 L of CH₃OH on SiO₂. Experimental points in open circles and CKS fits in red (ideal case, $x = 0$) and blue (fractional order). Deviation from an ideal layer-by-layer desorption for the 100 L, 200 L, and 500 L traces which was interpreted as effect of both the inherent roughness of the SiO₂ surface and H-bonding formation.</i>	105
3.6	<i>The upper panel shows TPD traces for desorption of 1 L, 2 L, 5 L and 10 L of CH₃OH on SiO₂. The thicker solid lines are the simulated traces of peak A assuming the distribution of energy being coverage dependent. The lower panel displays the plot of E_{des} as function of θ for each exposure obtained through inversion of the Polanyi-Wigner equation.</i>	107
3.7	<i>Arrhenius plot ($\ln(r_d)$ against $1/T$) for the low exposures of peak B of CH₃OH on SiO₂. Coverages are 2 L (in red), 5 L (in blue), and 10 L (in green). The best linear fit and the desorption energy for each coverage, is reported along the experimental traces.</i>	108
3.8	<i>TPD profiles for 2 L, 5 L, and 10 L exposures. Peak B (thick line) is modelled with a first-order kinetics using CKS package. Peak A (dashed line) is described by a distribution of binding energies. Dotted arrows highlight the observed desorption behaviour.</i>	109
3.9	<i>TPD traces for desorption of (CH₃CH₂)₂O on SiO₂ for a vast range of exposures from 1 L to 5000 L. Low coverages are reported in the upper row, and high coverages are displayed in the lower row. In the subplot labelled (I) both peak A and B can be observed: the former is assigned to (CH₃CH₂)₂O directly adsorbed on the SiO₂ surface, while the latter is assigned to the formation of a second layer (in the low exposures regime). The subplot labelled (II) displays the transition from monolayer to multilayer. The subplot labelled (II) shows desorption of bulk amorphous (CH₃CH₂)₂O (peak B in the high exposures regime) and of bulk crystalline (CH₃CH₂)₂O (peak C). Finally, the TPD curves in the bottom right panel (IV) show desorption of very high coverages of (CH₃CH₂)₂O subsequently adsorption on SiO₂ at 107 K. These traces were used for the multilayer analysis.</i>	111
3.10	<i>Binding energy of the global minimum (GM) and local minimum (LM) for dimethyl ether dimer. Calculations were performed at MP2/aug-cc-pVDZ level followed by a single point with aug-cc-pVTZ basis set. Counterpoise (CP) correction was included at every step.</i>	112

3.11	<i>Leading edge analysis for the kinetic order of desorption of bulk amorphous $(\text{CH}_3\text{CH}_2)_2\text{O}$ on SiO_2 (1000 L, 2000 L, and 5000 L). Linear fits give a slope close to zero ($\sim 10^{-2}$) with a standard deviation of the same order of magnitude, or a negative order. It was concluded that $x = 0$.</i>	113
3.12	<i>Arrhenius plot ($\ln(r_d)$ against $1/T$) for the multilayer desorption of 1000 L, 2000 L, and 5000 L of $(\text{CH}_3\text{CH}_2)_2\text{O}$ from SiO_2. Data points are in black open circles, the red line shows the fit to the experiment.</i>	114
3.13	<i>TPD traces for desorption of $(\text{CH}_3\text{CH}_2)_2\text{O}$ on SiO_2 in open circles and CKS fits in blue lines with the explicit fractional order. Exposures are of 500 L, 1000 L, 2000 L and 5000 L. Note that $x \rightarrow 1$ for the 500 L data and $x \rightarrow 0$ for the 5000 L experiment</i>	116
3.14	<i>TPD traces for desorption of 1000 L of $(\text{CH}_3\text{CH}_2)_2\text{O}$ on SiO_2: experimental data in open circles and CKS fits for different fractional order kinetics. Note that when $x \rightarrow 1$ both the leading edge and the maximum are best modelled.</i>	116
3.15	<i>Plot of binding energy as a function of surface concentration for $(\text{CH}_3\text{CH}_2)_2\text{O}$ on SiO_2 obtained through inversion of the Polanyi-Wigner equation for the 1 L, 2 L, 5 L, 10 L and 20 L TPD traces. Note that the calculated desorption energy spans over a very large range, from 34 kJ mol^{-1} to 55 kJ mol^{-1} and beyond.</i>	118
3.16	<i>(a) E_d as a function of surface concentration for the high temperature desorption peak of low coverages (1 L - 20 L) of $(\text{CH}_3\text{CH}_2)_2\text{O}$ from SiO_2. (b) Simulated high temperature TPD profiles for low exposures assuming a distribution of energies. The analysis supports the assignment of peak A to the first monolayer forming, filling adsorption sites at the SiO_2 interface ranging from 46 kJ mol^{-1} up to 52 kJ mol^{-1}.</i>	119
3.17	<i>(a) E_d as a function of surface concentration for the low temperature desorption peak of low coverages (1 L - 20 L) of $(\text{CH}_3\text{CH}_2)_2\text{O}$ from SiO_2. (b) Simulated low temperature TPD profiles for low exposures assuming a distribution of energies. The analysis supports the assignment of peak B to a second layer having desorption energy of $32.2 - 35.0 \text{ kJ mol}^{-1}$.</i>	120
3.18	<i>Simulated $(\text{CH}_3\text{CH}_2)_2\text{O}$ TPD profiles from SiO_2 of peak A and B at low coverages. A distribution of desorption energies was assumed and the inverted form of the Polanyi-Wigner equation was applied to successfully reproduce the experimental traces.</i>	121
3.19	<i>TPD traces for desorption of H_2O (upper row, CH_3OH, (central row), and $(\text{CH}_3\text{CH}_2)_2\text{O}$ (lower row) on SiO_2. The panels at the left show the desorption profiles of these species for low coverages ($\leq 20\text{L}$), while the subplots at the right display the TPD traces for higher coverages ($\geq 20\text{L}$).</i>	123

3.20	<i>Schematic of ideal derivation of ethers (ROR) from water (HOH) via the alcohol (ROH).</i>	124
3.21	<i>Rough energy schematic for the four main possible interactions of H₂O, CH₃OH, and (CH₃CH₂)₂O on SiO₂: 1) the interaction experienced by each XOX' molecule inside the bulk in solid phase, E_b; 2) the interaction between XOX' and one or few more XOX' molecules, E_b[*]; 3) the strong interaction between SiO₂ and the isolated XOX' molecule, E_H; 4) the weak, dispersive interaction between the isolated XOX' and the SiO₂ surface. E_{disp}. Note that X and X' can be an H atom and/or a CH₃ or CH₃CH₂ group.</i>	126
3.22	<i>RAIR spectra of CH₃OH deposited on amorphous SiO₂ film at 20 K (a) and 110 K (b) as the coverage is increased from 5 L to 500 L. The detailed assignment of the vibrational bands is reported in the text; note that the OH and CH stretches follow at high wavenumbers (3600 - 2700 cm⁻¹), while the CO and the silica bands can be found at lower wavenumbers (1450 - 400 cm⁻¹).</i>	129
3.23	<i>RAIR spectra of (CH₃CH₂)₂O deposited on amorphous SiO₂ film at 20 K (a) and 110 K (b) at increasing coverage from 1 L up to 500 L.</i>	132
3.24	<i>(a) Full spectrum and (b) high frequency region of RAIR spectra obtained for CH₃OH (50 L) deposited on amorphous SiO₂ at 20 K, then annealed at T = 40 K, 60 K, 80 K, 100 K and 120 K for 100 seconds, and finally cooled down to base temperature. The OH and CH stretching regions were considered individually to define a baseline specific for each frequency range. (c) Plot of integrated area for the OH stretching mode at each annealing step. The error bars are obtained propagating a 10% error during the integration.</i>	136
3.25	<i>(a) OH stretch vibrational mode evolution in RAIR spectra obtained for H₂O deposited on amorphous SiO₂ (50 L) at 20 K, then annealed at T = 40 K, 60 K, 80 K, 100 K and 120 K for 100 seconds and finally cooled down to base temperature. (b) Integrated area at each annealing step. The error bars are obtained propagating a 10% error during the integration.</i>	138
3.26	<i>High frequency region of RAIR spectra obtained for 50 L (a) and 100 L (b) of (CH₃CH₂)₂O deposited on amorphous SiO₂ at 20 K, then annealed at T = 40 K, 60 K, 80 K, 100 K and 120 K for 100 seconds, and finally cooled down to base temperature.</i>	140
4.1	<i>RAIR spectrum of the multilayer CH₃OH film (200 L; ~ 15.2 nm) grown on stainless steel in the Beam Rig for the C₆H₆ experiments. CH₃OH vibrations are labelled. The negative sharp features between 1800 and 1400 cm⁻¹ are due to the bending modes of gaseous H₂O in the air side of the chamber, in the IR path to the detector.</i>	150

4.2	<i>CO stretch TP-RAIR spectra when 200 L of CH₃OH is deposited at 105 K on stainless steel, then annealed at T = 110 K, 115 K, 120 K, 125 K, 130 K, 135 K, 140 K, 145 K, 150 K, 155 K, and 160 K for 100 seconds, and finally cooled down to base temperature. Note the transition from the amorphous to crystalline phase by the CO splitting.</i>	150
4.3	<i>Three replications of TPD experiments of 0.01 L, 0.02 L, 0.05 L, 0.1 L of C₆H₆ deposited on thick CH₃OH film (200 L; ~ 15.2 nm). The dotted line is the scaled CH₃OH TPD trace underlying 0.05 L of C₆H₆.</i>	151
4.4	<i>TPD traces of 0.1 L and 0.5 L of C₆H₆ deposited on thick CH₃OH film (200 L; ~ 15.2 nm). The dotted line is the scaled CH₃OH TPD trace underlying 0.05 L of C₆H₆. The four replications show different outcomes of the experiment.</i>	152
4.5	<i>TPD traces 0.01 L - 50 L of C₆H₆ deposited on thick CH₃OH film (200 L; ~ 15.2 nm). The left panel shows sub-monolayer exposures and the right panel displays the multilayer growth.</i>	153
4.6	<i>TPD traces 0.05 L of C₆H₆ deposited on thick CH₃OH film (200 L, ~ 15.2 nm), in black open circles. The contribution to the overall signal from the wires and the substrate are reported with red and blue lines respectively.</i>	154
4.7	<i>Plot of ln(r_d) against 1/T for the low exposures of C₆H₆ on CH₃OH. The best linear fit and the desorption energy for each coverage, is reported along the experimental traces.</i>	154
4.8	<i>TPD traces (in thin lines) of 1 L, 5 L and 50 L of C₆H₆ deposited on CH₃OH (200 L). Scaled CH₃OH TPD traces (in thick lines) underlying 1 L, 5 L and 50 L of C₆H₆.</i>	156
4.9	<i>TPD traces (in grey thick lines) of 50 L, 100 L, 200 L and 500 L of C₆H₆ deposited on CH₃OH (200 L). Methanol TPD traces (in thick orange lines) underlying 50 L, 100 L, 200 L and 500 L of C₆H₆ and CH₃OH TPD trace (in thin orange lines) underlying 0.02 L of C₆H₆.</i>	156
4.10	<i>Deviation from ideality for the CH₃OH TPD traces underlying 20 L, 50 L, 100 L, 200 L and 500 L of C₆H₆ as function of C₆H₆ exposures.</i>	158
4.11	<i>Maxwell-Boltzmann speed distribution for C₆H₆ during background dosing.</i>	159
4.12	<i>RAIR spectrum of the multilayer C₆H₆ on thick CH₃OH film (200 L; ~ 15.2 nm) at ~ 110 K. C₆H₆ vibrations are labelled in black and CH₃OH normal modes are labelled in dark yellow. Background subtraction was done using the RAIR spectrum of the substrate prior to CH₃OH deposition.</i>	160
4.13	<i>RAIR spectra of C₆H₆ on thick CH₃OH film (200 L) at increasing coverages. In the lower left panel the exposures from 0.1 L to 10 L have been offset for clarity. The reversed spectrum of pure CH₃OH in the same region is also labelled and reported in dark yellow for comparison.</i>	163

4.14	<i>RAIR spectrum of C₆H₆ on thick CH₃OH film (200 L) at increasing coverages up to 5 L.</i>	164
4.15	<i>Left side: RAIR spectrum of C₆H₆ on thick CH₃OH film (200 L) at increasing coverages up to 5 L. Right side: TP-RAIR spectra of pure CH₃OH in the same frequency range, reporting spectral evolution as the film is annealed for 100 s at T_{base} + 5 K, T_{base} + 10 K, T_{base} + 15 K ... T_{base} + 45 K.</i>	164
4.16	<i>RAIR spectra of pure CH₃OH (200 L) and C₆H₆ on CH₃OH (both at 200 L) are reported in black open circles and black line respectively in the 3000 - 3500 cm⁻¹ region. The change in the OH band is compatible with crystallisation observed in the TP-RAIR spectra of pure CH₃OH reported with shades of dark yellow for consistency with figures 4.1 and 4.12.</i>	165
4.17	<i>Upper panel RAIR spectrum of the multilayer (CH₃CH₂)₂O film (200 L, ~ 12.1 nm) grown on stainless steel in the Beam Rig for the C₆H₆ experiments. Lower panel RAIR spectrum of 200 L of C₆H₆ deposited on 200 L of (CH₃CH₂)₂O. C₆H₆ vibrations are labelled in black. Note that the S/N ratio is low around 600 cm⁻¹ due to the MCT detector cut-off.</i>	166
4.18	<i>TPD traces of 0.01 L, 0.02 L, 0.05 L, 0.1 L, 0.2 L and 0.5 L of C₆H₆ deposited on a thick (CH₃CH₂)₂O film (200 L; ~ 12.1 nm). The dotted line is the scaled (CH₃CH₂)₂O TPD trace underlying 0.05 L of C₆H₆.</i>	168
4.19	<i>TPD traces of 0.05 L, 0.1 L, 0.2 L, 0.5 L, and 1 L of (CH₃CH₂)₂O deposited on thick C₆H₆ film (200 L, ~ 7 nm). The left panel displays the raw TPD traces with (CH₃CH₂)₂O desorption occurring from wires holding the sample, from the C₆H₆ ice, and co-desorption of (CH₃CH₂)₂O mixed with C₆H₆. The right panel shows the deconvoluted TPD traces of (CH₃CH₂)₂O desorbing from the C₆H₆ ice. Details in the text.</i>	169
4.20	<i>E_d as a function of surface concentration derived through inversion of the Polanyi-Wigner equation from the (CH₃CH₂)₂O TPD traces on 200 L of C₆H₆. (CH₃CH₂)₂O exposures are: at 0.05 L, 0.1 L, 0.2 L, 0.5 L, and 0.1 L.</i>	170
4.21	<i>RAIR spectra of C₆H₆ on thick (CH₃CH₂)₂O film (200 L) at increasing coverages. In the right central panel the lower exposures for the CC aromatic stretching mode have been highlighted for clarity.</i>	172
4.22	<i>Geometry optimisation at MP2/aug-cc-pVDZ level of C₆H₆/CH₃OH dimer of different starting arrangements lead to the same minimum in the PES.</i>	174
4.23	<i>Energy minima of C₆H₆/CH₃OH and C₆H₆/(CH₃CH₂)₂O dimers. Optimisations were performed at MP2/aug-cc-pVDZ level with CP corrections. The Energy reported for each dimer is estimated by a single point at MP2/aug-cc-pVTZ level and corrected using CCSD(T) calculations. Details in the text.</i>	175

5.1	<i>EPD C_6H_6 signal obtained for 1 L of C_6H_6 on 140 L of compact ASW. Irradiation was conducted with 250 eV electrons and beam current of 300 nA.</i>	192
5.2	<i>EPD C_6H_6 signal obtained for 5 L of C_6H_6 on compact ASW of different thicknesses: 7.7 nm (70 L), 11 nm (100 L), 22 nm (200 L), and 55 nm (500 L). Irradiation was conducted with 250 eV electrons and beam current of 180 nA. The experimental trace is displayed in closed black circles, the bi-exponential decay fitting function in red. Time decay constants relative to the fast (1) and slow (2) components are reported for each subplot.</i>	194
5.3	<i>Cross-section values and error bars of the fast component in the EPD curve obtained for 5 L of C_6H_6 on compact ASW of different thicknesses: 7.7 nm (70 L), 11 nm (100 L), 22 nm (200 L), and 55 nm (500 L). Irradiation was conducted with 250 eV electrons and beam current of 180 nA (1st run) and 150 nA (2nd and 3rd run). A mean value of $(5.5 \pm 2.0) \times 10^{-16} \text{ cm}^2$ is found.</i>	196
5.4	<i>EPD C_6H_6 signal obtained for 5 L of C_6H_6 on H_2O ice. H_2O condensed at 110 K results into a compact-amorphous film (c-ASW), while higher deposition temperatures form a crystalline film (CI). Note that background dosing at 153 K leads to $\sim 36\%$ loss of H_2O, therefore the substrate was exposed to H_2O vapour for longer, as to obtain a similar film thickness of the other experiments. Irradiation was conducted with 250 eV electrons and beam current of 180 nA.</i>	198
5.5	<i>Distribution of penetration depths (solid lines) and backscattered electrons (circles) for 250 eV in the C_6H_6 (a) and in ASW film (b) using the CASINO software. The arrow points to the estimated thickness of 50 L C_6H_6 and 70 L H_2O which are also highlighted by the superimposed red line.</i>	199
5.6	<i>Cartoon of ASW deposited on the metal substrate. H_2O condensed at 110 K results into a compact-amorphous film (c-ASW). The roughness of the substrate is reflected on the morphology of thinner films.</i>	200

5.7	<i>C₆H₆ EPD signal obtained for 5 L of C₆H₆ on H₂O ice. H₂O condensed at 110 K results into a compact-amorphous film (c-ASW), while higher deposition temperatures form a polycrystalline film (poly-CI) at 138 K and a crystalline film (CI) at 153 K. Note that background dosing at 153 K leads to ~ 36% loss of H₂O, therefore the substrate was exposed to H₂O vapour for longer, as to obtain a similar film thickness of the other experiments. Irradiation was conducted with 250 eV electrons and beam current of 180 nA. Multi-exponential fitting curves are displayed in full lines: 2 c. indicates a bi-exponential function, 3 c. indicates a tri-exponential function. Details in the text. Experimental points are shown in open circles. All the intensities were scaled by the maximum of the most intense trace. Lattices, adapted from [38], show the transition of c-ASW to the ordered structure of the CI when annealing. In the latter case the coordination of each O-atom in the H₂O molecules is exclusively of four whereas the amorphous phase displays coordinations of two, three, four, and even five. Furthermore the surface area at the vacuum interface decreases in the ASW to CI change.</i>	201
5.8	<i>Highest occupied and lowest unoccupied molecular orbitals for H₂O, CH₃OH, and (CH₃CH₂)₂O and SOMOs for the analogous ions in the ground state. Isodensity value of ± 0.02 a.u. for the LUMO of the (CH₃CH₂)₂O, and ± 0.03 a.u. for all the others. ΔE₁ is the excitation HOMO to LUMO in eV, and ΔE₂ is the ionisation potential in eV. Calculations were carried at MP2/aug-cc-pVTZ level.</i>	205
5.9	<i>Distribution of penetration depths (red solid lines) and backscattered electrons (grey circles) for 250 eV in 15.2 nm thick CH₃OH ice (a) and in 12.1 nm thick (CH₃CH₂)₂O film (b) using the CASINO software.</i>	207
5.10	<i>C₆H₆ EPD signal obtained for 1 L, 5 L, 10 L, 20 L, and 50 L of C₆H₆ on thick CH₃OH film (15.2 nm). Irradiation started at t=0 s with 250 eV electrons and beam current of 150 nA.</i>	208
5.11	<i>C₆H₆ EPD signal obtained for increasing C₆H₆ coverage (1 L, 5 L, 10 L, 20 L, and 50 L) on thick (CH₃CH₂)₂O film (30.2 nm). Irradiation started at t=0 s with 250 eV electrons and beam current of 150 nA.</i>	209
5.12	<i>Molecular hydrogen, H₂, formation during irradiation of 1 L of C₆H₆ on thick films of H₂O (150 L), CH₃OH (250 L), or (CH₃CH₂)₂O (500 L). D₂ formation is also shown from the irradiation of 1 L of C₆H₆ on 150 L of D₂O. Irradiation was conducted with 250 eV electrons and beam current of 150 nA.</i>	214

5.13	<i>H₂ formation during irradiation of C₆H₆ (1 L) on thick film of (CH₃CH₂)₂O (500 L) or CH₃OH (250 L). D₂ formation is also shown from the irradiation of C₆H₆ (1 L) on D₂O (150 L). In the third subplot at the bottom, $\frac{m}{z} = 4$ was followed instead of $\frac{m}{z} = 2$ in order to distinguish between dehydrogenation of C₆H₆ and H₂O. Irradiation was conducted with 250 eV electrons and beam current of 150 nA.</i>	217
5.14	<i>Energy distribution of secondary electrons generated in primary events in liquid water for different incident H⁺ energies and for ⁴He ions. Plots taken from [14]</i>	220
5.15	<i>Energy deposited in c-ASW by electron and nuclear scattering per μm^{-1} and per H⁺ ion having energy between 10 keV and 100 MeV using the SRIM software. The plot at the bottom displays the ratio between the energy deposited in the ice by the two inelastic scattering events displaying the predominance of electron scattering in the energy range of interest.</i>	223
5.16	<i>Cartoon representing exciton formation in the solid H₂O bulk during electron irradiation and their migration to the vacuum interface leading to three main possible outcomes: C₆H₆ desorption, H₂ formation, reactions at the ASW interface such as hydrogenation of CO. The question mark indicates unknown processes at the SiO₂/H₂O interface.</i>	224
6.1	<i>Cartoon representing the H₂O-rich mantle on bare SiO₂ grain: (I) by reactive accretion, (II) diffusion and H₂O island formation, (III) ballistic deposition and (IV) enrichment of other species on bare grain, in the solid H₂O pores, on the H₂O surface. Time evolution is illustrated in terms of molecular and atomic hydrogen abundance ratio. This is less than one in diffuse clouds, and larger than one in dark clouds.</i>	233
6.2	<i>Cluster model of terminal silanol groups at the SiO₂ surface interacting with a H₂O molecule. Geometry optimisation was performed at MP2/aug-cc-pVDZ level followed by a single point at MP2/aug-cc-pVTZ to estimate the binding energy (34.0 kJ mol⁻¹).</i>	234
6.3	<i>One of the possible structures for C₆H₆ interacting with three CH₃OH molecules. Geometry optimisation was performed at MP2/aug-cc-pVDZ level.</i>	235
6.4	<i>Energy minima of C₆H₆ trimer structure. Figure adapted from [10].</i>	235
6.5	<i>Schematic of Förster (dipole-dipole coupling) and Dexter (molecular orbitals overlapping) mechanisms for excitation transfer. A is the acceptor molecule that is excited (A[*]) and D[*] is the excited donor molecule that relaxes to ground state (D).</i>	239

GLOSSARY

AES - Auger Electron Spectroscopy
AGB - Asymptotic giant branch
c-ASW - Compact Amorphous Solid Water
CC - Coupled-Cluster
CEM - Channel Electron Multiplier
CI - Crystalline Ice
CNM_a - Atomic Cold Neutral Medium
CNM_b - Molecular Cold Neutral Medium
DIB - Diffuse Interstellar Bands
DIG - Diffuse Ionized Gas
EELS - Electron Energy Loss Spectroscopy
EIC - Electron-induced Chemistry
EPD - Electron-promoted Desorption
ESPT - Excited State Proton Transfer
FIR - Far-Infrared
FRET - Förster Resonant Energy Transfer
HIM - Hot Ionized Medium
NIR - Near infrared
HOMO - Highest Occupied Molecular Orbital
HOPG - Highly Oriented Pyrolytic Graphite
ISO - Infrared Space Observatory
IR - Infrared
ISM - Interstellar Medium
LEED - Low Energy Electron Diffraction
LUMO - Lowest Unoccupied Molecular Orbital
MBS - Molecular Beam System
MCT - Mercury Cadmium Telluride
MP - Møller-Plesset
OFHC - Oxygen Free High Conductivity
PAH - Polycyclic aromatic hydrocarbons
PD - photo-desorption
PBN - Pyrolytic Boron Nitride
QCM - Quartz Crystal Microbalance
QMC - Quantum Monte Carlo
QMS - Quadrupole Mass Spectrometer
RAIRS - Reflective-Absorption Infrared Spectroscopy
REMPI - Resonance Enhanced Multiphoton Ionisation
SEM - Scanning Electron Microscopy

SOMO - Semi Occupied Molecular Orbital
SWS - Short Wavelength Spectrometer
TPD - Temperature Programmed Desorption
UV - Ultraviolet
UHV - Ultra-High Vacuum
VUV - Vacuum Ultraviolet
WIM - Warm Ionized Medium
WMN - Warm Neutral Medium
XPS - X-ray Photoelectron Spectroscopy

List of Publications and Conference Attendances

Publications:

- “Laboratory investigations of irradiated acetonitrile-containing ices on an interstellar dust analog”; A. Abdalgilil, D. Marchione, A. Rosu-Finsen, M. P. Collings and M. R. S. McCoustra, *J. Vac. Sci. Technol. A*, 2012, **30**, 0415051.
- “Laboratory studies of electron and ion irradiation of solid acetonitrile (CH_3CN)”; A. Abdalgilil, D. Marchione, J. D. Thrower, M. P. Collings, M. R. S. McCoustra, F. Islam, M. E. Palumbo, E. Congiu and F. Dulieu, *Phil. Trans. A*, 2013, **371**, 20110586.
- “Probing Model Interstellar Grain Surfaces with Small Molecules”; M. P. Collings, V. L. Frankland, J. Lasne, D. Marchione, A. Rosu-Finsen and M. R. S. McCoustra, *Mon. Not. R. Astron. Soc.*, 2015, **449**, 1826.
- “Highly efficient electron-stimulated desorption of benzene from solid water ice”; D. Marchione, J. D. Thrower, and M. R. S. McCoustra, *in preparation, Phys. Chem. Chem. Phys.*.
- “Wetting and De-wetting Behaviour on Model Interstellar Dust Grains”; D. Marchione, A. G. M. Abdalgilil, A. Rosu-Finsen, and M. R. S. McCoustra *in preparation, Phys. Chem. Chem. Phys.*.

Conference Attendances:

- Poster entitled “Electron-stimulated processes in astrophysical ices”; D. Marchione and M. R. S. McCoustra, Astrosurf, Heriot-Watt University, Edinburgh, UK, 31st August-2nd September 2011.
- Poster entitled “Electron stimulated processes of astrophysically relevant molecules at solid surfaces”; D. Marchione, J. D. Thrower, A. G. M. Abdalgilil, M. P. Collings, M. R. S. McCoustra, 29th European Conference on Surface Science, Edinburgh International Conference Centre, Edinburgh, UK, 3rd-5th September 2012.
- Poster entitled “Electron stimulated processes of astrophysically relevant molecules at solid surfaces”; D. Marchione, J. D. Thrower, A. G. M. Abdalgilil, M. P. Collings, M. R. S. McCoustra, The Chemical Cosmos, Museo Diocesano, Catania, IT, 2nd-5th October 2012.

- Poster entitled “*Electron stimulated processes of astrophysically relevant molecules on solid surfaces*”; D. Marchione, J. D. Thrower and M. R. S. McCoustra, Young Astrochemists’ Meeting; University College London, London, UK, 5th November 2012.
- Talk entitled *Electron and Ion Irradiation of Solid Acetonitrile (CH₃CN)*; D. Marchione, A. G. M. Abdugalil, J. D. Thrower, M. Collings, M. R. S. McCoustra, F. Islam, M. E. Palumbo, E. Congiu, F. Dulieu, 19th International Vacuum conference - Astrosurf, Le Palais des Congrès de Paris, Paris, FR, 9th-13th September 2013.
- Poster entitled “*Hydrogen Bonding and Interaction of Benzene with Icy Films*”; D. Marchione, M. P. Collings and M. R. S. McCoustra, Faraday Discussions 168: Astrochemistry of Dust, Ice and Gas; NH Conference Centre, Leiden, NL, 7th-9th April 2014.

Chapter 1

The Interstellar Medium

Contents

1.1	Introduction	2
1.2	A Historical Perspective	4
1.3	Molecular Clouds	6
1.3.1	Gas Phase Chemistry in Molecular Clouds	10
1.3.2	Dust in the ISM	13
1.3.3	Evidence for PAHs in the ISM	19
1.4	Grain Processes	22
1.4.1	Dust-catalysed Chemistry	22
1.4.2	Laboratory Studies of Desorption from Icy Mimics	24
1.5	Astrochemical models	29
1.6	Thesis Outline	33
	Bibliography	34

1.1 Introduction

The interstellar Medium (ISM) is a turbulent system comprising the matter which exists in the space between the star systems in a galaxy. It represents only 10-15% of the galaxy's mass, but most of its volume. Half of the mass of the ISM is in discrete interstellar clouds that occupy the 1-2% of the interstellar volume, thus it could be said that it is mainly “empty”, but in fact it is a highly inhomogeneous system enriched by complex physiochemical processes. The ISM is generally distinguished in five components according the physical conditions and the chemistry observed: Hot ionised medium (HIM), Warm ionised medium (WIM), Warm neutral medium (WMN), Atomic cold neutral medium (CNM_a) and Molecular cold neutral medium (CNM_b) (see **Table 1.1**) [1].

As can be seen from the **Table 1.1**, the temperature can range in the ISM from 10⁶ K to near 0 K, also the number of particles per unit of volume (in cm³) ranges from very low values, such as in the HIM, to the higher ones in the molecular clouds, where the inner parts are shielded from most of the VUV irradiation allowing atoms to bind in more and more complex molecules. The ISM plays an important role in the evolution of “present” Universe. When a star dies, it expels much of its matter into the surrounding ISM. Therefore the ISM becomes enriched with nucleo-synthesized elements heavier than H and He. Some stars die *via* spectacular supernova explosion; others lose mass through massive stellar outflows and novae [2–4]. Energy is injected into the ISM from supernovae explosions [5], VUV photons from massive O and B stars [6] and by the minor contribution of AGB stellar winds [1]. Therefore most of the molecules and clusters from the stellar remnants are destroyed, chemical bonds are dissociated by strong VUV radiation leaving only atoms and large stable molecules like polycyclic aromatic hydrocarbons (PAHs).

The above mentioned enrichment of matter and energy may lead to the formation of diffuse clouds. Actually the process is more complex than mentioned; one must recognise that the neutral ISM occurs in the galaxy as two phases: WNM and CNM [1]. They are in thermal equilibrium; the kinematics of atomic gas and molecular gas are similar [7] and the distinction between WNM and CNM is often not clear. However, a further discussion of this problem is not in the interest of this project, so for sake of simplicity it will just be assumed that at some stage diffuse clouds form as consequence of the flow of matter and energy following stellar death. Once formed they are presumed to be the precursors of molecular clouds. The link between the CNM_a and CNM_b could be simply gravity and/or a

ISM Component	Common Designation	Temperature / K	Number density ^I / cm ⁻³	State of Hydrogen	Ionisation fraction, x_e	Observational techniques
Atomic cold neutral medium (CNM _c)	Diffuse clouds	100	10-100	H and H ₂	10 ⁻³	Absorption in the UV, microwave radio (H 21.1 cm line absorption) and IR (3.4 μ m)
Molecular cold neutral medium (CNM _b)	Molecular Clouds, Dense clouds or Dark clouds	0-50	10 ³ -10 ⁵	H ₂	10 ⁻⁷ -10 ⁻⁸	Absorption and emission both in the IR and microwave radio range
Warm neutral medium (WNM)	Intercloud H I	8 × 10 ³ -10 ⁴	0.1	H	0.1	Microwave radio (H 21.1 cm line emission)
Warm ionised medium (WIM)	Diffuse ionised gas (DIG)	10 ⁴	> 10	H ⁺	1	UV, Vis (Hα), IR, pulsar dispersion
Hot ionised medium (HIM)	Coronal gas	10 ⁶	0.003	H ⁺	1	X-ray emission, UV absorption of highly ionised metals

Table 1.1: Components of the ISM and their physical properties. ^I Note that the density is referred to H₂ in molecular clouds and to atomic H in the other cases.

trigger process such as a stellar wind or a supernova explosion. The dark clouds can be considered the cradle of the chemistry in the ISM and perhaps in the entire Universe as we know it. The greater density, compared to that of diffuse clouds, up to 10^5 times, results in a significant shielding from intense VUV radiation. Cosmic rays, on the other hand, penetrate deeply inside the clouds producing H_3^+ and He^+ and promoting a prolific gas phase chemistry. In addition, the extremely cold temperatures, sometimes low as 10 K [8], cause molecules to freeze onto dust grains with a sticking coefficient close to unity. ISM dust is mostly formed “*in situ*”, likely derived from diffuse clouds, and then more and more species, both in number and in complexity, accretes to the grains, reaching sizes of $\sim 1 \mu\text{m}$ [2, 9–14]. The role of the dust in the ISM will be discussed later in greater detail.

Interstellar chemistry and physical processes in the diffuse clouds and molecular clouds determine the boundary conditions on the composition of the material that would then be included into the protostellar nebula and into cometary matter. Regions of higher density, inside the molecular clouds, could have the ideal conditions to accrete and collapse into a protostellar core. The latter would eventually become a star. Around this core, a protoplanetary disk is formed, where small grains can collide and join together giving birth to planets [15, 16]. Once formed the star system endures for a certain time on the main sequence, then when all the hydrogen is converted into helium by nuclear fusion, all the processes leading to the death of the star begin, with different results according the size of the star. For instance in the case of low-mass stars, like our Sun, the final stages results in an AGB (Asymptotic Giant Branch) star, but in any case the main effect is the enrichment of the surrounding ISM. Hence, the cycle of matter starts again. The reservoir of elements out of which the Solar System formed is the result of the mixing of nucleosynthetic products from at least two preceding generations of stars of different masses.

1.2 A Historical Perspective

Sir William Herschel (1738-1822), in the 1774, noticed a region of the Scorpio Constellation that he defined “Ein Loch in Himmel”, a hole in the sky; an area significantly “depleted” of stars. But he could not be certain whether there was an actual hole or simply something obscuring the background stars light. In 1847, Wilhelm Struve simply noticed that the density of the stars seems to diminish with the distance. He suggested that it was due to “something” in the interstellar medium causing a general obscuration and reddening of the star light. In 1919, Barnard first catalogued a dark cloud appearing as a black spot against a very

rich star field (**Figure 1.1**) It was later observed that at the edges of the cloud,

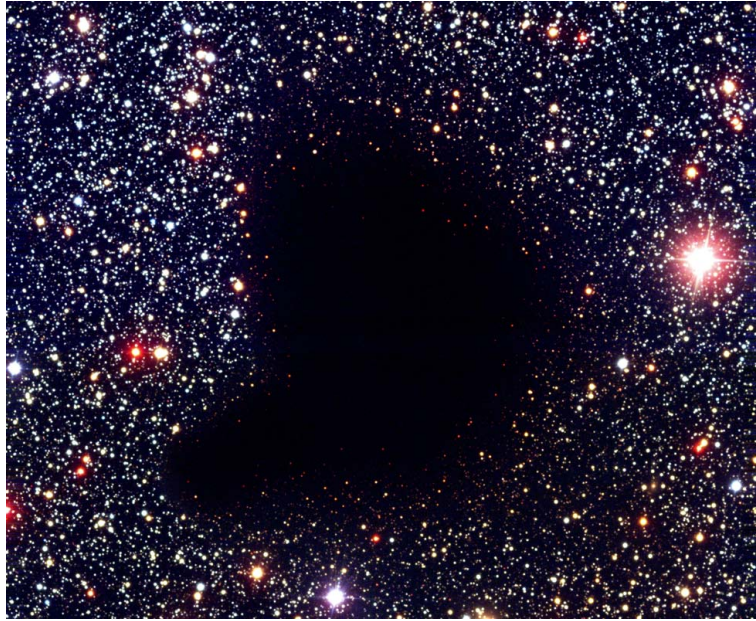


Figure 1.1: *An optical image of the famous molecular cloud Barnard 68 (B68). It is about 500 light years from Earth, towards the Ophiunchus constellation, available at: <http://apod.nasa.gov/apod/ap141214.html>.*

there is gradual decreasing of the intensity and a more and more pronounced reddening of the light coming from this object. Trumpler [17], in 1930, showed that the extinction is wavelength dependent (**Figure 1.2**). But it was only

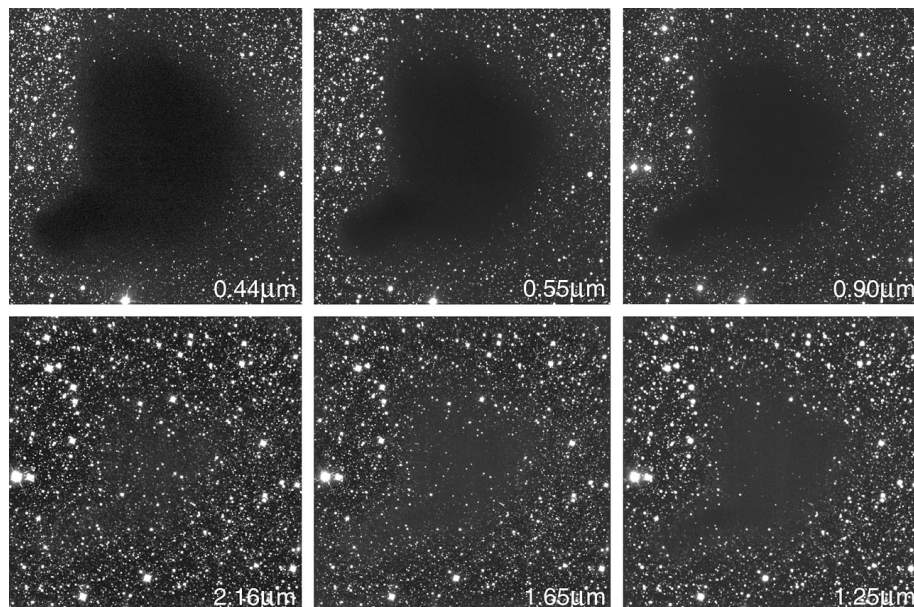


Figure 1.2: *This image represents the sky area of the B68 presented in six different wavelengths, clockwise from the blue to the near-infrared spectral region. It is evident that the obscuration caused by the cloud declines with increasing wavelength. Courtesy of ESO.*

thanks to the theory of light scattering developed by Mie and Lorenz that the

scientific community accepted that dust particles of size comparable to visible wavelengths cause the observed extinction. Furthermore in 1949, Hiltner and Hall independently discovered that optical radiation can be polarised in passing through the ISM. It was suggested that the differential extinction would have been caused by partially aligned asymmetric dust grains. Today, it is well known that the interstellar medium is made of both gas and dust mixed together and dark clouds are not just “holes in the sky” (**Figure 1.3**). It is reasonable at



Figure 1.3: *This image represents the sky region of the B68 presented in IR false-color. The yellow area would be dark when detecting visible light, while it is more transparent to less energetic photons. Courtesy of ESO.*

this point to consider why molecular clouds and their dust grain have such a significance in modern astronomy and astrochemistry.

1.3 Molecular Clouds

The aim of this project is to contribute to an understanding of the gas-grain interaction and related physiochemical processes in the ISM, particularly in the dark clouds (**Figure 1.4**). The reasons why the focus is mainly on one of the five components are numerous and the most relevant ones are listed below;

- Molecular clouds are where complex chemistry actually starts to take place during star and planet formation;

- Molecules formed therein allow small stars to form;
- Dark clouds play an important role in the exogenous theory for life development;
- The physical and chemical processes occurring in these environments are of fundamental interest.

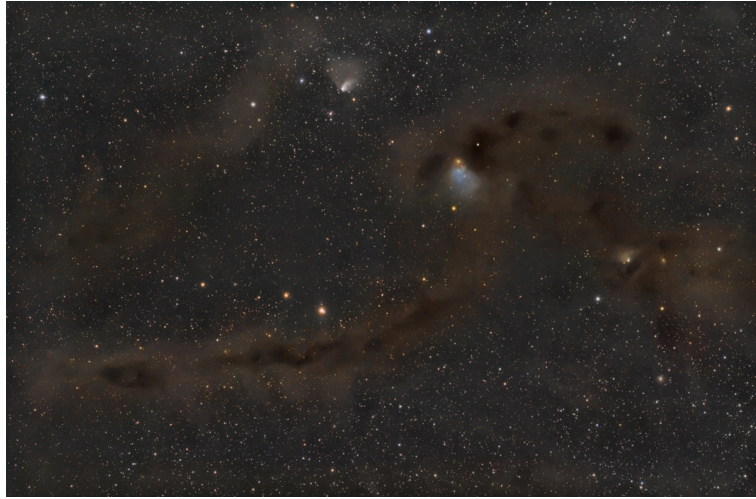


Figure 1.4: *Image of the molecular cloud in Taurus. NASA astronomy picture of the day, 25/04/2009.*

Let us go through each of these aspects. In the HIM, WIM, WNM and in the diffuse clouds the density is too low to guarantee any significant shielding from the VUV radiation of the interstellar environment. Therefore even for a simple molecule, such as H_2O , the destruction rate is greater than its formation rate. In other words, due to the low density and the strong flux of energetic photons, ion bombardment, shocks and heating, only particularly stable molecules remain, such as PAHs, or fairly simple ones, like CO, CH, CN, CH^+ and H_2 which have been identified in diffuse clouds [18]. Most of the gas phase in the other components of the ISM is dominated by atomic ion and neutral species. In dark clouds, a weak VUV flux combined with thermal processing and radiolysis (cosmic ray bombardment) promote a prolific chemistry, both in gas phase and on the grain surfaces. In the Orion molecular cloud several saturated species such as ethanol, propanonitrile, acetic acid or methylamine have been identified [19].

Dense clouds are the regions where high- and low-mass star form [1], specially in the higher density cores within clouds. During the collapse process leading to the protostellar formation, the temperature increases as consequence of the large amount of gravitational energy released. All the chemicals frozen into the

icy mantles desorb into the gas phase and start to collide with other molecules. While some thermal energy goes to promote reactive activated pathways, inelastic scattering converts some of the translational energy into other degrees of freedom, exciting molecules to higher rovibrational levels. The IR, microwave and longer wavelength radiative emissions are then observed following their relaxation to lower states. This results in an efficient cooling of the collapsing system permitting the collapse process to continue.

Molecular clouds are the point where interstellar chemistry starts to have direct relevance for cometary composition [20]. Comets are the agglomeration of residual icy grain material left over from star and planet formation. They contain a pristine record of the cold grain chemistry. For instance, it has been suggested that ethene (C_2H_4), found in comets, has an interstellar origin, likely forming from cold H additions in ices containing acetylene (C_2H_2) [21, 22]. But other molecules, such as nitriles, found in the ISM [23–25] could have a greater importance from a biological point of view. Biogenic species like amino acids, showing a chirality similar to that of life on Earth, have been isolated from carbonaceous chondrite meteorites [26], which are believed to be the remnants of the comets [27]. This could suggest that biogenic molecules formed in the ISM might have been delivered during the heavy cometary bombardment that occurred during the first few million years of our planet’s existence. Simple N-bearing species, such as CH_3CN , have been shown to produce amino acids in laboratory radiolysis of nitrile-containing ices [28]. The theory that seeks the origin of life outside the planet Earth, in the interstellar medium, is said to be the theory of “exogenous” delivery. This is in contrast to the well-known “endogenous” synthesis of the Urey-Millar experiment [29].

The last, but not least, point is that it is worthwhile highlighting the importance the physicochemistry of the interstellar medium has for basic science. Starting from very simple cocktail of species in the diffuse clouds comprising atoms or ions (e. g. H, O, C, C^+ , N, S, S^+), diatomic molecules (CH, CH^+ , CS, OH, CO, NH, H_2), PAHs and carbonaceous and silicate grains containing metals (Mg, Fe, Al), over 180 molecules¹ have been unambiguously identified in the dense clouds as of November 2014. Below are a few examples:

Two atoms : AlF, AlCl, C_2 , CH, CH^+ , CN, CO, CO^+ , CP, CS, CS, HCl, H_2 , KCl, NH, NO, NS, NaCl, OH, PN, SO, SO^+ , SiN, SiO, SiS, HF, SH, FeO, S_2 , CF^+ , O_2 , PO...

¹Full list available at <http://www.astro.uni-koeln.de/cdms/molecules>.

Three atoms : C₃, C₂H, C₂O, C₂S, CH₂, HCN, HCO, HCO⁺, HCS⁺, HOC⁺, H₂O, H₂S, HNC, HNO, MgCN, MgNC, N₂H⁺, N₂O, NaCN, OCS, SO₂, c-SiC₂, CO₂, NH₂, H₃⁺, AlNC, SiNC, HCP, CCP...

Four atoms : c-C₃H, I-C₃H, C₃N, C₃O, C₃S, C₂H₂, CH₂D⁺, HCCN, HCNH⁺, HNCO, HNCS, HOCO⁺, H₂CO, H₂CN, H₂CS, H₃O⁺, NH₃, SiC₃, C₃N⁻, PH₃...

Five atoms : C₅, C₄H, C₄Si, I-C₃H₂, c-C₃H₂, CH₂CN, CH₄, HC₃N, HC₂NC, HCOOH, CH₂NH, H₂C₂O, H₂NCN, HNC₃, SiH₄, H₂CO⁺, C₄H⁻, CNCHO...

Six atoms : C₅H, C₅O, C₂H₄, CH₃CN, CH₃NC, CH₃OH, CH₃SH, CH₃NH⁺, HC₂CHO, HCONH₂, I-H₂C₄, C₅N, HC₄N, c-H₂C₃O, CH₂CNH...

Seven atoms : C₆H, CH₂CHCN, CH₃C₂H, HC₅N, HCOCH₃, NH₂CH₃, c-C₂H₄O, CH₂CHOH, C₆H⁻...

Eight atoms : CH₃C₃N, HCOOCH₃, CH₃COOH, C₇H, H₂C₆, CH₂OHCHO, CH₂CHCHO, C₂H₆, CH₂CCHCN, NH₂CH₂CN...

Nine atoms : CH₃C₄H, CH₃CH₂CN, Me₂O, CH₃CH₂OH, HC₇N, C₈H, CH₃CONH₂, C₈H⁻, CH₂CHCH₃...

Ten atoms : CH₃C₅N, (CH₂OH)₂, (CH₃)₂CO, NH₂CH₂COOH, CH₃CH₂CHO, CH₂OHCH₂OH...

Eleven, twelve and thirteen atoms : HC₉N, CH₃C₆H, C₆H₆, CO(CH₂OH)₂, CH₃COOCH₃...

More than thirteen atoms : HC₁₁N, C₆₀, C₇₀...

This richness in chemistry is even more surprising considering the typical conditions in such interstellar clouds. They are in fact characterised by very different conditions to those experienced on Earth; the density is extremely low and the average temperature is 30 K and sometimes lower, down to 10 K, consequently the time scale of the chemical evolution of astronomical objects may be tens of thousands or even millions of years. In these conditions *gas phase chemistry*, mainly processes driven by cosmic-ray ionisation, is dominated by so-called *barrierless reactions*, where the anisotropy of the potential significantly affects the outcome of the collision. But new models show that such processes only reproduce the observed abundances of the smaller, open shell, species and certain linear chain molecules. *Surface processes* on the grains themselves and processes on and in ices adsorbed on interstellar dusts play an equally important role in favouring the formation of complex molecules.

1.3.1 Gas Phase Chemistry in Molecular Clouds

As above mentioned, gas phase reactivity in the interstellar medium is more complex and vital than the extreme conditions could suggest. This represents a challenge for astronomers and chemists and it is the reason why chemical modelling of interstellar molecular abundances has a long history. Reliable chemical networks of thousands of reactions now exist accounting for the hundreds of molecular species detected in space. This is illustrated by the latest version of the UMIST database [30] containing over 4573 binary gas phase reactions among 420 species involving He, C, N, O, F, Na, Mg, Si, P, S, Cl, and Fe. An alternative is provided by the “KInetic Database for Astrochemistry (KIDA)” originally developed at the Ohio State University [31]. Given such a large amount of reactive processes for the sake of simplicity only few examples will be illustrated and a summary scheme is reported in **Table 1.2**.

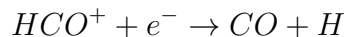
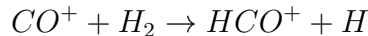
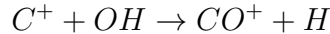
Most of the gas phase reaction processes that take place in molecular clouds also play a role in the diffuse clouds. For instance in both these ISM components, the charge transfer process (**Equation 1.2**) initiates a series of exchange reactions with H_2 culminating with dissociative recombination of H_3O^+ forming OH and H_2O ;



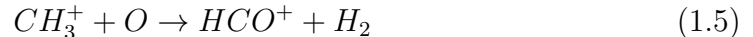
neutral exchanges lead to the formation of simple molecules as follows



CO is also thought to be partially obtained by



while an alternative pathway is



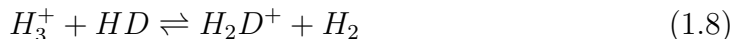
Name	Process
radiative recombination	$A^+ + e^- \Rightarrow A + h\nu$
radiative association	$e^- + B + M \Rightarrow B^- + M$ $e^- + B \Rightarrow B^-$
dissociative recombination (molecular)	$AB + e^- \Rightarrow B^- + A$ $AB^+ + e^- \Rightarrow B + A$
dipolar dissociation	$AB + e^- \Rightarrow A^- + B^+ + e^-$
radiative association photodissociation (reverse reaction)	$A + B \Rightarrow AB + h\nu$ $h\nu + AB \Rightarrow B + A$
neutral exchanges ion-molecule exchanges	$AB + D \Rightarrow BD + A$ $AB + D^+ \Rightarrow BD^+ + A$
charge transfer reactions	$AB + D^+ \Rightarrow AB^+ + D$
negative ion reactions	$A + B^- \Rightarrow AB + e^-$
three body reactions collisional dissociation (reverse reaction)	$A + B + M \Rightarrow AB + M$ $AB + M \Rightarrow A + B + M$

Table 1.2: *Gas-phase reactions in astrochemistry.*

In dense clouds, long exotic carbon-chain compounds, such as HC_5N , HC_7N [32] or HC_{11}N [33], are understood to be formed particularly starting from hydrocarbons, like C_2H_2 , reacting with C atoms or CN radicals [34]



There is considerable evidence for the important role of “cold” chemistry in dense clouds in explaining the origin of the enhanced isotopic fractionation found in comets and meteorites, as a consequence of the sensitivity of fractionation reactions to the gas temperature. The molecular zero-point energies can be an important factor in the gas phase kinetics considering the extremely low temperatures in the dark clouds. H_3^+ can be enriched of deuterium in the following equilibrium



as the process that goes from right to the left is slower than its reverse at 10 K. Also ions as CH_3^+ and CH_5^+ could go through similar reactions. The isotopic exchange between ^{13}C and ^{12}CO might lead to enhancements of ^{13}C in carbon monoxide and other organic molecules in general.

Hydrogen is the most abundant element in the Universe, and molecular hydrogen abundance is 10^4 times greater than second most abundant species, CO, and with respect to the OH radical. Gas-phase chemistry accounts for H_2 formation by the following mechanism



and



The first step in both these processes is a *radiative association* (**Equations 1.9** and **1.11**) and it is a common mechanism for many gas phase reactions occurring in the ISM. In the ISM, the pressure (or density) is such that energy transfer to a third particle during the bond formation (a three-body collision) would be an extremely rare event. An alternative route could be a radiative association as



However, the direct bonding of two hydrogen atoms is not significant because the

product, H_2 , has no permanent electric dipole moment and the only way for it to relax to the ground state would be by a quadrupole moment transition [35]. Such transitions, generally, have an intensity of four orders of magnitude lower compared to a dipole transition. This means that it's harder to detect, but, most of all, means that it is not an efficient process. There are other reactive pathways for hydrogen formation, however they are not likely to happen sufficiently to justify the observed abundance of H_2 in the ISM. That is the reason why interstellar dust, for long time considered to be inert, was proposed to participate in the chemistry of H_2 formation [36]. In the last decades, the idea of grains as efficient catalysts for H_2 synthesis and of many other molecules has gained more and more support [37].

1.3.2 Dust in the ISM

Interstellar dust is the microscopic solid part of the ISM, absorbing, emitting, and scattering at wavelengths across the electromagnetic spectrum. In other words, it obscures star light in its line-of-sight. So it comes as no big surprise that until a few decades ago astronomers were annoyed and frustrated by molecular clouds and the fact they couldn't see through them. But dust plays a vital role for interstellar chemistry; in reducing the VUV radiation, which causes molecular dissociation, and in catalysing the formation of H_2 , the most abundant interstellar molecule, as well as other species, such as CH_3OH . Grains can be investigated by measuring their spectroscopic features in both absorption and emission. From these studies it is now clear that the term "interstellar dust" actually refers to a variety of materials of widely varying properties. *Diffuse dust* is referred to dust existing in low-density ISM, in the diffuse clouds, dust in the outer parts of molecular clouds, investigated by VUV-Visible observations is called *outer-cloud dust*. Finally, the *inner-cloud dust* is observed by looking at the optical and NIR part of the spectrum deeply within the dense clouds.

The extinction of the radiation coming from the stars is by far the most studied of quantities in astronomy (**Figure 1.5**). It can be measured accurately over a wide range of wavelengths and for lines-of-sight sampling different physical conditions in the ISM. Observations confirm that the interstellar extinction curve shows a general trend as function of wavenumber despite the variation in grain composition and size in the ISM. The curve increases from left to right (see **Figure 1.5**), from NIR to the UV, showing a hump centered at *ca.* $4.6 \mu\text{m}^{-1}$ (217.5 nm).

Spectroscopy is a powerful tool to inform us about grain composition. In all

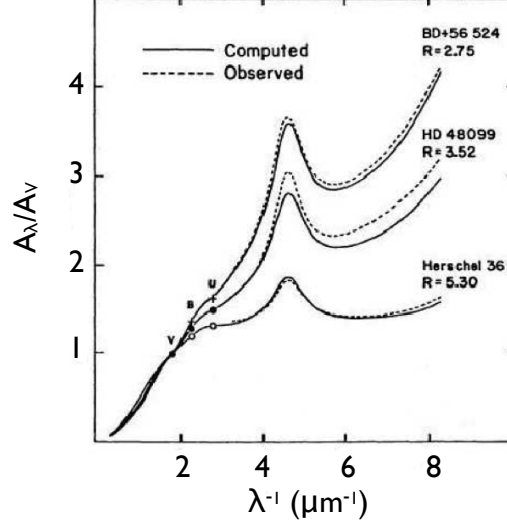


Figure 1.5: *Adaption of extinction curve reported in [38]. Three cases of a mean extinction law. Solid lines are obtained by fitting theoretical calculations and dashed line from the fitting of observational data. It is evident the common shape and feature at $4.60 \mu\text{m}^{-1}$ (217.5 nm).*

existing dust models, silicates are a key component. This is due to the strong evidence given by the absorption and emission bands between 1300 cm^{-1} and 500 cm^{-1} in the mid-IR that are characteristic of the Si-O stretching and of the O-Si-O bending modes. These features are usually more intense in the line-of-sight of oxygen-rich stars, that produce significant quantities of elemental silicon, while are very weak in the line-of-sight of carbon-rich stars. Despite the fact that the stoichiometry and composition of the silicates is still a matter of debate, it is not unreasonable to assume that they are:

1. orthosilicates with the formula $\text{Mg}_{2x}\text{Fe}_{2(1-x)}\text{SiO}_4$, where $0 \leq x \leq 1$.

Fayalite (Fe_2SiO_4) when $x = 0$;

Olivine (Mg,Fe) $_2\text{SiO}_4$ when $0 < x < 1$;

Forsterite (Mg_2SiO_4) when $x = 1$.

2. metasilicates with the formula $\text{Mg}_x\text{Fe}_{(1-x)}\text{SiO}_3$, where $0 \leq x \leq 1$.

Ferrosilite (Fe_2SiO_3) when $x = 0$;

Orthopyroxene (Mg,Fe) SiO_3 when $0 < x < 1$;

Enstatite (Mg_2SiO_4) when $x = 1$.

Recent findings seem to partially confirm this description. More than 50 dust particles were identified from the comet 81P/Wild 2 thanks to the NASA Stardust Interstellar Dust Collector [39]. Preliminary examination has classified seven dust

particle of probable interstellar origin, which are diverse in elemental composition, and crystal structure. Furthermore, two different size regimes were reported: three candidates are more than $1 \mu\text{m}$ in diameter ($\sim 3 \text{ pg}$ in weight), larger than the maximum dust size inferred for typical ISM grains from observations, while the other four are closer in size to the predicted values by astronomical means. A combination of X-ray diffraction, fluorescence, microscopy and FTIR revealed a composition rich in Si, O, Mg, Fe but also in S, suggesting a likely interstellar origin for these four particles (**Figure 1.6**). The presence of sulfide is still debated; most measurements indicate negligible depletion of sulfur in the ISM compared to the solar abundance that hints towards a lack of condensed sulfur-rich grains. However, since spectroscopy fails in a precise determination of ISM gas phase sulfur and to detect solid nanophase sulfides, the fact that FeS nanoparticles are a component of the ISM cannot be excluded on this basis.

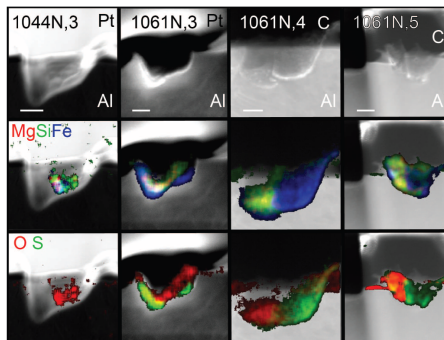


Figure 1.6: Top row reports the dark-field scanning transmission electron microscopy (STEM) images of the cross-section of the crater. composite element distribution maps shows the heterogeneous distribution of Mg-Si-Fe (central row) and the O-S (bottom row) in four candidates of probable interstellar origin. Scale bars indicate 100 nm. Pt and C refer to Focused Ion Beam deposited protective masks Image taken from [39]

Interstellar grains are unlikely to be only silicates. One of the reasons is that their production rate by all possible astronomical sources is an order of magnitude smaller than their destruction rate in the diffuse medium [9, 40–42]. Silica grains may be shielded by a layer of ice in cold clouds and by refractory organic material in the diffuse medium. The nature of the mantle is still today under debate, particularly about the strongest feature of the extinction curve at 217.5 nm ($4.6 \mu\text{m}^{-1}$ or also known as the 2175 \AA bump). Many candidates have been proposed as responsible for the hump, no single carrier is generally accepted. It is widely agreed that this transition is due to a $\pi \rightarrow \pi^*$ transition of a sp^2 carbon material. The first guess was graphite, however in that case the feature would be sensitive to the grain size, shape and coatings, which is not consistent with the observations [43, 44]. Moreover, the dust grains in circumstellar envelopes around carbon stars, which are the major sources of the carbonaceous material of

interstellar dust particles, are in amorphous form rather than graphitic [45]. In addition, physiochemical processes in the interstellar environment should make the carbonaceous grains disordered [46]. Despite this most experimental work relies on using highly oriented pyrolytic graphite (HOPG).

Others suggest that the hump carrier is a mixture of large PAHs. However, this is still controversial as experimentally the 217.5 nm feature in PAHs is generally accompanied by additional bands not observed in the interstellar extinction [47]. PAHs are also indicated as the most likely candidate to reproduce the Far UV region of the extinction curve. But since these species show strong peaks in the UV-Vis range, it is necessary to consider a mixture of many PAHs, which could produce a featureless continuum. Nevertheless this is still a matter of debate. In the region between 2.80 and 1.25 μm^{-1} (360 - 800 nm) there are many less intense peaks known as *Diffuse Interstellar Bands* (DIB). Among these, over 154 have been assigned with a reasonable certainty, while many others are still under debate. Probably the main carrier of such peaks are the ubiquitous PAHs, but also other more exotic species have been suggested as long chains with an odd number of carbon atom (C_{15} - C_{31}) and nanotubes [48] or fullerene ions (C_{60}^+) [49].

A reasonable and useful way to picture an interstellar grain is given by Li and Greenberg [46] as follows:

- medium size grains ($< 0.1\mu\text{m}$) thought to be made of a silicate core and a mantle of organic material, which is responsible for most of the features in the extinction curve. This dust is characteristic of dense clouds.
- small size grains ($0.003\mu\text{m}$), made of carbonaceous material, carrier of the $4.6 \mu\text{m}^{-1}$ band. This dust is characteristic of diffuse clouds.
- big PAHs with a smaller size than grains but with similar properties.

Mantle Composition

The mantle composition is extremely complex, enriched by molecules formed on the dust and in gas phase reactions accreting on the surface itself. Spectroscopy can help to identify these species. Looking at the SWS (short wavelength spectrometer) spectrum from the Infrared Space Observatory (ISO) (see **Figure 1.7** [50]), it is evident that water dominates over the other molecules in the ice mantle. Actually, the fractional abundance of H_2O as ice is typically of 10^{-4} with respect to H_2 and is comparable to that of the most abundant gas phase molecule containing heavy atoms like CO; the second most abundant species after H_2 in

cold clouds. The most evident feature of water is the O-H stretch around $3 \mu\text{m}$

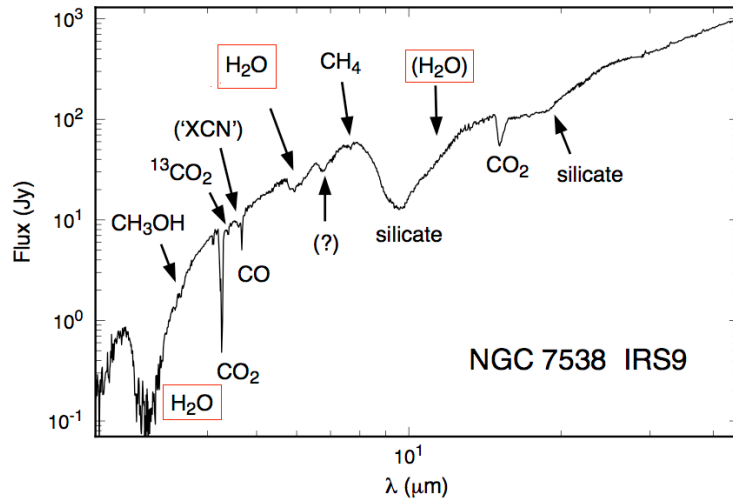


Figure 1.7: SWS spectrum of NGC 7538 URS9 adapted from [50]. The IR signatures, discussed in the text, of the main ice component are indicated and the water features are highlighted in red.

(3300 cm^{-1}). But a detailed interpretation, in terms of number density of the molecules, is complicated by the fact that other likely candidates have modes that fall at similar energy, for instance the N-H stretching modes of ammonia or amines are usually found at slightly higher wavenumbers, while C-H stretches are at lower. Further evidence of presence of water in the icy mantle of dust grains is the IR band assigned to the H-O-H bending mode. It is located in the $5 - 8 \mu\text{m}$ range ($2000 - 1250 \text{ cm}^{-1}$) centred at $6 \mu\text{m}$ (1667 cm^{-1}). But also in this case, features assigned to other molecules are superimposed on both the sides of the water band: $5.83 \mu\text{m}$ is attributed to HCOOH and H_2CO , $6.14 \mu\text{m}$ to NH_3 and $6.2 \mu\text{m}$ to aromatic compounds [51–53]. There is another useful feature of H_2O , it is the one assigned to the combination mode ($3\nu_L$, L means libration), but it's the weakest among the other water bands. It peaks at $4.5 \mu\text{m}$ (2200 cm^{-1}) and it's very broad, extending from $3.7 \mu\text{m}$ to $5 \mu\text{m}$ [54]. Actually it is just a baseline, a background component in a region dominated by $^{12}\text{CO}_2$, $^{13}\text{CO}_2$, CO and XCN (X could be a hydrogen, a methyl group or a longer carbon chain) features (**Figure 1.8**).

Of course water is not the only molecule in the icy mantle. CO_2 , as just mentioned above, has an asymmetric stretching mode at $4.27 \mu\text{m}$ (2342 cm^{-1}) (**Figure 1.8**) and a bending mode at $15 \mu\text{m}$ (667 cm^{-1}). CO_2 and CO are also abundant in the ice mantle with smaller abundances compared to solid water. Ices are also rich in methanol at more mature stages of cloud evolution, that forms from the hydrogenation of CO on the grains (mechanism shown in **Chapter 3**). CH_3OH is

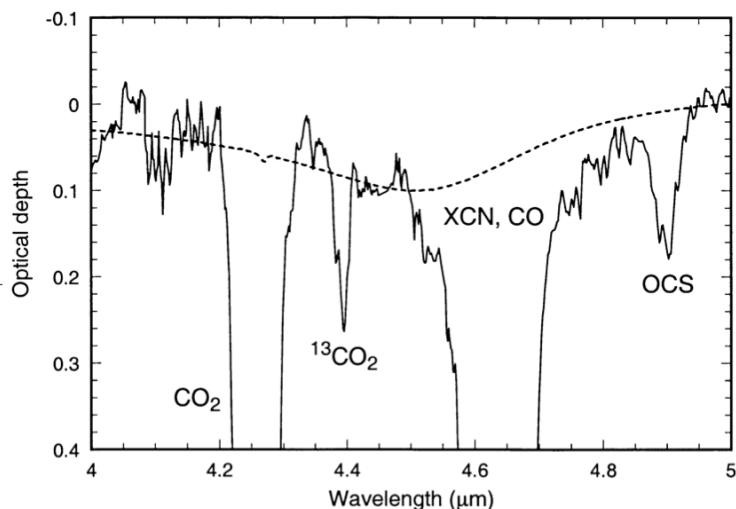


Figure 1.8: *Optical depth spectrum of W33A from 4 to 5 μm . The dashed curve is a laboratory spectrum of a $\text{H}_2\text{O}:\text{NH}_3$ mixture 100:9 ice at 50 K scaled conveniently to highlight the combination mode of water in the observed spectrum. Image taken from [55]*

detected through its bands at 3.54 (CH stretch at 2825 cm^{-1}) and/or $9.7\ \mu\text{m}$ (CO stretch at 1031 cm^{-1}). A recent laboratory study of Burke *et al.* [56] reported the potential for methanol to change the crystallisation kinetics of ASW, lowering the temperature of the phase change, it also affects the trapping and release of more volatile, guest molecules in the water matrix. For instance, the volcano desorption observed in binary water-dominated ices occurs at the ASW-CI transition; when methanol is added to the ice co-desorption with the bulk dominates. This result highlights the complex and sensitive dependence of physical processes, and likely chemical reactions, on the ice composition which is far from being trivial to model.

Concerning nitrogen-bearing species in interstellar ices, for long time, only the CN stretch mode at $4.62\ \mu\text{m}$ (2164 cm^{-1}) [57] was the sole evidence of their presence. Possible candidates could be both cyanates ($\text{R}-\text{O}-\text{C}\equiv\text{N}$) and isocyanates ($\text{R}-\text{O}-\text{N}\equiv\text{C}$), although the $\text{C}\equiv\text{N}$ stretch falls at higher energies (shorter wavelength) for nitriles in solid phase compared to isonitriles. N_2 , probably one of the most abundant species, has no dipole moment so it is not active in the microwave range nor in the IR, even though in principle some weak transitions are detectable due to electron cloud displacement induced by surrounding polar molecules. Its abundance is usually inferred from the N_2H^+ adduct². Detections of NH_3 , generally thought to be the precursor to nitriles [57], is complicated by the overlap between its vibrational modes with those from water. However some works reported the ammonia stretching mode at $2.95\ \mu\text{m}$ (3390 cm^{-1}) [58] and the

²This usually applies in the gas phase, but may be possible in the solid state if N_2H^+ abundance in solids is known.

inversion mode around $9.0 \mu\text{m}$ (1110 cm^{-1}) [59]. Gibb *et al.* [55] have published a 8 - 11 μm spectrum of W33A herein reported (**Figure 1.9**). The assignment

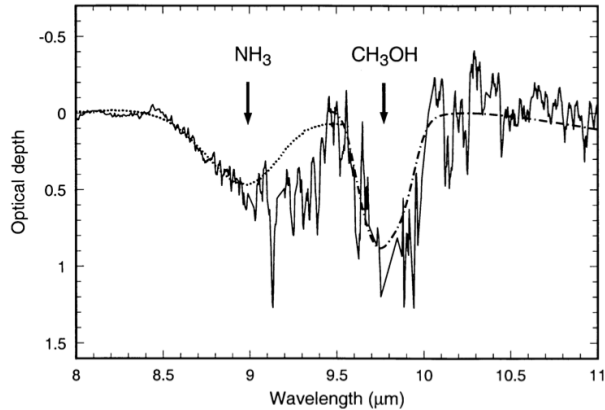


Figure 1.9: *Optical depth spectrum of W33A from 8 to 11 μm after further manipulation. In dotted curve the laboratory spectrum for $\text{H}_2\text{O}:\text{NH}_3$ mixture 100:9 ice at 50 K and dot-dashed curve for $\text{H}_2\text{O}:\text{CH}_3\text{OH}:\text{CO}_2$ (1.25:12:1.0) ice at 70 K. Image taken from [55]*

of the $9.0 \mu\text{m}$ feature to NH_3 and the one around $9.8 \mu\text{m}$ to CH_3OH was supported by laboratory experiments. Oxygen as O_2 suffers the same problem as N_2 detection, they are both “invisible” because of their zero dipole. However when surrounded by other molecules the transitions become weakly allowed, as the feature at $6.45 \mu\text{m}$ seems to prove [16]. In the end observations and careful analysis of spectra of ices associated with protostellar objects, like W33A, support an approximate composition of $\text{H}_2\text{O}:\text{CO}_2:\text{NH}_3:\text{CH}_4 \approx 100:17:14:3$ in the polar phase that is constant between different lines-of-sight. But other important identified compounds are CO , XCN , CH_3OH , OCS , H_2CO and HCOOH .

1.3.3 Evidence for PAHs in the ISM

PAHs are the largest molecules known in space and contain about 10-20% of the total available cosmic carbon. The presence of aromatic molecules (see **Figure 1.10**) in the ISM has been already mentioned, particularly in the dark clouds. They have been found in objects, such as meteorites, and in interplanetary dust particles, indicating their presence in the early stages of the formation of our Solar System. PAHs are thought to be responsible for certain UV-Visible absorption bands [60], known as DIBs, first observed in 1930. The identification of these compounds is also suggested by logical considerations and, as just mentioned, by spectroscopy. In the former case, given the harsh conditions of interstellar environments, especially in the diffuse clouds, PAHs possess the thermodynamic stability to exist in various charge states, (ionised or in neutral form) and the absorption of energetic photons, in the UV range, rarely leads to dissociative

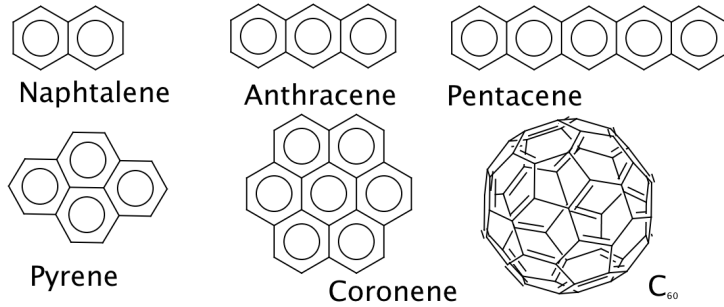


Figure 1.10: Some Polycyclic Aromatic hydrocarbons and the fullerene C₆₀.

states. Significant effort has been made to collect a large database of laboratory PAH spectra of various sizes and charges in order to help the identification of observed ISO features. In fact, strong emission peaks at 3.3, 6.2, 7.7, 8.6, 11.3 and 12.7 μm are common to a large number of astronomical sources and generally known as Unidentified Infrared (UIR) bands (**Figure 1.11**). These bands find a

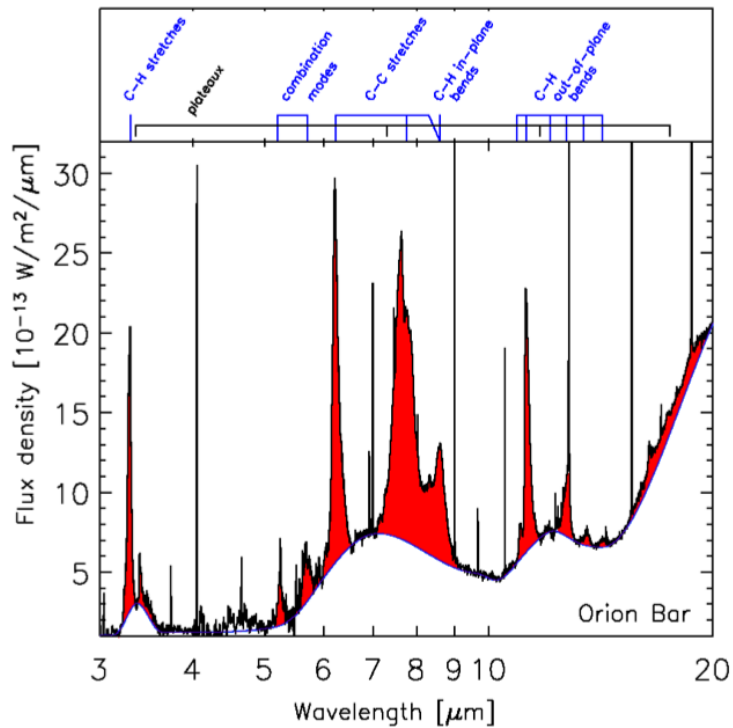


Figure 1.11: PAH emission features in the SWS spectrum of the Orion Bar PDR. Assignments in terms of C-H and C-C stretches are indicated. Image taken from [16, 61].

good match with the vibrational modes of PAHs [62]. It is clear that no single compound fits all the features in terms of band position and intensity, but the scientific community agrees that they are consistent with a mixture of neutral and ionised PAHs [63]. It is worth noting that ionisation alters significantly the PAH IR spectrum. Allamandola *et al.* [63] showed that going from neutral

PAHs (**Figure 1.12a**) to the cationic form (**Figure 1.12b**) there is a strong change on the relative intensities and a minor influence on peak frequencies. In particular, the C-H stretch is more intense for a neutral aromatic molecule and the opposite holds for C-C modes. This result has been correlated to the

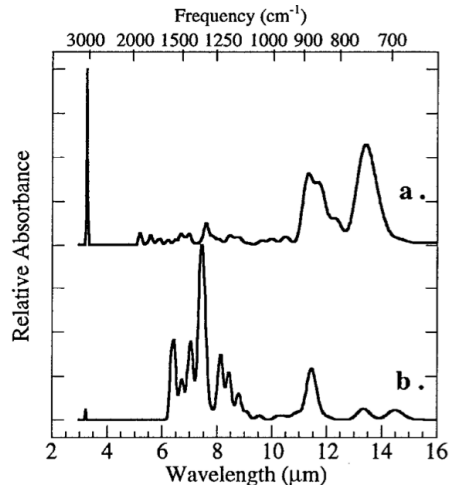


Figure 1.12: The absorption spectrum of (a), six neutral PAHs compared with the spectrum produced by the same PAHs in (b), the cationic form (anthracene, tetracene, 1, 2-benzanthracene, chrysene, pyrene, and coronene). Image taken from [63].

variations in the IR features observed going from diffuse clouds, strong VUV photons flux, to deeply in the molecular clouds, weak VUV flux. A certain variety of functional groups could be expected on the PAHs, such as $-\text{CH}_3$, $-\text{OH}$, $-\text{NH}_2$ or $-\text{CO}$, fortunately high-quality spectra give an insight to this matter and allow us to exclude or confirm the presence of each of these groups. For instance there seems to be no large aliphatic moieties due to the lack of strong 3.4, 6.85 and 7.3 μm features. Moreover high abundances ($\sim 10\%$) of deuterated aromatic PAHs (PADs) compounds have been estimated by the bands at 4.4 and 4.65 μm in two sources. It is important to stress the point that generally the comparison is carried between the emission features in a SWS ISO spectrum and the absorption spectrum produced from a mixture of neutral and cationic PAHs. It is well known that in principle a transition from a vibrational state to another of higher energy and *vice versa* overlap only if the population of the rotational levels is perfectly “symmetric” in the absorption and in the emission. Therefore a perfect match is ideally very hard to achieve. It is also true that this effect is negligible compared to the differences between the laboratory sample and the multitude of situations possible in the ISM considering ionisation, hydrogenation, de-hydrogenation and excitation energy processing the aromatic molecules. It has also been suggested that following a non-thermal excitation mechanism, such as absorbing a single UV photon, the aromatic compound emitting the IR radiations, must be small, 10 \AA , corresponding to PAHs with a number of carbon atoms going from 30 to

1.4 Grain Processes

Today, the importance of the role played by the interstellar dust in the chemical evolution of the star forming regions [64] is well known. The need to understand the heterogeneous chemistry, that takes place on the surface of the micrometre-sized grains, and the complexity of the physical processes occurring therein, has promoted a wide range of research, both theoretical and experimental in the last few years. Some interesting results of these studies are reported in the following paragraphs.

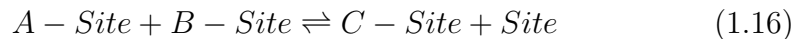
1.4.1 Dust-catalysed Chemistry

In 1963, Gould and Salpeter [36] first suggested that dust grains could catalyse the formation of those molecules whose abundance was not explained by gas phase only models. The best known case is H_2 formation. There are three accepted mechanisms for the synthesis of molecules on surfaces:

- **Langmuir-Hinshelwood:** This mechanism proposes that both molecules adsorb:



where A and B are general species and Site represent the adsorption site. The adsorbed molecules (A-Site and B-Site) diffuse over the surface until they encounter each other and undergo a bimolecular reaction culminating in the desorption of the product



- **Eley-Rideal:** Only one of the two reactants is thermally accommodated on the surface.



The second atom (or molecule) reacts directly with A-Site and reacts directly:



- **Harris-Kasemo:** Also known as *hot atom mechanism*. A hot atom collides with the surface, accommodates poorly and diffuses with negligible interaction. When it reaches an adsorbed atom (or molecule), it reacts.

These three mechanisms have a different dependence on the surface coverage, morphology and kinetic energy of the incoming atom. Grain-promoted H₂ formation in interstellar environments was first investigated by using atomic beams of H and D obtained by radio-frequency dissociation of molecular precursors [65, 66] and an olivine substrate. The results showed HD detection by a quadrupole mass spectrometer both while dosing and later in TPD experiments. It was stated that the formation of H₂ on a surface is a thermally-activated process, with a threshold temperature that likely depends on the nature (chemical composition and structure) of the grain surface. Evidence of second-order kinetics in the low-coverage regime means that, at low surface temperature, atoms accommodate on the surface and remain localised without recombining. But once this thermal energy threshold is reached, increasing the substrate temperature leads to a decline of the product yield due to a reduced residence time. Another laboratory experiment by Hornekær *et al.* [67] on HD formation on amorphous solid water films shows a very efficient recombination mechanism that occurs at surface temperatures as low as 8 K. The fact that the yield decreases going from H and D simultaneous to a sequential dosing, suggests fast mobility of H and D atoms even at this temperature. It was also concluded that these atoms undergo a Langmuir-Hinshelwood or hot atom recombination to form HD, which is then retained in the pores until the temperature is externally increased sufficiently to cause molecular desorption. Bond formation in molecular hydrogen releases about 436 kJ mol⁻¹ (4.52 eV), part of this energy can be transferred to the substrate and part of it stored as internal energy so that the H₂ newly formed is found in excited rovibrational states. This was proved by Resonance Enhanced Multiphoton Ionisation (REMPI) experiments which suggest that the rotational temperature of the H₂ molecules in conditions close to those of the ISM can be considerably higher than the target's surface temperature [68]. Recent experimental findings and kinetic simulations have highlighted the role of PAHs in the catalysis of molecular hydrogen formation [69–72]. This seems to confirm the observations that correlate the high rates of H₂ formation with the high abundances of PAHs in photo-dissociation/photo-dominated regions (PDRs). Coronene (C₂₄H₁₂), that presents three inequivalent binding sites for additional H atoms, is observed to form the complete deuterated analogue C₂₄D₃₆ when exposed to sufficiently high fluences of D atoms. Following the first addition of an H atom, C₂₄H₁₂D can bind to a second H atom *via* a barrierless reaction leading to C₂₄H₁₂D₂, which might either form H₂ *via* the Eley-Rideal abstraction mechanism or undergo further hydrogenation.

1.4.2 Laboratory Studies of Desorption from Icy Mimics

Reactions occurring in gas phase and those on dust grains are not isolated processes, molecules freeze onto the grains, enriching the icy mantle composition, and taking part in the heterogeneous processes happening on the grain surface. The products of such synthesis desorb from the mantle at some stage, then go through other reactive pathways in the gas phase. Therefore it is clear that desorption from dust is a “key step in coupling the chemistry of the grains and mantles to astrophysical gas phase” [73] (**Figure 1.13**). In the literature, four

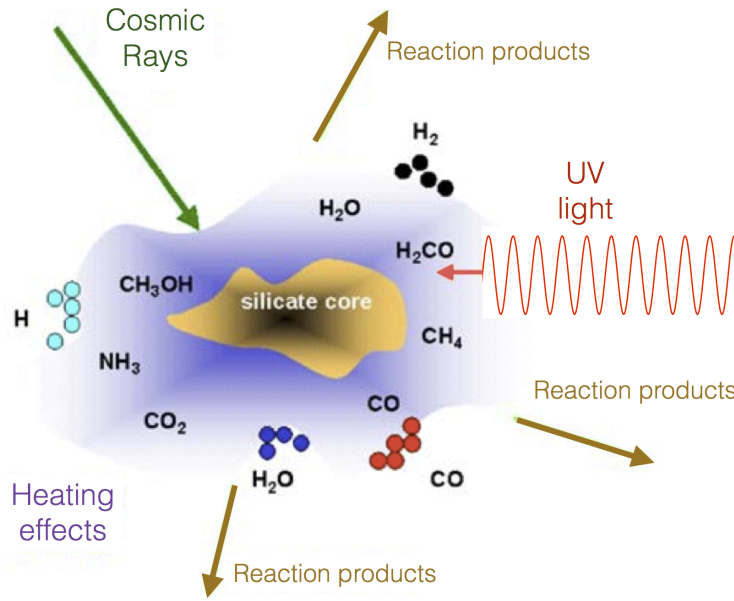


Figure 1.13: A cartoon summarising the complex physicochemical processes occurring on the interstellar dust [74].

basic mechanisms promoting desorption can be found:

1. Desorption promoted by *Reaction Enthalpy Release*;
2. Desorption promoted by *Collision*;
3. Desorption promoted by *Heating*;
4. Desorption promoted by *Electronic Excitation*.

Of course these processes all occur in parallel, however in certain conditions some are more significant while others are negligible. For instance in hot cores and hot corinos, thermal desorption dominates [75] and in the cold dense regions desorption is mainly due to electronic excitation. The latter can follow cosmic ray (H^+) bombardment or a direct and indirect interaction with VUV radiation [76].

Desorption Promoted by Reaction Enthalpy Release

Chemical reactions in astrophysical environments are often exothermic. The recombination of two H atoms releases 436 kJ mol^{-1} , between two O atoms 498 kJ mol^{-1} and up to 946 kJ mol^{-1} comes from N_2 formation. When reaction occurs on a surface this energy can be directed toward two different channels; it could be transferred to the grain molecules solvating the product as it reaches thermal equilibrium and/or may result in translational and rovibrational excitation of the gaseous products. The closed shell molecules mentioned above are weakly bound to the grain surface (physisorption), thus the enthalpy release is mainly converted to internal energy of the desorbed product, but in the other cases it is dissipated quickly ($\sim \text{ps}$ scale) into the heat bath provided by the grain itself. Lamberts *et al.* recently re-evaluated the effect of exothermicity in ice mantles on interstellar grains [77]. Focusing on the formation of two OH radicals by the reaction $\text{H} + \text{OH}_2$, the two products will move away from each other due to their high opposite relative momenta. Therefore, the excess energy from the reaction is employed to overcome diffusion barriers over the surface and eventually desorb. However, if the reaction occurs in the bulk, the two OH fragments might collide with the neighbouring molecules, losing their original directionality, and undergo a further reaction to form H_2O_2 .

Desorption Promoted by Collision

The energy necessary for a molecule to desorb can be transferred by inelastic collisions. Generally speaking, the latter can occur between atom and atom; between molecule and molecule; between atom and molecule; between ion and atom or molecule. In the ISM, perhaps one of the most frequent desorption mechanism is due to proton “hitting” the surface, in other words H^+ to collide with molecules in the icy mantle promoting physiochemical processes. This phenomenon is also known as cosmic ray interaction with interstellar dust leading to *cosmic ray sputtering*. The kinetic energy possessed by these ions ranges from keV to GeV; exceeding the typical surface binding energy (less than 50 kJ mol^{-1} , 0.52 eV). The question to answer is where does this translational energy go after the collision. Proton scattering can occur with both electrons and nuclei as a function of the target material nature and composition. Recalling the Rutherford experiment, it is not surprising that codes like SRIM/TRIM [78] suggest that cosmic rays, at energies between 10 keV and 100 MeV, are mainly scattered by electrons (*stopping* in the language of nuclear material science). Nuclear scattering, on the other hand, becomes important above 100 MeV. However it is very important to stress that in such software the scattering (stopping) and desorp-

tion (sputtering) are represented by simple empirically parameterised “billiard ball dynamics”. The electron scattering of the target molecules can result in a secondary electron flux with energies sufficient (up to 500 eV) to induce chemical reactions and desorption.

Desorption can also, in principle, take place subsequent to an inelastic collision with gas phase atoms or molecules. But in the dense cold regions of the molecular cloud this is unlikely to happen because the kinetic and vibrational energy (0.1 kJ mol^{-1}) transferable to the target is too small even for a weakly bound species. The process may become more significant mainly in shocked regions ($\sim 2400 \text{ kJ mol}^{-1}$ [79]). Finally, it is worthwhile highlighting that in proto-planetary disks around young stellar objects, grain-grain collisions might be important as a mechanism for desorption, however there is little or no attention to laboratory studies in this latter area.

Desorption Promoted by Heating

In star forming regions, gravitational collapse leads to a general increase of the temperature, warming the icy grains and favouring thermal desorption. In order to understand this mechanism in the past 20 years there has been extensive research in that direction by means of laboratory surface science experiments. The key findings seem to highlight four types of behaviour of adsorbed and absorbed molecules on astrophysically relevant icy mimics of ASW:

- Species, like NH_3 or CH_3OH , interact with water ice *via* hydrogen bonds and desorb together with the H_2O ;
- Species like H_2S or CH_3CN , with a sublimation temperature (T_{sub}) greater than the pore collapse temperature ($T_{porecollapse}$) could be trapped in the pores as they are deposited from the gas phase or form within the bulk of the mantle. When deposited on top of ASW, these species will desorb at their characteristic desorption temperature. When co-deposited with ASW, thus if formed in ice or accommodated in the pores, co-desorption and release during crystallisation (volcano desorption) are dominant. The smaller molecules, that possess limited ability to diffuse through the pores, can exhibit sub-monolayer desorption from ASW too;
- Species like N_2 or O_2 , with a sublimation temperature (T_{sub}) smaller than the pore collapse temperature ($T_{porecollapse}$). In this case experiments about CO on water [80, 81] are exemplary. Temperature Programmed Desorption (TPD) results show four features corresponding to the desorption of: solid

CO, CO adsorbed on H₂O, CO absorbed into pores of amorphous solid water (ASW), CO co-desorbing with H₂O;

- Species like metals or sulfur that desorb exclusively at higher temperatures (typically at 100°C).

While such a classification is effective and straightforward, the scientific community is becoming aware of its limits especially when considering phase transitions and more complex systems than binary mixtures [82]. As previously described, methanol, for instance, lowers the temperature of the phase change in ASW and favours co desorption over volcanoes [56] for a third species, such as CO or OCS. Finally, it is important to point out that the substrate may play a crucial role on the desorption and on the morphology of the adsorbed layer. Recent work TPD experiments on benzene (C₆H₆), a prototypical PAH, on ASW and C₆H₆ on amorphous silica are illuminating in that sense [83, 84]. C₆H₆ is more strongly bound to other C₆H₆ molecules than to water, hence it forms islands on that substrate. In contrast, the binding of C₆H₆ with the silica surface prevails over the bulk C₆H₆ interactions resulting in wetting behaviour.

Desorption Induced by Electronic transition (DIET)

The electronic excitation can also drive chemical transformations and physical processes such as phase change or desorption. The latter can be favoured by interaction with the electromagnetic field of interstellar radiation (photo-desorption) and by inelastic scattering with charged particles (ion-promoted desorption / electron-promoted desorption). DIET is often invoked to explain the observed gas phase abundances of species, such as water or CO₂, in conditions where their accretion value would be close to zero or, in other words, where complete freeze-out onto dust grains might otherwise be expected.

Photon-stimulated desorption (PSD), or simply photo-desorption (PD) of molecules from interstellar ice analogues has been widely investigated because it seems to play a significant role in protoplanetary disks and generally in all those regions where ices are exposed to VUV photons *e.g.* edges of clouds [85–87]. For instance, the work of Hollenbach *et al.* [88] concluded that the H₂O gas abundance is enhanced by orders of magnitude when including the photo-desorption rate of water ice in their model of molecular cloud using the results by Westley *et al.* [89]. A theoretical study of Andersson and van Dishoeck [90] shows that it is possible to have H₂O photo-desorption upon VUV absorption in the top five monolayers of an amorphous ice surface at 10 K. Once the water molecule is excited, it will dissociate into the H and OH fragments so as to: (i) recombine and desorb, (ii)

less likely, recombine releasing energy to desorb a neighbouring molecule, or (iii) an energetic H atom can kick-out another water molecule in the ice (*Kick-out mechanism*), even with translational energies as low as ~ 0.7 eV. In most cases, however, removal of an H₂O molecule from the ice is in the form of separate H and OH fragments. Öberg and coworkers using a VUV lamp emitting in the range 7.0- 10.5 eV, irradiated H₂O and D₂O ices at surface temperatures in the range 18-100 K [91]; they presented results suggesting that photo-desorption of H₂O and OH from the ice occurs mainly *via* direct excitation processes. Diffusion and reactions of photoproducts also occur as minor processes that gain importance with increasing temperature.

However, there is not much work investigating the role the electronic excitation due to low energy particle scattering and long wavelength (≥ 200 nm) radiation absorption. In fact, although the Lyman- α line (121.6 nm) is ubiquitous in the ISM [92], it is also true that the interstellar radiation field is strongest in the range going from the near-UV to the mid-IR [93]. Solid H₂O absorbs at the long wavelength end of this spectral region thanks to overtone and combination modes, while PAHs and unsaturated aliphatic compounds absorption moves from the UV to visible as the conjugation increases. For instance, when irradiating with 250 nm photons binary layered C₆H₆ and H₂O ices, transitionally hot C₆H₆ and H₂O are produced [94–96]. It is noteworthy that water has a negligible absorption cross-section in this spectral range, therefore, C₆H₆ desorption is explained in terms of direct absorption (“direct adsorbate-mediated”) or by absorption of the sapphire substrate (“substrate-mediate”), while H₂O desorption can only be rationalised in terms of excitation transfer from the C₆H₆ (“indirect adsorbate-mediated”).

Electronic excitation can also be induced by secondary electrons following the scattering of charged particles incident on the grain. It can be thought of as an indirect electronic effect, especially for cosmic ray stopping. These electrons lose energy and may generate excitons within the solid state that are resonant with valence electronic excitations of organic molecules [97–99]. Returning to the C₆H₆ and H₂O system in astronomical relevant environment, the work of Throver *et al.* [96, 100] shows evidence of enhanced electron-promoted C₆H₆ desorption requiring the presence of H₂O. It was suggested that the results are consistent with the generation of long-lived 10 to 12 eV excitons in the H₂O ice film diffusing to the surface of the film. Similar behaviour was found for CH₃CN during irradiation with 250-400 eV electrons [101]. These findings are in marked contrast with the dominant chemistry observed during 200 keV protons bombardment in the same

work, whereas in the former case no detectable products were identified. Since the passage of H^+ ions through the film might generate secondary electrons in the same energy range as for those used for direct exposure, the different outcome is paradoxical at first glimpse. The explanation, at least concerning acetonitrile, is found in relation with the film thickness: chemistry is a bulk process in the ice, while desorption is confined to a selvedge, therefore EPD, despite a large cross-section, will be a minor channel compared to reactive events in thicker ices. Further details about this competition between the two processes will be discussed in **Chapter 5**.

1.5 Astrochemical models

In order to understand and reproduce the physics and chemistry which determine the observed abundances of species in the ISM, astrochemists develop models, based on reaction networks, which are constantly updated. Hence, the chemical evolution in a certain environment, *e.g.* dark clouds is simulated and the results, in terms of abundances as a function of time compared to the observations. The three main and most established databases available for the astrochemistry community are: (i) the UMIST³ Database for Astrochemistry (UDfA) developed by Tom Millar and first released in 1991 [102–105]; (ii) the second one is the Ohio State University (OSU) database, initially created by Prasad and Huntress [106], then revised and updated by Herbst and collaborators [107]; and, (iii) the most recent database is the KInetic Database for Astrochemistry (KIDA) [108]. Despite the data content of the above mentioned databases being similar, differences exist because of (i) different choices of which reactions to include in the network, (ii) different approaches to estimating those rate coefficients not yet investigated in the laboratory, (iii) different choices of experimental values for rate constants when more than one is reported in the literature, (iv) different approximations regarding the temperature dependence of reactions. The OSU is best suited for cold sources, whereas the UDfA provides values also for hotter conditions (100 K such as in diffuse clouds). KIDA, on the other hand, is the most versatile as it includes reactions for modelling a plethora of astronomical environments and planetary atmospheres.

In principle, the master equations for simulations must be the same regardless the chemical network adopted; these kinetics describe the formation and the destruction of molecules both in the gas phase and on grain surfaces: For instance,

³UMIST: University of Manchester Institute of Science and Technology

for a species i , it follows:

$$\begin{aligned}\frac{dn_i}{dt} &= \sum_{l,m} k_{lm} n_l n_m + \sum_m k_m n_m - n_i [\sum_{i \neq l} k_l n_l + \sum_n k_n] + k_i^{des} n_i^s - k_i^{ads} n_i \\ \frac{dn_i^s}{dt} &= \sum_{l,m} k_{lm}^s n_l^s n_m^s + \sum_m k_m^s n_m^s - n_i^s [\sum_{i \neq l} k_l^s n_l^s + \sum_n k_n^s] - k_i^{des} n_i^s + k_i^{ads} n_i\end{aligned}\tag{1.21}$$

where n_i is the gas-phase concentration of the species i ; k_{lm} is the rate constant for the reaction between the species l and m forming i ; k_m is the rate constant for the photo-processes and/or cosmic ray processes leading to the formation of species i ; k_l is the rate constant for the destruction reaction of the species i with l ; k_n is the rate constant for the destruction of the species i due to electron or photon or ion irradiation; k_i^{des} and k_i^{ads} are the desorption and absorption rate constants respectively; the superscript s refers to the adsorbed species and processes on the grain.

The rate constants themselves are often not singly determined values, but each of them can be expressed by a more complex equation. However, it is beyond the scope of this thesis to list all the possible reaction rates and mechanisms which might be included in a model. Therefore, only a few equations, the main ones most relevant and widely used for the gas-phase chemistry and the surface-catalysed chemistry will be presented here. The notation, compatible with **Equation 1.21**, belongs to the one defined by the *Nautilus model* [109, 110] referring to the KIDA database. For instance, *ionisation and dissociation rates* by direct excitation due to the cosmic rays, k_{CR} , or UV photons, k_{FUV} , are calculated by the model using equations as those suggested by Wakelam *et al.* [108]:

$$k_{CR} = A_i \xi_{CR}\tag{1.22}$$

$$k_{FUV} = A e^{-CA_v} \chi$$

where ξ_{CR} is the cosmic ray ionisation rate (typical value of $1.3 \times 10^{-17} \text{ s}^{-1}$ [109]); A_v is the visual extinction; χ is the FUV flux, while A_i and A are parameters defining the rate coefficients; the exponential term containing the parameter C takes into account the continuum attenuation from the dust (Lambert-Beer law); A_i , A and C are taken from the networks. These expressions can also be applied to dissociation of molecules on the grain induced by cosmic rays or energetic photons [111, 112].

Gas-phase bimolecular reaction constant rates follow an Arrhenius trend:

$$k(T) = \alpha \left(\frac{T}{300} \right)^\beta e^{(-\frac{\gamma}{T})} \quad (1.23)$$

where α is the part of reaction rate which is temperature independent; β expresses the temperature dependence of the pre-exponential; γ is the activation barrier ⁴; α , β , and γ are also tabulated for each reaction in the database.

Coefficients for accretion of the species i by *deposition* from the gas-phase are given by:

$$k_i^{ads} = \sigma_d \bar{v}_i n_i n_d \quad (1.24)$$

where σ_d and n_d designate the cross-section and the number density of the grains respectively, while \bar{v}_i is the velocity of the species i and n_i is its density. A specific case of this equation will be presented in the **Chapter 2** as **Equation 2.3**.

Thermal desorption from the surface is described by the well-known *Polanyi-Wigner* equation which will be best explained in the next chapter (**Equation 2.10**), its rate coefficient is:

$$k_i^{des} = \nu_0 e^{-\frac{E_d}{T_g}} \quad (1.25)$$

where E_d is the desorption energy in Kelvin for the species i ; T_g is the grain temperature, often assumed to be 10 K in dark clouds; the pre-exponential ν_0 is expressed as:

$$\nu_0 = \sqrt{\frac{2n_s E_d}{\pi^2 m_i}} \quad (1.26)$$

where n_s is the number of adsorption sites and m_i is the mass of the species i .

Desorption due to *heat release* following exothermic reactions can also be implemented and it is for the Nautilus model:

$$P = \left[1 - \frac{E_d}{E_{reac}} \right] \quad (1.27)$$

where P is the probability for desorption, E_d is the desorption energy of the product molecule, and E_{reac} is the released reaction energy.

Reactive accretion on the grain surface can occur according to the three mechanisms outlined in this chapter; assuming a Langmuir-Hinshelwood formation, the

⁴In general astronomers report energies as temperatures. The conversion in units of Kelvin is obtained by dividing the energy in J mol⁻¹ by the Avogadro's number and the Boltzmann's constant.

reaction rate between the species i and j is given by:

$$r_{ij} = \kappa_{ij}(r_i^{diff} + r_j^{diff})n_i^s n_j^s n_d \quad (1.28)$$

where n_i^s and n_j^s are the number of molecules of the species i and j respectively; r^{diff} is the diffusion rate; κ_{ij} is the probability for the reaction to take place and it depends exponentially on the reaction activation barrier, E_a :

$$\kappa_{ij} \propto \alpha e^{-\frac{E_a}{T_g}} \quad (1.29)$$

Furthermore, especially for a Langmuir-Hinshelwood reaction, diffusion of the reactants over the surface must be taken into account. This can be described as *thermal hopping* between a site to another requiring a time t_{hop} defined as:

$$t_{hop} = \nu_0^{-1} e^{\frac{E_{diff}}{T_g}} \quad (1.30)$$

where E_{diff} is the energy barrier to overcome for the species to diffuse, while ν_0 and T_g were defined above. Light atoms, such as H or even O atoms, can also diffuse over the surface by *quantum tunnelling* [113], and this mechanism should also be included in the model.

More processes can be added to those listed so far and implemented into the model increasing its level of complexity. However, the computational cost rises with the number of species that are considered, rather than with the number of physical and chemical equations. For instance, in recent work, the Nautilus model was employed to simulate the evolution in time of more than 700 species between atoms, molecules, ions, and radicals in dark clouds [109]: 403 species in the gas phase and 199 on grain surfaces were followed, for a total of 8624 reactions. In the case of dark clouds, initial conditions are defined by the elemental abundances in diffuse clouds, hence, the model is let to run under the constraint of the mass conservation law. The calculated abundances can be converted as relative abundances by dividing by the column densities of hydrogen (*e.g.* $6 \times 10^{22} \text{ cm}^{-2}$ [114]), hence, the results are compared with the observational data and discussed.

Non-thermal desorption has only been implemented recently in the astrochemical models: desorption due to cosmic rays has been considered as result of local impulsive heating [109, 115] leading to a temporary increase of the grain temperature; photon-stimulated desorption has traditionally been treated as a non-selective mechanism with uniform yields for all species [116], and models have evolved to consider molecule-specific yields only in the last years following reliable experi-

mental results [91, 117]. The beneficial interplay between novel laboratory results and astrochemical models is clear: while the latter ones validate and test the impact of new experimental findings by predicting the observations, the laboratory results are crucial to the development of more in-depth and accurate reaction networks.

1.6 Thesis Outline

This thesis focuses on thermal and non-thermal desorption of simple molecules on interstellar ice mimics. Emphasis is given to the balance between the adsorbate-adsorbate and adsorbate-surface interactions. The change in the types of the intermolecular bindings within simple ices (pure substances on silica, and binary layered systems) is probed by means of surface science techniques, and the resulting experimental findings placed in an astrophysical context. In particular, EPD of C_6H_6 on different substrates is extremely sensitive on the nature of the underlayer, demonstrating the crucial role of hydrogen bonding in propagating electronic excitation to the solid-vacuum interface where C_6H_6 desorption can occur. An overview of the contents illustrated in the next chapters follows below:

- **Chapter 2** presents the two ultrahigh vacuum chambers used in the experiments reported in this thesis. A brief description will follow on the surface science techniques, computational tools and background employed relevant for this study.
- **Chapter 3** describes the film growth of three different ices: H_2O , CH_3OH , and $(CH_3CH_2)_2O$ on amorphous silica (SiO_2) at cryogenic temperatures (20 K). Firstly the thermal desorption of these pure species will be discussed highlighting the interplay between the intermolecular and adsorbate-surface interactions established. Then infrared spectroscopy was used to probe the solids by an *in situ* technique providing complementary information to TPD. Ballistic deposition and a combination of the two techniques above reveal evidence of a relatively high energy barrier for diffusion of water on bare silica grain with implications on the ice mantles growth in different cooling environments (*e.g.* dense clouds *vs.* diffuse clouds).
- **Chapter 4** considers the interaction of C_6H_6 with two different substrates (CH_3OH and $(CH_3CH_2)_2O$) compared to previously reported studies of the same aromatic molecule on compact ASW. Both TPD and IR spectroscopy were used once again to outline a picture of the C_6H_6 film growth on these

ices with the aid of high level computational chemistry on model systems that highlights the key types of interactions. The results draw also special attention to unexpected changes to the ice morphology and even phase during standard background vapour deposition of C_6H_6 , along with the intrinsic challenging character of experiments on organic molecules with similar thermal behaviour.

- **Chapter 5** extends the study on electron-promoted desorption of C_6H_6 on H_2O previously reported by Thrower [100, 118] changing the film thickness of the underlayer and its phase. EPD of C_6H_6 was then also investigated from CH_3OH , and $(CH_3CH_2)_2O$ with direct evidence revealed of the impact that hydrogen-bonding and carbon-rich ices have on the suggested mechanism in transferring the excitation. Preliminary, but convincing evidence of enhanced electron-induced chemistry in methanol or ether ices, as opposed to almost negligible EPD of the adsorbate, embeds the interplay among the physiochemical processes following ionisation of interstellar dust mantles. Conclusions related to the impact of these observations on the early phase of icy interstellar grain chemistry is finally discussed by comparison with photo-desorption.
- **Chapter 6** concludes the thesis, summarising the key findings with emphasis on future developments of the presented work.

Bibliography

- [1] D. H. Wooden, S. B. Charnley and P. Ehrenfreund, *From the interstellar medium to comet particles and molecules.*, University of Arizona Press, Tucson, 2004.
- [2] A. P. Jones, *Philos. Trans. R. Soc.*, 2001, **A359**, 1961.
- [3] C. Chiappini, D. Romano and F. Matteucci, *Mon. Not. R. Astron. Soc.*, 2003, **339**, 68.
- [4] C. J. Wheeler, C. Sneden and J. W. J. Truran, *Annu. Rev. Astrophys.*, 1989, **27**, 279.
- [5] C. F. McKee and J. P. Ostriker, *Astrophys. J.*, 1977, **218**, 148.
- [6] M. G. Wolfire, C. F. McKee, D. Hollenbach and A. G. G. M. Tielens, *Astrophys. J.*, 2003, **587**, 278.
- [7] D. A. Grabelsky, R. S. Cohen, L. Bronfman, P. Thaddeus and J. May, *Astrophys. J.*, 1987, **315**, 122.
- [8] P. F. Goldsmith and W. D. Langer, *Astrophys. J.*, 1978, **222**, 881.
- [9] A. P. Jones, A. G. G. M. Tielens, D. J. Hollenbach and C. F. McKee, *Astrophys. J.*, 1994, **433**, 797.
- [10] A. P. Jones, A. G. G. M. Tielens and D. J. Hollenbach, *Astrophys. J.*, 1996, **469**, 740.
- [11] A. P. Jones, *J. Geophys. Res.*, 2000, **105**, 10257.
- [12] A. G. G. M. Tielens, *Astrophys. J.*, 1998, **499**, 267.
- [13] B. T. Draine, *Annu. Rev. Astron. Astrophys.*, 2003, **41**, 241.
- [14] B. T. Draine, *Space Sci. Rev.*, 2009, **143**, 333.
- [15] I. N. J. Evans, *Annu. Rev. Astron. Astrophys.*, 1999, **37**, 311.

- [16] E. F. van Dishoeck, *Annu. Rev. Astron. Astrophys.*, 2004, **42**, 119.
- [17] R. J. Trumpler, *Preliminary results on the distances, dimensions and space distribution of open star clusters*, University of California Press, 1930.
- [18] R. Lucas and H. S. Liszt, *Astron. Astrophys.*, 2000, **358**, 1069.
- [19] A. M. Shaw, *Astrochemistry. From astronomy to astrobiology.*, John Wiley & Sons, 2006.
- [20] W. D. Langer, E. F. van Dishock, E. A. Bergin, G. A. Blake and A. G. G. M. Tielens, *Chemical evolution of protostellar matter. In Protostars and Planets IV*, University of Arizona, Tucson, 2000.
- [21] M. J. Mumma, M. A. Disanti, N. dello Russo, M. Fomennkova, K. Magee-Sauer, C. D. Kaminski and D. X. Xie, *Science*, 1996, **272**, 1310.
- [22] K. Hiraoka, T. Takayama, A. Euchii, H. Handa and T. Sato, *Astrophys. J.*, 2000, **532**, 1029.
- [23] P. M. Solomon, K. B. Jefferts, A. A. Penzias and R. W. Wilson, *Astrophys. J.*, 1971, **168**, L107.
- [24] B. L. Ulich and E. K. Conkling, *Nature*, 1974, **248**, 121.
- [25] L. E. Snyder and D. Buhl, *Astrophys. J.*, 1971, **163**, 147.
- [26] M. P. Bernstein, J. P. Dworkin, S. A. Sandford, G. W. Cooper and L. J. Allamandola, *Nature*, 2002, **416**, 401.
- [27] S. Pizzarello and G. W. Coope, *Nature*, 2001, **36**, 897.
- [28] R. Gomes, H. F. Levison, K. Tsiganis and A. Morbidelli, *Nature*, 2005, **435**, 466.
- [29] S. L. Miller, *Science*, 1953, **117**, 528.
- [30] J. Woodall, M. Agúndez, A. J. Markwick-Kemper and T. J. Millar, *Astron. Astrophys.*, 2007, **466**, 1197.
- [31] V. Wakelam, E. E. Herbst, J. C. Loison, I. W. M. Smith, V. Chandrasekaran, B. Pavone, N. G. Adams, M. C. Bacchus Montabone, A. Bergeat, K. Béroff, V. M. Bierbaum, M. Chabot, A. Dalgarno, E. F. van Dishoeck, A. Faure, W. D. Geppert, D. Gerlich, D. Galli1, E. Hébrard, F. Hersant, K. M. Hickson, P. Honvault, S. J. Klippenstein, S. Le Picard,

- G. Nyman, P. Pernot, S. Schlemmer, F. Selsis¹, I. R. Sims, D. Talbi, J. Tennyson, J. Troe, R. Wester and L. Wiesenfeld, *Astrophys. J. Supp.*, 2012, **199**, 21.
- [32] J. Dickenson, W. D. Langer and T. Velusamy, *Astrophys. J.*, 2001, **558**, 693.
- [33] M. B. Bell, P. A. Feldman, M. J. Travers, M. C. McCarthy, C. A. Gottlieb and P. Thaddeus, *Astrophys. J.*, 1997, **483**, L61.
- [34] I. Cherchneff and A. E. Glassgold, *Astrophys. J. Lett.*, 1993, **419**, L41.
- [35] D. Hollenbach and E. E. Salpeter, *Astrophys. J.*, 1971, **163**, 155.
- [36] R. J. Gould and E. E. Salpeter, *Astrophys. J.*, 1963, **138**, 393.
- [37] J. M. Greenberg, *Surf. Sci.*, 2002, **500**, 793.
- [38] J. S. Mathis, *Annu. Rev. Astron. Astrophys.*, 1990, **28**, 37.
- [39] A. J. Westphal, M. R. Stroud, H. A. Bechtel, F. E. Brenker, A. L. Butterworth, G. J. Flynn, D. R. Frank, Z. Gainsforth, J. K. Hillier, F. Postberg, A. S. Simionovici, V. J. Sterken, L. R. Nittler, C. Allen, D. Anderson, A. Ansari, S. Bajt, R. K. Bastien, N. Bassim, J. Bridges, D. E. Brownlee, M. Burchell, M. Burghammer, H. Changela, P. Cloetens, R. Davis, A. M. Doll, C. Floss, E. Grün, P. R. Heck, R. Hoppe, B. Hudson, J. Huth, A. Kearsley, A. J. King, B. Lai, J. Leitner, L. Lemelle, A. Leonard, H. Leroux, R. Lettieri, W. Marchant, R. Ogliore, W. J. Ong, M. C. Price, S. A. Sandford, J. A. Sans Tresseras, S. Schmitz, T. Schoonjans, K. Schreiber, G. Silversmit, V. A. Solé, R. Srama, F. Stadermann, F. Stephan, J. Stodolna, S. Sutton, m. Trieloff, P. Tsou, T. Tyliczszak, B. Vekemans, L. Vincze, J. Von Korff, N. Wordsworth, D. Zevin, M. E. Zolensky and Stardust@home, *Science*, 2014, **345**, 6198.
- [40] B. T. Draine and E. E. Salpeter, *Astrophys. J.*, 1979, **28**, 37.
- [41] B. T. Draine and E. E. Salpeter, *Astrophys. J.*, 1979, **28**, 37.
- [42] C. F. McKee, *IAU Symposium 135, Interstellar Dust*, L. A. Allamandola and A. G. G. M. Tielens (eds), 1989, 431.
- [43] B. T. Draine, *Astrophys. J.*, 1988, **333**, 848.
- [44] B. T. Draine and S. Malhotra, *Astrophys. J.*, 1993, **414**, 632.
- [45] M. Jura, *Astrophys. J.*, 1986, **303**, 327.

- [46] A. Li and M. Greenberg, *Astron. Astrophys.*, 1997, **323**, 566.
- [47] C. Joblin, A. Léger and P. Martin, *Astrophys. J.*, 1992, **393**, L79.
- [48] Z. Zhou, M. Y. Sefir, L. Zhang, M. S. Hybertsen, M. Steigerwald and L. Brus, *Astrophys. J.*, 2006, **638**, L105.
- [49] H. Kroto and M. Jura, *Astron. Astrophys.*, 1992, **263**, 275.
- [50] D. C. B. Whittet, W. A. Schutte, A. G. G. M. Tielens, A. C. A. Boogert, T. de Graauw, P. Ehrenfreund and P. A. Gerakines, *Astron. Astrophys.*, 1996, **315**, L357.
- [51] W. A. Schutte, *Astron. Astrophys.*, 1996, **315**, L333.
- [52] W. A. Schutte, K. van der Hucht, D. Whittet, A. Boogert, A. Tielens, P. Morris, J. Greenberg, P. Williams, E. van Dishoeck, J. Chiar and T. de Graauw, *Astron. Astrophys.*, 1998, **337**, 261.
- [53] W. A. Schutte, D. Whittet, A. Boogert, A. Tielens, P. Morris, J. Greenberg, P. A. Gerakines, E. van Dishoeck, J. Chiar, P. Ehrenfreund and T. de Graauw, *Astron. Astrophys.*, 1999, **343**, 966.
- [54] W. Hagen, A. Tielens and J. Greenberg, *Chem. Phys.*, 1981, **56**, 367.
- [55] E. L. Gibb, D. C. B. Whittet, W. A. Schutte, A. C. A. Boogert, P. Chiar, J. E. Ehrenfreund, P. A. Gerakines, J. V. Keane, A. Tielens, E. F. van Dishoeck and O. Kerkhof, *Astrophys. J.*, 2000, **536**, 347.
- [56] D. J. Burke and W. A. Brown, *Mon. Not. R. Astron. Soc.*, 2015, **448**, 1807.
- [57] Y. J. Pendleton, A. Tielens, A. T. Tokunaga and M. P. Bernstein, *Astrophys. J.*, 1999, **513**, 294.
- [58] J. E. Chiar, A. G. G. M. Tielens, D. C. B. Whittet, W. A. Schutte, A. C. A. Boogert, D. Lutz, E. F. van Dishoeck and M. P. Bernstein, *Astrophys. J.*, 2000, **537**, 749.
- [59] J. H. Lacy, H. Faraji, S. A. Sandford and L. J. Allamandola, *Astrophys. J.*, 1998, **501**, L105.
- [60] P. Ehrenfreund, S. Rasmussen, J. H. Cleaves and L. Chen, *Astrobiology*, 2006, **6**, 490.
- [61] E. Peeters, L. J. Allamandola, S. Hudgins, Hony and A. G. G. M. Tielens, *ASP Conf. Ser.*, 2004, **309**, 141.

- [62] W. W. Duley and D. A. Williams, *Mon. Not. R. Astron. Soc.*, 1981, **196**, 269.
- [63] L. J. Allamandola, D. M. Hudgins and S. A. Sandford, *Astrophys. J. Lett.*, 1999, **511**, L115.
- [64] V. S. Wakelam, I. W. M. Smith, J. Herbst, E. Troe, W. Geppert, H. Linnartz, K. Öberg, E. Rouleff, M. Agundez, P. Pernot, H. M. Cuppen, J. C. Loison and D. Talbi, *Space Sci. Rev.*, 2010, **156**, 13.
- [65] V. Pirronello, C. Liu, L. Shen and G. Vidali, *Astrophys. J.*, 1997, **475**, L69.
- [66] V. Pirronello, O. Biham, C. Liu, L. Shen and G. Vidali, *Astrophys. J.*, 1997, **483**, L131.
- [67] L. Hornekær, A. Baurichter, V. V. Petrunin, D. Field and A. C. Luntz, *Astrophys. J.*, 2003, **302**, 1943.
- [68] J. S. A. Perry, J. M. Gingell, K. A. Newson, J. To, N. Watanabe and S. D. Price, *Meas. Sci. Technol.*, 2002, **13**, 1414.
- [69] V. Mannella, L. Hornekær, J. D. Thrower and M. Accolla, *Astrophys. J. Lett.*, 2012, **745**, L2.
- [70] J. D. Thrower, B. Jørgensen, E. E. Friis, S. Baouche, V. Mannella, A. C. Luntz, M. Andersen, B. Hammer and L. Hornekær, *Astrophys. J.*, 2012, **752**, 3.
- [71] J. D. Thrower, E. E. Friis, A. L. Skov, B. Jørgensen and L. Hornekær, *Phys. Chem. Chem. Phys.*, 2014, **3381**, 16.
- [72] A. L. Skov, J. D. Thrower and L. Hornekær, *Faraday Discuss.*, 2014, **168**, 223.
- [73] M. R. S. McCosutra and M. P. Collings, *European Conference on Laboratory Astrophysics*, EAS Publications Series, 2012, vol. 58, p. 315.
- [74] R. Srama, T. Stephan, E. Grün, N. Pailer, A. Kearsley, A. Graps, R. Laufer, P. Ehrenfreund, N. Altobelli, K. Altwegg, S. Auer, J. Baggaley, M. J. Burchell, J. Carpenter, L. Colangeli, F. Esposito, S. F. Gree, H. Henkel, M. Horanyi, A. Jäckel, S. Kempf, N. McBride, G. Moragas-Klostermeyer, H. Krüger, P. Palumbo, A. Srowig, M. Trieloff, P. Tsou, Z. Sternovsky, O. Zeile and H. Röser, *Exp. Astron.*, 2009, **23**, 303.

- [75] S. Viti, M. P. Collings, J. W. Dever, M. R. S. McCoustra and D. A. Williams, *Mon. Not. R. Astron. Soc.*, 2004, **354**, 1141.
- [76] E. Herbst and H. M. Cuppen, *P. Natl. Acad. Sci. USA*, 2006, **103**, 12257.
- [77] T. Lamberts, X. de Vries and H. M. Cuppen, *Faraday Discuss.*, 2014, **168**, 327.
- [78] J. F. Ziegler, J. P. Biersack and M. D. Ziegler, *The Stopping and Range of Ions in Solids*, Pergamon Press, New York, 2008.
- [79] T. Sashida, T. Oka, K. Tanaka, K. Aono, S. Matsumura, M. Nagai and M. Seta, *Astrophys. J.*, 2013, **774**, 10.
- [80] M. P. Collings, J. W. Dever, H. J. Fraser, M. R. S. McCoustra and D. A. Williams, *Astrophys. J.*, 2003, **583**, 1058.
- [81] M. P. Collings, J. W. Dever, H. J. Fraser and M. R. S. McCoustra, *Astrophys. Space Sci.*, 2003, **285**, 633.
- [82] D. J. Burke and W. A. Brown, *Phys. Chem. Chem. Phys.*, 2010, **12**, 5947.
- [83] J. D. Thrower, M. P. Collings, F. J. M. Rutten and M. R. S. McCoustra, *Mon. Not. R. Astron. Soc.*, 2009, **394**, 1510.
- [84] J. D. Thrower, M. P. Collings, F. J. M. Rutten and M. R. S. McCoustra, *J. Chem. Phys.*, 2009, **131**, 244711.
- [85] K. Willacy and W. D. Langer, *Astrophys. J.*, 2000, **544**, 903.
- [86] C. Dominik, C. Ceccarelli, D. Hollenbach and M. Kaufman, *Astrophys. J. Lett.*, 2005, **635**, L85.
- [87] D. Hollenbach, M. Kaufman, E. A. Bergin and G. J. Melnick, *Astrophys. J.*, 2009, **690**, 1497.
- [88] V. Guzmàn, J. Pety, J. R. Goicoechea, M. Gerin and E. Roueff, *Astron. Astrophys.*, 2011, **534**, A49.
- [89] M. S. Westley, R. A. Baragiola, R. E. Johnson and G. A. Baratta, *Nature*, 1995, **373**, 405.
- [90] S. Andersson and E. F. van Dishoeck, *Astron. Astrophys.*, 2008, **491**, 907.
- [91] K. Öberg, H. Linnartz, R. Visser and E. F. van Dishoeck, *Astron. Astrophys.*, 2009, **693**, 1209.

- [92] W. Landsman and T. Simon, *Astrophys. J.*, 1991, **366**, L79.
- [93] J. S. Mathis, P. G. Mezger and N. Panagia, *Astron. and Astrophys.*, 1983, **128**, 212.
- [94] J. D. Thrower, D. J. Burke, M. P. Collings, A. Dawes, P. D. Holtom, F. Jamme, P. Kendall, W. A. Brown, I. P. Clark, H. J. Fraser, M. R. S. McCoustra, N. J. Mason and A. W. Parker, *Astrophys. J.*, 2008, **673**, 1233.
- [95] J. D. Thrower, D. J. Burke, M. P. Collings, A. Dawes, P. D. Holtom, F. Jamme, P. Kendall, W. A. Brown, I. P. Clark, H. J. Fraser, M. R. S. McCoustra, N. J. Mason and A. W. Parker, *J. Vac. Sci. Technol. A*, 2008, **26**, 919.
- [96] J. D. Thrower, A. G. M. Abdugalil, M. P. Collings, M. R. S. McCoustra, D. J. Burke, W. A. Brown, A. Dawes, P. D. Holtom, N. J. Mason, F. Jamme, H. J. Fraser and F. J. M. Rutten, *J. Vac. Sci. Technol. A*, 2010, **28**, 799.
- [97] J. C. Ashley, *IEEE trans. Nucl. Sci.*, 1980, **27**, 1453.
- [98] N. G. Petrik and G. A. Kimmel, *J. Chem. Phys.*, 2005, **123**, 054702.
- [99] J. Bergeld and D. Chakarov, *J. Chem. Phys.*, 2006, **125**, 141103.
- [100] J. D. Thrower, M. P. Collings, F. J. M. Rutten and M. R. S. McCoustra, *Chem. Phys. Lett.*, 2011, **505**, 106.
- [101] A. Abdugalil, D. Marchione, J. D. Thrower, M. P. Collings, M. R. S. McCoustra, F. Islam, M. E. Palumbo, E. Congiu and F. Dulieu, *Phil. Trans. A*, 2013, **371**, 20110586.
- [102] T. J. Millar, A. Bennett, J. M. C. Rawlings, P. D. Brown and S. B. Charnley, *Astron. Astrophys.*, 1991, **87**, 585.
- [103] T. J. Millar, P. R. A. Farquhar and K. Willacy, *Astron. Astrophys.*, 1997, **121**, 139.
- [104] Y. H. Le Teuff, T. J. Millar and A. J. Markwick, *Astron. Astrophys.*, 2000, **146**, 157.
- [105] J. Woodall, M. Agúndez, A. J. Markwick and T. J. Millar, *Astron. Astrophys.*, 2007, **466**, 1197.
- [106] S. S. Prasad and J. W. T. Huntress, *Astrophys. J.*, 1980, **43**, 1.

- [107] E. Herbst, <http://faculty.virginia.edu/ericherb/research.html>, website, 2008.
- [108] V. Wakelam, H. E., J.-C. Loison, I. W. M. Smith, V. Chandrasekaran, B. Pavone, N. G. Adams, M. C. Bacchus-Montabonel, A. Bergeat, K. Béroff, V. M. Bierbaum, M. Chabot, A. Dalgarno, v. E. F., A. Faure, W. D. Goppert, D. Gerlich, D. Galli, E. Hébrard, F. Hersant, K. M. Hickson, P. Honvault, S. J. Klippenstein, S. Le Picard, G. Nyman, P. Pernot, s. Schlemmer, F. Selsis, I. R. Sims, d. Talbi, J. Tennyson, J. Troe, R. Wester and L. Wiesenfeld, *Astrophys. J. Suppl. Ser.*, 2012, **199**, 21.
- [109] L. Reboussin, V. Wakelam, S. Guilloteau and F. Hersant, *Mon. Not. R. Astron. Soc.*, 2014, **440**, 3557.
- [110] D. Semenov, *Astron. Astrophys.*, 2010, **552**, A42.
- [111] R. T. Garrod, S. L. Widicus Weaver and E. Herbst, *Astrophys. J.*, 2008, **682**, 283.
- [112] J. Kalvāns, *Astrophys. J.*, 2015, **803**, 52.
- [113] M. Minissale, E. Congiu, S. Baouche, H. Chaabouni, A. Moudens, F. Dulieu, M. Accolla, S. Cazaux, G. Manicó and V. Pirronello, *Phys. Rev. Lett.*, 2013, **111**, 053201.
- [114] J. K. Jørgensen, F. L. Schöier and E. F. van Dishoeck, *Astron. Astrophys.*, 2004, **416**, 603.
- [115] T. I. Hasegawa and E. Herbst, *Mon. Not. R. Astron. Soc.*, 1993, **261**, 83.
- [116] J. F. Roberts, J. M. C. Rawlings, S. Viti and D. A. Williams, *Mon. Not. R. Astron. Soc.*, 2007, **382**, 733.
- [117] K. Öberg, E. F. van Dishoeck and H. Linnartz, *Astron. Astrophys.*, 2009, **496**, 281.
- [118] J. D. Thrower, *PhD thesis*, Heriot-Watt University, 2009.

Chapter 2

Experimental and Computational Methods

Contents

2.1	Introduction	44
2.2	From Theory to Vacuum Techniques	45
2.3	Ultrahigh Vacuum Chambers	49
2.4	The Beam Rig	49
2.4.1	Instrumentation	50
2.4.2	Sample Mounting	52
2.4.3	Substrate Heating and Temperature Control	54
2.4.4	Line-of-sight Detection	56
2.4.5	Thin Film Deposition	58
2.5	The Ice Rig	63
2.5.1	Instrumentation	63
2.5.2	Sample Mounting and Cryogenic System	65
2.5.3	Glass Gas Lines	67
2.6	From Metal Substrates to Grain Analogues	68
2.7	Experimental Techniques	71
2.7.1	Temperature Programmed Desorption	71
2.7.2	Reflection-Absorption Infrared Spectroscopy	74
2.8	Computational Chemistry	79
2.8.1	Hartree-Fock Method	79
2.8.2	MP2-CCSDT Methods	81
2.8.3	Towards Statistical Large Systems	84

2.1 Introduction

There are three different approaches to investigating the role of interstellar grains in the molecular clouds, and more generally in the ISM.

- Observations
- Computational studies
- Experiments

The first one is perhaps the most direct and straightforward way to gain an insight about icy-mantle compositions and abundances of molecules both in the gas phase and in the solid state. The source of information is mainly the spectroscopic features in a large range of wavelengths and along different lines-of-sight. Theoretical work can be ideally split into two *modus operandi*. The first, essentially a top-down approach, focuses on modelling thousands of reactions and hundreds of species in order to couple empirical results and observations. The other relies on the tools of modern computational chemistry (quantum mechanics, molecular mechanics and hybrid methods) to describe the relevant physics and chemistry from the bottom up. Laboratory experiments, on the other hand, are the keystone of a proper and reliable understanding of the physics and chemistry in the ISM. Gas phase spectra initially helped observations by identifying the detected molecular spectroscopic features, then chemical reactions were investigated in laboratories under similar extreme conditions as in the ISM in order to explain the observed abundances. However, in the last 30 years, it has been realised that great benefits accrue from laboratory surface science, especially concerning the understanding of interstellar ices composition and chemical evolution by means of molecular beam techniques, surface scattering, and spectroscopy. Among these three approaches, the latter sets the boundaries and background to this PhD project. Therefore an overview about basic gas kinetics and experimental techniques is presented in the following paragraphs. This chapter will first outline the importance of vacuum technology, the theory behind it and its applications, as to describe the two experimental rigs and then the techniques used to collect the data presented in this thesis. Furthermore, some calculations were carried out to aid experimental interpretation, therefore the theory and the fundamental principles of the methods used will be reported.

2.2 From Theoretical Background to Vacuum Techniques

The study of the atom-surface and molecule-surface systems is fundamental to understanding some crucial aspects of heterogeneous catalysis, new materials synthesis and gas storage (*e.g.* H₂) on surfaces. A simple model is the following. When a gas phase particle hits a surface, which is assumed to be clean, it can be back-scattered, can get trapped on the surface for a definite time before desorbing or is adsorbed indefinitely. In the latter case, the kinetic energy of the incoming particle is transferred to the surface itself exciting phonons or to the internal degrees of freedom (rovibrational excitement and relaxation) of the molecule itself. On the surface, *chemisorption sites*, where the particle binds chemically forming chemical bonds, and *physisorption sites*, where the particle interacts by non-covalent forces, predominantly van der Waals in nature, can be distinguished. Moreover, in the latter case, when the atom (molecule) is weakly bound it can diffuse over the surface and may eventually be chemisorbed. Most of the time, the long range attraction leading to physisorption is dominated by dispersion forces. The mathematical foundation that describes this is different from that describing the interaction between two particles (molecules or atoms) in the gas phase as it arises from the collective effect of all the atoms and/or molecules within the surface. For instance, considering a neutral particle incoming to the surface, the long range attraction potential is mainly given by **Equation 2.1**:

$$U(z) = -\frac{2\pi C\rho_s}{m-2} \int_{z=D}^{z=\infty} \frac{dz}{z^{m-2}} = -\frac{2\pi C\rho_s}{(m-2)(m-3)} \frac{1}{D^{m-3}} \quad (2.1)$$

if $m > 3$, and assuming that the global interaction is simply the sum of many single attractions between the atom/molecule and a particle in the surface. C is a constant; ρ_s is the solid density; D is the distance; and m is the exponent reported by the law describing the interaction between the incoming particle with the single particle of the surface ($-\frac{C}{r^m}$). When $m = 6$:

$$U(z) = U(D) = -\frac{C_3}{D^3} \quad (2.2)$$

Another important property of the surface is the energy associated with the plasmons and magnons within the surface itself. The former describe the electric dipole propagation-dispersion along the surface; the latter magnetic dipoles propagation. Plasmons are involved when the interaction between incoming gas phase particle and surface takes place; magnons, also known as quantised spin waves, are related to ferromagnetic and antiferromagnetic properties of the crystal lattice.

The experimental study of “elementary” physical and chemical processes on surfaces needs ultrahigh vacuum (UHV) conditions (see **Table 2.1**) to avoid surface contamination; and to isolate the dynamical aspects of the single phenomena of interest in the best way possible. At atmospheric pressure, these processes occur in parallel and their identification and control is not achievable.

Grade	Range / mbar
Rough	1000 - 1
Medium	1 - 10^{-3}
High	10^{-3} - 10^{-7}
Ultra	10^{-7} - 10^{-12}

Table 2.1: Grades of vacuum and relative pressure ranges. Note that the pressure between the Earth and the Moon is 10^{-7} - 10^{-8} mbar and interplanetary space is less than 10^{-14} mbar

The simple kinetic theory of gases is enough to explain why surface science benefits from vacuum techniques. The rate of collisions for a gas with a surface, R_c , expressed in units of molecules, time and area, is given by:

$$R_c = \frac{1}{4}n\bar{v} \quad (2.3)$$

where n is number of molecules per volume and \bar{v} is the average velocity obtained from the Maxwell-Boltzmann distribution. Typical values are $\bar{v} = 4 \times 10^4 \text{ cm s}^{-1}$ and $n = 3 \times 10^{19} \text{ molec cm}^{-3}$. **Table 2.2** shows τ , the time taken to grow a complete monolayer at a pressure P . Thus, it is clear that only in UHV is the

P / mbar	R_c / molecule $\text{cm}^{-2} \text{s}^{-1}$	τ / s
1	$3 \times 10^{23} (\approx \frac{1}{2} \text{mol cm}^{-2} \text{s}^{-1})$	3×10^{-9}
10^{-7}	3×10^{13}	30
10^{-11}	3×10^9	$3 \times 10^5 (\approx 92 \text{ h})$

Table 2.2: Table reporting number of collisions and time for a monolayer to form at different background pressures in the chamber.

surface cleanness assured for a sufficiently long period of time for an experiment to be conducted. But it must be stressed that the τ value in **Table 2.2** is a

lower limit because it was assumed that each collision corresponds to adsorption of a particle. Returning to **Equation 2.3**, it is possible to define the sticking probability (S) as the ratio between the adsorption rate (u_a) and the number of collisions (R_c):

$$S = \frac{u_a}{R_c} = \frac{u_a}{P} \sqrt{2\pi m k_B T} \quad (2.4)$$

T is the temperature, m is the mass and P the pressure. From here the adsorption rate is obtained:

$$u_a = \frac{SP}{\sqrt{2\pi m k_B T}} \quad (2.5)$$

Once it is clear that UHV conditions are crucial for surface science, it is straightforward to understand why they are also necessary conditions to study gas-grain processes in the ISM. On one hand, UHV guarantees an ability to investigate elementary phenomena occurring at the grain surface while on the other hand the actual conditions in the ISM are reproduced as closely as possible.

In molecular clouds, typical densities are of 10^4 particles cm^{-3} [1] (see **Table 1.1**), corresponding to an average pressure of 10^{-14} mbar¹. This is much lower than the base pressure in the two UHV chambers used for the experiments reported in this thesis, which is of $\sim 10^{-10}$ mbar. This mismatch between the dark clouds and laboratory conditions is intimately linked to the impossibility of replicating the astronomical times in the laboratory. However, this represents no real limitation to the reliability of the results. In the first place, the higher base pressure in the UHV chambers means that the surface can be assumed to be clean for ~ 10 hours on the same basis as the calculations that led to the values listed in **Table 2.2**. In contrast, a monolayer of contaminants would take much longer to form in a molecular cloud (typically 10-100 years). However, given the time scale of an ordinary experiment, ~ 5 hours, it is sensible to assume that the contamination is limited also in the experiments. In fact, the residual gas for both the chambers is mainly molecular hydrogen (H_2), coincidentally the most abundant molecule in the ISM, which is far too volatile to adsorb on the surfaces used in this work.

A lower base pressure means a lower flux of molecules colliding against the grain surfaces and being adsorbed. **Equation 2.5** can be applied to estimate this flux for H_2O in dark clouds: keeping in mind an average temperature of 10 K, a number density of 10^4 molecules cm^{-3} , and hence 10^{-14} mbar as pressure, and assuming unit sticking coefficient, the resulting flux (u_a^{ISM}) would be 2×10^7

¹By applying the ideal gas law.

molecules $\text{cm}^{-2} \text{s}^{-1}$ which can be conveniently rewritten as 2×10^{-7} molecules $\text{nm}^{-2} \text{s}^{-1}$. Defining the Langmuir unit (L) as $1 L = 10^{-6} \text{ mbar s}$, the 0.1 L dose used in the experiment was conducted by leaking a room temperature ($T = 300 \text{ K}$) gas at 10^{-9} mbar for 100 seconds. This results into a flux (u_a^{LAB}) of 3.6×10^{11} molecules $\text{cm}^{-2} \text{s}^{-1}$ or 3.6×10^{-3} molecules $\text{nm}^{-2} \text{s}^{-1}$. However, when depositing multilayer films, larger doses are required (*e.g.* 100 L), that will result in higher fluxes (3.6×10^{13} molecules $\text{cm}^{-2} \text{s}^{-1}$), given the higher pressure used (10^{-7} mbar).

Let us imagine the grain surface to be completely clean, with just one molecule of interest adsorbed, it is desirable to compare the time, τ_c , which is required for a second molecule to collide onto the first one using the typical ISM and the laboratory fluxes reported above. In order to make this comparison, the surface area, Σ_m , of the target adsorbed molecule has to be estimated. A crude, but sensible assumption, would be to consider the molecule as a sphere having radius r . The latter could be obtained by the average of the C-C, C-H, O-H bonds [2], giving 1.2 \AA for r , and $\sim 0.2 \text{ nm}^2$ for the area Σ_m . It follows that:

$$\tau_c^{ISM} = \frac{\Sigma_m}{u_a^{ISM}} \tag{2.6}$$

$$\tau_c^{LAB} = \frac{\Sigma_m}{u_a^{LAB}}$$

From **Equation 2.6** a value of ~ 12 days is obtained for τ_c^{ISM} , and values of 0.5 s and 55 s are estimated for τ_c^{LAB} corresponding to a 100 L and a 0.1 L dose respectively. This range of values is still larger than the time required for a molecule to roam over the surface and accommodate, which takes fractions of seconds, before being hit by another molecule. For example, kinetic Monte Carlo trajectories were calculated for CO adsorbed on a H_2O -dominated ice at 50 K [3] and demonstrated that the molecules are mobile only for a very short time; an estimated 7 ns when starting from a weakly bound surface site and diffusing to a strongly bound site and stopping. Hence, despite the mismatch between experimental and typical molecular cloud deposition fluxes, no change in the morphology of the deposited ice should be expected as surface accommodation is faster than the collision rate with other gas-phase molecules.

On the other hand, the surface temperature can significantly affect the rates of most of the thermal processes, such as diffusion or desorption, exhibit Arrhenius behavior. One of the instruments employed in this work is capable of reaching a base temperature of 20 K, which better resembles the cold parts of molecular clouds. The second machine, which operates at a base temperature of $\sim 110 \text{ K}$, therefore allows us to mimic the physics and chemistry in warmer environments

such as hot cores.

2.3 Ultrahigh Vacuum Chambers

The two experimental set-ups used to collect the data reported in this thesis are outlined as follows. The first apparatus presented here, called the Beam Rig, and the related experimental procedures used at the astrochemistry group at Heriot-Watt University, have been described in detail in previous works [4–6]; the design evolves from a set-up studied to look at the interaction dynamics between a gas molecule and a metal surface [7] using a combination of techniques such as Temperature Programmed Desorption (TPD); Reflection-Absorption Infrared Spectroscopy (RAIRS); Resonance Enhanced MultiPhoton Ionisation (REMPI) and Auger Electron Spectroscopy (AES). Since this chamber has been extensively used for the thesis’ results (**Chapter 4** and **5**), its description will be addressed in larger detail. Then, the second chamber’s description will follow. Called the Ice Rig, it was originally designed to investigate CO deposited on H₂O ices by means of TPD and RAIRS [8]. Results shown in **Chapter 3** were collected with this chamber. Also equipped with a quartz crystal microbalance (QCM), the chamber was later fitted with a dual atomic beam system to explore H₂O formation on interstellar dust grains [9].

2.4 The Beam Rig

The experimental set-up, called the Beam Rig (**Figure 2.1**), consists of a 40 cm diameter stainless steel chamber, capable of holding a base pressure as low as 10⁻¹⁰ Torr. To achieve this pressure, three types of pumps are used: a liquid

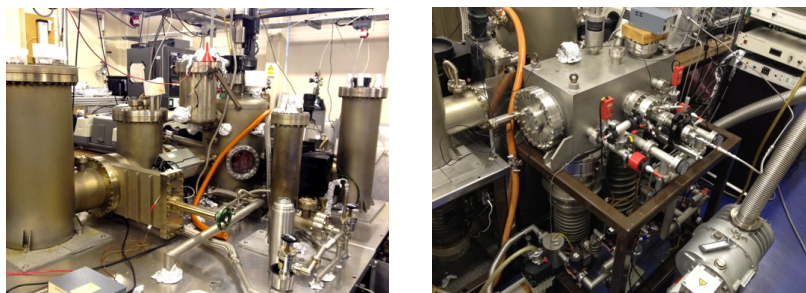


Figure 2.1: *Beam Rig: main chamber at the right and molecular beam source at the left.*

nitrogen trapped 9” oil diffusion pump, charged with *Santovac 5* (polyphenyl ether) and backed by an oil sealed mechanical rotary pump (Edwards E2M40); a small 8 dm³ s⁻¹ diode ion pump (Varian VacIon); and titanium sublimation pump (Leisk Engineering), coupled with a liquid nitrogen reservoir, attached

between the chamber and a gate valve next to the diffusion pump (see **Figure 2.2**). A second differential pumping stage for the molecular beam system is fitted inside the chamber and separated by internal walls with an orifice of a tunable diameter in line-of-sight to the centre of the chamber itself. Pumping is provided by a second liquid nitrogen trapped 6" oil diffusion pump (Edwards High Vacuum E06), also charged with *Santovac 5* and backed by an oil sealed mechanical rotary pump (Edwards High Vacuum E2M18). UHV conditions in the 10^{-10} Torr range are achieved routinely by baking the system at a temperature of 120 °C for 60 hours in order to reduce the amount of water adsorbed on the internal chamber walls and to let the substrate and filaments degas. After baking only the 9" diffusion pump trap is kept cooled by liquid nitrogen, which has the double advantage of preventing oil backstreaming and acting as cryopump condensing residual water. The nitrogen reservoir on top of the smaller diffusion pump is not used as it does not affect the background pressure of the chamber, however it would guarantee a better vacuum for the expansion of the molecular beam during direct dosing. The titanium sublimation pump is fired generally just after the bake, in order to pump away most of the residual oxygen. In addition to that, the ion pump helps to achieve a better quality vacuum by removing residual gases such as H₂ and CO. A schematic of the pumping arrangement is reported in **Figure 2.2**. An uncalibrated Bayard-Alpert type ion gauge (Caburn MDC Ltd.) with two tungsten filaments, and with an operating range of 10^{-3} - 4×10^{-10} mbar, is routinely used for background dosing and to check the base pressure. Diffusion pump backing pressure is measured using a Pirani gauge (Vacuum Generators). Both connected to the same controller (VG Pirani-Ion Gauge Controller) as the two extra Pirani gauges which are located in between each diffusion pump and the foreline trap adjacent the supporting rotary pump.

2.4.1 Instrumentation

The chamber is designed in such a way that experiments can be performed in two planes normal to the z-axis. Only the lower level was used for the results shown in this thesis so it will be described in greater detail. It will suffice to mention that the upper level was meant to look at single crystal substrates and therefore was equipped with an ion gun for cleaning, low energy electron loss (LEED) optics, and an electron gun plus an hemispherical electron analyser (VG Microtech CLAM 100) for Auger electron spectroscopy. Of all this, only the latter is still fitted to the chamber. As shown in **Figure 2.3** at the bottom of the chamber there is a quadrupole mass spectrometer (QMS, VG Microtech PC300D) with a modified design from its original line-of-sight to cross-beam QMS; further modi-

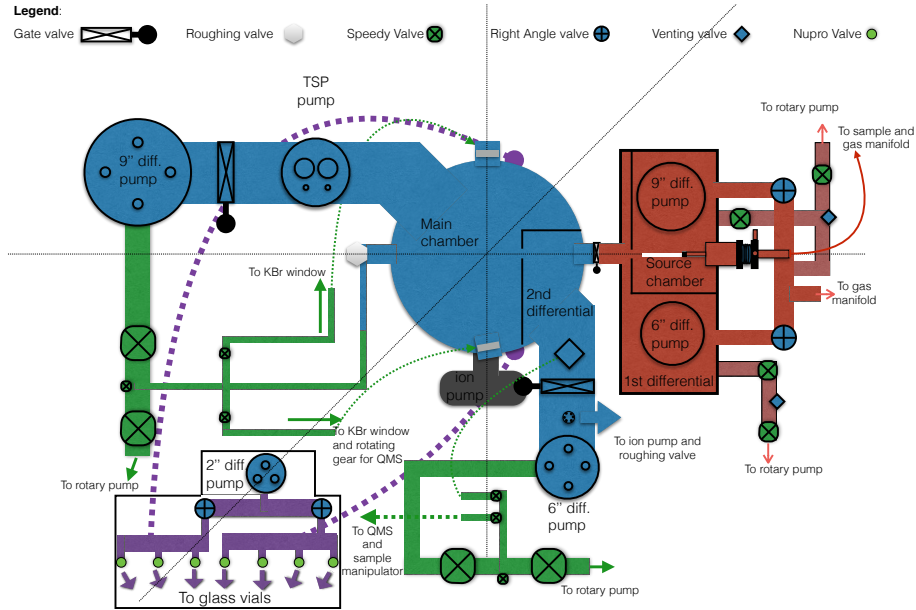


Figure 2.2: *General schematic highlighting the pump locations in the Beam Rig.*

fications were done by European Spectrometry Systems allowing pulse counting with new compatible electronics and new channeltron. The quadrupole is allocated on a flange connected to a differentially pumped rotary gear feedthrough allowing the QMS to form a semicircle around the centre of the chamber with temporary and negligible loss of the quality of the vacuum. The design was meant to perform angle resolved solid surface scattering experiments, but the angle can currently only be changed between 60° and 135° , without causing electrical shorts by twisting the wires and collisions against other parts of the equipment *e.g.* electron gun. A residual gas analyser (RGA, SRS 200) is fitted to the chamber by a $1\frac{3}{4}$ " flange, in line-of-sight with the molecular beam to check its purity and to maximise the beam flow with respect to the substrate. Perpendicularly to the axis passing through the orifice for the molecular beam expansion into the main chamber and the RGA, there are two KBr windows strategically arranged in order to collect Infrared spectra in reflection at nearly grazing geometry. Moreover, a low energy electron gun (Kimball Physics ELG-2) points to the centre of the chamber for electron irradiation experiments [4, 10]. The standard refractory thermionic emitter, a Tantalum disc cathode mounted on a hairpin filament wire, is capable of providing a circular, planar emission of electrons when the filament wire is heated by the voltage source. The electron beam is accelerated and focused by a series of electrostatic lenses and a four-pole deflection plate system, allowing direct control on the beam energy, current, and divergence. However, the chamber itself is made of steel and not of mu-metal (a nickel-iron alloy), thus it is not shielded against static or low-frequency magnetic fields, therefore, although the electron energy could range from 5 eV up to 2 keV, with a spread of

0.5 eV, it was troublesome getting a stable electron beam at energies below 200 eV.

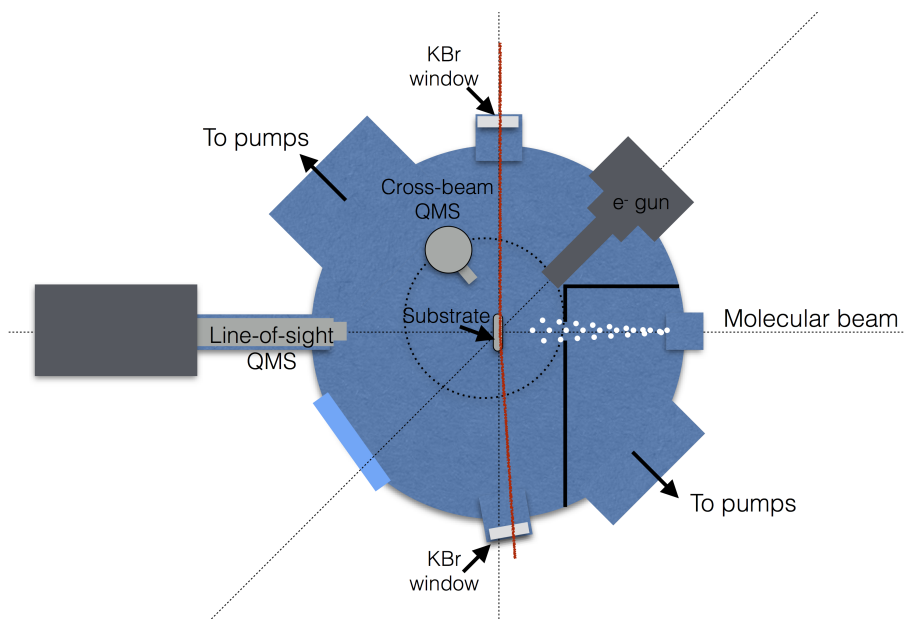


Figure 2.3: Schematic of the experimental level in the UHV chamber.

2.4.2 Sample Mounting

The substrate used for the experiments is a polished stainless steel disc, 10 mm in diameter and 2 mm thick, that is positioned at the centre of the chamber. Two 1 mm holes are drilled near the edges, opposite one another, allowing a convenient number of Ta wires (0.40 mm or 0.25 mm of diameter) to pass through so that the disc can be suspended and provided with thermal contact to the rest of the cryogenic apparatus. These wires are also spot-welded to two nickel foils (0.075 mm thick), each of these is wrapped around and spot-welded to 2 mm diameter molybdenum rods, see **Figure 2.4**. Each of these is silver soldered into a semi-circular oxygen free high conductivity (OFHC) copper blocks that connect to the copper heating wires. The blocks underlie a sapphire disc without touching with each other. On top of the sapphire disc there is a cylindrical OFHC copper mount. This sandwich-like structure is kept together by 2 mm screws electrically insulated from the copper blocks by home-made polyimide sleeves and washers. The particular design guarantees appropriate cooling of the sample and makes it float relative to the chamber thanks to the peculiar features of the sapphire: excellent thermal conductivity at low temperatures combined with a stable dielectric constant with the temperature and good electrical insulation. Chromel (90% Ni, 10% Cr) and alumel (95% Ni, 2% Mn, 2% Al, 1% Si) wires were spot-welded at the bottom to the edge of the metal substrate making a K-thermocouple junc-

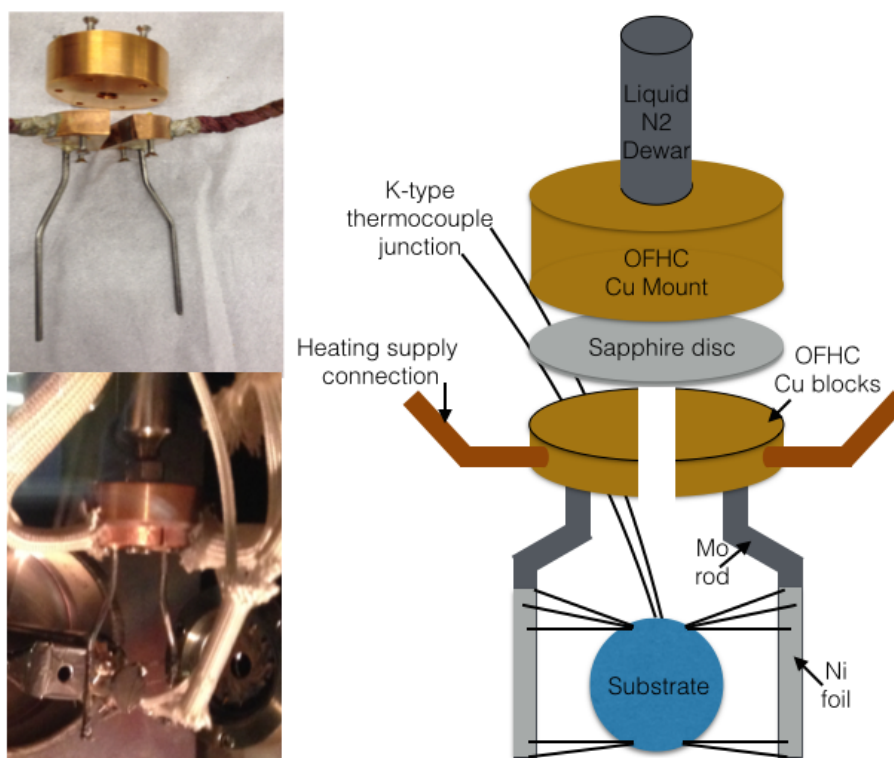


Figure 2.4: Pictures and schematic of the substrate and its mounting in the UHV chamber. Please note that in the upper photograph some components are not shown.

tion to monitor the sample temperature. Both these wires and the heating wires were insulated using peribraid sleeves, previously cleaned with isopropyl alcohol to wash off the organic residuals, and connected to appropriate feedthroughs at the top of the manipulator. Right at the centre of the upper copper block there is a tapped-hole which screws in a copper rod welded at the base of a stainless steel re-entrant. Usually a quantity of small gold leaf is interposed between the rod and the bottom of the hole in order to even up the surfaces and ensure a better thermal contact. The re-entrant is a long and narrow Dewar cooling the substrate down to ~ 110 K once filled with liquid nitrogen; moreover it supports the substrate keeping it orthogonal to the molecular beam, the electron gun or the line of sight tube of the quadrupole. Sample mobility is guaranteed by the manipulator, where the re-entrant is fitted. While movements in the x, y plane (parallel to the circular diameter of the chamber) can be more precisely controlled by a platform using a micrometer scale, the z translation is much more coarse relying on a control hand wheel combined with flexible edge-welded bellows, however a micrometer control of up to 25 mm movement is also available for fine tuning. A precision differentially pumped rotary feedthrough (DPRF; Vacuum Generators DPRF25) is mounted at the top of the manipulator using PTFE ring seals and connected to one of the rotary pump; this standard design significantly reduces the leak rate during rotation retaining UHV conditions and allows to orientate

the sample in the best way possible inside the chamber. The schematic of the manipulator assembly is shown in **Figure 2.5**.

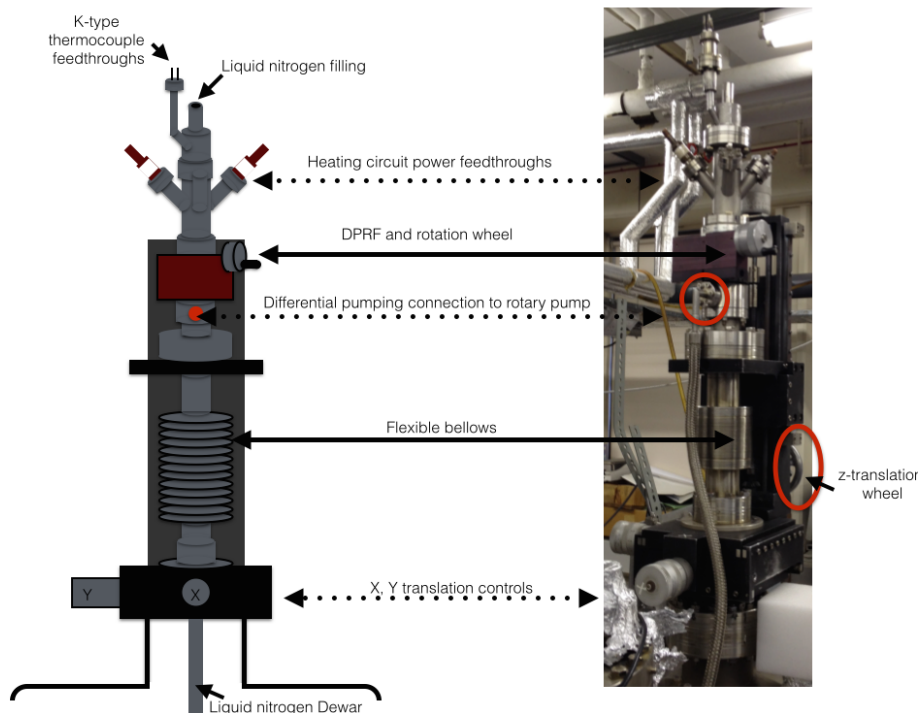


Figure 2.5: Schematic and picture of the sample manipulator in the Beam Rig.

2.4.3 Substrate Heating and Temperature Control

The lowest temperature achievable with this apparatus is ~ 110 K thanks to the thermal contact between the substrate and the liquid nitrogen inside the re-entrant as previously explained. The base temperature is higher than the actual temperature in the cold dense clouds, but low enough to freeze molecules as C_6H_6 , H_2O or $(CH_3CH_2)_2O$ on the disc. Although one could argue that the deposition temperature could affect the experimental results, which will be discussed in more detail in the next chapter, for now it will suffice to say that the experimental findings still apply to dust grains in the vicinity of hot cores and corinos.

In order to desorb the organics deposited on the cold substrate or simply to clean and anneal the substrate before any experiment, it is necessary to heat the disc as much as homogeneously possible while controlling the increase of temperature. *Joule heating* arises from the tantalum wires attached to the supportive Mo rods (**Figure 2.4**) as they have a higher resistance than the copper used in the rest of the heating circuit. An external power supply (Farnell Type H60/50) provides the current needed, up to 50 A, *via* the appropriate feedthroughs; the K-type thermocouple junction interfaced with the temperature read-out unit (FLUKE 51

K/J thermometer) allows monitoring of the substrate temperature, which can be manually controlled by adjusting the voltage and current supplied. In principle, this could be automated by using for example a Eurotherm proportional-integral-derivative controller (PID) controller interfaced to both the power supply and the thermocouple, but technical issues with the Eurotherm device (model 2404) and sudden changes with the electrical grounding in the laboratory did not make this feasible. A more simple and direct manual control provided a reliable solution. During TPD experiments the QMS molecular ions signal as function of time has to be synchronously recorded with the surface temperature. The latter is collected by the mass spectrometer itself; in fact the input going to the QMS is the raw voltage of the K-type thermocouple passing through a homemade designed amplification device which mainly consists of an integrated circuit (Analog Device AD595C) that returns an output of about 10 mV/°C then stored by the QMS. The amplified voltage is finally converted into temperature using an empirical calibration curve obtained by simulating a TPD experiment and tabulating the values from the temperature readout unit. The resulting plot of T versus V is conveniently fitted with a 6th order polynomial function that will be routinely applied for the analysis of the QMS voltage data. An example is reported in **Figure 2.6**.

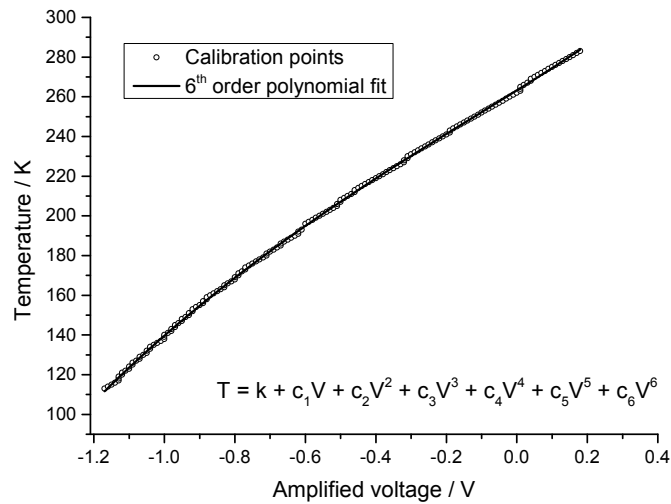


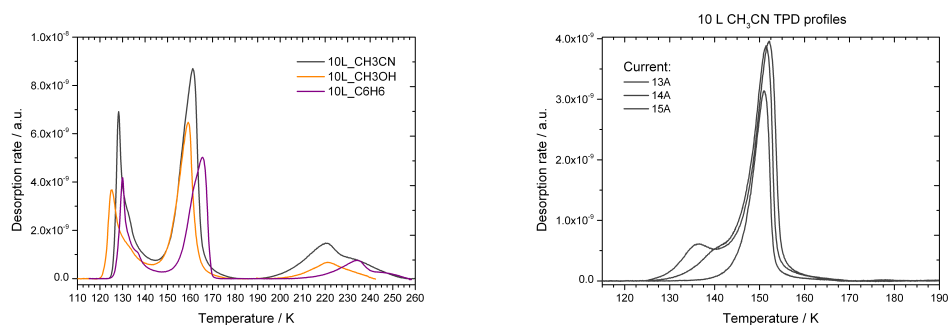
Figure 2.6: Empirical calibration curve for K-type thermocouple in the Beam Rig. Coefficients are: $k = (261.38 \pm 0.10)K$, $C_1 = (108.03 \pm 0.36)KV^{-1}$, $C_2 = (-9.18 \pm 0.98)KV^{-2}$, $C_3 = (-0.40 \pm 1.2)KV^{-3}$, $C_4 = (-2.6 \pm 2.2)KV^{-4}$, $C_5 = (7.90 \pm 0.94)KV^{-5}$, $C_6 = (2.1 \pm 1.3)KV^{-6}$.

2.4.4 Line-of-sight Detection

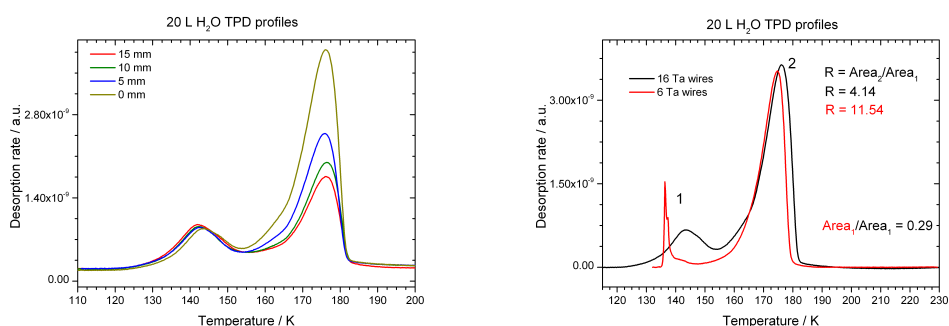
Preliminary TPD traces were significantly affected by the desorption of molecules from the sample mounting to a degree where the data could not be used. Postponing a detailed description of the physical meaning given by the TPD traces to a following paragraph, at the moment attention will be paid to highlight some experimental artifacts that led to small but essential modifications of the experimental set up. **Figure 2.7** shows the desorbing rate of molecules (H_2O , C_6H_6 , CH_3OH , CH_3CN) from the stainless steel disc as function of the substrate temperature. Typically there are 2 or 3 features and it is only the most intense that can be regarded as the real signal. The band at higher temperature shown in the upper left panel is due to molecules desorbing from all the sample mounting. It is easily distinguished and can be cut as being well above the temperature range of interest. This unfortunately is not the case of the initial band, which seems to be due to molecules desorbing from the tantalum wires, and likely from the supportive rods, as result of the following facts:

- This band appears independently with the chemical nature of the desorbing molecules. It was observed for C_6H_6 , CH_3OH , H_2O , and CH_3CN (left upper panel of **Figure 2.7**). This hints to a physical reason behind it.
- It gets more intense and broader as the current passed through the heating circuit increases (right upper panel of **Figure 2.7**).
- Changing the sample position orthogonally to the normal of the QMS pin-hole the lower temperature band stays constant in intensity and shape for a given exposure and substance (left lower panel of **Figure 2.7**). In other words as the disc is moved sideways with respect to the quadrupole line-of-sight the rods and the wires on one side gets further while the other rod and wires approach consecutively the associated signal should stay roughly constant.
- Reducing the number of tantalum wires decreases the area of the band, labelled **1**, (right lower panel of **Figure 2.7**). Furthermore the ratio between the area of the two peaks improves for the trace after the adaptations (in red) with respect to the initial TPD profile (in black).

In order to constrain detection of desorbing molecules to those coming from the sample surface two modifications were made to the QMS and sample mounting from their original design. The major change was to build a ~ 45 mm long line-of-sight tube using a tantalum foil 0.25 mm thick with an orifice of ~ 5 mm of diameter. The design was inspired on the that of Jones and Turton [11–13]. As



(a) Changing the chemical nature of the desorbing molecules. (b) Changing the current intensity through the heating circuit.



(c) Changing the disc position with respect to the QMS. (d) Cutting down the number of wires.

Figure 2.7: Tests of TPD profiles aimed at identifying and investigating the desorption from different areas of the sample mounting.

the tube is not cooled all the molecules responsible for undesirable artifacts in the TPD traces would bounce around in the chamber and eventually find a way to the QMS ion source. Therefore there will still be some degree of “contamination” in the final results. Since the latter is inevitable at this stage, a further improvement was made in the direction of narrowing down the unwanted band and reducing its intensity as much as possible. As shown in the right lower panel of **Figure 2.7**, reducing the number of tantalum wires serves this purpose, the signal is not only smaller, but also less broad and further away from the TPD band as the molecules on the wires are flashed away as soon as the current passes through. The best arrangement found for the disc mounting is shown in **Figure 2.8**.

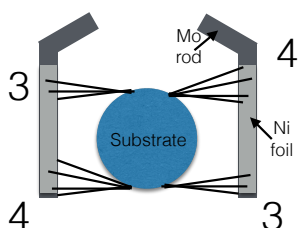


Figure 2.8: Final arrangement for tantalum wires supporting the disc to minimise and isolate desorption from the wires themselves.

2.4.5 Thin Film Deposition

The deposition of thin films on the cold substrate can be carried out in different ways depending on the phase of the chemical (in standard conditions) and the degree of uniformity desired. In general, the vapour in equilibrium with the substance is collected and conveniently leaked inside the chamber. If one wants to dose molecules with a high molecular weight, that will likely be solid at room temperature, such as large PAHs, and have low vapour pressure, then a Knudsen cell can be used. Liquids on the other hand, can be much more volatile and easy to get into the chamber. But even in this case, two different methods of vapour deposition are commonly used:

- *Background dosing*
- *Direct dosing*

The former guarantees a uniform film on the substrate, but as molecules diffuse everywhere in the chamber also the back of the sample will have adsorbed molecules. Direct deposition avoids this disadvantage keeping the base pressure low during the dose and the chamber clean, with a very low deposit on the back of the substrate, but the resulting film will not be uniform unless an array of capillaries is used. Within the Beam Rig both the methods are possible: using the gas manifolds for background dosing and the molecular beam system (MBS) for the direct deposition.

Gas Manifolds

As can be seen in **Figure 2.9**, the main chamber gas manifolds consist of two lines kept isolated by two right angle valves (Caburn MDC), controlling the access to a 2" oil diffusion pump (Edwards High Vacuum Ltd, E02), which is backed by a rotary pump (Edwards High Vacuum Ltd, E2M5). The lines are also directly connected to the latter by a pair of ball valves for evacuation of large quantities of gases, and they are connected to the chamber by long convoluted-core polytetrafluoroethylene (PTFE) hoses leading to fine control leak valves (Vacuum Generators MD95). Two Pirani gauges, one bakeable, in front of the diffusion pump, and a second Pirani, attached to the rotary pump, are used to monitor the pressure inside the gas manifolds and control the freeze-pump-thaw degassing of liquids. These liquids are situated in an array of glass vials connected by Nupro valves to the DN16CF ports of the gas-lines. One manifold was used for back-filling the chamber with H_2O , CH_3OH or $(\text{CH}_3\text{CH}_2)_2\text{O}$ and the other one for C_6H_6 . The thickness of the deposited layer can be estimated by applying **Equation 2.5** assuming the sticking coefficient to be unity and knowing the density

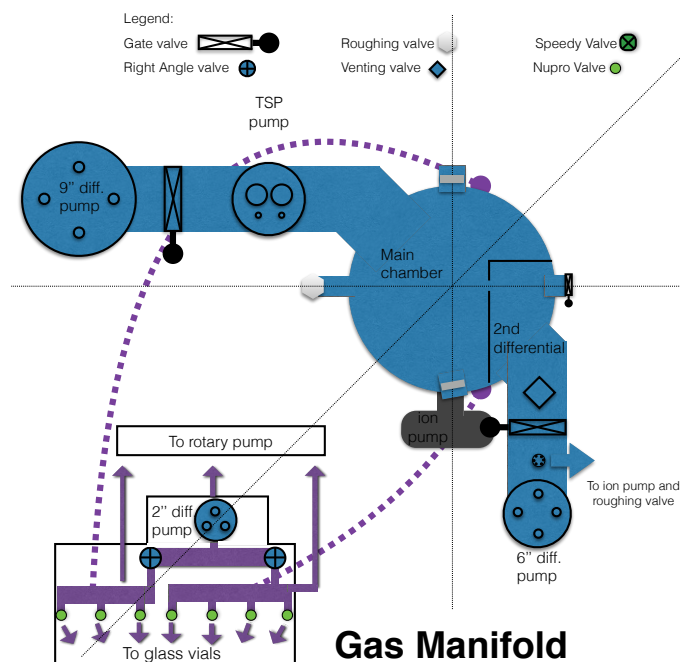


Figure 2.9: Schematic of the gas manifolds used for background deposition (in violet).

of the deposited solid film. **Equation 2.5** gives the number of molecules that accumulate on the substrate per unit of surface for a given “exposure time” during gas dosing when the pressure at the ion gauge is corrected by the ionisation coefficient. Dividing by the molecular density, it is possible to obtain an upper limit for the film thickness with the assumption that the molecular density and deposition rate are homogeneous in time and everywhere on the substrate. More conveniently the Langmuir unit (L) is commonly used in surface science, as in this thesis, to quantify the dose of a certain substance, and it is simply defined by multiplying the pressure of the gas by the time of exposure (**Equation 2.7**)

$$L = P \times t \quad (2.7)$$

where P is in Torr and t in seconds.

Molecular Beam Source

Direct deposition of gas onto the substrate is possible by formation and expansion of an effusive or supersonic molecular beam into the main chamber, but as it was not used for the experiments discussed in this thesis, only a brief description of the apparatus will follow. The vapour phase of the liquid is collected in a similar fashion as described above, from a glass-bulb connected to the source chamber *via* the MBS gas manifold. The latter can be also adapted to connect a gas cylinder for gas-surface scattering experiments or collision-induced desorption experiments. The gas enters the source chamber through a stainless steel

tube where a 6 mm diameter glass nozzle is attached using Swagelok fittings and a graphite ferrule. If a ceramic nozzle is used instead, it could also accommodate a solid powder of low-volatile chemicals and make a molecular beam of it by resistively heating a tungsten coil wrapped around the ceramics under a carrier gas flow. The nozzle is mounted on a x,y translation stage inside edge-welded flexible bellows which allows manual control to get the optimum beam alignment; the glass pinhole has a diameter of ~ 0.5 mm through which the gas expands into the vacuum. A 5 mm diameter orifice, that can be moved using two linear devices, separates the source chamber from the 1st differential chamber; both are housed in the same high vacuum (HV) chamber, as shown in **Figure 2.10**. There, pumping is provided by the combination of a 6" oil diffusion pump

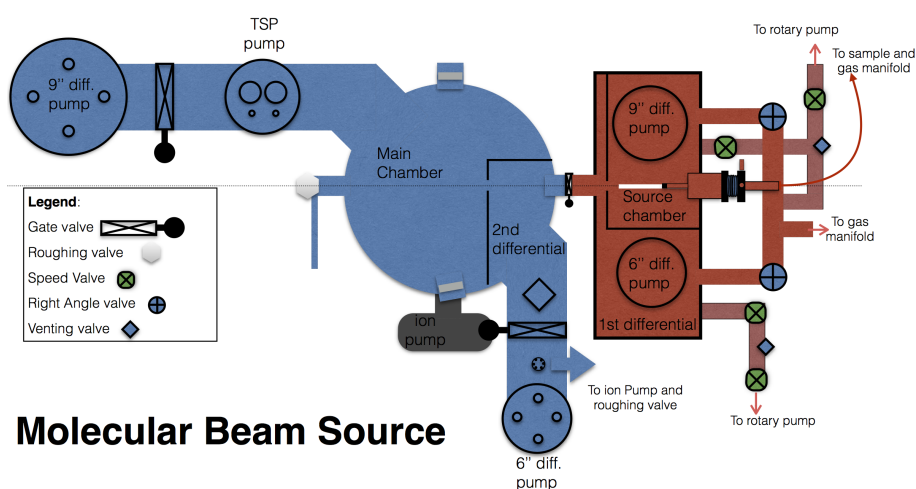


Figure 2.10: Schematic of the molecular beam apparatus adjacent to the chamber.

(Edwards High Vacuum E06), supported by a rotary vane pump (Edwards High Vacuum, E2M18) for the 1st differential chamber and a 9" diffusion pump (Edwards High Vacuum E09) backed by an oil sealed rotary pump (Edwards High Vacuum E2M40) combined with a mechanical booster (Edwards High Vacuum EH250) for the source chamber; both diffusion pumps are charged with silicone fluid (Dow Corning DC-704). Base pressure is 10^{-7} mbar but it rises up to 10^{-6} mbar in the 1st differential chamber and up to 10^{-4} mbar in the source chamber during continuous beam operation which requires the mechanical booster to be on in order to guarantee adequate pumping speed. Pressures are measured by Penning gauges (Edwards High Vacuum CP25-K) and Pirani gauges (Edwards High Vacuum, PRL10) controlled by two Edwards High Vacuum Pirani Penning 1005 controllers; two additional Pirani gauges (Edwards High Vacuum, PRH10) were also fitted to monitor backing pressure at the rotary pumps. The second differential chamber, inside the main UHV chamber, has a line-of-sight aperture of variable diameter. A gate valve attached to a DN38CF flange, separates the HV

chamber and the UHV chamber isolating the former from the backout region. Film thickness can be estimated as described in the previous paragraph, however, once the molecular beam is aligned and optimised, the dose must be calibrated with respect to the background dose. This is feasible by comparing the relative number of molecules desorbed from the substrate during sets of temperature programmed desorption (TPD) experiments after both direct and background deposition.

Knudsen Cell

Recently the Beam Rig was equipped with a Knudsen cell (K-cell) in order to introduce large aromatic molecules such as coronene or fullerene, which exhibit a very low vapour pressure at room temperature, since background deposition using the gas manifolds is not possible or convenient. Direct deposition is still feasible *via* a hot ceramic nozzle in the molecular beam source chamber. Initially this Ph.D. thesis was supposed to look at large PAHs desorbing from water ice and a silica substrate, therefore care has been given to the possible K-cell designs. However the Knudsen-cell has not been used apart from preliminary tests due to time constraints and various, more fundamental, experimental difficulties, therefore a description and no results will be presented.

Ideally, a K-cell is an isothermal enclosure with an infinitesimally small exit aperture, bounded by vanishingly thin walls, from which an effusive molecular beam forms. The K-cell has been successfully used to determinate equilibrium parameters, like vapour pressure [14, 15] and dissociation bond strength [16]. Moreover it has also been used as a flow reactor for the last 40 years to accurately measure rate constants for homogeneous gas phase reactions and for heterogeneous gas-solid and gas-liquid reactions [17, 18]. More recently, with some interest in biomaterial science and engineering, amino acids films have been prepared by the vaporisation of L-tyrosine in a K-cell and their properties have been investigated by Scanning Electron Microscopy (SEM) and X-ray photoelectron spectroscopy (XPS) [19]. Of course there are many possible designs for a K-cell, but they all share the same basic idea and thus some common components:

- A crucible, usually made of pyrolytic boron nitride (PBN) or graphite, to hold and evaporate the substance of interest;
- A thermocouple to monitor the temperature;
- A resistive heater;

- An exit orifice, which size determine the intensity spatial distribution of the beam in function of the sample distance.

A commercial K-cell from Chell (**Figure 2.11**) was chosen as the best compromise between cost and performance. It is an internal K-cell, thus has the disadvantage



Figure 2.11: *Picture of the Knudsen cell from Chell as shown in its website (http://www.-chell.co.uk/product_details/vacuum-products/kcell).*

of venting the whole chamber if sample change or maintenance are required. However it is an efficient design, low-cost and versatile to implement with any chamber. The furnace housing hosts a very fine grain graphite crucible, heated by tantalum foil element insulated with PBN shields. A PBN liner, designed to make inserting source material easy, is fitted into the graphite crucible; it avoids contamination in the furnace cartridge, which can be reused to evaporate different materials just changing the liner. Two caps, that can be also easily changed, have an orifice 1 mm aperture to guarantee 80-90% of the total flux adsorbed on a 5 mm radius sample and 60-70% of the beam intensity at the edges for an estimated working distance of 125 mm from the sample. A remote controlled shutter minimises any unwanted sample vapour outflow inside the chamber. A K-type thermocouple, embedded in the graphite crucible and the heater connections pass *via* the appropriate feedthroughs to the temperature tracker (Data Track Process Instruments, Tracker 200) and power supply (Coutant Electronics Ltd. LB 2000.2). The K-cell has been degassed to reduce contamination before its first use, to do so it was kept at ~ 500 °C for 48 hours in high vacuum. Film thickness could be estimated in a similar fashion as indicated in the previous paragraph: comparing the TPD traces at different coverages after dosing with the gas manifolds and the K-cell. One would need a substance that is volatile enough, like naphthalene ($C_{10}H_8$), to be compatible with both the deposition methods.

2.5 The Ice Rig

In contrast to the previous apparatus, the Ice Rig (**Figure 2.12**) was genuinely designed for astrochemistry surface science experiments as the study of Collings and co-workers shows [8, 20]. In the following years, it was also equipped with a dual atomic beam system to explore water formation on interstellar ices and the relative experimental procedures are widely described in previous and future works [9, 21]. However, the latter add-on was not used for this thesis, in fact only TPD traces and IR spectra of molecular species will be considered in the following chapter. Therefore, it will suffice to give a brief description of the UHV main chamber and its equipment as presented below.



Figure 2.12: *Pictures of the left and right side of the Ice Rig.*

2.5.1 Instrumentation

The apparatus, **Figure 2.13**, revolves around the central main chamber, 30 cm of diameter, made of stainless steel, capable of reaching UHV conditions (2×10^{-10} mbar) routinely when baked at 120 °C for 72 hours. Pumping is provided by liquid nitrogen trapped 6" oil diffusion pump (Edwards High Vacuum E06), charged with *Santovac 5* and backed by an oil sealed mechanical rotary pump (Edwards High Vacuum E2M18). This is supplemented by a titanium sublimation pump (AML, TSP2) fitted with a liquid nitrogen trap between the gate valve and the main chamber. Pressure is measured by a nude Hot Cathode Ionisation gauge with thoria coated filaments (Instrument Technology Ltd.), while active Pirani gauges (Edwards High Vacuum, APG-L) are located between the diffusion pump and the rotary pump. All of them interfaced to an active gauge controller (Edwards). Two fine control leak valves (Vacuum Generators MD95) are attached at the lower level of the main chamber, connecting it to the glass gas line. It should be stressed that within this arrangement (see bottom panel of **Fig. 2.13**) the leak valve is closer to the gauge and the diffusion pump than it is to the substrate, which lies in the upper level. Although dosed molecules expand in the vacuum in all directions, an instantaneous concentration gradient towards one

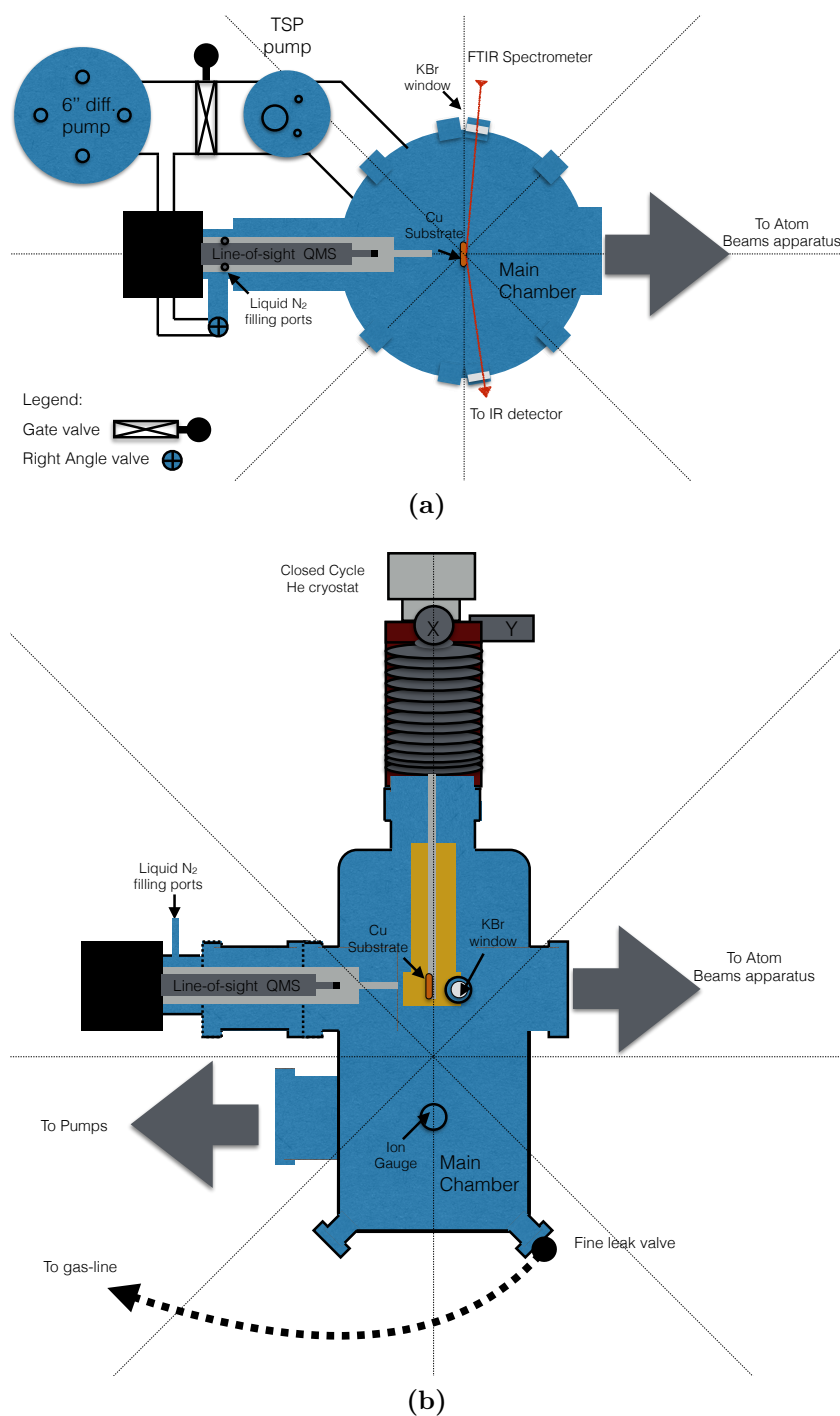


Figure 2.13: *Schematic of the experimental level and the pumping for the Ice Rig.*

end of the chamber might be emphasised by the vicinity of the diffusion pump, generating a weak flux in its direction, whose intensity, read by the closer ion gauge, might be recorded as higher than the actual value associated to the local flux ongoing to the sample surface. Therefore, the dose of a certain substance might differ in the Ice Rig with respect to what is obtained in the Beam Rig for a given Langmuir unit (L). A custom built shroud (Instrument Technology Ltd.), based on the work of Jones and collaborators [11–13], contains a pulse

counting Hiden Analytical QMS (HAL301) in line-of-sight with the substrate surface (**Figure 2.13**) and differentially pumped *via* the 6" diffusion pump. The combination between the liquid nitrogen reservoir around the quadrupole and the line-of-sight tube significantly minimises the signal of molecules from the sample mount and cold finger, especially for those having a desorption temperature above 78 K, resulting in neater TPD traces. The chamber is also equipped with two KBr windows to allow RAIRS experiments passing the radiation from the FTIR spectrometer (Varian 670-IR) on the sample at 75° and reflecting them to the external mercury cadmium telluride detector (MCT).

2.5.2 Sample Mounting and Cryogenic System

The most striking difference between the Ice Rig and the Beam Rig is that the former was intentionally designed for astrochemistry purposes. The most direct consequence of this fact is expressed by the closed cycle helium cryostat mounted on the top of the chamber, **Figure 2.14**, which is differentially pumped by a oil sealed mechanical rotary pump (Edwards High Vacuum E2M18). The cryostat allows a base temperature as low as 20 K to be reached which better describes and mimics the cold interstellar clouds. The substrate is a silica coated copper block representing the dust grain cores. It is mounted by 4 screws insulated by home-made polyimide sleeves and washers on a OFHC copper gold plated support; a sapphire plate is interposed between the substrate and the mounting so that the former is electrically floating. Gold leaves are also used at the interfaces to enhance thermal contact. Below the substrate, there is also the QCM front plate holding two quartz crystals, one behind the front plate, used as reference, and the other on top of it, exposed to the same gases as the substrate. The whole block is connected to the cold finger, cooled by a closed-cycle compressed helium gas cryostat (APD Cryogenics, HC-2). The latter is fitted into a x, y, z manipulator in a similar fashion to the Beam Rig allowing micrometer control in the plane and coarse adjustment along the z.

The substrate has a small re-entrant hole at its side that hosts a cartridge heater (Heatwave Labs Inc., TB-175) insulated by ceramic beads; its connections, also kept insulated by peribraid sleeves, pass through a cavity in the support block and tied around the cold finger, up to the appropriate feedthroughs, leading to an external home-made power supply. Temperature is monitored by two KP-type junctions (gold and chromel): one at the sample and one at the base of the cold finger, both of them follow a similar way out as the heating circuit elements, insulated by peribraid and wrapped around the cold finger, to be interfaced with

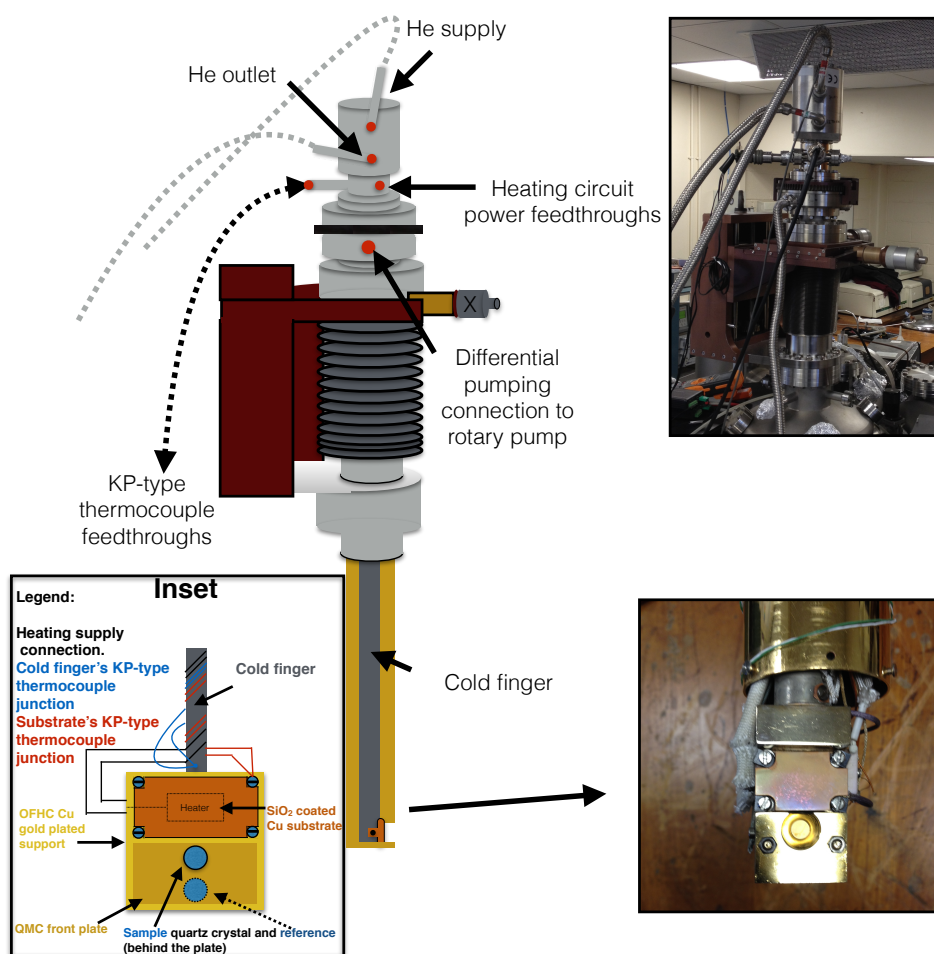


Figure 2.14: Temperature control system schematic. The inset at the bottom shows a detailed representation of the sample mounting.

the controllers at the air side (IJ Instruments Ltd.). Once the closed cycle helium cryostat is turned on, the sample gradually cools down to base temperature, reaching a steady state when the heat removal due to the cryostat itself matches the heat supply from the chamber (*e.g.* ion gauge and chamber's wall). If a constant voltage is applied to the heating circuit, this will result into an additional source of heat, and therefore, the sample temperature will increase until it levels to a plateau that stays constant in time. This new steady state will be established at higher temperatures than base conditions. By manually controlling the voltage, it is possible to adjust the temperature of the sample to a desired value (*e.g.* 110 K).

As previously described, when conducting TPD experiments the QMS ions signal as function of time has to be recorded along with the surface temperature. The original design adopted the same logic seen for the Beam Rig, where the

temperature is recorded by the QMS as amplified thermocouple voltages and converted back into Kelvins post-experimentally, *via* a calibration curve. This procedure evolved due to experimental difficulties, and now the temperature *via* the controllers and the ion traces by the Hiden quadrupole are both independently recorded as a function of universal time. The two data-sets are subsequently synchronised to obtain the desired TPD plots.

2.5.3 Glass Gas Lines

Molecules are deposited onto the cold surface by background filling of the chamber *via* two leak valves. Each of these are connected to a gas line and to a glass bulb that works as a temporary reservoir of volatile molecules such as O₂, N₂, CO, CO₂, N₂O and so on. The two lines (see **Figure 2.15**) merge together, after the bulbs, in a single apparatus entirely made of glass that culminates into an array where the test-tubes containing liquids or gas bottles are. The two lines can still be kept isolated from each other by closing valves (standard plastic taps with viton o-rings) conveniently located. A ball valve controls the access to the oil sealed mechanical rotary pump (Edwards High Vacuum E2M18) as to evacuate the line and to allow freeze-pump-thaw cycles for liquid purification. Pressure is read by a Pirani gauge located in between the pump and the gas lines.

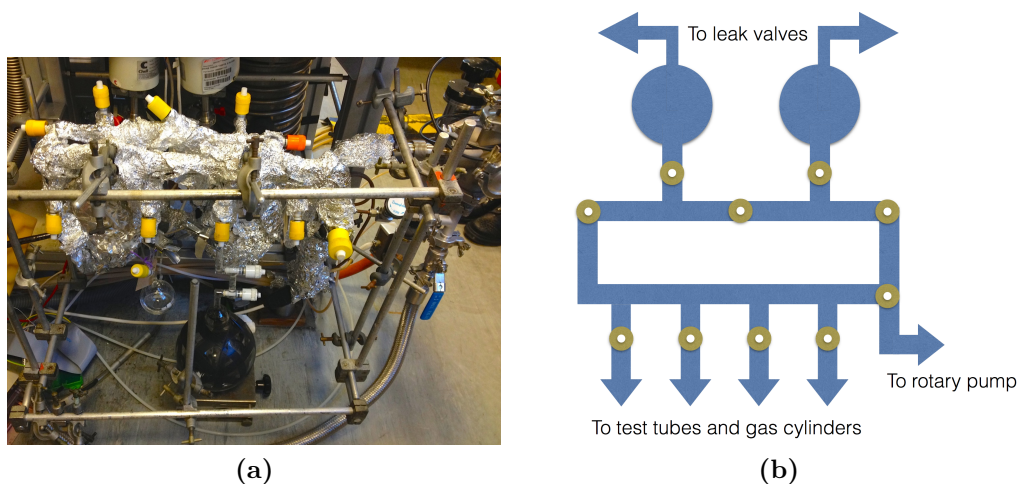


Figure 2.15: *Picture (a) and schematic (b) of the glass gas line.*

2.6 From Metal Substrates to Grain Analogues

Traditionally surface science experiments are performed on metal substrates (*e.g.* single crystal metals) especially because of the general interest around material science and heterogeneous catalysis [22–28]. Moreover, this is a convenient design choice that allows the use of RAIRS and maximises the thermal conductivity of the sample, which can then be easily brought to extreme low temperatures. Therefore, because of this common background, it is not surprising that many astrochemistry-oriented experimental set-ups use metal substrates [29–31], including the two outlined in this thesis. In the Beam Rig, the substrate is a polished stainless steel disc (an alloy of iron and other elements, such as carbon, and a minimum of 10.5 % chromium content by mass), while in the Ice Rig it is a polished polycrystalline copper block.

However, it should be stressed that depositing molecules directly onto the metals affects the binding of the first adsorbed layers, which will be chemisorbed, instead of being physisorbed as typically occurs in the ISM. For instance, it is well-known in literature that molecular oxygen (O_2) on heavy metals, such as palladium (Pd) and gold (Au), dissociates into the two O atoms. This occurs because the binding mechanism between metal and molecule involves charge transfer to the adsorbate with a concomitant activation of the O-O bond to a superoxo-like state [32–34]. Even when dissociation is not observed [35], the desorption energy is significantly higher for O_2 on gold (142 kJ mol^{-1}) than on astrophysical relevant surfaces (7.5 kJ mol^{-1}) [36]. Chemisorption *via* partially negatively charged species was found also for carbon dioxide (CO_2) on polycrystalline copper [37, 38]. Carbon monoxide (CO) leads to another example: CO is one of the main building blocks in the icy mantles of the interstellar grains where desorption is observed at very low temperatures (20 - 40 K) [36, 39], while, in contrast, it is chemisorbed on gold nanoparticles [40], requiring significantly higher temperatures (100 - 200 K) to leave the surface [41].

As mentioned in **Chapter 1**, the notion that the carbonaceous material is an important component of the dust grains is widely accepted, while heavy metal contents are likely to be found in the oxidised form (*e.g.* Fe in olivine). Therefore, many studies have adopted highly oriented pyrolytic graphite (HOPG) as substrate instead of a metal, which also allows us to use RAIRS thanks to the electronic and optical properties of the graphite [42–45], although, more recently, nanostructured graphite surfaces have been indicated as a more realistic choice [46].

In order to mimic the interstellar grain surfaces or icy mantles and, at the same time, being capable of using a metal substrate, two different, but complementary, strategies can be adopted:

1. *Depositing “thick” ices* by dosing hundreds of L units. The effect of the metal on the binding to the adsorbate does not extend further than the first layers. Therefore, the multilayer will behave in the same way regardless the substrate. This is confirmed by comparing high coverages TPD experiments of methanol (CH_3OH) on silica (SiO_2), polycrystalline gold and HOPG, while differences emerge only at low exposures [31]. It is worth noticing that no sub-monolayer data for CH_3OH on polycrystalline gold are displayed in the aforementioned reference, but an older study [47] reports desorption energies for CH_3OH from Au(110) (50 kJ mol^{-1}) and from Cu(110) (70 kJ mol^{-1}) that are higher than from graphene (45.4 kJ mol^{-1}) [29]. Further support for the strategy of using thick ices is found in the work of Thrower [5] where consistent behaviour was confirmed for the bulk C_6H_6 desorption on stainless steel, on stainless steel coated with SiO_2 , and on compact amorphous solid water. Thus, in order to avoid any direct effect of the metal substrate on the molecule of interest, in **Chapter 4** and **5** “onion layered” films of C_6H_6 deposited on top of thick ices were investigated. The relatively large distance of the ice/ C_6H_6 interface from the stainless steel disc validates the results presented therein as applicable to the astronomical context.
2. *Coating the metal support with films mimicking the interstellar grains* such as carbonaceous material [29] or amorphous SiO_2 as used herein. For the experiments reported in this thesis, grain analogues were obtained by depositing amorphous SiO_2 on the copper block (used as substrate in the Ice Rig, see **Chapter 3**) using electron beam evaporation of bulk SiO_2 . The procedure is also efficient for the stainless steel disc employed in the Beam Rig, although it was not successful for the the results discussed in **Chapter 4** and **5**. The deposition was performed in a separate high vacuum chamber, with a base pressure of around 5×10^{-7} Torr, using 7 keV electrons. Film thickness was monitored during deposition by means of a quartz crystal microbalance mounted close to the deposition region and was estimated to be $\sim 300 \text{ nm}$. As this chamber was unbaked, the residual gas environment was rich in water vapour. It is therefore reasonable to assume the presence of a significant number of silanol groups (**Figure 2.16**). Furthermore, exposure to the ambient environment in order to transfer the substrate to the UHV

chamber would further facilitate the formation of silanol groups. A full characterisation of the nature of the resulting surface on the substrates is far from straightforward, and beyond the scope of this thesis. However, atomic force microscopy (AFM) images of the film have been discussed elsewhere [4, 5, 48] and indicate a uniform coverage of amorphous SiO_2 across the substrate with a high degree of roughness (see **Figure 2.16**). Consequently, it was previously observed from TPD experiments a 4-5 fold increase in the surface area available for adsorption when the metal is coated with silica [5]. For a ~ 200 nm thick SiO_2 film, the roughness was estimated to be of the order of 40 nm, but it increases for higher exposures during the electron evaporation (*e.g.* going from 100 nm to 200 nm). Therefore, the ~ 300 nm film used in **Chapter 3** will likely display a much more complex and structured topography than the sample used by Thrower.

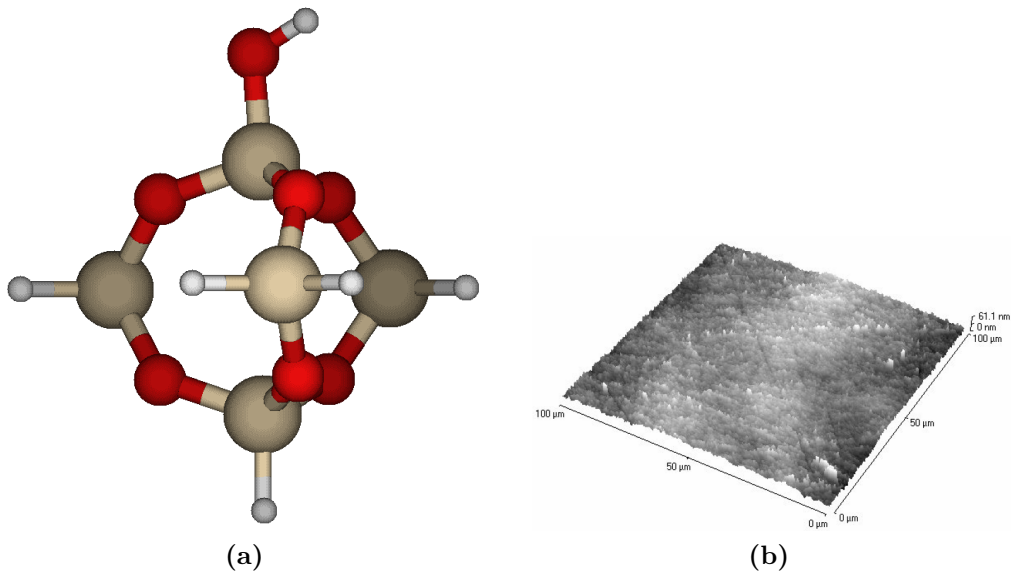


Figure 2.16: *On the left: cluster model of terminal silanol groups at the amorphous SiO_2 surface. The H atoms connected to the Si atoms are a simplification for the surrounding O-Si-O network. On the right: $100 \times 100 \mu\text{m}$ AFM image taken from [5] of amorphous silica (~ 100 nm) deposited on the stainless steel substrate. The apparent curve in the film is an experimental artefact.*

It can be concluded that the characterisation of the substrate is not as simple as it is for single crystal and polycrystalline metal substrates, but it is complicated by the deposition of the amorphous SiO_2 . However, this surface displays a morphology more consistent with that of interstellar grains than any metal substrate, which is crucial to investigating the desorption kinetics of sub-monolayer quantities of adsorbates to be included into astrochemical models.

It is important to stress that the model proposed above is actually a simplification of real silicate interstellar grain cores which seem to display a much more complex and rich elemental composition as suggested by the latest experimental findings [49]. Seven particles captured by the NASA Stardust Interstellar Dust Collector from the comet 81P/Wild 2 and returned to Earth seem to have a probable interstellar origin; a combination of X-ray diffraction, fluorescence, microscopy and FTIR revealed a composition rich in Si, O but also in Mg and Fe, in agreement with the average values inferred for the ISM dust composition from observations [50] (see **Chapter 1**).

2.7 Experimental Techniques

2.7.1 Temperature Programmed Desorption

Atoms and molecules adsorbed on the surface can return to the gas phase. However *desorption* occurs only if particles possess the necessary energy to “escape” from the potential well they are localised in. The time spent on the surface was called by Frenkel in 1924 “*sojourn time*” [51]. It depends on the nature of the interactions established between adsorbate and the surface and on experimental conditions. Its phenomenological law is:

$$\tau = \tau_0 e^{-\frac{\Delta_{ad}H}{RT}} \quad (2.8)$$

where $\Delta_{ad}H$ is the adsorption enthalpy; R is the gas constant; τ_0 is the oscillation period mainly referring to vibrational modes perpendicular to the surface, which ranges from 10^{-12} - 10^{-14} s. If the adsorption has an activation energy, E_a , hence, then it follows:

$$\tau = \tau_0 e^{\frac{E_a - \Delta_{ad}H}{RT}} = \tau_0 e^{\frac{E_d}{RT}} \quad (2.9)$$

where E_d is the global desorption energy. At this point the desorption rate, u_d , can be defined as:

$$u_d = \frac{n_s \theta^x}{\tau} = \frac{n_s \theta^x}{\tau_0} e^{-\frac{E_d}{RT}} \quad (2.10)$$

This is the well-known *Polanyi-Wigner* equation. n_s is the number of adsorption sites, θ is the surface coverage and x is the kinetic order. Sometimes **Equation 2.10** can be found without explicit dependence to n_s . It is important to note that no recombination was considered for the desorption, otherwise θ should be described by a more complex function ($f(\theta)$).

Desorption mechanisms were reviewed in **Chapter 1**. Thermal desorption is readily simulated and investigated by a well-known surface science experiment, TPD. The analysis of its results rely on the theoretical background illustrated above providing information that concerns the strength of interactions between the surface and the adsorbed species [52], though what is actually measured is the rate of the desorption from the substrate as function of the temperature. The experiment is carried out as follows:

- UHV conditions to ensure sample cleanness;
- Sufficiently high pumping speed to exceed the desorption rate. In this way the signal is proportional to the molecules instantly leaving the surface and does not depend also on molecules that accumulated in the chamber.
- Ideally heating only the sample by a linear ramp (in fact supporting wires are generally used that, by Joule’s law, resistively heat the substrate);
- A thermocouple is used to monitor the sample temperature;
- A detector, such as a quadrupole mass spectrometer (QMS), counts the desorbing particles.

As the temperature increases the thermal energy available becomes sufficient for particles to “escape” from the interaction potential well. The expected result (**Figure 2.17**) exhibits one or more features which are distributions of desorbing particles as function of temperature, each for a given desorption energy. **Equation 2.10** can be rearranged to give:

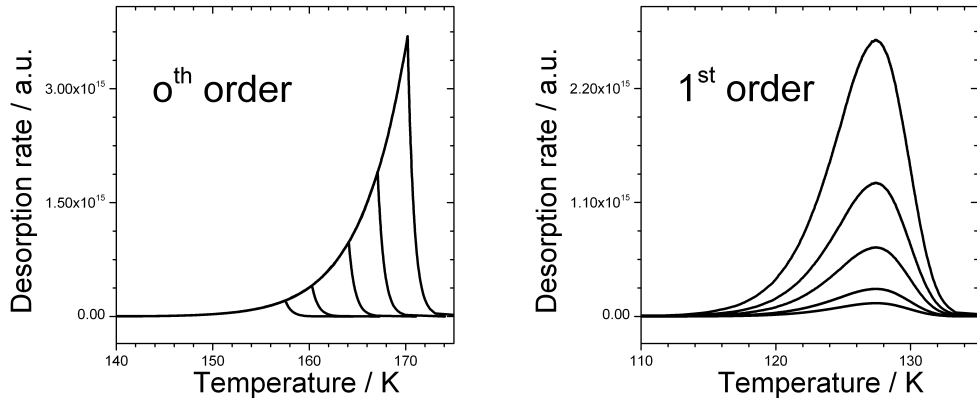
$$u_d = -\frac{\partial\theta}{\partial t} = -\frac{\partial\theta}{\partial T} \frac{\partial T}{\partial t} = -\frac{\partial\theta}{\partial T} \beta \quad (2.11)$$

$$-\frac{\partial\theta}{\partial T} = \frac{u_d}{\beta} = \frac{n_s \theta^x}{\tau_0 \beta} e^{-\frac{E_d}{RT}} \quad (2.12)$$

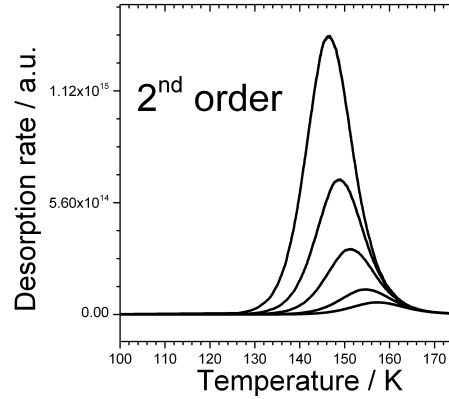
where β is the heating rate. **Equation 2.12** gives a more direct representation of the TPD experiment. Plus, after further manipulation, it follows that:

$$\frac{E_d}{RT_{max}^2} = \frac{n_s}{\tau_0} x \theta^{x-1} e^{-\frac{E_d}{RT_{max}}} \quad (2.13)$$

which gives the temperature corresponding to the maximum observed thermal desorption rate. These useful relations (**Equations 2.12** and **2.13**) are the basis for any TPD data analysis. Chemisorbed monolayers generally show first or second order desorption kinetics, while multilayer systems, with the same intermolecular interactions of the pure solid phase, exhibit zero-order kinetics.



(a) 0^{th} order desorption. Coincident leading edges; increasing maximum temperature. (b) 1^{st} order desorption. The maximum is always at the same temperature.



(c) 2^{nd} order desorption. Coincident trailing edges; decreasing maximum temperature.

Figure 2.17: Some examples of TPD profiles.

Referring to **Equation 2.13**, when $x = 1$, it follows that the desorption peak maximum position (temperature) does not depend on the adsorbate coverage, thus increasing the latter effects only the intensity (more desorbing particles) (see **Figure 2.17b**). When $x = 2$, T_{max} is, in first approximation, inversely proportional to the surface coverage. Therefore (see **Figure 2.17c**) as the number of molecules forming the monolayer on the substrate increases there is a shift of T_{max} to lower values but with higher intensities. It is important to stress that it has been assumed that both the activation energy and the pre-exponential factor are coverage independent and that desorption occurs in a single step. For zero-order kinetics, T_{max} shifts to higher values as the coverage increases and the curves have a common leading edge (see **Figure 2.17a**). As the Arrhenius

trend is limited only by the number of particles forming the multilayer, for an infinitely thick layer it is clear that $T_{max} \rightarrow \infty$. However, it is worthwhile noting that experiments can sometimes result in more complex kinetics with fractional orders. Moreover the area under a TPD curve, for a known coverage, can be used as a calibration standard in a series of desorptions of unknown coverage layers.

2.7.2 Reflection-Absorption Infrared Spectroscopy

Detailed information about the geometry of the adsorbed molecules, and the nature and the strength of their interaction with the surface is provided by the combined use of UHV conditions and Reflective-Absorption Infrared Spectroscopy (RAIRS). The technique was first introduced by Greenler [53] to investigate the spectroscopic properties of any thin layer on a metal surface in the IR range solving a long standing problem related to these kinds of studies. In fact, the free electrons inside the metals absorb strongly in the infrared preventing transmission techniques to probe adsorbate vibrational modes. Nowadays, RAIRS is widely used as the reviews by Sheppard [54] and Trenary [55] prove. If one considers an incident photon perpendicularly to a metal surface, the reflected wave will combine with the incident to form a standing wave. The latter, to the first approximation, has a node at the surface, thus the electric field (\vec{E}) is zero. The intensity, I , is also zero since $I \propto |E^2|$. For an IR photon, *e.g.* 2000 cm^{-1} , the distance between a node and the closest antinode of the standing wave is thousands times greater than the thickness of a 50 nm adsorbed layer. In other words, one should expect little or no absorption of IR radiation from the molecules on the surface. Luckily for a non-normal incidence this intuitive analysis fails. The component of the incident light polarised parallel to the surface (perpendicular to the normal of the plane, case **a** in **Figure 2.18**) results in a phase change, after the reflection, which remains constant around 180° for all the angles of incidence (see case **a** in **Figure 2.19**).

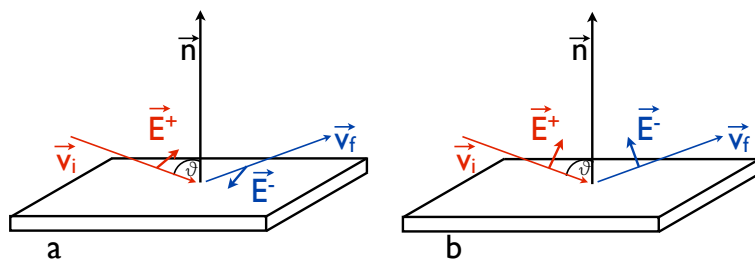


Figure 2.18: Cartoon representing the relative phase of the electric field vector (\vec{E}) for a parallel polarisation (a) and for a perpendicular polarisation (b) before and after the reflection from the surface. \vec{v} is the propagation vector and \vec{n} is the normal to the plane. Adapted from [53].

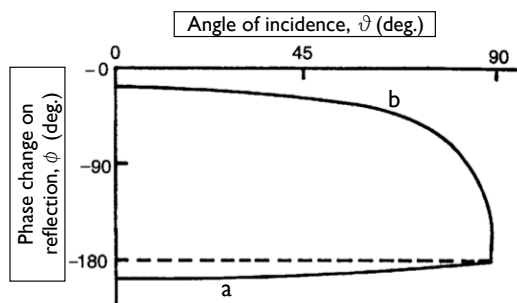


Figure 2.19: Phase change ($\Delta\phi$) following the reflection on the metal surface as function of the incidence angle (θ) for a polarised light parallel (a) or perpendicular (b) to the plane of incidence. Image adapted from [53].

This means that for this polarisation state, at the surface, the intensity of the radiation is in fact zero because the electric vector of the incoming light (in red) cancels out with the electric field of the reflected light (in blue). Therefore, negligible absorption should be expected for this conditions. In contrast, the phase shift of the polarised radiation perpendicular to the surface (case **b** in **Figure 2.18**) changes continuously from nearly zero to π (case **b** in **Figure 2.19**) with the angle of incidence. It is important to stress that at high angles, but not grazing geometries the phase is shifted by $\frac{\pi}{2}$ upon reflection. This results in a significant enhancement of the radiation intensity because the electric field of the incoming and reflected light sum to each other. In other words, the standing wave formed is elliptically polarised with a significant component of \vec{E} perpendicular to the surface. Thus, the adsorbed molecules “feel” a field almost doubled with respect to the radiation actually used. Any variation in the recorded reflectance (R)² is the consequence of a vibrational modes excitation. But it needs to be pointed out that in principle only molecules with vibrational modes having a dipole oriented normal to the surface will interact with the \vec{E} perpendicular component of the radiation. Although R is not the primary quantity desired, it can be readily correlated to a more convenient absorption factor, A .

$$A = \frac{R^0 - R}{R^0} \quad (2.14)$$

where R^0 is the value of the reflectance when no absorption occurs [53, 56]. At this stage, it is clear that RAIRS exhibits a greater sensitivity compared with other IR methods; for weak absorbers, such as simple hydrocarbons, good quality spectra can be obtained at the monolayer level on a metal single crystal surface

²The reflectance is defined as the ratio of the intensities of the incident and reflected light.

while for strong absorbers it is even possible to collect resolved spectra for small fractions of monolayer.

There is an important difference between RAIRS and the standard transmission IR technique. It is the so-called *metal surface selection rule*. Only vibrational modes that belong to the totally symmetric representation in the point group of the surface-adsorbate will be active [57, 58]. A simple way to see this is to consider how the electron distribution at the metal surface polarises in response of the dipole momentum of the complexed carbon monoxide (**Figure 2.20**). Only

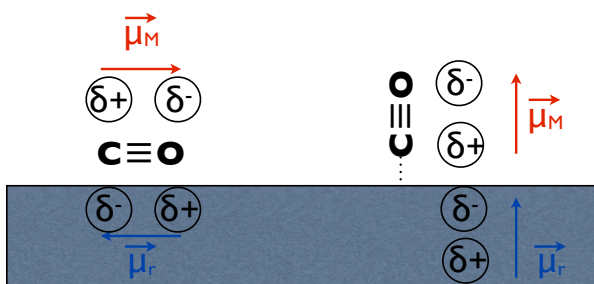


Figure 2.20: *Cartoon of the complexed CO on a metal surface. On the left side the electric dipole of the molecule cancels out with the image dipole at the interface. On the right the molecular and image dipoles re-enforce and IR absorption will be further enhanced.*

vibrations with a change of the dipole moment perpendicular to the surface will be IR active.

From a practical perspective a RAIRS experiment is relatively simple: requiring a standard FTIR spectrometer, a polariser (for polarisation modulation RAIRS), common IR optics and a detector such as a mercury cadmium telluride (MCT) which in principle ensures a range of 800-5000 cm^{-1} . The main advantages are:

- RAIRS is a highly versatile technique that can operate in a variety of conditions, from UHV to elevated pressures.
- It can achieve high resolution ($\leq 1 \text{ cm}^{-1}$) and sensitivity ($\frac{\Delta R}{R} < 0.001$)

Of course RAIRS, as all the experimental techniques, is not exempt from negative aspects, such as the complex dependence of the absorption factor (**equation 2.14**) on the thickness of the adsorbed layer, on the angle of incidence, and on optical constants of the substrate and overlayer. Thus sometimes RAIRS cannot be as sensitive as it could under optimum conditions especially if the adsorbates sit on the substrate preferentially with a geometry that aligns the dipole moment parallel to the surface. For instance, three papers relating the effects of UV photolysis on CO ice might be considered. One of these studies is based on RAIR

spectroscopy [59], the other two are based on transmittance spectroscopy [60, 61]. The latter show that after UV photolysis about 2% of the original CO is converted into CO₂. On the other hand in the work based on RAIR spectroscopy no CO₂ formation is observed. This does not mean that it is not formed and maybe the amount of product is too small to be detected by RAIRS in the conditions used. Therefore, it is important to recall that no perfect technique exists and being aware of the limits of the experiment being performed is crucial in interpreting the results. It is important to bear in mind that unless otherwise said the spectra shown in this thesis were collected using a metal substrate previously front coated with silica (SiO₂, ~ 300 nm thick). This means that (i) some wavelengths (*e.g.* 1350 - 1050 cm⁻¹) will be absorbed by the silica itself, and that (ii) the metal selection rule will still apply, although it will not appear to do so. In fact, the dosed molecules will deposit onto a rough surface and will be randomly oriented, therefore adsorbates having the dynamic dipole perpendicular to the metal surface might be either parallel either perpendicular to the silica interface.

Both the experimental chambers used for this thesis were equipped with a Fourier transform infrared spectrometer to conduct RAIRS measurements. A FTIR apparatus is based on two key elements: the Michelson interferometer and the Fourier transform. A schematic of the former is shown in **Figure 2.21**. The

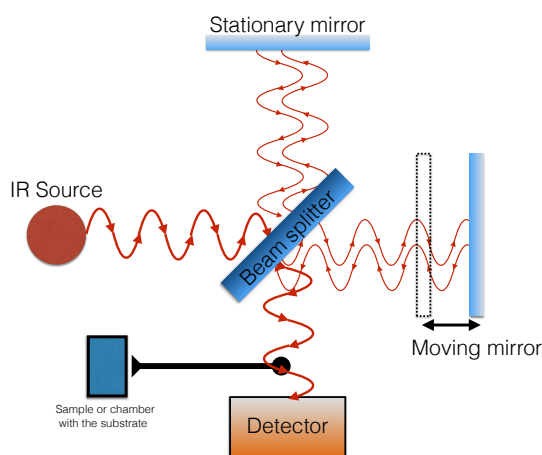


Figure 2.21: Schematic of a Michelson interferometer. The sample is just before the detector.

radiation coming from the source is directed towards a *beam splitter* that reflects only the 50% of the radiation and lets through the other 50%. The transmitted part of the incoming beam is incident on a *stationary mirror* while the reflected part propagates towards a *moving mirror* that slides back and forth changing the length of the optical path at every instant. In other words, the incoming beam is split in two and the two fractions are combined back at the beam splitter, then

sent to the detector acquiring the signal $I(t_0)$ at the instant t_0 with no optical delay. Immediately after, at t_i , the moving mirror has changed the optical path by a certain distance resulting in a phase difference, and therefore the intensity $I(t_i)$ perceived by the detector at t_i is increased or decreased due to interference effects at the beam splitter. The final data-set consists of the detected intensity as function of the optical delay, this is called the Interferogram and it is given by:

$$I(t) = \int_0^{\infty} I(\omega) \cos(\omega t) d\omega \quad (2.15)$$

This is then transformed into the following by using a Fourier transformation:

$$I(\omega) = \int_0^{\infty} I(t) \cos(\omega t) dt \quad (2.16)$$

which is the single beam spectrum.

In principle, RAIRS measurements can also be performed with dispersion spectrometers, its arrangement is shown in **Figure 2.22** and briefly described. The IR radiation coming from the source is split in two, one part sent to the sample and the other along a clean optical path. A chopper lets only one of them pass through the entry slit of the monochromator at the user's discretion. Thus the transmitted or the reference intensity is separated into its monochromatic components and one very narrow frequency range of the outgoing beam is selected and directed to the filter and the exit slit. The IR radiation finally reaches the detector, where the intensity is directly collected as a function of the frequency. While source and detector are of the same type for both the arrangements, the

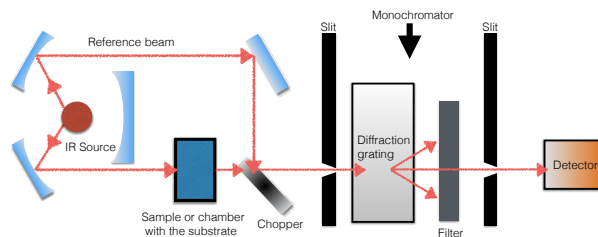


Figure 2.22: Schematic of a dispersive IR spectrometer. A monochromator is located in between the sample and the detector.

main difference is that for an FTIR the sample (or chamber with the substrate) lies just before the detector and the signal is recorded in the time domain, for a dispersion spectrometer the sample (or chamber with the substrate) is located after the source, before a monochromator and the detector, the data are collected in the frequency domain. This results in a FTIR being much faster in acquiring the data (*Fellgett advantage*). During the time that a dispersion spectrometer acquires the intensity passing through the exit slit a FTIR collects an entire

spectrum. Therefore more spectra can be readily collected and averaged to improve the signal/noise (S/N) ratio. This is possible thanks to the accuracy and continuity of the frequency scale (*Connes advantage*) (all the frequencies having the same resolution). A laser, such as a HeNe laser, dynamically controls the moving mirror shifts so as to guarantee a high degree of stability over extended periods of time. Furthermore, the radiation outcoming from the sample is collected directly in the time domain without passing through slits as it occurs for a dispersion spectrometer, thus the higher intensity (S/N) results into a greater gain for a FTIRs (*Jacquinot advantage*). However it is important to bear in mind that when the signal is acquired in the time domain it has to be converted into its analogue in the frequency domain using a Fourier transformation. This is not a straightforward step, but care must be taken when phase corrections and apodization functions are used as they could lead to erroneous spectral features. FT used to be a limiting factor when the first FTIR spectrometers were developed, but nowadays, given efficient computing hardware and improved algorithms (Fast Fourier Transform, FFT), this is no longer a problem. But the *Fellgett disadvantage* might still apply, meaning that if the source radiation is noisier in a certain frequency region it will spread throughout the spectrum in a FTIR spectrum, unless a noise-limited detector is used. Finally, but most importantly many FTIR instruments have a single beam while dispersion spectrometers have double beam, so the former needs to be constantly purged of CO₂ and vapour H₂O in order to have a background collected in the same conditions as for the sample scan. To conclude the benefits outnumber the disadvantages for using an FTIR rather than a dispersion instrument, justifying the choice to design the RAIRS set up with a Thermo Nicolet Nexus 870 and Varian 670-IR FTIRs for the Beam Rig and Ice Rig respectively combined with the same external liquid nitrogen cooled MCT detector (range of 800-5000 cm⁻¹).

2.8 Computational Chemistry

In this section, the fundamental principles of *ab initio* methods are outlined in order to highlight the theoretical background underlying the quantum mechanical calculations presented in the thesis.

2.8.1 Principles of Quantum Mechanics: the Hartree-Fock Approach

The starting point is the time-independent Schrödinger equation within the Born-Oppenheimer approximation:

$$H\psi(r, R) = E(R)\psi(r, R) \quad (2.17)$$

where the Hamiltonian has this form:

$$H = -\frac{\hbar^2}{2m_e} \sum_i^{n_e} \nabla_i^2 - j_0 \sum_i^{n_e} \sum_l^{n_n} \frac{Z_l}{r_{il}} + \frac{1}{2} j_0 \sum_{i \neq j}^{n_e} \frac{1}{r_{ij}} \quad (2.18)$$

that includes the kinetic energy of the electrons, the interaction of each electron with the nuclei and the electron repulsion term. The nucleus-nucleus repulsion term is usually added as a classical term at the end of the calculation. There is no exact way to solve the equation for systems with many electrons, thus a large variety of methods with different underlying approximations are used. The most established and fundamental method is the Hartree-Fock self-consistent field methods. It describes each electron as moving in the electrostatic fields of the nuclei and the average field of the other n_e-1 electrons (**eq. 2.22**). In other words the Hamiltonian is decomposed into mono-electronic Hamiltonians, h_i , neglecting the electron-electron repulsion term. It follows that:

$$H = H^0 + \frac{1}{2} j_0 \sum_{i \neq j}^{n_e} \frac{1}{r_{ij}} = \sum_{i=1}^{n_e} h_i + \frac{1}{2} j_0 \sum_{i \neq j}^{n_e} \frac{1}{r_{ij}} \quad (2.19)$$

As a first assumption, the many-electron wavefunction is described by the wavefunction ψ^0 obtained by solving $H^0\psi^0 = E^0\psi^0$, which has the form of

$$\psi^0 = \prod_i \psi_i^0 \quad (2.20)$$

and when the requirement intrinsic to the Pauli principle is taken into account ψ^0 is given by:

$$\psi^0 = \frac{1}{\sqrt{n_e!}} \det | \phi_a(1)\phi_b(2)\dots\phi_z(n_e) | \quad (2.21)$$

where the $\phi_m(i)$ is the spinorbital (the product between the orbital wavefunction and a spin function) for the i^{th} -electron in the spinorbital m (molecular orbital m and with a certain spin state, say $\alpha(i)$). The determinantal wavefunction is found by the spinorbitals that give the lowest energy $E = \langle \psi^0 | H | \psi^0 \rangle$ under the constraint that spinorbitals are orthonormal and normalised. This leads to the Hartree-Fock (HF) equations for each spinorbital:

$$h_1\phi_i(1) + \sum_{j=1}^{N_{SO}} \{ J_j(1)\phi_i(1) - K_j(1)\phi_i(1) \} = \sum_{j=1}^{N_{SO}} \epsilon_{i,j}\phi_j(1) \quad (2.22)$$

$$f_1\phi_i(1) = \sum_{j=1}^{N_{SO}} \epsilon_{i,j}\phi_j(1)$$

Thus the **Fock operator** is

$$f_1 = h_1 + \sum_{j=1}^{N_{SO}} \{ J_j(1) - K_j(1) \} \quad (2.23)$$

where \mathbf{J}_j and \mathbf{K}_j are the Coulomb and Exchange operator respectively. The latter represents the quantum mechanical Columbic repulsion between electrons, while the exchange operator has no corresponding meaning in classical mechanics and takes into account the effects of spin correlation. For closed-shell molecules all spatial functions are doubly occupied, so the Fock operator can be rewritten as:

$$f_1 = h_1 + \sum_m^{N_{SO}} \{ 2J_{m'}(1) - K_{m'}(1) \} \quad (2.24)$$

where

$$\begin{aligned} J_{m'}(1)\psi_m(1) &= j_0 \left(\int \psi_{m'}^*(2) \frac{1}{r_{12}} \psi_{m'}(2) d\tau_2 \right) \psi_m(1) \\ K_{m'}(1)\psi_m(1) &= j_0 \left(\int \psi_{m'}^*(2) \frac{1}{r_{12}} \psi_m(2) d\tau_2 \right) \psi_{m'}(1) \end{aligned} \quad (2.25)$$

The sum is over all the occupied spatial wavefunctions. Each molecular orbital is obtained by solving **Equation 2.22** iteratively until convergence.

2.8.2 Beyond HF: Møller-Plesset Many-body Perturbation and Coupled-cluster Methods

Although the HF method appears to be robust and reliable, it ignores electron correlation entirely as the effect of n_e-1 electrons on the electron i is averaged. Therefore efforts have been made to move beyond this limitation towards a more precise description of the ‘exact’ wavefunction. Perturbation theory (PT) provides us with the theoretical background to estimate the correlation energy. An example of direct application of PT is the Møller-Plesset perturbation theory (MPPT), a procedure developed by C. Møller and M. S. Plesset in 1934 [62], only more recently developed and adapted for QM software [63, 64]. In MPPT the zeroth-order Hamiltonian is given by the sum of the one-electron Fock operators:

$$H^0 = H^{HF} = \sum_{i=1}^{n_e} f_i \quad (2.26)$$

associated with the following equation:

$$H^{HF}\psi_0 = E_0^{(0)}\psi_0 \quad (2.27)$$

$$\sum_{i=1}^{n_e} f_i \psi_0 = \sum_{j=1}^{N_{SO}} \epsilon_{i,j} \phi_j(1)$$

where the ground state wavefunction is the eigenfunction of H_{HF} with eigenvalue $E_0^{(0)} = \sum_{j=1}^{N_{SO}} \epsilon_{i,j}$. The first-order perturbation term at the Hamiltonian is simply H^1 given by:

$$H^1 = H - H_{HF} \quad (2.28)$$

$$H^1 = \sum_i h_i + \frac{1}{2} j_0 \sum_{i \neq j} \frac{1}{r_{ij}} - \sum_{i=1} f_i = j_0 \sum_{i \neq j} \frac{1}{r_{ij}} - \sum_m \{ 2J_m(i) - K_m(i) \} \quad (2.29)$$

where the sum over m is over the occupied molecular orbitals. The first-order correction to the energy is

$$E_0^{(1)} = \langle \psi_0 | H^1 | \psi_0 \rangle \quad (2.30)$$

which sums to the zero-order energy $E_0^{(0)}$ to return the HF energy. In order to finally move beyond the HF method, one shall consider the second order correction to the energy that according the perturbation theory is expressed as follows:

$$E_0^{(2)} = \langle \psi_0 | H^{(2)} | \psi_0 \rangle + \sum_{k \neq 0} \frac{\langle \psi_k | H^{(1)} | \psi_0 \rangle \langle \psi_0 | H^{(1)} | \psi_k \rangle}{E_0^{(0)} - E_k^{(0)}} \quad (2.31)$$

ψ_k is a multiply excited determinant, an eigenfunction of H_{HF} . The energy as here reported, $E^{(0)} + E^{(1)} + E^{(2)}$, is the result given by the MP2 method, which in other words means correcting the energy up the second term of the following:

$$E_0 = E_0^{(0)} + \sum_n \lambda^n E_0^{(n)} \quad (2.32)$$

If the 3rd, 4th, 5th and nth, correction energy term is included then it shall be referred to the method as MP3, MP4, MP5, and MPn. It should be noted that whereas perturbation theory is size-consistent, it is not variational. This holds as true for the MPPT as for the *coupled-cluster method* (CC). The latter defines the exact wavefunction in terms of the *cluster operator* C

$$\psi = e^C \psi_0 \quad (2.33)$$

where e^C can be expressed by the series expansion

$$e^C = \sum_{n=0}^{\infty} \frac{C^n}{n!} = 1 + C + \frac{1}{2!} C^2 + \frac{1}{3!} C^3 + \frac{1}{4!} C^4 + \dots \quad (2.34)$$

where n is a numerical index in the Taylor expansion. The explicit form of the operator C is not known but it can be described as follows:

$$C = C_1 + C_2 + C_3 + \dots + C_{n_e} \quad (2.35)$$

$$C_1\psi_0 = \sum_{a,p} t_a^p \psi_a^p$$

where

$$C_1\psi_0 = \sum_{a,p} t_a^p \psi_a^p; \quad C_2\psi_0 = \sum_{a,b,p,q} t_{ab}^{pq} \psi_{ab}^{pq}; \quad \dots \quad (2.36)$$

C_1 is the one-electron excitation operator, C_2 is the two-electron excitation operator, C_{n_e} is the n_e -electron excitation operator, t_a^p are the single-excitation amplitudes, t_{ab}^{pq} are the double-excitation amplitudes. Combining the **Equations 2.34** and **2.35** into **Equation 2.33** results in linear, quadratic, cubic and n -th order terms in C_n and mixed terms such as $C_1C_2\psi_0$ or $C_1C_2C_3\psi_0$. The $C_1\psi_0$ term gives a *single excited determinant*, while $C_2\psi_0$ results in doubly excited determinants. The latter is said to be *connected* and arises from the double excitation amplitude, and differs from the *disconnected* double excitation term, which is linked to a product of single-excitation amplitudes, such as $C_1C_1\psi_0$. The same difference also applies to the terms with an order superior to the second: *e.g.* $C_3\psi_0$ is a *connected triple-excitation* contribution and $C_1^3\psi_0$ or $C_1C_2\psi_0$ are disconnected terms. Depending on which term the exponential operator is truncated in the Taylor expansion the coupled-cluster approach is referred as CCD, CCSD, CCSDT.

$$C = C_2 \longrightarrow CCD$$

$$C = C_1 + C_2 \longrightarrow CCSD \quad (2.37)$$

$$C = C_1 + C_2 + C_3 \longrightarrow CCSDT$$

Nowadays, performing couple-cluster calculations is considered one of the most reliable and accurate method of estimating the correlation energy in addition to the HF energy, however it scales with N^9 where N is the number of basis set functions, thus it is still not realistic to use coupled-cluster methods on molecular systems with more than ~ 8 atoms (unless there are many hydrogens). The MP2 method, on the other hand, although less accurate with a finite basis set, has been developed and well implemented into QM software such as Gaussian or Molpro to such a level that it scales with N^2 - N^4 and in some cases even linearly. These many wavefunction based correlation methods are essential to

accurately describe non-covalent interactions, especially where density functional theory fails without a judicious choice of the functional. However, the applicability of MP2 and CC methods extends only to small systems such as dimers and clusters of molecules with dozens of atoms overall at the best. By introducing additional approximations, such as the resolution-of-the-identity (RI) for the four-index electron repulsion integrals (ERIs) with optimised auxiliary basis set, RI-MP2 can be applied to systems with hundreds of atoms. However, the efficiency and the accuracy depend on the choice of the auxiliary basis set, which should be optimised for the particular orbital basis used in the calculation. In conclusion, at the moment using MP2 or CC methods is not a feasible strategy to directly model the adsorbate-surface interaction and surface processes. However, the key interactions acting locally at molecule-to-molecule scale (*e.g.* dimer or small representative clusters) will be accurately described and still significant and semi-quantitative applicable to the extended systems of interest. Moreover, these high level calculations build a solid ground for large scale theoretical simulations: for instance, CCSD(T) calculations were performed for the CO dimer on a grid of geometries in order to extrapolate and analyse the CO-CO potential which was then used for Monte Carlo calculations [3].

2.8.3 Towards Statistical Large Systems

Stochastic methods attempt to probabilistically determine the state of a system without predicting it precisely (probability theory). This applies to the so-called non-deterministic systems, which have, in other words, a random probability distribution of a certain observable. Monte Carlo methods are the most established examples of this theory, randomly sampling the system of interest under the constraint of satisfying a fundamental balance condition each time. An example of this method's application is found in the *chemical kinetics simulator* (CKS), a package developed by IBM Almaden Research Centre [65]. It is a simple code that performs Monte Carlo integration to solve the differential equations given as input, the larger the number of events the better is the outcome. It can be used, for instance, to model TPD traces by a system of differential equation representing the kinetic steps of each key physical processes involved until a good fit of the experimental data is reached. Stochastic algorithms can be also coupled with QM fundamentals in order model the interaction of ions and electrons with a solid, as these processes involve many particles (molecules/atoms) and multiple events such as charging, electronic excitations, ionisations, and formation of secondary electrons.

These phenomena are of astrophysical relevance when cosmic rays bombardment on dust grains is considered and it will be object of further discussion in the **Chapter 5**. Therefore it is convenient to describe the key-principles concerning the interactions between energetically charged particles (ions or electrons) and solids. An ion moving inside a medium can lose energy by scattering with nuclei (nuclear stopping) or electrons (electron stopping). The starting point is the theoretical model developed by Lindhard, Scharff and Schiott [66] for stopping power at low velocity; it uses the Thomas-Fermi statistical model [67] to describe the atomic structure like a free-electron gas and predicts values of electron and nuclear stopping proportional to the projectile velocity. The nuclear stopping power can be described as a change of the ion energy with respect to its propagation $\left(\frac{\partial E}{\partial x}\right)_n$, where the subscript n refers to the scattering with nuclei, and the ion energy (E), and the range (R) are scaled as expressed below:

$$\epsilon = C_{TF} \frac{A_T}{A_{tot}} \frac{E/2E_B}{Z_P Z_T Z_{tot}^{\frac{1}{2}}} \quad (2.38)$$

$$\rho = 4\pi(a_B C_{TF})^2 \frac{A_P A_T}{A_{tot}^2} \frac{R N_\rho}{Z}$$

where C_{TF} is the Thomas-Fermi constant $\left(\frac{9\pi^2}{27}\right)$; A_T and A_P are the atomic mass number of the target and projectile atom respectively, and A_{tot} is the their sum; E_B is the Bohr energy and a_B is the Bohr radius; N_ρ is the number density of the target material; and Z is the atomic number of the projectile or the target. The $\left(\frac{\partial E}{\partial x}\right)_n$ is then expressed as $\left(\frac{\partial \epsilon}{\partial \rho}\right)_n$ that gives a function $f(\epsilon)$ depending only on the Thomas-Fermi interaction potential alone and can be calculated numerically [68]. The electron stopping power, $\left(\frac{\partial E}{\partial x}\right)_e$, is similarly related to the following:

$$\left(\frac{\partial \epsilon}{\partial \rho}\right)_e = \frac{32}{3\pi} \sqrt{\frac{m_e c^2}{m_{amu} c^2}} \frac{Z_P^{\frac{1}{2}} Z_T^{\frac{1}{2}}}{Z_{tot}^{\frac{3}{4}}} \frac{A_{tot}^{\frac{3}{2}}}{A_P^{\frac{3}{2}} A_T^{\frac{1}{2}}} Z_P^{\frac{1}{6}} \sqrt{\epsilon} \quad (2.39)$$

where the subscript e refers to the scattering by the electrons. Later on the model was improved by the introduction of more realistic Hartree-Fock atoms and describing the collision of an incoming ion and the atom including exchange and correlation interactions between the overlapping electron shells. Software like Stopping and Range of Ions in Matter and Transport of Ions in Matter (SRIM/TRIM) [69, 70] refer to this theoretical framework combined with empirically derived parameters (particularly for the definition of Z in the above equations and because derives $f(\epsilon)$ from a fit to experimental data) and Monte Carlo statistical algorithms to simulate the ion propagation and energy loss averaging the collision results.

In a similar fashion, but on purely first principles basis, the monte Carlo Simulation of electron trajectory in solids (CASINO) [71] can be used when it is desirable to look at an electron trajectory rather than an ion moving inside a molecular medium. This computer program, in a sense complementary software to SRIM, is especially designed for low electron beam interaction in a bulk and thin foil and aims to simulate enough electron trajectories to replicate the scanning electron microscope (SEM) images. It relies on quantum Monte Carlo (QMC) electronic structure calculations, an explicitly many-body method, applicable to both finite and periodic systems, guaranteeing high accuracy but fairly low scaling of computational cost.

Bibliography

- [1] E. F. van Dishoeck, *Faraday Discuss.*, 2014, **168**, 9.
- [2] W. H. Brown, C. S. Foote and B. L. Iverson, *Organic Chemistry*, Thomson Learning, Inc., 2005.
- [3] L. J. Karssemeijer, S. Ioppolo, M. C. van Hemert, A. van der Avoird, M. A. Allodi, G. A. Blake and H. M. Cuppen, *Astrophys. J.*, 2014, **781**, 16.
- [4] J. D. Thrower, M. P. Collings, F. J. M. Rutten and M. R. S. McCoustra, *Mon. Not. R. Astron. Soc.*, 2009, **394**, 1510.
- [5] J. D. Thrower, *PhD thesis*, Heriot-Watt University, 2009.
- [6] G. M. A. Abdulgalil, *PhD thesis*, Heriot-Watt University, 2013.
- [7] V. Fiorin, *PhD thesis*, University of Nottingham, 2001.
- [8] M. P. Collings, J. W. Dever, H. J. Fraser, M. R. S. McCoustra and D. A. Williams, *Astrophys. J.*, 2003, **583**, 1058.
- [9] V. L. Frankland, *PhD thesis*, Heriot-Watt University, 2011.
- [10] A. Abdulgalil, D. Marchione, A. Rosu-Finsen, M. P. Collings and M. R. S. McCoustra, *J. Vac. Sci. Technol. A*, 2012, **30**, 0415051.
- [11] S. Turton and R. G. Jones, *Surf. Sci.*, 1997, **377**, 719.
- [12] R. G. Jones and C. J. Fisher, *Surf. Sci.*, 1999, **424**, 127.
- [13] S. G. Hessey and R. G. Jones, *Surf. Interface Anal.*, 2015, **47**, 587.
- [14] J. W. Ward, N. R. Mulford and M. Kahn, *J. Chem. Phys.*, 1967, **47**, 1710.
- [15] P. C. Nordline and P. W. Gilles, *J. Chem. Phys.*, 1981, **74**, 5242.
- [16] P. Boudininkas, R. K. Edwrds and P. G. Wahlbeck, *J. Chem. Phys.*, 1968, **48**, 2859.

- [17] D. M. Golden, G. N. Spokes and S. W. Benson, *Angew. Chem.*, 1973, **14**, 602.
- [18] M. J. Rossi, *Chimia*, 1996, **50**, 199.
- [19] I. Sugimoto, T. Matsumoto, H. Shimizu, R. Munakata, M. Seyama and J. Takahashi, *Thin Solid Films*, 2009, **517**, 3817.
- [20] M. P. Collings, J. W. Dever, H. J. Fraser and M. R. S. McCoustra, *Astrophys. Space Sci.*, 2003, **285**, 633.
- [21] A. Rosu-Finsen, *PhD thesis*, Heriot-Watt University, 2015.
- [22] A. Gerbi, L. Savio, L. Vattuone, D. Pirani, F. Cappelletti and M. Rocca, *Angew. Chem. Int. Ed.*, 2006, **45**, 6655.
- [23] L. Vattuone, F. Savio, D. Cappelletti, M. Okada and M. Rocca, *Prog. Surf. Sci.*, 2010, **85**, 92.
- [24] K. K. Kolasinski, *Surface Science: Foundations of Catalysis and Nanoscience*, Wiley, 2012.
- [25] R. J. Madix, *Surface Reactions*, Springer, Berlin, 1994.
- [26] L. A. Creager, S. E. and Hockett and G. K. Rowe, *Langmuir*, 1992, **8**, 854.
- [27] M. Haruta, N. Yamada, T. Kobayashi and S. Iijima, *J. Catal.*, 1989, **115**, 301.
- [28] M. Gostein and G. O. Sitz, *J. Chem. Phys.*, 1997, **106**, 7378.
- [29] R. S. Smith, J. Matthiesen and B. D. Kay, *J. Phys. Chem. A*, 2014, **118**, 8242.
- [30] V. D. DeSimone, A. J. Crowell, C. D. Sherrill and T. M. Orlando, *J. Chem. Phys.*, 2013, **139**, 164702.
- [31] S. D. Green, A. S. Bolina, R. Chen, M. P. Collings, W. A. Brown and M. R. S. McCoustra, *Mon. Not. R. Astron. Soc.*, 2009, **398**, 357.
- [32] Z. Wang, X. Jia and R. Wang, *J. Phys. Chem. A*, 2004, **108**, 5424.
- [33] B. Yoon, H. Hakkinen and U. Landman, *J. Phys. Chem. A*, 2003, **107**, 4066.
- [34] S. A. C. Carabineiro and B. E. Nieuwenhuys, *Gold Bull.*, 2009, **42**, 288.

- [35] J. Kim, E. Samano and B. E. Koel, *Surf. Sci.*, 2006, **600**, 4622.
- [36] M. P. Collings, V. L. Frankland, J. Lasne, D. Marchione, A. Rosu-Finsen and M. R. S. McCoustra, *Mon. Not. R. Astron. Soc.*, 2015, **449**, 1826.
- [37] G. C. Chinchin, P. J. Denny, D. G. Parker, M. S. Spencer and D. A. Whan, *Appl. Catal.*, 1987, **30**, 333.
- [38] R. G. Copperthwaite, P. R. Davies, M. A. Morris, M. W. Roberts and R. A. Ryder, *Appl. Catal.*, 1988, **1**, 11.
- [39] K. Acharyya, G. W. Fuchs, H. J. Fraser, E. F. van Dishoeck and H. Linnartz, *Astron. Astrophys.*, 2007, **466**, 1005.
- [40] J. Pischel and A. Pucci, *J. Phys. Chem. C*, 2015, **119**, 18340.
- [41] S. K. Shaikhutdinov, R. Meyer, M. Naschitzki, M. Bäumer and H. J. Freund, *Catal. Lett.*, 2003, **86**, 211.
- [42] D. Chakarov, L. Österlund and B. Kasemo, *Langmuir*, 1995, **11**, 1201.
- [43] D. Chakarov, L. Österlund and B. Kasemo, *Vacuum*, 1995, **46**, 1109.
- [44] A. S. Bolina, A. J. Wolff and W. A. Brown, *J. Chem. Phys. B*, 2005, **109**, 16836.
- [45] A. S. Bolina, A. J. Wolff and W. A. Brown, *J. Chem. Phys.*, 2005, **122**, 044713.
- [46] A. Clemens, L. Hellberg, H. Grönbeck and D. Chakarov, *Phys. Chem. Chem. Phys.*, 2013, **15**, 20456.
- [47] D. A. Outka and R. J. Madix, *J. Am. Chem. Soc.*, 1987, **109**, 1708.
- [48] A. Abdulgalil, D. Marchione, J. D. Thrower, M. P. Collings, M. R. S. McCoustra, F. Islam, M. E. Palumbo, E. Congiu and F. Dulieu, *Phil. Trans. A*, 2013, **371**, 20110586.
- [49] A. J. Westphal, M. R. Stroud, H. A. Bechtel, F. E. Brenker, A. L. Butterworth, G. J. Flynn, D. R. Frank, Z. Gainsforth, J. K. Hillier, F. Postberg, A. S. Simionovici, V. J. Sterken, L. R. Nittler, C. Allen, D. Anderson, A. Ansari, S. Bajt, R. K. Bastien, N. Bassim, J. Bridges, D. E. Brownlee, M. Burchell, M. Burghammer, H. Changela, P. Cloetens, R. Davis, A. M. Doll, C. Floss, E. Grün, P. R. Heck, R. Hoppe, B. Hudson, J. Huth, A. Kearsley, A. J. King, B. Lai, J. Leitner, L. Lemelle, A. Leonard, H. Leroux,

- R. Lettieri, W. Marchant, R. Ogliore, W. J. Ong, M. C. Price, S. A. Sandford, J. A. Sans Tresseras, S. Schmitz, T. Schoonjans, K. Schreiber, G. Silversmit, V. A. Solé, R. Srama, F. Stadermann, F. Stephan, J. Stodolna, S. Sutton, m. Trieloff, P. Tsou, T. Tyliczszak, B. Vekemans, L. Vincze, J. Von Korff, N. Wordsworth, D. Zevin, M. E. Zolensky and Stardust@home, *Science*, 2014, **345**, 6198.
- [50] H. Kimura, I. Mann and E. K. Jessberger, *Astrophys. J.*, 2003, **583**, 314.
- [51] J. H. de Boer, *The Dynamical Character of Adsorption*, Clarendon Press, 1968.
- [52] G. Attard and C. Barnes, *Surfaces*, Oxford University Press, 2011.
- [53] R. G. Greenler, *J. Chem. Phys.*, 1966, **44**, 310.
- [54] N. Sheppard, *Ann. Rev. Phys. Chem.*, 1988, **39**, 589.
- [55] M. Trenary, *Ann. Rev. Phys. Chem.*, 2000, **51**, 381.
- [56] O. S. Heavens, *Optical Properties of Thin Solid Films*, Academic Press Inc., 1955.
- [57] J. E. Katon and D. B. Phillips, *Appl. Spec. Rev.*, 1973, **7**, 1.
- [58] N. Sheppard, *Appl. Spec.*, 1984, **38**, 471.
- [59] K. I. Öberg, G. W. Fuchs, Z. Awad, H. J. Fraser, S. Schlemmer, E. F. van Dishoeck and H. Linnartz, *Astrophys. J.*, 2007, **662**, L23.
- [60] M. J. Loeffler, G. A. Baratta, M. E. Palumbo, G. Strazzulla and R. A. Baragiola, *Astron. and Astrophys.*, 2005, **435**, 587.
- [61] G. M. Muñoz Caro, A. Jiménez-Escobar, J. A. Martín-Gago, C. Rogero, C. Atienza, S. Puertas, J. M. Sobrado and J. Torres-Redondo, *Astron. and Astrophys.*, 2010, **522**, A108.
- [62] C. Møller and M. S. Plesset, *Phys. Rev.*, 1934, **46**, 618.
- [63] S. Saebo and P. Pulay, *Chem. Phys. Lett.*, 1985, **113**, 13.
- [64] M. Schütz, G. Hetzer and H. J. Werner, *J. Chem. Phys.*, 1999, **111**, 5691.
- [65] *IBM Almaden Research Centre, CKS*, IBM Corporation, 1995.
- [66] J. Lindhard, M. Scharf and H. E. Schiott, *Mat. Fys. Medd. Dans. Viden. Selskab.*, 1963, **33**, 1.

- [67] E. Fermi and E. Teller, *Phys. Rev.*, 1947, **72**, 399.
- [68] J. Lindhard, V. Nielsen and M. Scharff, *Mat. Fys. Medd. Dan. Vid. Selsk.*, 1968, **36**, 1.
- [69] J. F. Ziegler, *SRIM/TRIM*, <http://www.srim.org>, 2013.
- [70] J. F. Ziegler, J. P. Biersack and M. D. Ziegler, *The Stopping and Range of Ions in Solids*, Pergamon Press, New York, 2008.
- [71] *Theory of Condensed Matter Group Cambridge*, *CASINO V 2.13*, <http://www.gel.usherbrooke.ca/casino/What.html>, 2014.

Chapter 3

Adsorption of Small Molecules on Amorphous Silica

Contents

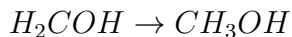
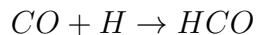
3.1	Introduction	93
3.2	TPD	93
3.2.1	Experimental Procedure	95
3.2.2	TPD: Results and Discussion	95
3.2.3	Comparison of TPD Traces	122
3.3	RAIRS	127
3.3.1	RAIRS: Results and Discussion	127
3.3.2	TP-RAIRS: Results and Discussion	135
3.4	Conclusions	141
	Bibliography	142

3.1 Introduction

This chapter reports the experimental results for adsorption of water (H_2O), methanol (CH_3OH), and diethyl ether ($(\text{CH}_3\text{CH}_2)_2\text{O}$) onto a silica (SiO_2) substrate. Firstly temperature programmed desorption (TPD) traces of these species will be presented and their adsorption behaviour compared, then Reflection-Absorption Infrared Spectroscopy (RAIRS) results will be used to further describe the interaction of each species at the interface.

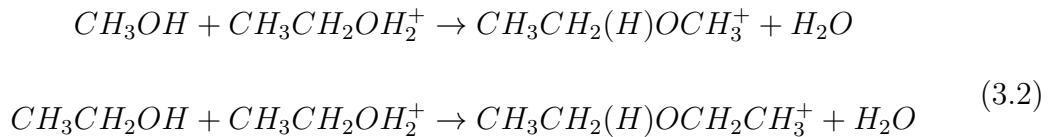
3.2 TPD of Water, Methanol, Diethyl Ether from Silica

In the first chapter, the importance and the role of interstellar grains have been highlighted reporting the main processes that favour chemical complexity starting from very small molecules and atoms. In the first stages of cloud and star formation, the key reactions involving interstellar dust grains as chemical “factories” are hydrogenation of atoms on top of the silicate cores resulting in H_2O dominated ice with a high CO_2 concentration. Subsequently the mantles enriched with CO allow further CO_2 formation along with CH_3OH synthesis by a four step process [1]:



Hydrogenation of CO on dust grains is believed to be the main route to CH_3OH formation, while CH_3OH synthesis in the gas phase and subsequent accretion on the grain mantle is thought to be negligible. Therefore, although H_2O remains the principal component of interstellar ices [2], CH_3OH , CO and CO_2 are the other main building blocks [3–6]. Dust mantles would finally be depleted of CO predominantly during the protostellar stage by thermal desorption starting at 20 K, which modifies their morphology and composition (*e.g.* $\text{H}_2\text{O}:\text{CO}_2$ segregation). It is worthwhile noting that during the lifetime of a molecular cloud, vacuum ultraviolet photons and cosmic rays promote radical chemistry within the icy mantles producing an incredible variety of species including: simple ethers (such

as dimethyl ether, CH_3OCH_3); esters (methyl formate HCOOCH_3); carboxylic acids (ethanoic acid, CH_3COOH); all the so-called complex organic molecules (COMs) including glycolaldehyde (HOCH_2CHO) [7–10], nitriles [11] as well as amines and amino acids [12]. Some of these molecules have been detected in the gas phase by their rotational spectroscopic features and only their precursors might have formed on the grains. This is the case for ethers, like ethyl methyl ether ($\text{CH}_3\text{CH}_2\text{OCH}_3$) and diethyl ether ($\text{CH}_3\text{CH}_2\text{OCH}_2\text{CH}_3$), because dimethyl ether is in high abundance in hot-core type sources within dense interstellar clouds [13]. The increase of temperature in hot cores causes the evaporation of icy mantles from interstellar dust grains releasing large amounts of simple alcohols like methanol (CH_3OH) and ethanol ($\text{CH}_3\text{CH}_2\text{OH}$). These species can be protonated in the gas phase and lead to the efficient production of ethers [7, 14]:



The protonated ethyl methyl ether and diethyl ether formed according to this alkyl-transfer reaction scheme [15] would then undergo dissociative recombination reactions to form neutral ethers.

A combination of TPD and RAIRS has been used to investigate the interaction of H_2O , CH_3OH and $(\text{CH}_3\text{CH}_2)_2\text{O}$ with the surface of amorphous SiO_2 at a temperature range of 20 K to over 150 K and surface coverages from the sub-monolayer to multilayer. While H_2O and CH_3OH have high abundances within the ice of the interstellar dust, $(\text{CH}_3\text{CH}_2)_2\text{O}$ is an unlikely candidate as grain mantle component. The choice of these particular systems was made to better understand the role of hydrogen bonding in H_2O ice on SiO_2 compared to other similar molecular systems with weaker intramolecular interactions; and how this relates to the adsorption and accommodation onto the surface. In other words, moving from a strong H-bond network to aliphatic intramolecular bonds exemplifies the range of the main interactions and interplay existing between adsorbate-adsorbate and adsorbate- SiO_2 . Furthermore, the results will provide a solid base for the studies highlighted in the next chapters, especially the electron-promoted desorption experiments, which were done on the Beam Rig, where the lowest temperature (105 - 110 K) is barely enough to adsorb $(\text{CH}_3\text{CH}_2)_2\text{O}$ and too high to adsorb simpler ethers like $(\text{CH}_3)_2\text{O}$.

3.2.1 Experimental Procedure

The surface used in these experiments was a copper substrate front-coated with ~ 300 nm thick film of amorphous silica (SiO_2) that was mounted on a closed-cycle helium cryostat, as described in the previous chapter for the Ice Rig, routinely achieving a base temperature of 20 K. The substrate was heated to 300 K before cooling prior to conducting experiments. Although by doing so it is unlikely to remove all the residual carbon contamination that might have arisen from decomposition of alcohol and ether on the surface there was no discernible change in TPD traces over time. Therefore reproducibility was achieved without performing annealing and Ar^+ sputtering cycles that could lead to more morphological changes and/or partial crystallisation of the SiO_2 film. Sample position was optimised to guarantee the best signal for the QMS or the IR detector. The average heating rate during the TPD experiments was 0.7 K s^{-1} and temperature was monitored with a precision better than 0.5 K. Dosing was conducted by background deposition *via* the gas manifolds collecting the vapour phase of the liquids, which were previously degassed and purified by freeze-pump thaw cycles. Exposures are expressed in Langmuir units (L) and uncorrected for the ionisation coefficient.

3.2.2 TPD: Results and Discussion

Firstly TPD traces of CH_3OH will be presented and discussed, then the same experiments will be discussed for $(\text{CH}_3\text{CH}_2)_2\text{O}$. Finally the desorption behaviour of H_2O , CH_3OH and $(\text{CH}_3\text{CH}_2)_2\text{O}$ will be described and compared.

TPD of Methanol on Silica

Figure 3.1 shows desorption traces for sub-monolayer (upper row) and multilayer (lower row) CH_3OH from a SiO_2 surface when deposited at ~ 20 K monitoring at $m/z = 31$ and $m/z = 32$ (not shown). The heating rate was set at $\sim 0.7 \text{ K s}^{-1}$. Possible H_2O contamination from the background residual gas was ascertained to be negligible by monitoring at $m/z = 18$. It is worth noting that the experiment was repeated dosing molecules at 110 K and there are no differences between the two sets except that the heating rate was slightly higher ($\sim 0.8 \text{ K s}^{-1}$) in the latter case, thus resulting in a systematic shift towards higher temperatures. The consistency is expected as TPD probes the adsorbate arrangement at equilibrium and as temperature is increased from 20 K to 110 K there is negligible CH_3OH loss; while molecules are free to diffuse over the surface and thermalise in the range spanned by the two base temperatures. In other words the desorption begins from the same thermodynamically stable configuration whether molecules

TPD of CH₃OH

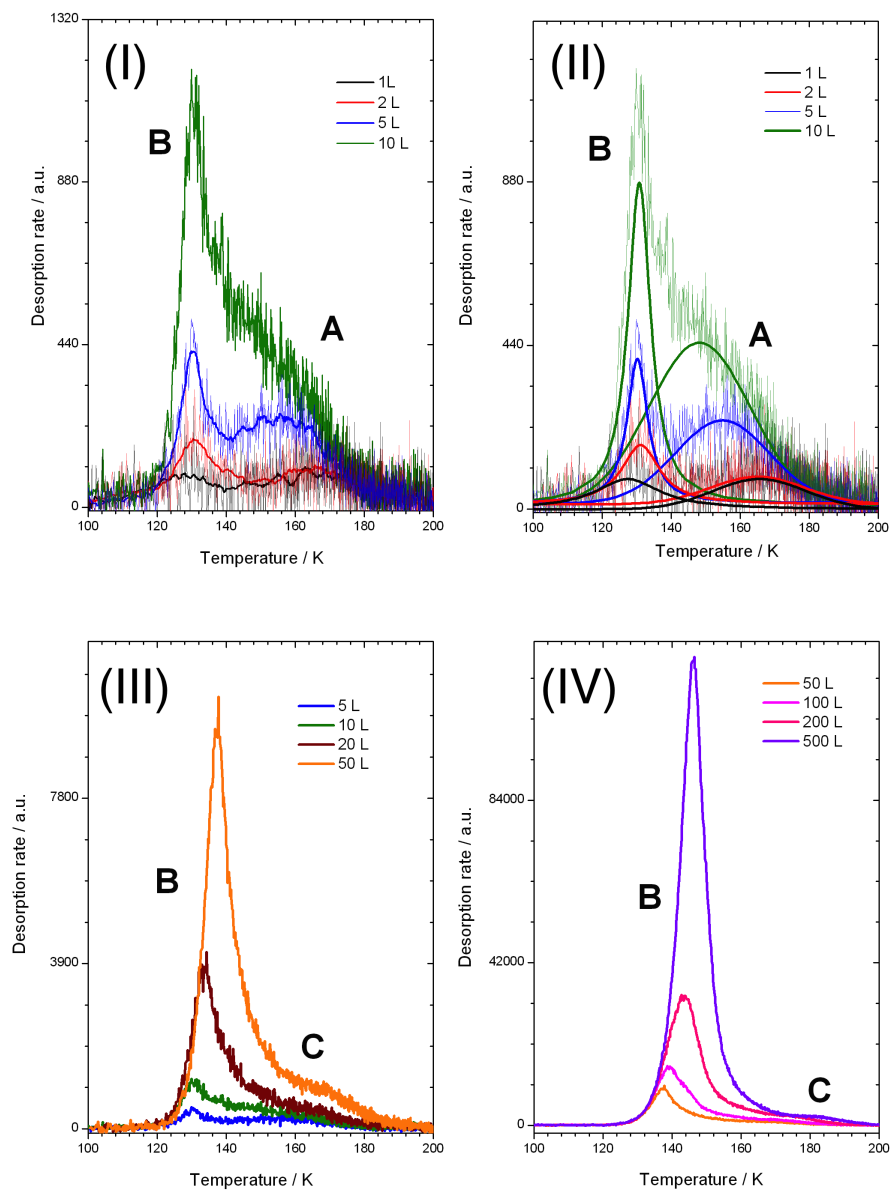


Figure 3.1: TPD traces for desorption of 1 L to 500 L of CH₃OH on SiO₂. Low coverages are reported in the upper row panels and high coverages are displayed in the lower row. In the subplot labelled (I) both peak A and B can be observed. Peak A is assigned to the desorption of physisorbed CH₃OH on the SiO₂ surface. In the low exposures regime (upper row panel) peak B is assigned to the formation of a second CH₃OH layer. The subplot labelled (II) shows the fitting functions for these two features clarifying their growth behaviour. The subplots (III) and (IV) display the peaks B and C. The former is consistent with bulk amorphous CH₃OH for exposures larger than 10 L. Peak C is consistent with bulk crystalline CH₃OH.

are dosed at 110 K or at 20 K and then activated to diffuse over the silica reaching the energetic minimum upon heating up to 110 K.

The lowest exposure traces (1 to 10 L) clearly display two desorption features, a broader high temperature peak (referred as *peak A* from now on) and a sharper low temperature feature (*peak B*). The former has a maximum that moves to lower temperatures as the coverage increases. It is centred around 165 K for the 2 L trace and 155 K for the 5 L, it finally merges with the other features at 10 L and above. Peak A can be assigned to the desorption of physisorbed CH₃OH on the SiO₂ interface. However, the shift of the maximum towards lower temperatures as the coverage increases is typical of second-order kinetics (**Figure 2.17**), but if that were the case then this would imply dissociative adsorption and subsequent associative desorption. With a molecular, non-metallic interface such as SiO₂ this possibility can be discarded for physisorbed adsorbates like CH₃OH, (CH₃CH₂)₂O and H₂O on SiO₂. Deviation from first-order kinetics and the high temperature tail have been previously reported for benzene (C₆H₆) on the same substrate by Thrower *et al.* [16] displaying resemblance with similar studies of CO on porous ASW [17], and N₂ [18] or D₂ on compact ASW [19, 20]. Hence, the broad feature can be explained in terms of (i) distribution of binding sites and/or (ii) lateral repulsion between two neighbouring adsorbates and/or (iii) delayed desorption from the SiO₂ pores. Given the inherent roughness of the surface there is a larger interface than the geometrical area of the flatter polished metal substrate, this means that low coverages (≤ 10 L) would reflect a desorption regime typical of sub-monolayer exposures despite a relatively high number of adsorbed molecules. This also means that lateral repulsion is unlikely to play a role in the deviation from first-order kinetics. Furthermore, this interpretation is supported by the fact that this peak saturates around 10 L, meaning that there is still uncovered SiO₂ below this exposure. In conclusion, the growth of peak A is affected by a distribution of binding site energies.

The sharper feature (peak B), on the other hand, follows first-order kinetics up to 10 L, with a maximum around 130 K, appearing clearly from the lowest exposure at 2 L and it also seems to emerge from the background noise in the 1 L TPD trace. Peak B could indicate the formation of a second layer of CH₃OH. It is worthwhile noticing that it appears at the same time as Peak A alongside the first monolayer growth, long before the latter saturates. In order to clearly show the growth trends for peak A and B, TPD traces from 1 L to 10 L were fitted with a Gaussian and a Lorentzian function respectively, using the software package Origin Pro Version 8.6 (OriginLab). It is important to stress that a satisfactory

and definitive modelling of these two features will be presented at the end of the next paragraph below, along with a detailed quantitative analysis. However, this preliminary distinction of the two components in the experimental trace is crucial to both confirm the qualitative interpretation given for the TPD spectra up to 10 L and to provide a sensible estimate of the number of CH₃OH molecules relevant to each peak that will be used in the quantitative analysis. Two key aspects were taken into account for the fitting procedure: (i) the reproducibility of the overall desorption trace in the best way possible, and (ii) matching each of the two peaks with just one function having a sensible and a clear physical meaning. The first criterion was met by achieving the smallest reduced χ^2 , a R^2 value as close as possible to 1, and for a fit that gave the most random distribution of the residuals around 0. The fitting functions that are commonly used in spectroscopy, and by extension for the analysis of the TPD data [21], are Gaussian and Lorentzian functions. These ones were the designed choice for the two components. One should recall that a Lorentzian lineshape is best suited to fit the experimental curve in case of homogeneous broadening, whereas a Gaussian lineshape is the best choice in case of inhomogeneous broadening. Therefore, since peak A appears to display a dispersion of the desorption energies, this feature is best fitted by a Gaussian. In contrast, peak B is consistent with one main desorption energy (regardless the kinetic order), and hence, a Lorentzian function would be the preference. Furthermore, the possibility of using a Gaussian for peak B was explored and compared to the fit with the Lorentzian. In both cases the overall trace is reproduced with almost identical quality by the cumulative curve, but in the former case the broadness of the other component (associated to peak A) is unrealistically exaggerated and the maximum of peak B not correctly reproduced. These inconveniences disappear or are significantly minimised by the choice of using a Lorentzian lineshape. **Table 3.1** lists the main relevant outputs of the fit for the TPD traces in the 1 - 10 L range, while the fitting functions are displayed in the upper right panel in **Figure 3.1**. Therein, the shift to lower temperatures of peak A is more clear than looking just at the experimental traces and it can also be noted that the component in the 1 L trace deviates from the first-order kinetics outlined by the curves fitting peak B. This could be due to the fact that the S/N ratio is of poor quality and therefore the fit is not reliable. Above 10 L, peak B shifts its maximum towards higher temperatures, in a fashion compatible with zero-order kinetics; displaying coincident leading edges up to 500 L, thus indicating desorption of amorphous bulk CH₃OH. Moreover, the 20 L trace shows an additional broad shoulder (Peak C) that grows slowly in intensity and shifting to higher temperatures for increasing exposure. These results are not dissimilar from what has been shown by the work of Bolina *et al.* [21]. When

Coverage / L	Peak A			Peak B		
	T_{max}/K	FWHH / K	Area [†]	T_{max}/K	FWHH / K	Area [†]
1	165.6 ± 0.2	31.8 ± 0.6	49%	127.4 ± 0.2	22.9 ± 0.9	51%
2	165.0 ± 0.2	32.1 ± 0.5	43%	131.14 ± 0.08	13.4 ± 0.3	57%
5	154.8 ± 0.4	32 ± 1	63%	130.2 ± 0.1	7.3 ± 0.4	37%
10	148.2 ± 0.6	34 ± 1	60%	130.77 ± 0.06	7.9 ± 0.3	40%

Table 3.1: Table listing the values of maxima, full width at half heights, and areas obtained from the fit of peak A and B of the CH_3OH TPD traces in the 1 L - 10 L range. Note that the smoothed curves (16 point adjacent-averaging method) for the 1 L and 2 L traces were used for the fits instead of the experimental traces. The area is reported in % as ratio with respect to the area of the cumulative peak.

CH_3OH is dosed on HOPG low coverages TPD traces reveal two features: a higher temperature peak that is assigned to the first monolayer; and a lower temperature peak, which firstly appears as shoulder and then becomes progressively dominant as the coverage increases. This feature is assigned to the desorption of amorphous multilayer CH_3OH and keeps increasing in high coverage traces. A third peak is also observed at high temperature in the multilayer regime; additional RAIRS experiments upon annealing the surface allows the assignment of desorption of crystalline bulk CH_3OH . Further confirmation comes from TPD traces displaying enhancement for this feature following adsorption to high exposures when dosing at 130 K. The results shown in **Figure 3.1** highlight a similar behaviour for peak C shown in the 20 L - 500 L traces which therefore suggests desorption of crystalline multilayer CH_3OH .

Discussion

It is possible to attempt to estimate the binding energies and determine the desorption kinetics from the TPD traces discussed above. The *Polanyi-Wigner* equation (**Equations 2.10 and 2.12**) can be rewritten as follows:

$$r_d \equiv -\frac{\partial\theta}{\partial T} = \frac{u_d}{\beta} = \frac{\theta^x}{\tau_0\beta} e^{-\frac{E_d}{RT}} \quad (3.3)$$

$$\ln(r_d) = \ln\left(\frac{\nu_0}{\beta}\right) + x\ln(\theta) - \frac{E_d}{RT} \quad (3.4)$$

where r_d denotes the desorption rate and ν_0 is the reciprocal of τ_0 , called the frequency factor. It is obvious that the first term on the right of **Equation 3.4** is constant if the heating rate, the nature of the surface and of the adsorbate do not change. It is desirable to determine the desorption order x for the highest coverages, in order to confirm the assignment of peak B to multilayer desorption of CH₃OH. Therefore, for the set of TPD traces shown in the lower right panel of **Figure 3.1**, the desorption order was experimentally evaluated by applying **Equation 3.4**, assuming the pre-exponential factor and the desorption energy not to change with temperature and coverage. This holds to be reasonable in the case of physisorbed species even when there is a small variation of the E_d with θ . Therefore, a linear relationship is established:

$$\ln(r_d) \propto x\ln(\theta) \quad \forall T \ll T_{Max} \quad (3.5)$$

It should be noted that relative coverages were used, which are directly proportional to the absolute values. Thus, given the properties of the logarithms, this results in a constant offset along the $\ln(\theta)$ axis. Leading edge analysis for the kinetic order of desorption of bulk amorphous CH₃OH is displayed in **Figure 3.2**. The series of data at 125 K clearly display an outlier from the trend indicated by the rest of the other values; therefore it was considered as a bad data point and discarded from the fit. This is sensible considering the low S/N ratio at that temperature and that the traces are very sensitive to small changes in the baseline. Nevertheless, even if this point is considered, the general message remains unaffected: at low temperatures the order is zero, but it becomes fractional, 0.21 - 0.3, as higher temperatures are taken into account. Even though the data at 135 K are in disagreement with this trend, it could be argued that the data-set, being derived from just three points, has a lower statistical relevance compared to the 130 K and 132.5 K sets. In conclusion, the average desorption order is fractional, 0.2 ± 0.1 . This value is slightly higher than that expected from a perfect layer by layer desorption kinetics, but consistent with similar studies [21–23] and could

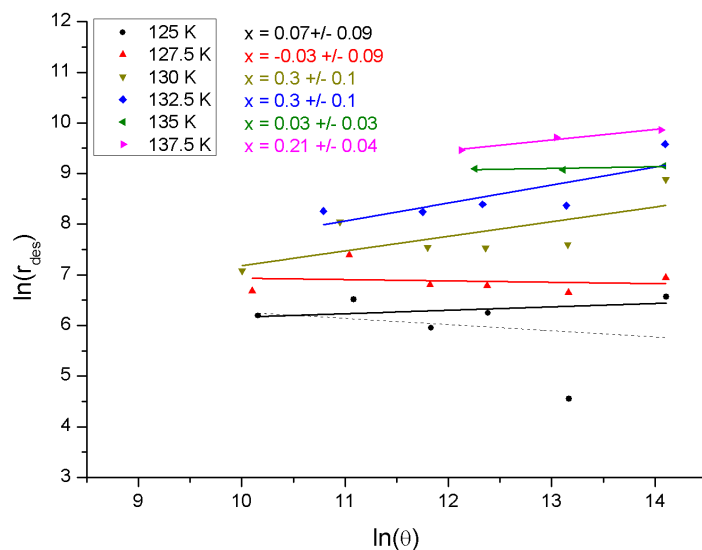


Figure 3.2: Leading edge analysis for the kinetic order of desorption of bulk amorphous CH_3OH on SiO_2 . At low temperatures the order is zero, but it becomes fractional, 0.21 - 0.3, as higher temperatures are taken into account. In conclusion, the average desorption order is fractional, 0.2 ± 0.1 .

be explained in terms of the presence of hydrogen bonding that leads to strong interactions and the inherent roughness of the surface that induces deviation from bulk ice desorption kinetics.

Furthermore, **Equation 3.4** could also be used to plot (r_d) as a function of $\frac{1}{T}$ (*Arrhenius plot*). Desorption energy can be determined from the slope, provided that coverage and order are known. Assuming a perfect zero-order desorption the linear relationship is straightforward, but the results above determined a fractional order, therefore **Equation 3.4** could be rewritten as:

$$\ln(r_d) - x \ln(\theta) = \ln\left(\frac{\nu_0}{\beta}\right) - \frac{E_d}{RT} \quad (3.6)$$

$$\ln(r_d) - x \ln(\theta_{rel}) = -x \ln(\alpha) + \ln\left(\frac{\nu_0}{\beta}\right) - \frac{E_d}{RT}$$

where α is a coefficient taking into account the fact that relative coverages are considered instead of the absolute values. This has the drawback in precluding the determination of the pre-exponential factor, but has no effect on the slope. Thus plotting $\ln(r_d) - x \ln(\theta_{rel})$ versus $\frac{1}{T}$ yields a straight line with the slope proportional to the desorption energy, as shown for the 500 L and 200 L traces in **Figure 3.3** This analysis was applied to the leading edges of all the TPD traces

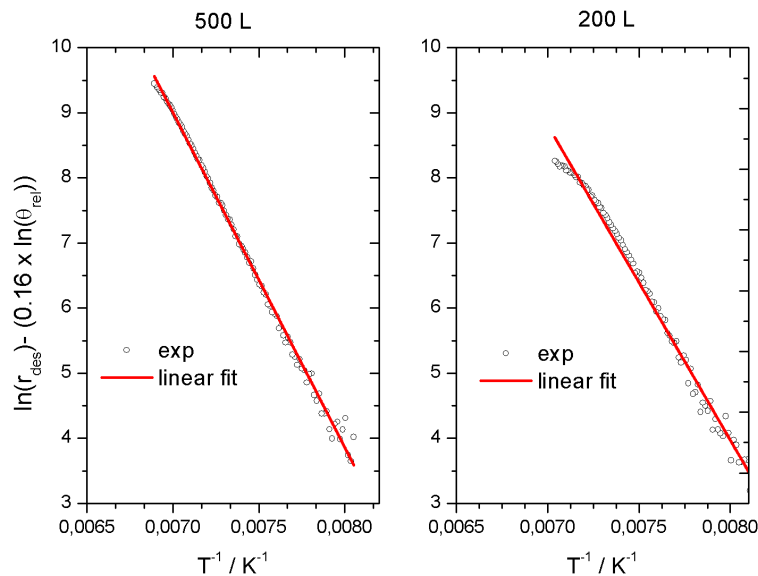


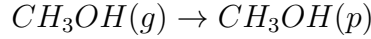
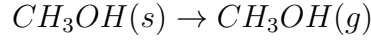
Figure 3.3: Plot of $(\ln(r_d) - x \ln(\theta_{rel}))$ against $1/T$ for the multilayer desorption of 200 and 500 L of CH_3OH from SiO_2 . The red line shows the fit to the experimental data points, which are reported in black open circles.

from 20 L up to 500 L; with the results presented in **Table 3.2**. An average value of $42.8 \pm 0.9 \text{ kJ mol}^{-1}$ for the desorption energy of multilayer CH_3OH can therefore be experimentally estimated.

Coverage / L	$E_d / \text{kJ mol}^{-1}$		
	LEA	CKS ($x = 0$)	CKS ($0.1 \leq x \leq 0.8$)
20	41.9 ± 0.9	41.9	42 for $x = 0.4$
50	46.0 ± 0.4	42.0	42 for $x = 0.4$
100	43.3 ± 0.5	41.8	42 for $x = 0.5$
200	40.2 ± 0.4	42.0	42 for $x = 0.7$
500	42.7 ± 0.2	41.8	42 for $x = 0.3$

Table 3.2: Table reporting the calculated desorption energy of bulk amorphous CH_3OH by LEA and using CKS. Exposures are of: 20 L, 50 L, 100 L, 200 L, and 500 L. In the latter case both an ideal zeroth-order desorption and more realistic fractional kinetics were taken into account.

The CKS stochastic integration package described in the previous chapter [24] was then used to further model the kinetics associated with peak B. This approach has successfully aided the fit and analysis of the experimental traces [17, 25–28] and is based on a very simple two-step process:



which involves three different species of CH₃OH: adsorbed solid (s) CH₃OH; gaseous (g); and pumped (p) methanol. It is important to bear in mind that CKS relies on a stochastic integration of differential equations that treat each species as a generic entity, with no chemical characterisation. The physiochemical processes are outlined by each step in terms of stoichiometry, rate constant and its Arrhenius parameters, initial concentration, heating rate, and whether equilibrium is allowed to be reached or not. Once the output is obtained, this is compared to the experimental trace to test the goodness of the fit; the input parameters are then changed from the initial guess to achieve a better agreement. Of course, the initial concentration and the heating rate are well defined for each exposure matching experimental conditions, where the former was estimated by simply applying the gas kinetic theory. Defining a Langmuir unit as $L = P \times t$, where P is the uncorrected pressure, **Equation 3.7**, reported below, allows to calculate the number of molecules that accumulate on the substrate per unit of surface for each “exposure time” during dosing.

$$u_a = \frac{SP^*}{\sqrt{2\pi mk_B T}} \quad (3.7)$$

m is the mass and T is the temperature of the colliding molecules and was measured to be 293 K on average. S is the sticking coefficient assumed to be one given the low surface temperature, P^* is the corrected pressure (in Pascal) at the ion gauge when P is divided by the ionisation coefficient (γ). In this case an average value of 1.87 was used for γ [29–31]. Dividing $u_a \times t$ by the molecular density it is possible to obtain an upper limit for the film thickness with the assumption that the molecular density and deposition rate are homogeneous in time and space on the substrate. Initial coverage (θ) and film thickness are reported for each exposure (L) in **Table 3.3** assuming a molecular density of 1.91×10^{22} molecules cm^{-3} [27]. The pumping speed, being the second step rate constant in the above simple model, must be kept constant in the simulation for each coverage. In order to meet experimental conditions, an arbitrarily high value of 1.1 s^{-1} was chosen. The heating rate β had a fixed value of 0.7 K s^{-1} . The initial guess for

Coverage / L	θ / molecule cm^{-2}	d / Å	Coverage / L	θ / molecule cm^{-2}	d / Å
0.1	1.45×10^{13}	0.0759	10	1.45×10^{15}	7.59
0.2	2.90×10^{13}	0.152	20	2.90×10^{15}	15.2
0.5	7.25×10^{13}	0.379	50	7.25×10^{15}	37.9
1	1.45×10^{14}	0.759	100	1.45×10^{16}	75.9
2	2.90×10^{14}	1.52	200	2.90×10^{16}	152
5	7.25×10^{14}	3.79	500	7.25×10^{16}	379

Table 3.3: Table listing the estimated number of adsorbed molecules and film thickness for each exposure. Note that for the lowest coverages the monolayer is not yet complete and the thickness reported aside is an average.

the desorption energy was set to what was experimentally determined ($42.8 \pm 0.9 \text{ kJ mol}^{-1}$), and was let to vary during the optimisation process. Instead of using the value of 0.2 for the desorption order (x) as suggested by the previous analysis, for each TPD trace the best fit was achieved using a fixed value of x ranging from 0 to 0.8 and step 0.1. The fits for perfect zeroth-order kinetics and the most applicable fractional value are displayed in **Figure 3.4**.

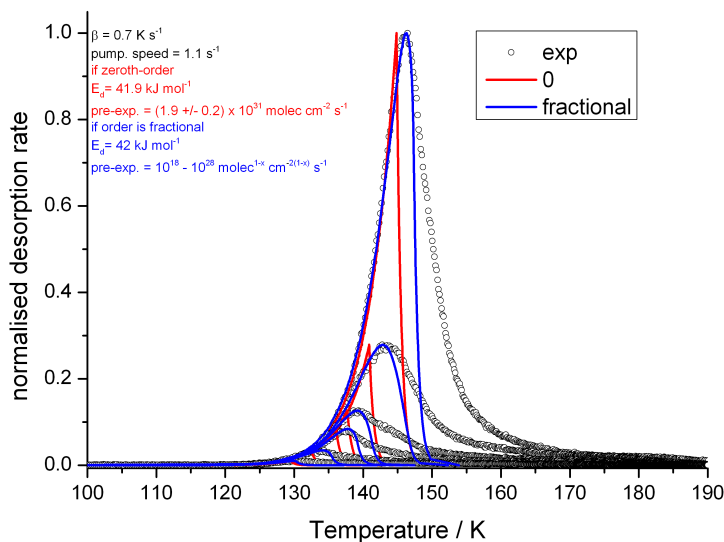


Figure 3.4: TPD traces for desorption of CH_3OH on SiO_2 in open circles and CKS fits in red (ideal case, $x = 0$) and blue (fractional order). Coverages are of 20 L, 50 L, 100 L, 200 L, and 500 L in the order of increasing signal.

Table 3.2 lists the values of desorption energy determined with the leading edge analysis along the predicted values using the *CKS* model for both an ideal zeroth-order desorption and for more realistic fractional kinetics. The average value of $42.8 \pm 0.9 \text{ kJ mol}^{-1}$ determined by the direct analysis of the data defines a range of energies, 43.7 and 41.9 kJ mol^{-1} , that includes the average E_d obtained by the CKS fits regardless the order. This is close to the heat of enthalpy of sublimation of CH_3OH (44.9 kJ mol^{-1}) [23], and to the reported literature values of multilayer CH_3OH from HOPG ($\sim 40 \text{ kJ mol}^{-1}$) [21], from graphene (44.6 kJ mol^{-1}) [32], and previous studies by Green *et al.* on similar surfaces ($43.2 \pm 2 \text{ kJ mol}^{-1}$, $45.4 \pm 1 \text{ kJ mol}^{-1}$) [27]. The results confirm the assignment of peak B to physisorbed molecules in the multilayer regime. However, it is important to stress that only when a convenient fractional value of x is considered, the temperature associated with the maximum and the shape of the leading edge are accurately modelled. This fact further highlights the effect of the inherent roughness of the SiO_2 surface and of the H-bonding to deviate desorption from an ideal layer-by-layer desorption, which is especially true for the 100 L and 200 L traces (**Figure 3.5**). The highest coverage curve, on the other hand seems to match more an

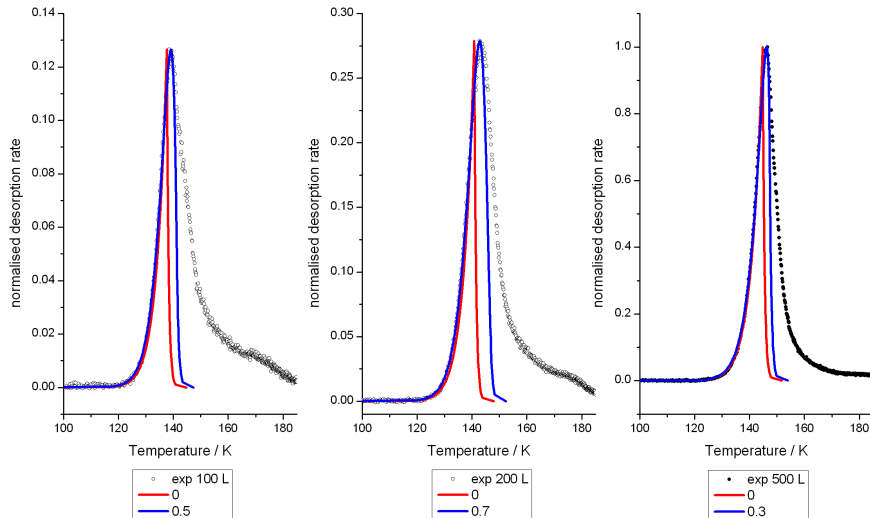


Figure 3.5: TPD traces for desorption of 100 L, 200 L and 500 L of CH_3OH on SiO_2 . Experimental points in open circles and CKS fits in red (ideal case, $x = 0$) and blue (fractional order). Deviation from an ideal layer-by-layer desorption for the 100 L, 200 L, and 500 L traces which was interpreted as effect of both the inherent roughness of the SiO_2 surface and H-bonding formation.

ideal situation since the underlying roughness is progressively smoothed by the accretion of CH_3OH layers. It is harder to explain why the desorption order is closer to one for the 100 L and 200 L than it is for the 20 L and 50 L, but it could be argued that for the higher coverages the phase transition becomes significantly competitive to the bulk amorphous CH_3OH desorption, adding a further contri-

bution to the fractional order.

The *CKS* model also allows an estimate of the pre-exponential parameter to be made, giving an average value of $(1.9 \pm 0.2) \times 10^{31}$ molecules $\text{cm}^{-2} \text{s}^{-1}$ if a perfect zeroth-order desorption is assumed, while it changes vastly otherwise (10^{18} - 10^{28} molecules $^{1-x} \text{cm}^{-2(1-x)} \text{s}^{-1}$). Such a large range in the latter case does not seem reasonable and expresses the limits of the simple two step model used to describe the desorption kinetics. On the other hand, constraining $x = 0$, a reasonable agreement exists in the work of Green *et al.* [27] within an order of magnitude.

The low coverage analysis is much more complex as the first layer grows along the second layer and the signal/noise ratio is lower. Firstly the TPD traces (1 L - 10 L) has to be deconvoluted into the two main features as explained above. A Lorentzian function for peak B and a Gaussian for peak A were used. Any other attempt of fits with two Gaussians or Lorentzians resulted into a higher χ^2 . The broad feature deviates from first-order kinetics mainly because of the existence of a range of binding sites at the SiO_2 interface. Therefore, the first step consists in estimating the desorption energy coverage dependence in order to simulate the high temperature component in the TPD traces. The Polanyi-Wigner equation is manipulated to obtain:

$$E_d = -RT \ln \left(\frac{r_d \beta}{\nu_0 \theta} \right) \quad (3.8)$$

then (i) constraining the integrated area of each curve to be equal to the respective initial coverage reported in **Table 3.3** and (ii) setting the heating rate to 0.7 K s^{-1} it follows that:

- $\theta = \Sigma - \sigma_i$ is estimated at every step, where Σ is the initial coverage and σ counts the desorbed molecules at the instant t obtained by partial integration of the area up to a temperature $T(t)$.
- the frequency factor, ν_i , is assumed to be 10^{13} s^{-1} to be consistent with previous analysis [16].
- R is the gas constant ($8.31446 \text{ J K}^{-1} \text{ mol}^{-1}$).

Figure 3.6 shows the energy distribution (lower panel) as function of θ for each trace. In principle, it would be desirable to find one function that fitted all the calculated distributions. However, this is clearly not the case. The curve associated with the 1 L TPD decays very quickly with respect to the others.

This could easily be explained as the TPD trace is highly noisy and this would strongly affect the estimated values of E_d as function of θ . The same noise issues could affect the 2 L curve. It can be concluded that a universal function describing the distribution of the energies could not be obtained. However, the TPD traces can still be reproduced by applying the specific dependency of E_d on θ in the expression of r_d (**Equation 3.3**) assuming a first-order kinetics. This is displayed in the upper panel of **Figure 3.6** while the energy range for each trace is reported in **Table 3.4**.

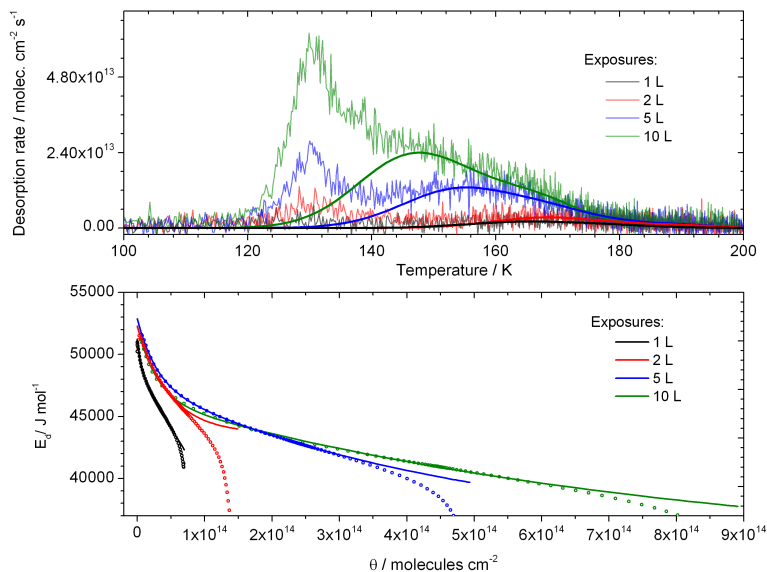


Figure 3.6: The upper panel shows TPD traces for desorption of 1 L, 2 L, 5 L and 10 L of CH_3OH on SiO_2 . The thicker solid lines are the simulated traces of peak A assuming the distribution of energy being coverage dependent. The lower panel displays the plot of E_{des} as function of θ for each exposure obtained through inversion of the Polanyi-Wigner equation.

Coverage / L	E_d / kJ mol^{-1}
1	42 - 50
2	44 - 50
5	40 - 51
10	39 - 51

Table 3.4: Table reporting the range of $E(\theta)$ found for peak A of 1L, 2 L, 5 L, and 10 L CH_3OH on SiO_2 .

It is also desirable to estimate the desorption energy for peak B at these low

exposures (2 L - 10 L). A simple relationship between E_d and T_{max} was derived by Redhead [33] starting from **Equation 3.3** recognising that at $T = T_{max}$ the condition

$$\left(\frac{\partial r_d}{\partial T}\right)_{T_{max}} = 0$$

must be satisfied so that **Equation 3.9** is obtained:

$$\frac{E_d}{RT_{max}^2} = \frac{\nu_0}{\beta} x \theta^{x-1} e^{-\frac{E_d}{RT_{max}}} \quad (3.9)$$

For first-order kinetics and assuming that activation parameters are independent of surface coverage it follows:

$$E_d = RT_{max} \left[\ln \left(\frac{\nu_0 T_{max}}{\beta} \right) - \ln \left(\frac{E_d}{RT_{max}} \right) \right] \quad (3.10)$$

The term $\ln \left(\frac{E_d}{RT_{max}} \right)$ is usually small and assumed to be equal to 3.64 if $10^8 K^{-1} < \frac{\nu_0}{\beta} < 10^{13} K^{-1}$ within an error of 1.5%. According this final expression [33]:

$$E_d = RT_{max} \left[\ln \left(\frac{\nu_0 T_{max}}{\beta} \right) - 3.64 \right] \quad (3.11)$$

a desorption energy of $34.1 \pm 0.5 \text{ kJ mol}^{-1}$ is estimated if $\nu_0 = 10^{13} \text{ s}^{-1}$. In principle a more accurate estimate for E_d should be given by the *Arrhenius plot* in a similar fashion as it was done for the multilayer peak B. **Figure 3.7** displays

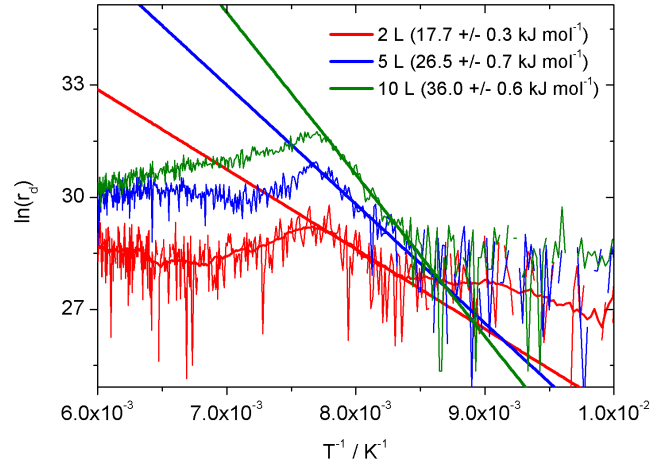


Figure 3.7: Arrhenius plot ($\ln(r_d)$ against $1/T$) for the low exposures of peak B of CH_3OH on SiO_2 . Coverages are 2 L (in red), 5 L (in blue), and 10 L (in green). The best linear fit and the desorption energy for each coverage, is reported along the experimental traces.

how the slope, and thus the desorption energy, of each plot increases with the exposure. This is not entirely unexpected. If the interpretation given so far holds

to be true and peak B is associated to a weakly physisorbed second layer, then as more molecules add up the stabilising multi-body interaction increases driving the desorption energy towards the higher value as determined for the multilayer regime ($\sim 42 \text{ kJ mol}^{-1}$). However, it is important to stress that once again the poor quality signal of the 2 L trace might result into a higher error ($\sim 10 \text{ kJ mol}^{-1}$) than the fit standard deviation (0.3 kJ mol^{-1}), which was obtained by looking at the smoothed curve rather than the QMS counts. Therefore, a *CKS* analysis is needed in order to better determine the E_d value. In order to assume a correct coverage for peak B in each of the analysed traces, the total area of the scaled experimental curve seen in **Figure 3.6** was subtracted with the area underlying the function obtained for peak A, then the *CKS* package was used to simulate Peak B at these low exposures assuming a first-order kinetics. In **Figure 3.8** it can be seen that the low temperature feature is reasonably reproduced with a desorption energy of 35 kJ mol^{-1} and a pre-exponential value of $2 \times 10^{13} \text{ molecules cm}^{-2} \text{ s}^{-1}$. Heating rate and pumping speed are consistent with the multilayer analysis. The peak intensity for the 10 L TPD trace is not perfectly reproduced and this is due to a third layer growing and/or a deviation from a first-order kinetics towards a fractional behaviour. The value found for E_d (35 kJ

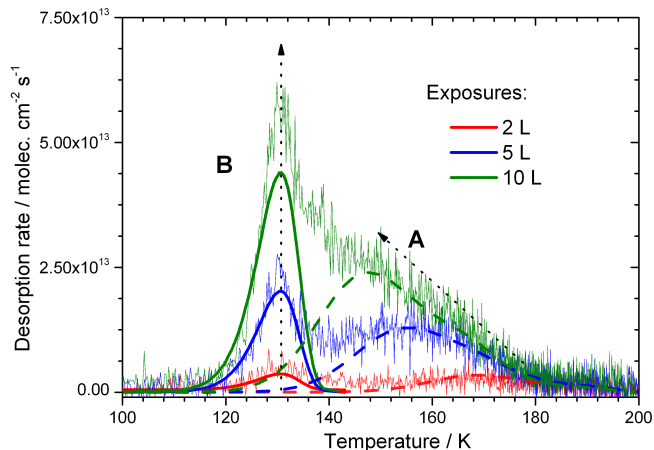


Figure 3.8: TPD profiles for 2 L, 5 L, and 10 L exposures. Peak B (thick line) is modelled with a first-order kinetics using *CKS* package. Peak A (dashed line) is described by a distribution of binding energies. Dotted arrows highlight the observed desorption behaviour.

mol^{-1}) is in good agreement with that determined by the leading edge analysis at 10 L (36 kJ mol^{-1}). The analysis so far seems to support and strengthen the assignment of the TPD features: peak B and peak A together with the relative desorption parameters (pre-exponential term and energy); while peak C is not resolved enough for its kinetics to be quantitatively obtained and discussed.

TPD of Ether on Silica

Figure 3.9 shows desorption traces for sub-monolayer (upper row) and multilayers (lower row) of $(\text{CH}_3\text{CH}_2)_2\text{O}$ on SiO_2 when deposited at ~ 20 K monitoring at $m/z = 31$ and $m/z = 59$ (not shown). Possible H_2O contamination from the background residual gas was ascertained to be negligible by monitoring at $m/z = 18$. As for CH_3OH , TPDs of $(\text{CH}_3\text{CH}_2)_2\text{O}$ on SiO_2 were repeated dosing molecules at 110 K. Although desorption starts above 105 K (see **Figure 3.9**) the two sets showed a consistent behaviour with only two minor differences: (i) the heating rate is slightly higher ($\sim 0.8 \text{ K s}^{-1}$) in the 110 K experiments, thus resulting in a systematic shift towards higher temperatures, and (ii) the intensity is slightly higher when molecules are dosed at 20 K, especially at low exposures. Therefore, when conducting high temperature experiments, $(\text{CH}_3\text{CH}_2)_2\text{O}$ desorption from a SiO_2 surface is competitive with deposition. Furthermore, in multilayer conditions, the thicker films might delay and partially inhibit the desorption from the SiO_2 interface favouring other processes like crystallisation.

Returning to the upper panel of **Figure 3.9**, there are two features, a lower and a higher temperature peak (B and A respectively). In contrast with what CH_3OH displays at similar coverages, both peak A and B appear to exhibit kinetics that appear as second-order with the maximum temperature shifting towards lower values as higher exposures are probed: peak A moves from 174 K (2 L) down to 144 K (20 L); peak B from 122 K (1 L) down to 116 K (20 L). Again, as dissociative adsorption is unlikely to happen for physisorbed molecules like $(\text{CH}_3\text{CH}_2)_2\text{O}$ on SiO_2 , the two features might rather be described by a first-order kinetics in a similar fashion as reported for the CH_3OH peak A. Thus, the observed behaviour for peak A in **Figure 3.9** could also arise as a result of the existence of a range of binding sites on the surface that leads to a gradual decrease in binding energy as the most efficient sites are filled. Peak A could be assigned to physisorbed $(\text{CH}_3\text{CH}_2)_2\text{O}$ at sub-monolayer coverages; peak B may be indicative of a second layer forming along the first with a weaker binding energy. If one accepts the picture of the SiO_2 surface having terminal silanol groups, these would be perfect binding sites with hydrogen bonds to the $(\text{CH}_3\text{CH}_2)_2\text{O}$ oxygen. A hypothetical second molecule that were to coordinate to the above mentioned adsorbed $(\text{CH}_3\text{CH}_2)_2\text{O}$ would face the aliphatic chains allowing a weaker van der Waals interaction that is likely to be less stable than the two minima for the $(\text{CH}_3\text{CH}_2)_2\text{O}$ dimer. MP2 geometry optimisations on the more simple dimethyl ether dimer (DME) system highlight the existence of two energy minima where DME molecules are hydrogen bonded (see **Figure 3.10**). The same type of

TPD of $(\text{CH}_3\text{CH}_2)_2\text{O}$

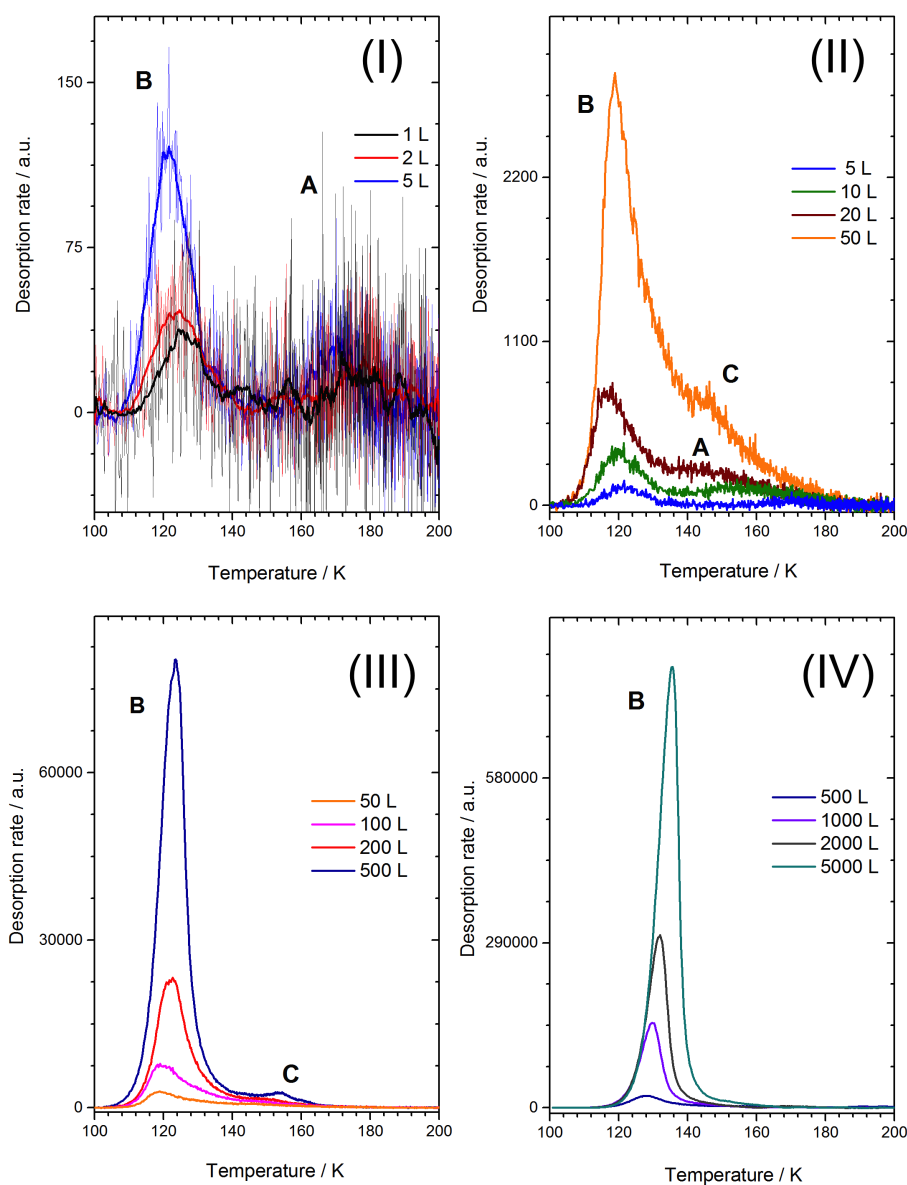


Figure 3.9: TPD traces for desorption of $(\text{CH}_3\text{CH}_2)_2\text{O}$ on SiO_2 for a vast range of exposures from 1 L to 5000 L. Low coverages are reported in the upper row, and high coverages are displayed in the lower row. In the subplot labelled (I) both peak A and B can be observed: the former is assigned to $(\text{CH}_3\text{CH}_2)_2\text{O}$ directly adsorbed on the SiO_2 surface, while the latter is assigned to the formation of a second layer (in the low exposures regime). The subplot labelled (II) displays the transition from monolayer to multilayer. The subplot labelled (II) shows desorption of bulk amorphous $(\text{CH}_3\text{CH}_2)_2\text{O}$ (peak B in the high exposures regime) and of bulk crystalline $(\text{CH}_3\text{CH}_2)_2\text{O}$ (peak C). Finally, the TPD curves in the bottom right panel (IV) show desorption of very high coverages of $(\text{CH}_3\text{CH}_2)_2\text{O}$ subsequently adsorption on SiO_2 at 107 K. These traces were used for the multilayer analysis.

interactions exist for two diethyl ether (DEE) molecules, moreover the CH_3CH_2 chains would further shield the ether oxygen bound to the silanol groups from other molecules. Peak B also displays a similar deviation from first-order kinetics as peak A and it could either be explained by a distribution of adsorption sites or by lateral Pauli repulsion between neighbouring molecules. Peak A and B both

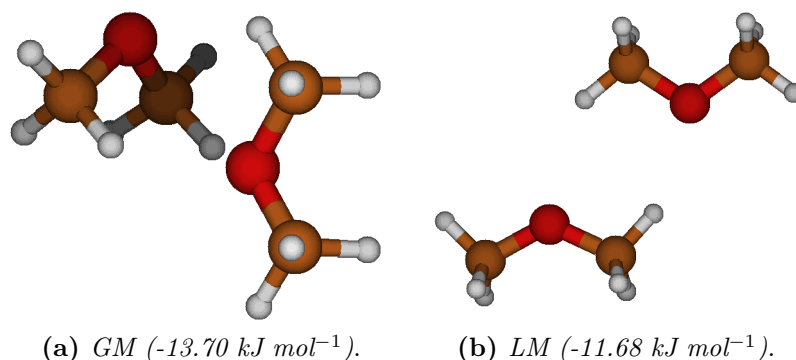


Figure 3.10: Binding energy of the global minimum (GM) and local minimum (LM) for dimethyl ether dimer. Calculations were performed at MP2/aug-cc-pVDZ level followed by a single point with aug-cc-pVTZ basis set. Counterpoise (CP) correction was included at every step.

saturate between 20 L and 50 L as the maxima shift towards higher temperatures. These exposure values are higher than the saturation range for the first two layers observed for CH_3OH on SiO_2 (between 10 L and 20 L); the multilayer is clearly formed above 50 L despite its desorption seem to obey a zeroth-order kinetics only at extremely high exposures while being fractional below 500 L. The fact that the expected layer-by-layer desorption is observed above 1000 L is of tricky interpretation. A possible explanation could be linked to the inherent roughness of the SiO_2 surface that might favour a macroscopic behaviour at intermediate-high exposures strongly deviating from the ideal zeroth-order kinetics. Thus, despite the silica surface might still offer exposed areas to the vacuum interface, locally large *quasi-macroscopic* clusters of $(\text{CH}_3\text{CH}_2)_2\text{O}$ could display a pressure difference across the bulk-fluid interface (*e.g.* Young-Laplace equation ¹). A new peak (*peak C*) appears at 50 L shifting its maximum to higher temperatures when coverage is increased. It might be assigned to the α to β phase change [34].

Analysis

The multilayer desorption data were analysed in the same way as for the desorption of CH_3OH on amorphous SiO_2 . However, $(\text{CH}_3\text{CH}_2)_2\text{O}$ exhibits a fractional desorption up to very high coverages (500 L) and its analysis is extremely complex, it was not possible to obtain realistic simulations on the basis of a simple

¹ $\Delta P = -\Gamma \left(\frac{1}{R_1} + \frac{1}{R_2} \right)$ where Γ is the surface tension and R_1 and R_2 the principal radii of curvature.

kinetic model as previously adopted and beyond the scope of this thesis. Therefore three higher exposures (1000 L, 2000 L, and 5000 L) TPD experiments were performed in order to understand at what value of surface coverage the layer-by-layer desorption would have taken place as to estimate the bulk desorption energy of $(\text{CH}_3\text{CH}_2)_2\text{O}$. Although three traces alone do not provide a reliable statistical basis, the order analysis was carried out by applying **Equation 3.4**, at eight values of temperature. For physisorbed species, the pre-exponential factor and E_d do not change with T and θ , thus plotting $\ln(r_d)$ as a function of $\ln(\theta)$ should yield a straight line with a slope equal to the desorption order. **Figure 3.11** shows the leading edge analysis for the kinetic order of desorption of bulk amorphous $(\text{CH}_3\text{CH}_2)_2\text{O}$; however, it is important to stress once again, that relative coverages were used instead of absolute values, This results into a constant offset along the $\ln(\theta)$ axis with no effect on the order determination. Most of the

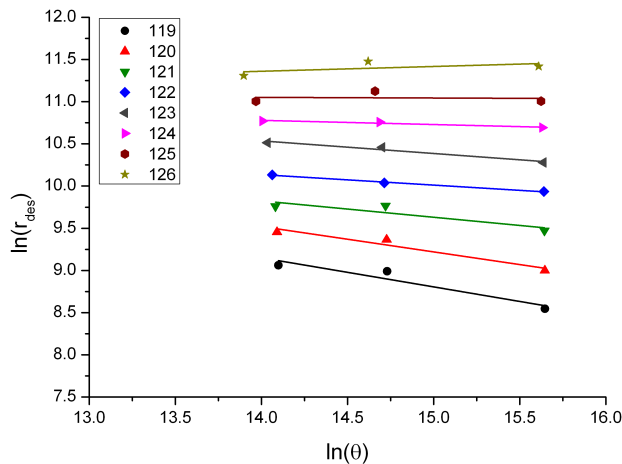


Figure 3.11: *Leading edge analysis for the kinetic order of desorption of bulk amorphous $(\text{CH}_3\text{CH}_2)_2\text{O}$ on SiO_2 (1000 L, 2000 L, and 5000 L). Linear fits give a slope close to zero ($\sim 10^{-2}$) with a standard deviation of the same order of magnitude, or a negative order. It was concluded that $x = 0$.*

linear fits gave a slope close to zero ($\sim 10^{-2}$) with a standard deviation of the same order of magnitude, or a negative order. The latter case has no physical meaning and arises from a poor statistics and/or baseline effects, thus it was assumed that $x = 0$. However, it should be highlighted that despite three points per temperature are not enough to obtain a reliable determination of the kinetic order, repeating the analysis on such a large number of temperature values along the leading edge strengthens the confidence range of the final result.

Equation 3.4 can be used to plot (r_d) as function of $\frac{1}{T}$ (*Arrhenius plot*) in order to evaluate E_d assuming a perfect zero-order desorption (**Figure 3.12**).

The leading edge was fitted with a linear equation since its slope is directly proportional to the desorption energy ($slope = -\frac{E_d}{R}$). The latter was found to

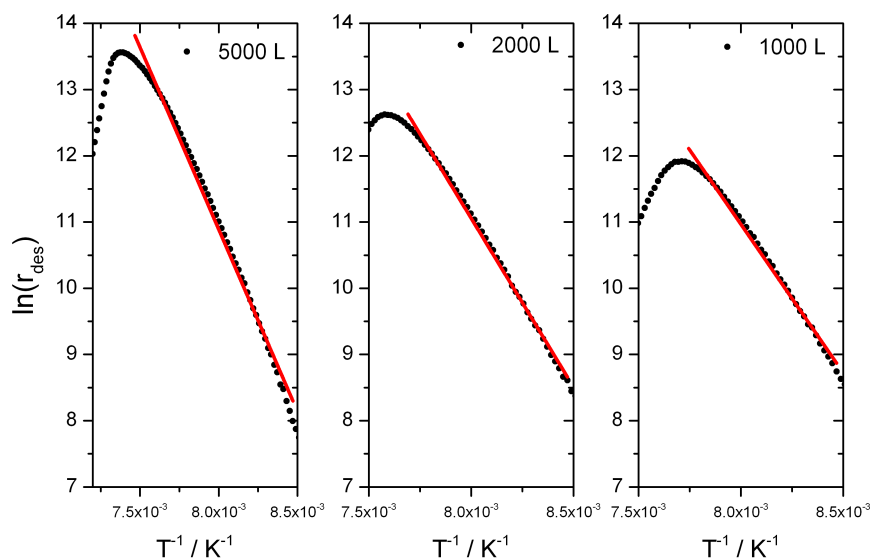


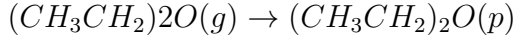
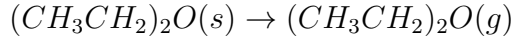
Figure 3.12: Arrhenius plot ($\ln(r_d)$ against $1/T$) for the multilayer desorption of 1000 L, 2000 L, and 5000 L of $(\text{CH}_3\text{CH}_2)_2\text{O}$ from SiO_2 . Data points are in black open circles, the red line shows the fit to the experiment.

be 41.8 kJ mol^{-1} by averaging the values derived for each exposure (see **Table 3.5**).

Coverage / L	$E_d / \text{kJ mol}^{-1}$	
	LEA	CKS ($0.4 \leq x \leq 0.8$)
500	33.3 ± 0.5	44.9 for $x = 0.8$
1000	37.3 ± 0.5	45 for $x = 0.6$
2000	42.3 ± 0.3	44.8 for $x = 0.4$
5000	45.7 ± 0.5	44.8 for $x = 0.4$

Table 3.5: Table reporting the calculated desorption energy of amorphous bulk $(\text{CH}_3\text{CH}_2)_2\text{O}$ from SiO_2 by LEA and using CKS. The range of exposures is: 500 L - 5000 L.

In order to corroborate the values obtained for the desorption order and energy the kinetics were modelled using the CKS package as before for CH_3OH . The model is a simple two-steps process, where:



The first step is rate determining and its kinetic parameters are adjusted in order to reproduce the experimental traces as closely as possible. The pumping speed, the second step rate constant, was kept constant in the simulation for each coverages at an arbitrary value of 1.1 s^{-1} . The heating rate β had a fixed value of 0.77 K s^{-1} for the 500 L and 1000 L exposures and 0.76 K s^{-1} for the remaining two traces consistently with the experiments. Initial surface coverage was estimated in a similar fashion as previously explained for CH_3OH on SiO_2 . The number of molecules per unit of surface is obtained for each exposure unit, correcting pressure readings for the ionisation coefficient ($\gamma = 5.1$ [29]) Then it was assumed that the liquid bulk density ($5.80 \times 10^{21} \text{ molecules cm}^{-3}$) was the same as in the solid $(CH_3CH_2)_2O$, and was used to estimate the average film thickness at each coverage (see **Table 3.6**). The TPD curves are best described by a fractional

Coverage / L	θ / molecule cm^{-2}	d / Å	Coverage / L	θ / molecule cm^{-2}	d / Å
1	$3.50(5) \times 10^{13}$	0.605	100	$3.50(5) \times 10^{15}$	60.5
2	7.01×10^{13}	0.121	200	7.01×10^{15}	121
5	1.75×10^{14}	3.02	500	1.75×10^{16}	302
10	$3.50(5) \times 10^{14}$	6.05	1000	3.50×10^{16}	605
20	7.01×10^{14}	1.21	2000	7.01×10^{16}	1210 (121 nm)
50	1.75×10^{15}	30.2	5000	1.75×10^{17}	3020 (302 nm)

Table 3.6: Table listing the estimated number of adsorbed molecules and film thickness for each exposure of $(CH_3CH_2)_2O$ from SiO_2 . Note that for the lowest coverages the monolayer is not yet complete yet and the thickness reported should be regarded as average.

order even at these high exposures (**Figure 3.13**) although the simulation trace fails to model the experimental trailing edge as the surface coverage decreases. Also in this case different values of x were considered, from 0 to the one reported, and only when the order was fractional a good model of the leading edge and peak position was achieved. For instance, the relevance of the fractional order for

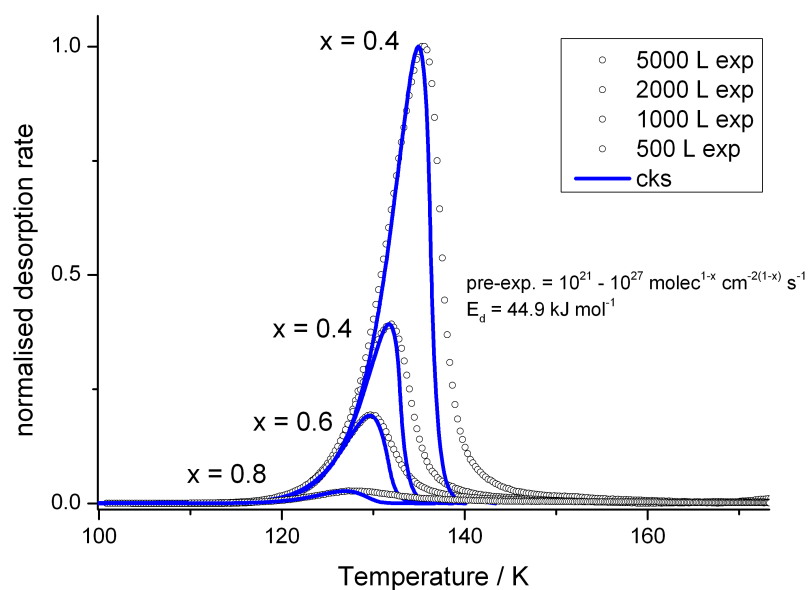


Figure 3.13: TPD traces for desorption of $(\text{CH}_3\text{CH}_2)_2\text{O}$ on SiO_2 in open circles and CKS fits in blue lines with the explicit fractional order. Exposures are of 500 L, 1000 L, 2000 L and 5000 L. Note that $x \rightarrow 1$ for the 500 L data and $x \rightarrow 0$ for the 5000 L experiment

the simulated kinetics is best highlighted by **Figure 3.14** where the CKS model is compared to the 1000 L trace progressively changing the value of x . **Table 3.5**

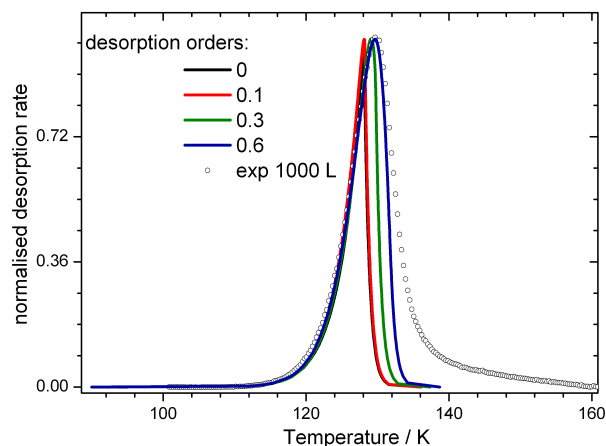


Figure 3.14: TPD traces for desorption of 1000 L of $(\text{CH}_3\text{CH}_2)_2\text{O}$ on SiO_2 : experimental data in open circles and CKS fits for different fractional order kinetics. Note that when $x \rightarrow 1$ both the leading edge and the maximum are best modelled.

lists the desorption energy values obtained by the leading edge analysis (LEA) and the CKS models. It is noticeable that in the latter case the values are all very close to each other, and deviate about 0.2% from the average calculated desorp-

tion energy ($\sim 44.9 \text{ kJ mol}^{-1}$). This number is also close to the one obtained by applying LEA at the highest exposure (45.7 kJ mol^{-1}), which might not be accidental. If the *CKS* estimates were to be considered somehow more reliable than what determined by the analysis of experimental data, then this would imply that taking into account a fractional value of x best reproduces the bulk desorption energy. In fact, the 2000 L and 5000 L TPD profiles display a desorption order of 0.4, which is closer to zero, thus the underlying assumption used for the plots in **Figure 3.12** is more realistic than it is for lower coverages (*e.g.* 1000 L) and a better agreement between the *CKS* model and LEA is expected for E_d . No direct comparison was found within the literature concerning the multilayer desorption energy of amorphous $(\text{CH}_3\text{CH}_2)_2\text{O}$. However, considering that the enthalpy of vaporisation is $27.53 \text{ kJ mol}^{-1}$ [35], the enthalpy of fusion is 7.19 kJ mol^{-1} [34] and assuming the heat capacity to average $86.5 \text{ J mol}^{-1} \text{ K}^{-1}$ between 106 K - 140 K [34, 36], it is possible to give an estimate of 37.6 kJ mol^{-1} for the heat of sublimation. This is clearly lower than what was determined in this thesis, but it is important to stress that the cited values were determined under pressure conditions far from the UHV used in this thesis. Finally, the determination of the pre-exponential factor associated to the multilayer desorption could not be accurately determined, because the leading edge analysis is complicated due to fractional order and the large range of values predicted by the *CKS* model ($10^{21} - 10^{27} \text{ molecules}^{1-x} \text{ cm}^{-2(1-x)} \text{ s}^{-1}$) is symptomatic of the crudeness and artlessness inherent to the two-step process used in the simulation.

As already said, the behaviour of $(\text{CH}_3\text{CH}_2)_2\text{O}$ at low exposures (1 L - 20 L) displays two broad peaks, A and B. The intensity of these features increases as the exposure is increased, while the peak maximum shifts to lower temperature. The desorption energy coverage dependence can be extracted by the inverted form of the *Polanyi-Wigner* equation as described previously with **Equation 3.8** for the sub-monolayer analysis of CH_3OH . The procedure and the assumptions regarding the ν_0 and β values are exactly the same as before, with the only difference being that the empirical E_d plot as a function of θ was first obtained from the whole TPD trace rather than from a single fit component. In other words, peak A and B both show a similar behaviour but with different binding energies, thus in principle there is no reason why the two components should be individually considered. In contrast, the two features displayed by the low exposure CH_3OH TPDs are described by different kinetics, therefore, in this case, it was desirable to disentangle and highlight the two contributions. The calculated desorption energy, shown in **Figure 3.15**, spans over a very large range, from 34 kJ mol^{-1} to 55 kJ mol^{-1} and beyond. The functions decrease very rapidly with increasing

surface coverage meaning that the most favourable adsorption sites are soon filled. The curves associated with the 10 L and 20 L exposures display a more gentle decay as a result of a larger number of molecules populating less effective sites both at the SiO_2 and $(\text{CH}_3\text{CH}_2)_2\text{O}$ interface (sub-monolayer and second layer forming respectively). The other curves descend to lower energy values more abruptly highlighting a stronger discontinuity between the two related distributions and responding to a more enhanced separation between the two peaks in the TPD spectra. Only at very high energies do the functions seem to assume a similar behaviour, however the inherent noise of the starting TPD traces results in scattering and broadening of the desorption energy lineshape preventing an unambiguous trend in that range to be found. In other words, it was not feasible to find a satisfactory and univocal empirical function for all the coverages of E_d versus θ , even when narrowing down the independent variable range at the first high energy part. In order to evaluate the two sets of energies associated to peak

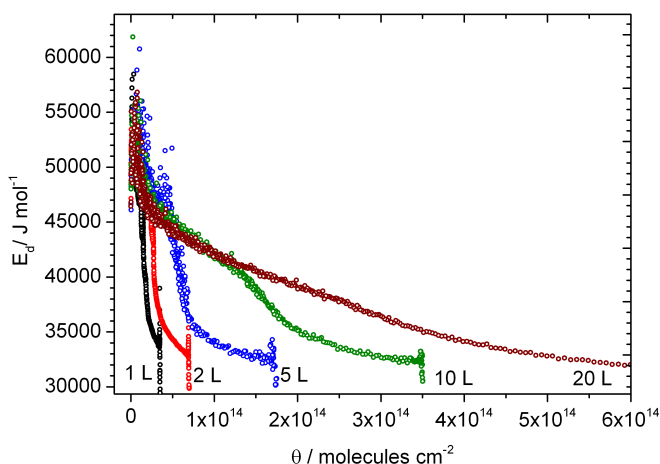
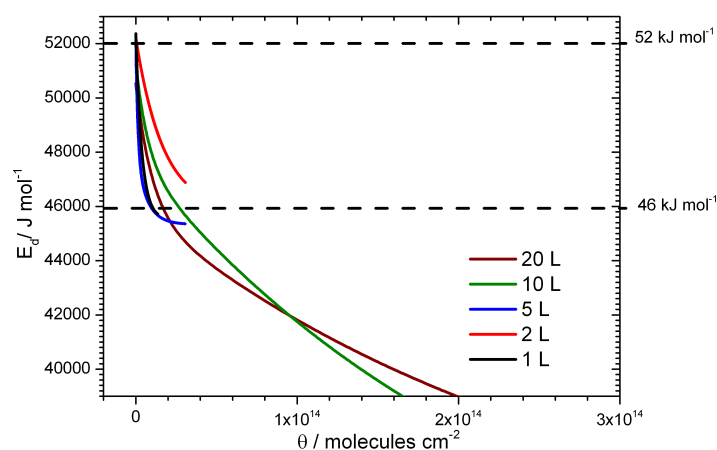


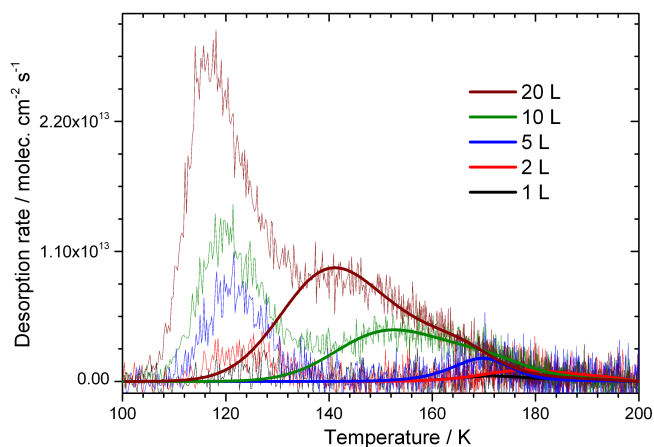
Figure 3.15: Plot of binding energy as a function of surface concentration for $(\text{CH}_3\text{CH}_2)_2\text{O}$ on SiO_2 obtained through inversion of the Polanyi-Wigner equation for the 1 L, 2 L, 5 L, 10 L and 20 L TPD traces. Note that the calculated desorption energy spans over a very large range, from 34 kJ mol^{-1} to 55 kJ mol^{-1} and beyond.

A and B, each TPD trace was fitted with two Voigt profiles that granted the lowest χ^2 . The single-fit components were used as a starting point to estimate the number of molecules per peak and thus to derive the related desorption energy coverage dependencies accordingly. The latter are displayed in the upper panel of **Figure 3.16** and of **Figure 3.17** for the high energy peak (A) and low energy peak (B) respectively. Also in these cases it is not possible to find an universal function of $E_d(\theta)$ in both the two energy ranges because of several reasons: First of all, the high noise level that especially affects the 1 L and 2 L traces makes the correct baseline determination tricky resulting in large effects on the lineshape.

Furthermore, the TPD traces had to be smoothed introducing an additional level of approximations in the analysis. The 10 L and 20 L TPD curves might display a third layer forming at intermediate energies, as further confirmed by a gradual decrease of the overall $E_d(\theta)$ functions as well as those specific to the high and low temperature features showing a smoother transition between the two regimes. This behaviour is not dissimilar to what was encountered for the 10 L TPD trace of CH_3OH on SiO_2 .



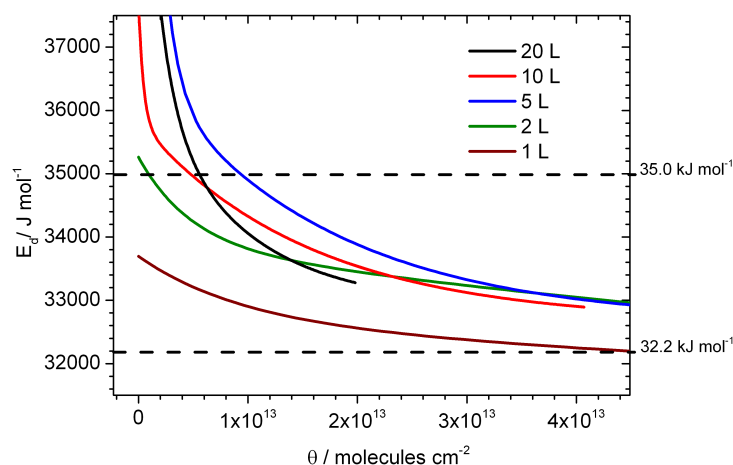
(a)



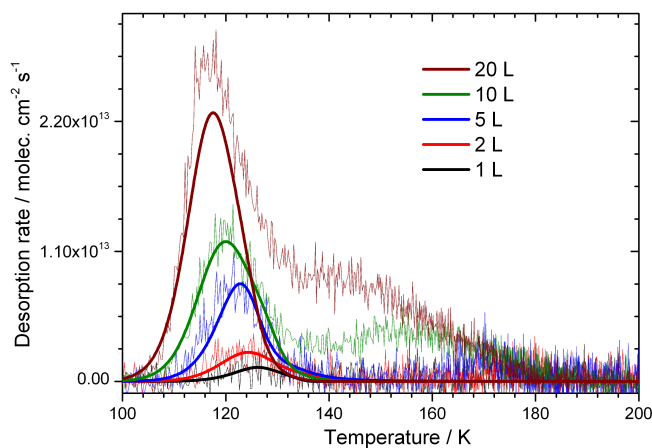
(b)

Figure 3.16: (a) E_d as a function of surface concentration for the high temperature desorption peak of low coverages (1 L - 20 L) of $(\text{CH}_3\text{CH}_2)_2\text{O}$ from SiO_2 . (b) Simulated high temperature TPD profiles for low exposures assuming a distribution of energies. The analysis supports the assignment of peak A to the first monolayer forming, filling adsorption sites at the SiO_2 interface ranging from 46 kJ mol^{-1} up to 52 kJ mol^{-1} .

It is clear that the kinetic and thermodynamical aspects are not trivial and the



(a)



(b)

Figure 3.17: (a) E_d as a function of surface concentration for the low temperature desorption peak of low coverages (1 L - 20 L) of $(\text{CH}_3\text{CH}_2)_2\text{O}$ from SiO_2 . (b) Simulated low temperature TPD profiles for low exposures assuming a distribution of energies. The analysis supports the assignment of peak B to a second layer having desorption energy of 32.2 - 35.0 kJ mol^{-1} .

analysis procedures adopted so far are pushed to their limits. However, it is feasible to assign without doubt the extremes for the energy domain of both the two peaks. Peak A consists of the first monolayer forming, filling adsorption sites at the SiO_2 interface ranging from 46 kJ mol^{-1} up to 52 kJ mol^{-1} at the threshold between physisorption and chemisorption hinting perhaps to H-bond-like interactions with the silanol groups. For comparison, it is reported in literature that $64 \pm 2 \text{ kJ mol}^{-1}$ was estimated for the monolayer of $(\text{CH}_3\text{CH}_2)_2\text{O}$ chemisorbed on $\text{Cu}(111)$ [37]. Given the relatively long alkyl chain and the possible conformers of ether molecules bound to the SiO_2 surface, a modest range of binding energy

would exist also for a second and possibly even to a third layer (Peak B). Remembering that peak B was assigned to a second layer forming along the first one, a change of $\sim 3 \text{ kJ mol}^{-1}$ from 32.2 kJ mol^{-1} up to 35.0 kJ mol^{-1} and beyond is estimated for the desorption energy of this feature. It is noticeable that the functions (**Figure 3.17a**) decay very slowly as coverage is increased with respect to the high energy functions (**Figure 3.16a**). Implying a flat distribution of energies for the second layer. If a third layer were to form at higher exposures (10 L, 20 L) this would also display a change in E_d as the coverage is increased ($37 - 40 \text{ kJ mol}^{-1}$). The latter would occur within a range set at larger values than that assigned to the second layer ($32.2 - 35.0 \text{ kJ mol}^{-1}$) being in a region of transition between a weakly bound second layer and the more thermodynamically stable bulk. Using a suitable and purely empirical fitting function for each of the $E_d(\theta)$ trends, the relative TPD peaks (**Figures 3.17b** and **3.16b**) were accurately modelled and reproduced on the basis of first-order kinetics and all the assumptions previously outlined ($\nu_0 = 10^{13} \text{ s}^{-1}$; $\beta = 0.7 \text{ K s}^{-1}$). It should be noted that any variation in desorption energy that results from intermolecular repulsion is also contained within the distribution as is the desorption from any impurity sites on the SiO_2 surface associated with carbon contamination, which is not unrealistic for real interstellar grains. The simulated TPD traces related to the two energy ranges are also shown in **Figure 3.18** for direct comparison.

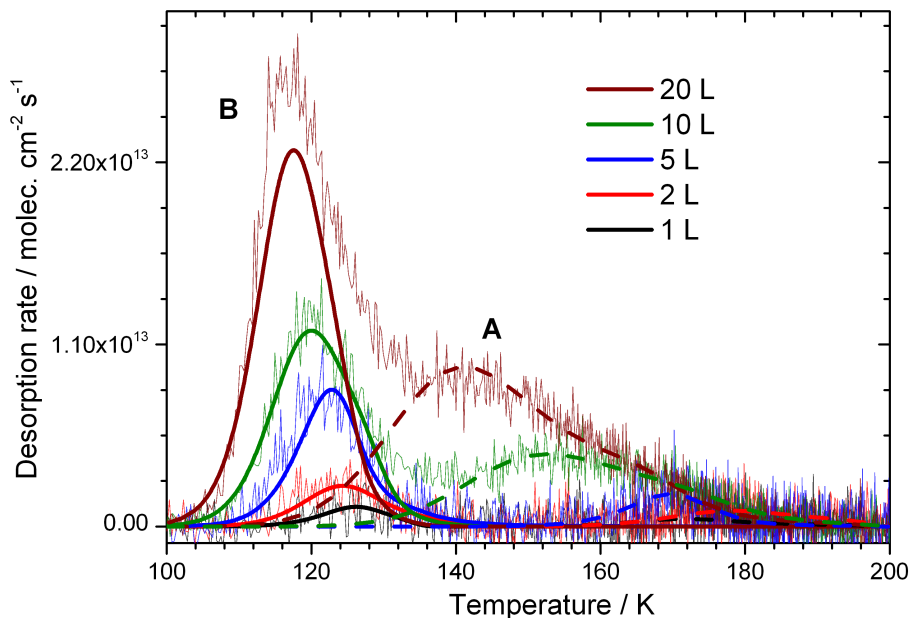


Figure 3.18: Simulated $(\text{CH}_3\text{CH}_2)_2\text{O}$ TPD profiles from SiO_2 of peak A and B at low coverages. A distribution of desorption energies was assumed and the inverted form of the Polanyi-Wigner equation was applied to successfully reproduce the experimental traces.

3.2.3 Comparison of TPD Data for Water, Methanol, and Ether

TPD experiments of H_2O on SiO_2 have been exhaustively discussed for both the UHV chambers in previous works [38, 39], and most recently by Collings *et al.* [28]. Therefore, in this paragraph the main results will be presented, while a detailed kinetic analysis is omitted since it will suffice to refer to the above mentioned works when it is appropriate. Despite this, TPD experiments of H_2O on SiO_2 were recorded using the same substrate as for the other molecules previously discussed to assure consistency with older published results and granting direct comparison between H_2O , CH_3OH and $(\text{CH}_3\text{CH}_2)_2\text{O}$ on SiO_2 in similar range of exposures (**Figure 3.19**). As can be seen in the upper panel, H_2O exhibits zeroth-order kinetics from the very lowest coverages, as suggested by the common leading edge and can be explained by a two-dimensional gas-island equilibrium and an island growth mechanism as recently reported for H_2O on a graphene substrate [32]. At very low coverage regimes (left upper panel of **Figure 3.19**) H_2O desorption is from the amorphous phase as there is little or no evidence for crystallisation of these small islands, while desorption of crystalline H_2O gains significance at the highest exposures (right panel). Phase transition is marked by the well-known “bump” as can be seen above 100 L. Its appearance depends mainly on kinetic factors, such as its rate constant compared to the heating rate, and on the relative coverage. It is important to stress that in previous works [38] the bump has been indicative of low coverages to high coverages regime change, and in this thesis it appears only at the highest exposures. As mentioned while discussing $(\text{CH}_3\text{CH}_2)_2\text{O}$ TPDs, the surface used is extremely rough, with a large interface area and it seems that even at hundreds of Langmuir of dosed molecules there are still regions of the SiO_2 exposed to the vacuum. It is important to highlight this concept in order to better understand what will be presented at the end of the chapter with temperature programmed RAIR spectra. Looking at the H_2O TPD traces it can be concluded that the H_2O - H_2O interaction exceeds the SiO_2 - H_2O interaction and the H_2O molecule is mobile over the SiO_2 surface, *i.e.* the H_2O de-wets from silica.

In contrast, $(\text{CH}_3\text{CH}_2)_2\text{O}$ on SiO_2 (lower panel in **Figure 3.19**) displays first-order kinetics (having a desorption energy coverage dependence) in a similar fashion to acetonitrile (CH_3CN) [38, 40] or C_6H_6 [16] on SiO_2 . The interaction of SiO_2 - $(\text{CH}_3\text{CH}_2)_2\text{O}$ is very high and about 30% larger than the ether-ether interaction when comparing the average values of E_d for the first to the second monolayer (**Table 3.7**). It is noticeable that even the bulk desorption energy is

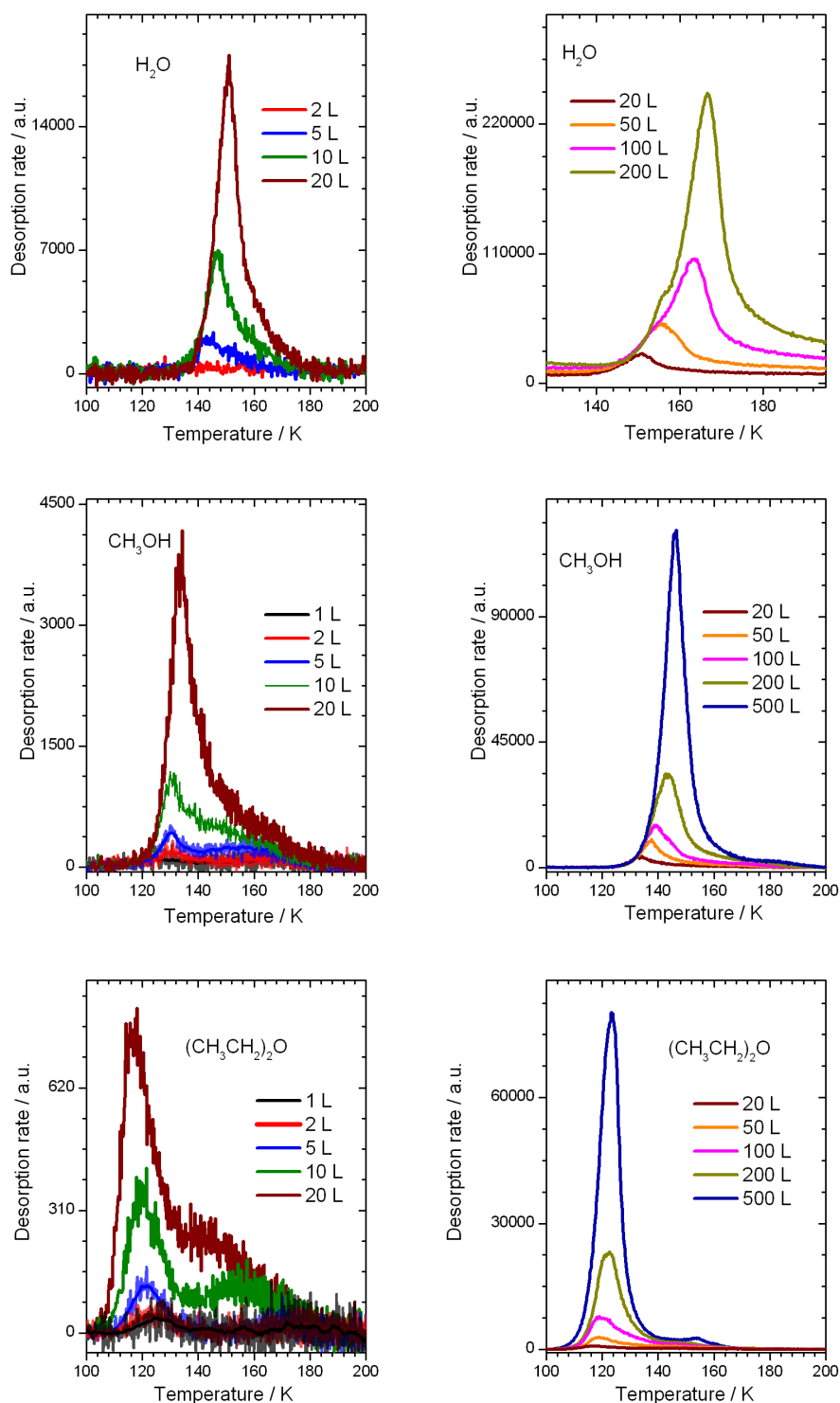


Figure 3.19: TPD traces for desorption of H_2O (upper row, CH_3OH , (central row), and $(\text{CH}_3\text{CH}_2)_2\text{O}$ (lower row) on SiO_2 . The panels at the left show the desorption profiles of these species for low coverages ($\leq 20\text{L}$), while the subplots at the right display the TPD traces for higher coverages ($\geq 20\text{L}$).

exceeded by the desorption energy of sub-monolayer $(\text{CH}_3\text{CH}_2)_2\text{O}$ on SiO_2 . The conclusion is that $(\text{CH}_3\text{CH}_2)_2\text{O}$ wets silica.

Adsorbate	$E_d / \text{kJ mol}^{-1}$		
	1 st layer	2 nd layer	multilayer
H ₂ O	42.1 ± 1 (46.4 ± 0.9 [32])		49.3 ± 2 48.0 ± 0.5 [25] 47.7 ± 0.9 [32]
CH ₃ OH	(41.2 - 50.5) ± 0.5	35.0 ± 1 44.6 ± 0.9 [32]	42.0 ± 1
(CH ₃ CH ₂) ₂ O	(46 - 52.0) ± 0.5	(35.0 - 32.2) ± 0.5	44.9 ± 1

Table 3.7: Table reporting the calculated desorption energy (E_d) for H₂O, CH₃OH, and (CH₃CH₂)₂O on SiO₂. When available literature values for bulk desorption and for the second layer are reported below the results of this work. Note that H₂O has no defined transition from monolayer to multilayer; desorption energy of amorphous H₂O was assigned to the low coverages and desorption energy of crystalline H₂O was assigned to the high coverages taking the values estimated in previous works [28, 38]

TPD profiles of CH₃OH on SiO₂ (see central panel in **Figure 3.19**) exhibit features with aspects in common with both H₂O and (CH₃CH₂)₂O. This is not surprising if one simply recalls that in the first place any alcohol can be thought as derived from H₂O with an hydrogen atom (H) substituted with an alkyl group (R), while a further substitution on the second H atom would lead to ethers (**Figure 3.20**). There is a high temperature peak associated with strongly ad-

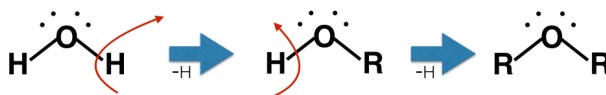


Figure 3.20: Schematic of ideal derivation of ethers (ROR) from water (HOH) via the alcohol (ROH).

sorbed CH₃OH having desorption energy of 45.8 kJ mol⁻¹ on average (see **Table 3.7**). This value and the kinetics of peak A in CH₃OH TPDs are not dissimilar to the desorption of the analogous feature for (CH₃CH₂)₂O. The low temperature peak displays characteristics typical of first-order desorption up to 10 L, then as multibody interaction assumes relevance, the peak quickly acquires zero-order desorption characteristics (common leading edge and increasing peak temperature with coverage) and points again to the two-dimensional gas-island equilibrium and an island growth mechanism as also reported elsewhere [32]. This is reminiscent of H₂O TPD profiles. Thus, to conclude, CH₃OH desorbing from

SiO₂ has a duality that resembles both H₂O and (CH₃CH₂)₂O depending on the relative strengths of the interaction involved. A possible interpretation of these data acknowledges the importance of four types of interactions:

- The interaction experienced by each XOX' (where X and X' are either an H atom, or CH₃, CH₃CH₂ group) molecule inside the bulk in solid phase (*bulk interaction*, E_b).
- The interaction between XOX' and one or few more XOX' molecules (*pseudo-bulk interaction*, E_b^*).
- The strong interaction between silica and the isolated XOX' molecule (*favourable adsorption*, E_H).
- The weak, dispersive, interaction between the isolated XOX' and the silica (*weak physisorption*, E_{disp}).

The SiO₂ surface is likely to appear as shown in the basic model in **Figure 2.16** with terminal silanol groups. These can form a donor H-bond with the oxygen of (CH₃CH₂)₂O, CH₃OH or H₂O and an acceptor H-bond with the last two molecules of the series. Both cases have similar binding energy values [41–43] and stronger than any van der Waals force, thus they can represent the observed strong interaction with adsorbate-SiO₂. **Figure 3.21** shows an arbitrary, but sensible representation of the four possible interaction energy scales for each molecular system. Starting from a clean surface at 20 K, an hypothetical H₂O molecule is likely to hit and stick, then as temperature increases, it will populate one of the *favourable adsorption* sites. As for the lowest exposure of these experiments, as more than one molecule lies on the surface and since are free to diffuse above 40 K, they will prefer to bind together as the water dimer, water trimer and bulk interaction are more thermodynamically stable. Thus, zero-order desorption is observed at all coverages because hydrogen-bond network formation is clearly the driving force to island formation. A single (CH₃CH₂)₂O molecule, will also hit and stick on the surface at low temperature. As the latter increases, (CH₃CH₂)₂O diffuses binding to the silanol groups in a similar fashion as H₂O (and CH₃OH). However, this interaction is stronger than the other possible three. Therefore, (CH₃CH₂)₂O would rather fill the *favourable adsorption* sites. As more molecules are dosed, the *weak physisorption* and the *pseudo-bulk interaction* seem to be interchangeable from a thermodynamical point of view since no further stabilisation seems to derive from the *bulk interaction* where the H-bond is almost non existing. Thus, (CH₃CH₂)₂O wets the SiO₂ surface. CH₃OH again would stick to the SiO₂ surface wherever it collides at 20 K, and as the temperature

is increased the molecule would also populate *favourable adsorption* sites. However as these are filled, islands of CH_3OH form since E_b , E_b^* and E_H are similar in value (see **Table 3.7** to have a semi-quantitative comparison), and all larger than E_{disp} , therefore CH_3OH wets the SiO_2 surface exclusively at low coverage (like $(\text{CH}_3\text{CH}_2)_2\text{O}$), while islands formation (like H_2O) is most favoured when only weak interaction sites are available at the SiO_2 interface.

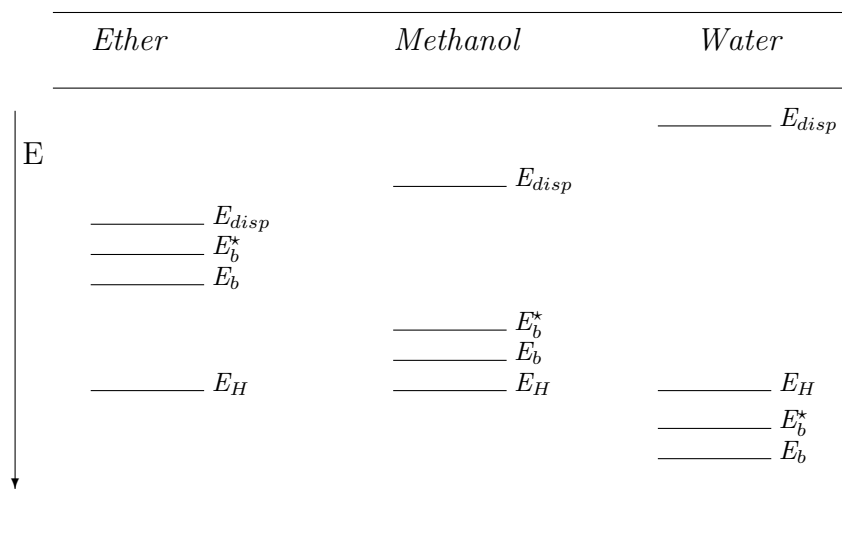


Figure 3.21: Rough energy schematic for the four main possible interactions of H_2O , CH_3OH , and $(\text{CH}_3\text{CH}_2)_2\text{O}$ on SiO_2 : 1) the interaction experienced by each XOX' molecule inside the bulk in solid phase, E_b ; 2) the interaction between XOX' and one or few more XOX' molecules, E_b^* ; 3) the strong interaction between SiO_2 and the isolated XOX' molecule, E_H ; 4) the weak, dispersive interaction between the isolated XOX' and the SiO_2 surface, E_{disp} . Note that X and X' can be an H atom and/or a CH_3 or CH_3CH_2 group.

3.3 RAIRS of Water, Methanol, and Diethyl Ether on Silica

RAIR spectra often provide useful and complementary information to TPD data in the characterisation of molecules at the SiO₂ interface through how different interactions impact on the normal modes of the adsorbed molecules. Furthermore, phase transitions appear evidently in the peaks lineshape and, in some extent, a rough insight about diffusion over the surface can be obtained when RAIR spectral evolution with temperature is followed. The two experiments that will be presented are:

1. RAIR spectra as a function of the surface coverage (θ). This is done by sequential background-dosing starting from 1 L of the species of interest, then the spectrum was recorded, a further 1 L was dosed as to obtain a 2 L exposure. A new spectrum was collected and so on, increasing θ , all the way up to 500 L reproducing the same surface coverages seen in the TPD experiments.
2. Temperature programmed RAIR spectroscopy (TP-RAIRS) was used to look at the change of vibrational modes with the temperature. Once the spectrum of the adsorbate for a suitable exposure is obtained, temperature is slowly increased to a set point (T_i) and annealed for 100 seconds. Then the substrate is left to cool to base temperature (T_{base}) as to collect the spectrum.

The Ice Rig was used for both cases where the substrate was cleaned as previously explained by heating up to 300 K. Once the sample position was optimised for the best interferogram intensity, it was left unmoved for the duration of the RAIRS experiments. Each spectrum consists of 1024 averaged scans recorded in transmittance (T_S) at a resolution set to 1 cm⁻¹. Two background spectra (T_B) were collected for each data-set and the most recent subtracted to each sample acquisition subsequently dosing (RAIRS) or annealing (TP-RAIRS). The resulting spectrum was converted into absorbance ($A = \log_{10} \left(\frac{T_B}{T_S} \right)$) and subtracted by a convenient baseline along the frequency range of interest.

3.3.1 RAIRS: Results and Discussion

RAIR spectra of CH₃OH and (CH₃CH₂)₂O deposited at 20 K and 110 K will be presented and discussed. The multilayer spectra were used as reference for peaks assignment.

RAIRS of Methanol on Silica

A set of RAIR spectra of CH₃OH is displayed in **Figure 3.22** of increasing coverage at 20 K or 110 K. Assignments were made by careful inspection of the highest exposure (500 L) spectrum and comparison with literature values [21] (**Table 3.8**) and simple frequency calculations of a single CH₃OH molecule. The most striking difference is that at 20 K the film is amorphous, while it has a crystalline component at 110 K (α phase). In the former case, the features are broad, less intense and less resolved. This is not due to instrumentation limits (which are the same for the two sets), but it is due to the existence of a larger variety of chemical environments, locally, around each CH₃OH molecule, resulting in a small spectral shift with respect to that of a perfectly ordered arrangement. Particularly the asymmetric methyl stretches, A' and A'' , are almost completely merged together at 20 K peaking at 2978 cm⁻¹ and 2956 cm⁻¹ respectively, while they are more discernible at 110 K as they shift towards opposite directions (2985 cm⁻¹ and 2947 cm⁻¹ respectively). Both the OH (3000 - 3400 cm⁻¹) and CO (\sim 1040 cm⁻¹) stretching modes split in two bands when deposition temperature is changed. The methyl rocking mode, $\rho(\text{CH}_3)$, shifts from 1137 cm⁻¹ to 1146 cm⁻¹. The spectra also display the transverse optical (TO) and longitudinal optical (LO) modes of the silica substrate and this fact is noticeable considering that they should be cancelled by background subtraction. The phenomenon has been repeatedly observed by previous experiments within this group on similar SiO₂ substrates and its nature is still unclear. However, it could be proposed that in RAIRS experiments the deposition of thin films on top of the substrate changes the optical properties (refractive index) of the system and hence the direction of the refracted light. Therefore, changes in the background might arise as optical effects. This might also explain why the LO SiO₂ mode slightly shifts in the 20 K data-set. The sharp features around \sim 1400 cm⁻¹ and 3600 cm⁻¹ are assigned to the bending mode and stretch mode of gaseous H₂O in the purge gas in optics.

It would be desirable to look at the differences in the frequency modes going from low exposures to the multilayer regime. A close inspection of the spectra up to 5 L, and for some aspects up to 10 L, revealed that most of the features are merged with background oscillations and changes in its optical properties and total intensity at the interferogram. At these exposures, the only discernible signal from CH₃OH is a very broad, and weak peak due to the OH stretch (3000 - 3400 cm⁻¹). This grows rather homogeneously for increasing doses at 20 K slightly shifting its maximum towards lower wavenumbers. When the deposition temperature is 110 K the band looks broad as in the purely amorphous spectrum

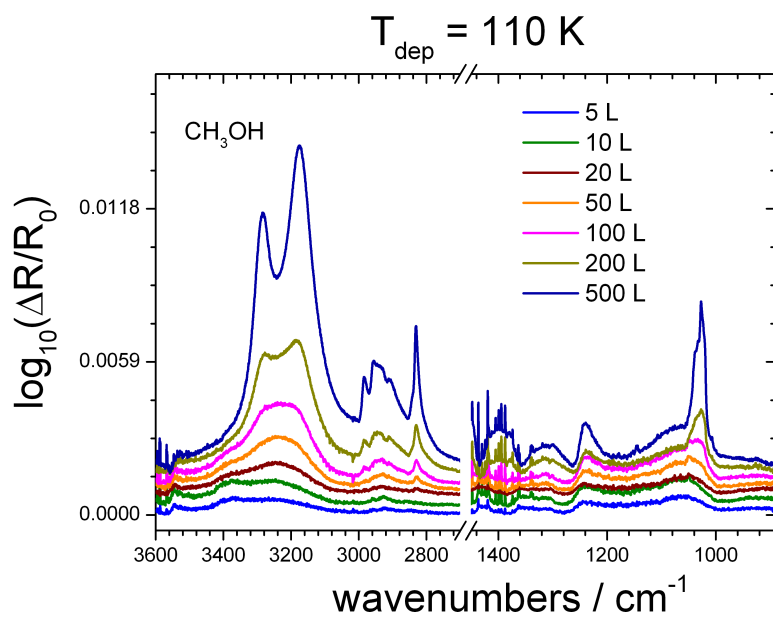
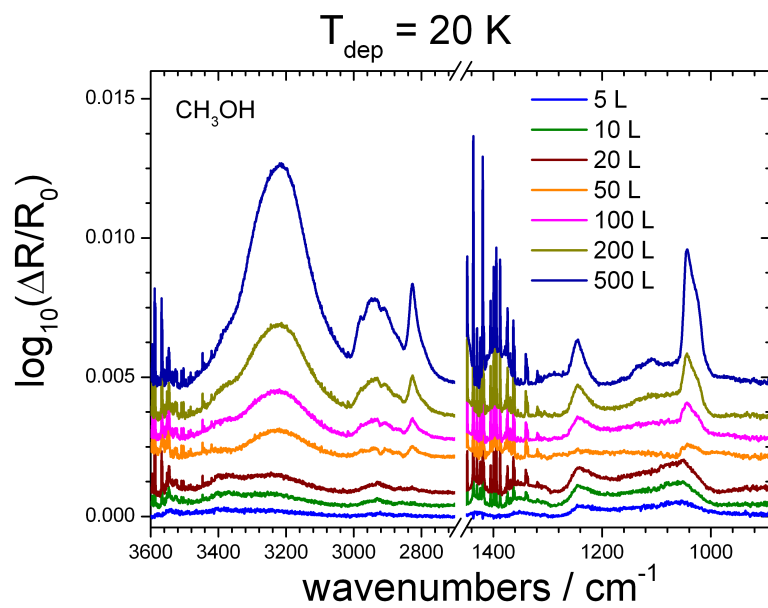


Figure 3.22: RAIR spectra of CH_3OH deposited on amorphous SiO_2 film at 20 K (a) and 110 K (b) as the coverage is increased from 5 L to 500 L. The detailed assignment of the vibrational bands is reported in the text; note that the OH and CH stretches follow at high wavenumbers (3600 - 2700 cm^{-1}), while the CO and the silica bands can be found at lower wavenumbers (1450 - 400 cm^{-1}).

Assignment	IR Frequencies / cm^{-1}			
	20 K	110 K	97 K [21]	130 K [21]
$\nu(\text{C-O})$	1043	1038 1027	1045	1037 1027
SiO_2 TO mode	1050	1050	n/a	n/a
SiO_2 LO mode	1239	1244	n/a	n/a
$\rho(\text{CH}_3)$	1137	1146	1132	1145
$\nu_s(\text{CH}_3)$	2826	2831	2833	2833
$\nu_a(\text{CH}_3), A''$	2956 2930	2947 2930	2956	2958
$\nu_a(\text{CH}_3), A'$	2978	2985	2983	2983
$\nu(\text{O-H})$	3213	3281 3176	3260	3290 3174

Table 3.8: List of vibrational modes of CH_3OH multilayer (500 L) adsorbed on amorphous SiO_2 at 20 K and 105 K and on HOPG at 97 K and 130 K for comparison [21]. Note that there could be contributions to the higher frequency region from the asymmetric A' and A'' CH_3 bendings at 2956 cm^{-1} and 2908 cm^{-1} respectively.

at 50 L, then the feature develops two peaks that gradually move apart from each other meaning that the crystalline component starts to dominate. The symmetric methyl stretching mode seem to appear at 20 L centred around 2827 cm^{-1} when the deposition temperature is 110 K and at 10 L, falling at 2830 cm^{-1} , when dosing at 20 K. In both cases it grows rather homogeneously and any small observed shift in the peak maximum is due to bulk accretion. The highest frequency C-H vibration is clearly observed only from 20 L for both data-sets. The remaining asymmetric methyl CH stretching modes at higher wavenumbers point to a marked regime change in the film growth between 5 L and 20 L since certain peaks are saturated above 20 L: At the lowest exposures there is one broad peak centred at 2921 cm^{-1} (10 L) at 20 K, and two peaks, at 2922 cm^{-1} (5 L) and at 2959 cm^{-1} (5 L, 10 L), are observed at 110 K. When coverage is increased to above 20 L, these features saturate and merge with the broad profile of the bands that peak at 2947 cm^{-1} and 2956 cm^{-1} at 500 L. This turning-point from 5 L to 20 L is compatible with what is observed from TPD data, where bulk behaviour is predominant above 20 L. The $\nu(CO)$ starts to be visible from 50 L, especially in the partially crystalline phase at 110 K, as a shoulder to the TO silica mode, then it peaks at 1043 cm^{-1} in **Figure 3.22a** and 1027 cm^{-1} in **Figure 3.22b**. It should be noted that RAIR spectra of CH_3OH below 5 L are not shown in this thesis. This is due to inconsistency between replicas of the same experiment below 5 L and for some aspects also up to 20 L.

RAIRS of Diethyl ether on Silica

RAIR spectra of diethyl ether, $(CH_3CH_2)_2O$, deposited at 20 K and 110 K as a function of the surface coverage are reported in **Figure 3.23**. The multilayer spectra at 500 L are taken as reference for the assignment of observed vibrational modes (**Table 3.9**). Despite background subtraction prior to the analysis some regions, especially in the $1300 - 900\text{ cm}^{-1}$, appear affected by the SiO_2 bands, baseline artifacts, and changes in the background optical properties as already seen for CH_3OH . Nevertheless, comparison with literature findings and frequencies calculations of the isolated $(CH_3CH_2)_2O$ molecule provided a solid base for a reliable assignment of the IR features. The most intense peaks are the C-H stretches in the methyl (CH_3) and methylene (CH_2) groups: $\nu_a(CH_3)$, $\nu_a(CH_2)$ and $\nu_s(CH_3) + \nu_s(CH_2) + 2 \times \delta(CH_3)$ in the $3000 - 2850\text{ cm}^{-1}$ range and this is consistent with what has been previously found (**Table 3.9**). A good agreement is found also for the C-O-C and C-C stretching, bending and rocking modes in the fingerprint region ($1400 - 1100\text{ cm}^{-1}$). Exception must be made for a small peak around 1081 cm^{-1} that is seen only at the highest coverage at 20 K. The calculated gas phase spectrum (not shown) allowed identification of this feature

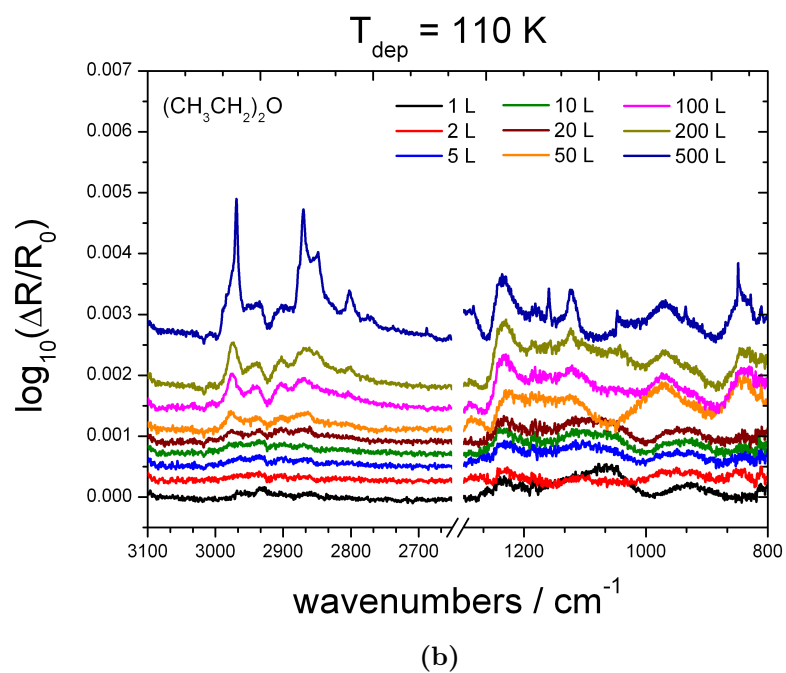
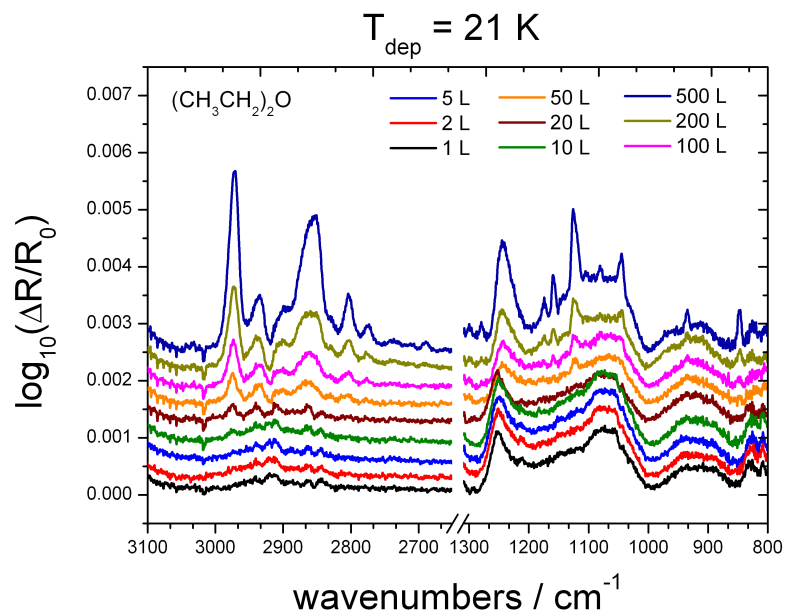


Figure 3.23: RAIR spectra of $(\text{CH}_3\text{CH}_2)_2\text{O}$ deposited on amorphous SiO_2 film at 20 K (a) and 110 K (b) at increasing coverage from 1 L up to 500 L.

as one of the combinations of C-C and C-O-C stretches.

Assignment	IR Frequencies / cm^{-1}			
	20 K	110 K	Ru(0001) [44]	Cu(111) [37]
$\rho(\text{CH}_3 + \text{CH}_2)$	826	828	827	830
$\nu_s(\text{COC}) [\nu\text{CC}]$	846	848	849	848
$\nu(\text{CC} + \text{CO}) + \rho(\text{CH}_3)$	934	934 972	935	937
$2\rho(\text{CH}_3) + \nu(\text{CC})$	1045	1047	1048	1046
$\nu(\text{COC}) + \nu(\text{CC})$	1081			
$\nu_a(\text{COC}) [\nu\text{CO}]$	1125	1124	1120	1122
$\rho(\text{CH}_3) + \nu(\text{CO})$ + $\nu(\text{CC})$ + bends	1159	1159	1159	1159
$\rho(\text{CH}_2 + \text{CH}_3)$	1174	1181	1176	1178
$\nu_s(\text{CH}_3) + \nu_s(\text{CH}_2)$ + $2 \times \delta(\text{CH}_3)$	2854 2900	2848 2870 2900	2856 2872	2875
$\nu_a(\text{CH}_2)$	2934	2934	2932	2934
$\nu_a(\text{CH}_3)$	2971 (2804) (2773) (2689)	2968 (2802) 2983 (2773) 2989 (2688)	2970 2987	2971 2992

Table 3.9: List of vibrational modes of multilayer $(\text{CH}_3\text{CH}_2)_2\text{O}$ (500 L) adsorbed on amorphous SiO_2 at 20 K and 110 K.

Furthermore, there is a set of three peaks at high wavenumbers: 2804, 2773 and 2689 cm^{-1} at 20 K and 2802, 2773 and 2688 cm^{-1} at 110 K. These peaks seem to find no match with the reported multilayer IR frequencies of $(\text{CH}_3\text{CH}_2)_2\text{O}$ on Ru[44] or Cu [37], but interestingly their pattern has a surprisingly similar spacing to that of the C-H stretches in the methyl (CH_3) and methylene (CH_2) groups. Similar bands are also well-known to appear in the liquid phase spectrum and referred as C-H stretches in organic chemistry [45].

The small negative feature at 3017 cm^{-1} is due to gaseous methane present in the optics in the air side of the chamber. When comparing the two sets of experiments, the 500 L spectrum at 110 K is less intense than the analogous spectrum at lower dosing temperature. This is consistent with the TPD experiments that showed desorption to start below 105 K, meaning that the accommodation coefficient² on SiO_2 is less than 1 at this temperature. However it is important to highlight that despite the loss of $(\text{CH}_3\text{CH}_2)_2\text{O}$ molecules during dosing at 110 K, a crystalline multilayer film is still formed. As seen for CH_3OH , this results in sharper peaks with a maximum at lower frequencies than in amorphous phase, and some features are more resolved, *e.g.* the C-H methyl stretches above 2968 cm^{-1} (**Table 3.9**).

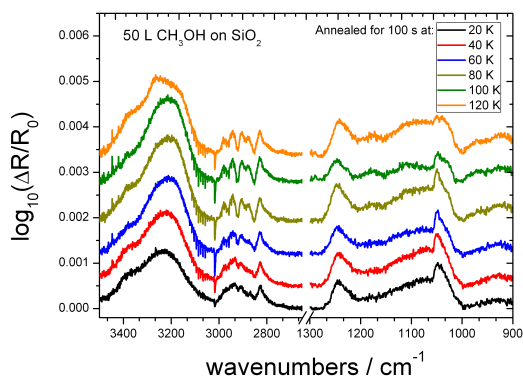
The C-H stretching bands are the most intense and therefore the most reliable to investigate and follow their evolution as the surface coverage increases. The methyl CH stretches, that fall around 2971 cm^{-1} , do not seem to show any significant shift as the coverage increases at 20 K, while it appears at slightly lower wavenumbers at 110 K for low coverages ($\leq 5\text{ L}$). The methylene CH stretch at 2934 cm^{-1} exhibits some degree of dependence on coverage and deposition temperature. It is centred around 2940 cm^{-1} for low exposures ($\leq 20\text{ L}$) at 20 K, while it decreases towards 2934 cm^{-1} when θ and temperature are changed. The combination of CH stretches has a similar behaviour: centred at $\sim 2902\text{ cm}^{-1}$ in the multilayer and at all coverages at 110 K, while peaking around 2912 cm^{-1} for doses less than or equal to 20 L. In the same low coverage and low temperature regime as above, a peak around 2844 cm^{-1} seem to arise from above the background noise to merge with other features at higher doses. The remaining bands seem to be constant in the maximum position, and not surprisingly they grow broad and more intense as the coverage is increased. The observed shifts suggest 20 L - 50 L as turning point from one regime to another. This is consistent with TPD data showing multilayer behaviour being dominant from 50 L. However, it is most important to stress that the background is not stable during the whole data-set, small variation in the interferogram intensity could be accentuated by baseline artifacts resulting in peaks that otherwise would not appear. This especially affects the low coverages spectra up to 5, 10 L. Some degrees of inconsistency has been found also for some features at coverages as high as 50 L. In order to properly assess the $(\text{CH}_3\text{CH}_2)_2\text{O-SiO}_2$ (and also $\text{CH}_3\text{OH-SiO}_2$) interaction, a flat crystalline film of SiO_2 should be used in future studies allowing for a cleaner background in the IR high frequency region.

²The accommodation coefficient, α is defined as $\alpha = S - \frac{u_d}{u_a}$, where u_a and u_d are the adsorption and desorption rates.

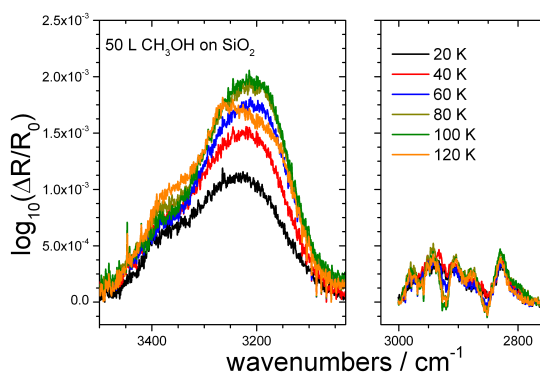
3.3.2 TP-RAIRS: Results and Discussion

In principle, when molecules are dosed at 20 K they stick randomly to the amorphous SiO₂ surface and are unable to diffusively explore the substrate surface. Warming the substrate provides enough thermal energy for molecules to overcome the activation energy barrier needed for diffusion and move around driven by the most thermodynamically stable arrangement. This accommodation is already achieved as molecules are dosed at 110 K, therefore the two sets of TPD data are identical (except for the partial loss of (CH₃CH₂)₂O). RAIRS, on the other hand, probes the adsorbate at a fixed surface temperature and might provide information about its arrangement at base conditions. Therefore, TP-RAIR spectra at sub-monolayer coverages could potentially shed light upon molecular diffusion over the silica and its effect on film growth. However, changes in the interferogram intensity during the experiment lead to oscillations in the background optical properties and resulted in inconsistencies at low coverages. Therefore TP-RAIRS experiments were performed for 50 L exposures, as being much more reliable with respect to spectra at lower doses. This might appear as inconvenient as, recalling the TPD data, CH₃OH and (CH₃CH₂)₂O were both found to complete 2 layers below 50 L. This is likely to occur for H₂O as well, despite the fact that a monolayer cannot be rigorously defined in this case because H₂O exhibits zeroth-order desorption from 2 L up to 200 L.

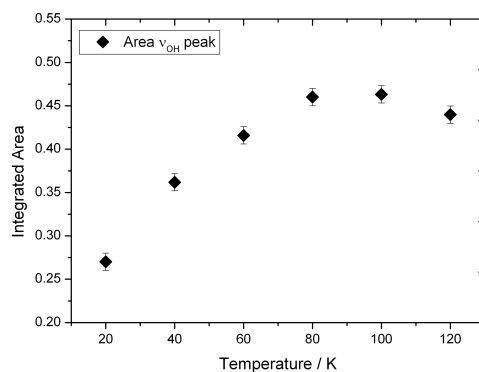
However, it has been highlighted more than once that the SiO₂ surface (300 nm thick) is extremely rough and presents an interface area that is much larger than the geometrical area of the underlayer metal substrate. This resulted in strong deviations from a perfect layer-by-layer desorption in the TPD traces, especially for (CH₃CH₂)₂O, where fractional order are observed up to 5000 L. This means that ballistic deposition of H₂O, CH₃OH or (CH₃CH₂)₂O at 20 K might still imply a large number of molecules adsorbed on SiO₂ even at 50 L. **Figure 3.24** displays in black the 50 L RAIR spectrum of CH₃OH deposited on SiO₂ at 20 K. The substrate was slowly heated up to 40 K and annealed for one hundred seconds, then it was left to cool down to base conditions. The resulting spectrum is shown in red. This procedure was repeated for the set point temperatures of 60 K (spectrum in blue), 80 K (spectrum in dark yellow), 100 K (spectrum in olive) and 120 K (spectrum in orange). In the fingerprint region (900 - 1400 cm⁻¹), only the enhancement of the CO band is observed at 100 K, probably due to crystallisation, but it cannot be excluded that this arises from a change in the background's optical properties. Focusing on the high frequency region (**Figure 3.24b**), the C-H stretches stay constant in intensity at every T step, while be-



(a)



(b)



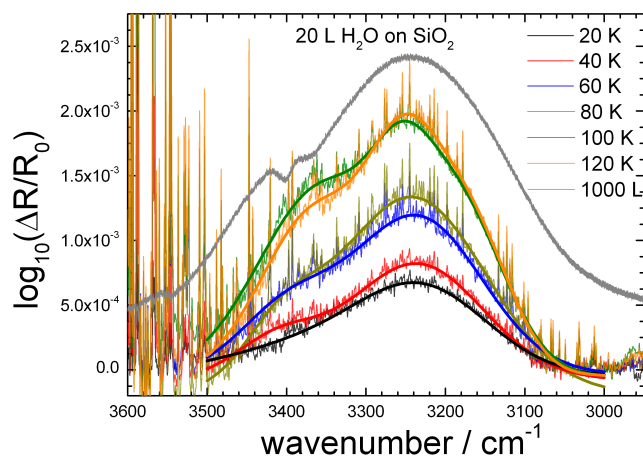
(c)

Figure 3.24: (a) Full spectrum and (b) high frequency region of RAIR spectra obtained for CH_3OH (50 L) deposited on amorphous SiO_2 at 20 K, then annealed at $T = 40$ K, 60 K, 80 K, 100 K and 120 K for 100 seconds, and finally cooled down to base temperature. The OH and CH stretching regions were considered individually to define a baseline specific for each frequency range. (c) Plot of integrated area for the OH stretching mode at each annealing step. The error bars are obtained propagating a 10% error during the integration.

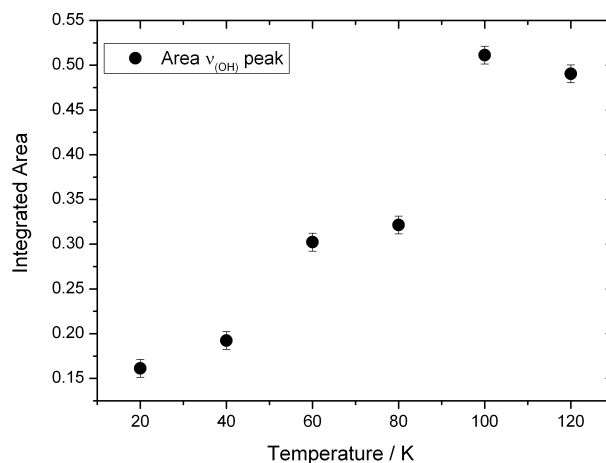
coming more resolved at 60 K. The sudden change of the OH stretch intensity is much more striking. As the temperature is increased from 20 K to 40 K, and then up to 80 K, the band progressively grows and peaks at lower wavenumbers; it stays roughly constant in shape and area when CH₃OH is annealed at 100 K. At 120 K, the band profile undergoes a further evolution with the appearance of a high wavenumber peak ($\sim 3250\text{ cm}^{-1}$), most likely due to crystallisation.

In **Figure 3.24c**, the area of the OH stretching mode is plotted *versus* the annealing temperature. Two distinctive regimes are observed: a near-linear growth from 20 K up to 80 K, and a plateau from 80 K and 120 K. The small decrease in the band area at 120 K, although within the error, can be easily explained as a consequence of the phase change. In contrast, the temperature range when the initial increase of the band area occurs is too low to be explained purely in terms of phase change within the bulk.

In order to better assess this matter, the equivalent experiment was performed for H₂O. The H₂O dipole moment is much larger than that of CH₃OH, which results in the OH stretching mode being a better probe to look at. In this case (**Figure 3.25a**) the O-H stretch grows and shifts in intensity, from 3232 cm^{-1} to 3250 cm^{-1} along the appearance of a new shoulder at 3353 cm^{-1} . It is clear that the signal strengthens significantly when annealing at 60 K and with a further intensity “jump” at 100 K. For comparison the spectrum at 1000 L of exposure dosed at 20 K was conveniently scaled and overlapped for the sake of comparison. The set of spectra show a change in the OH vibrational mode towards a bulk band-profile. The integrated area of the O-H stretching band is plotted *versus* the annealing temperature in **Figure 3.25b**, quantifying an increase of 50% from 40 K to 60 K and 150% when reaching 100 K. In IR spectroscopy, the band intensity depends on the dipole moment variation with the extension of the chemical bond and obviously depends on the number of absorbing molecules. H₂O desorption at 60 K is null, therefore any change in the intensity is due to a change in the dynamic dipole moment. It is well-known in the literature that the H₂O dipole increases moving from the isolated molecule to the dimer, up to larger clusters [46, 47], and in general when a bulk forms. As the absolute number of dosed molecules is fixed for the whole experiment, such enhancement of the O-H stretch is confidently consistent with thermal activation of bulk behaviour, and hence, of diffusion of isolated or small H₂O cluster randomly stuck to the SiO₂ surface that group together to form condensed phase islands. Given that diffusion is activated above 40 K, **Equation 3.11** (*Redhead equation*) provides a rough estimate for the barrier to diffusion [48] to be around 10 - 15 kJ mol⁻¹



(a)



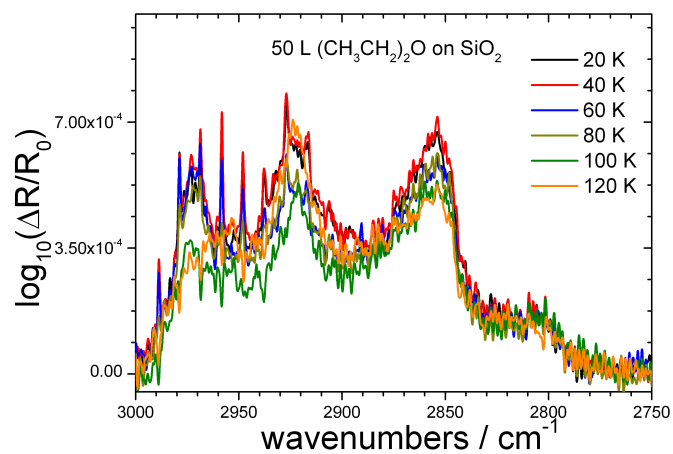
(b)

Figure 3.25: (a) OH stretch vibrational mode evolution in RAIR spectra obtained for H_2O deposited on amorphous SiO_2 (50 L) at 20 K, then annealed at $T = 40$ K, 60 K, 80 K, 100 K and 120 K for 100 seconds and finally cooled down to base temperature. (b) Integrated area at each annealing step. The error bars are obtained propagating a 10% error during the integration.

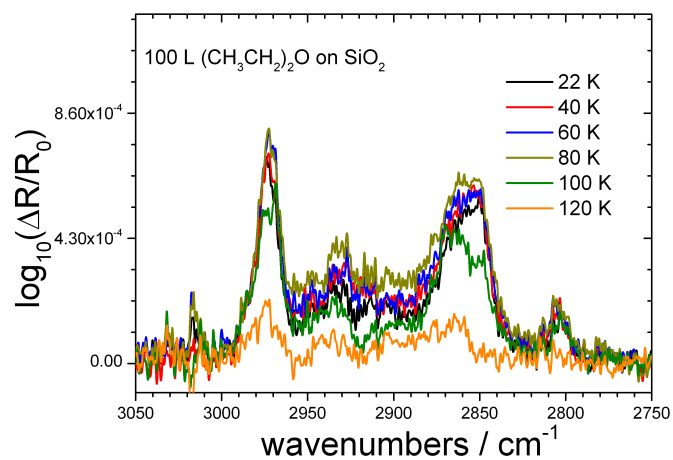
assuming a $\nu_0 = 10^{13} \text{ s}^{-1}$ and $\beta = 0.1 \text{ K s}^{-1}$; which value is consistent with the energy of a hydrogen bond between the terminal silanol groups and a H_2O molecule. This result is higher than the $\sim 4 \text{ kJ mol}^{-1}$ predicted by the “rule of thumb” [49] which states that the diffusion barrier is roughly 10 per cent of the desorption energy (**Table 3.7**). Surely this discrepancy depends on the fact the latter is derived from a large statistics of adsorbates on transition-metal surfaces so that the interactions involved are of different nature. The change in the O-H stretch seen with CH_3OH from 40 K could also be interpreted according to a similar logic, and hence, the diffusion barrier is deduced to be roughly the half

of H₂O on silica (5 - 11 kJ mol⁻¹). The accurate determination of the diffusion barrier requires the exact knowledge of the transition state and initial state for the diffusive jump and it is beyond the available data outlined in this thesis.

In contrast, the intensities in the C-H stretching region of the RAIR spectra (**Figure 3.24**) do not show any temperature dependence behaviour. The small apparent changes in intensities result mainly from baseline artifacts. **Figure 3.26a** displays the analogous experiment with (CH₃CH₂)₂O with an additional set at 100 L exposure (**Figure 3.26b**). Also in this case no change is observed in each feature intensity up to 80 K within the background fluctuations, as can be seen by the gaseous methane narrow bands around 3000 cm⁻¹. Above 100 K, (CH₃CH₂)₂O starts to desorb and at 120 K the surface concentration is likely to be halved, hence the area of the peaks is expected to decrease. Interestingly this evidently occurs in **Figure 3.26b**, while in **Figure 3.26a** the difference is less striking. This might suggest that the IR signature displayed at 50 L arises predominantly within the first two, three layers. Since (CH₃CH₂)₂O wets SiO₂, as thermal diffusion is activated no change in the IR features would be expected to occur at sub-monolayer coverages. This is compatible with our results, but it is also true that while diffusion could be invoked as responsible for the O-H band evolution, the same cannot be proposed for the C-H stretches, which show no variation. The weak interaction (van der Waals) that would involve the alkyl ends of the adsorbates with the SiO₂ results in small shifts that cannot be detected with such broad bands. It can be concluded that there is no direct nor conclusive evidence to assess molecular diffusion by looking at the C-H vibrational modes for both (CH₃CH₂)₂O or CH₃OH, but neither it can be excluded *a priori*. The related work of Collings *et al.* [28], presents the TP-RAIRS of sub-monolayer quantities of CO (0.6 monolayer) for the same substrate and experimental setup used for this thesis. The CO band is observed to be constant in intensity and position from base temperature up to 24 K, after which it desorbs. The invariance of the carbonyl feature is, of course, consistent with the CO being able to readily diffuse over the SiO₂ surface to eventually sample the most energetically favourable binding sites. This might be also the case for (CH₃CH₂)₂O as TPD profiles show they share a similar affinity with the SiO₂ surface.



(a)



(b)

Figure 3.26: High frequency region of RAIR spectra obtained for 50 L (a) and 100 L (b) of (CH₃CH₂)₂O deposited on amorphous SiO₂ at 20 K, then annealed at $T = 40$ K, 60 K, 80 K, 100 K and 120 K for 100 seconds, and finally cooled down to base temperature.

3.4 Conclusions

This work is focused on three components of the icy mantles that are found in the cold dense regions of the ISM; H_2O , CH_3OH and $(\text{CH}_3\text{CH}_2)_2\text{O}$ with their TPD and RAIRS. Multilayer films of the three materials display desorption behaviour of (or close to) zero-order kinetics. The activation energies for desorption are consistent with literature reports of these quantities where available. The sub-monolayer behaviour of the three solids show variations that can be interpreted in terms of relative strengths of intermolecular forces; H_2O desorbs by zero-order kinetics consistent with two-dimensional gas-solid interaction on the surface and de-wetting from the amorphous SiO_2 surfaces; $(\text{CH}_3\text{CH}_2)_2\text{O}$ desorbs in a first-order manner consistent with wetting of the SiO_2 surfaces; and CH_3OH TPD presents aspects of first order behaviour in the monolayer regime and resembles H_2O desorption as soon as the most favourable adsorption sites on silica are filled. Ballistic deposition and TP-RAIRS have revealed for the first time direct evidence for the thermal activation of H_2O diffusion over the amorphous SiO_2 surface between 40 K and 60 K, corresponding to a diffusive barrier of around 10 to 15 kJ mol^{-1} . This suggests that H_2O molecules, adsorbed at low temperatures with two hydrogen-bonds to the SiO_2 surface, have one of their hydrogen-bonds broken above 40 K. This allows diffusion, which could be pictured as a penguin-like random walk between adsorption sites, until the H_2O molecule finds a more stable adsorption site by islanding with other H_2O molecules. In this configuration, water molecules form on average three hydrogen-bonds, as suggested by the desorption energy of H_2O multilayers of $\sim 50 \text{ kJ mol}^{-1}$. TP-RAIRS of CH_3OH also suggests that diffusion might be thermally activated between 20 K and 40 K with an energy barrier of 5 to 10 kJ mol^{-1} . No conclusive evidence was found for $(\text{CH}_3\text{CH}_2)_2\text{O}$ diffusion on SiO_2 .

As CH_3OH and H_2O are both key components of the interstellar ice inventory, it is invaluable to understand their interaction with amorphous SiO_2 . At typical dense cloud temperatures (10-15 K), according these results H_2O would not be able to diffuse over the surface until the temperature of the dust grain is raised to above 40 K by an external heat source. At the low temperatures of dense clouds, the surface of the water ice layer covering the grains is therefore static, and all H_2O molecules formed in this environment or impinging on the grains surface would freeze in their initial position, confirming the view of a ballistic deposition, provided that there are terminal silanol groups in the grains of the ISM. The diffusion rate in astrochemical models of the water molecules on the interstellar grains should reflect the existence of an energy barrier for diffusion over the SiO_2 surface as the

one reported herein. Desorption temperatures obtained from TPD data cannot be directly used in the models, but need to be scaled to astrophysical contexts, where the heating rate is significantly lower than in the laboratory. In fact, as seen in **Chapter 1**, astrochemical models describe thermal desorption by applying the Polanyi-Wigner equation, therefore the relevant data to the astrochemistry community are the desorption energy and the pre-exponential factor. The kinetic order is also important. The results reported in this chapter highlight that the desorption kinetics of organic molecules, such as CH_3OH and $(\text{CH}_3\text{CH}_2)_2\text{O}$, is rather complex and that the value of E_d and the kinetic order are not the same for the bulk and the sub-monolayer coverages on the SiO_2 surface. Thus, a single equation, with a constant kinetic order and E_d value, for the thermal desorption of the species i (*e.g.* CH_3OH) might not be a sensible simplification. A detailed model describing the evolution of the grain through the warming up stage, from cold environments to the hot core/corino region, should consider that (i) H_2O would form islands leaving some parts of the SiO_2 surface exposed, and (ii) that organic molecules, such as CH_3OH , could diffuse from the H_2O interface to the bare grain where the desorption energy can be relatively high and the kinetic order is not zero.

Bibliography

- [1] S. B. Charnley, A. G. G. M. Tielens and S. D. Rodgers, *Astrophys. J.*, 1997, **482**, L203.
- [2] E. A. Bergin, G. J. Melnick, J. R. Stauffer, M. L. N. Ashby, G. Chin, N. R. Erickson, P. F. Goldsmith, M. Harwit, J. E. Howe, S. C. Kleiner, N. D. A. Koch, D. G., B. M. Patten, R. Plume, R. Schieder, R. L. Snell, V. Tolls, Z. Wang, G. Winnewisser and Y. F. Zhang, *Astrophys. J.*, 2000, **539**, L129.
- [3] E. L. Gibb, D. C. B. Whittet, W. A. Schutte, A. C. A. Boogert, P. Chiar, J. E. Ehrenfreund, P. A. Gerakines, J. V. Keane, A. Tielens, E. F. van Dishoeck and O. Kerkhof, *Astrophys. J.*, 2000, **536**, 347.
- [4] A. C. A. Boogert, K. M. Pontoppidan, C. Knez, F. Lahuis, J. Kessler-Silacci, E. F. van Dishoeck, G. A. Blake, S. E. Augereau, J. C. Bisschop and S. Bottinelli, *Astrophys. J.*, 2008, **678**, 985.
- [5] K. I. Öberg, A. C. A. Boogert, K. M. Pontoppidan, B. Saskia, E. F. van Dishoeck, B. Sandrine, A. B. Geoffrey and N. J. Evans II, *Astrophys. J.*, 2011, **740**, 109.
- [6] E. Dartois, K. Demyk, L. d'Hendecourt and P. Ehrenfreund, *Astron. Astrophys.*, 1999, **351**, 1066.
- [7] S. B. Charnley, P. Ehrenfreund and Y. J. Kuan, *Spectrochim. Acta A*, 2001, **57**, 685.
- [8] J. M. Hollis, F. J. Lovas and P. R. Jewell, *Astrophys. J.*, 2000, **540**, L107.
- [9] L. E. Snyder, *Proc. Natl. Acad. Sci. U. S. A.*, 2006, **103**, 12243.
- [10] J. M. Hollis, S. N. Vogel, L. E. Snyder, P. R. Jewell and F. J. Lovas, *Astrophys. J.*, 2001, **554**, L81.
- [11] E. Herbst and E. F. van Dishoeck, *Ann. Rev. Astron. Astrophys.*, 2009, **47**, 427.

- [12] O. Botta and J. L. Bada, *Surv. Geophys.*, 2002, **23**, 411.
- [13] M. Ikeda, M. Ohishi, A. Nummelin, J. E. Dickens, P. Bergman, A. Hjalmarsson and W. M. Irvine, *Astrophys. J.*, 2001, **560**, 792.
- [14] I. Medvedev, M. Winnewisser, F. C. De Lucia, E. Herbst, E. Yi, L. P. Leong, R. P. A. Bettens, E. Biankowska-Jaworska, O. Desyatnyk, L. Pszczónkowski and Z. Kisiel, *Astrophys. J. Suppl. Ser.*, 2003, **148**, 593.
- [15] Z. Karpas and M. Mautner, *J. Phys. Chem*, 1989, **93**, 1859.
- [16] J. D. Thrower, M. P. Collings, F. J. M. Rutten and M. R. S. McCoustra, *J. Chem. Phys.*, 2009, **131**, 244711.
- [17] M. P. Collings, J. W. Dever, H. J. Fraser and M. R. S. McCoustra, *Astrophys. Space Sci.*, 2003, **285**, 633.
- [18] T. Zubkov, R. S. Smith, T. R. Engstrom and B. D. Kay, *J. Chem. Phys.*, 2007, **127**, 184707.
- [19] L. Hornekær, A. Baurichter, V. V. Petrunin, A. C. Luntz, D. B. Kay and A. Al-Halabi, *J. Chem. Phys.*, 2005, **122**, 124701.
- [20] L. Amiaud, F. Dulieu, H. H. Fillion, A. Momeni and J. L. Lemaire, *J. Chem. Phys.*, 2007, **127**, 144709.
- [21] A. S. Bolina, A. J. Wolff and W. A. Brown, *J. Chem. Phys.*, 2005, **122**, 044713.
- [22] M. Wu and G. D. W. Truong, C. M. and, *J. Phys. Chem.*, 1993, **97**, 9425.
- [23] S. Y. Nishimura, R. F. Gibbons, Tro and N. J., *J. Phys. Chem. B*, 1998, **102**, 6831.
- [24] *IBM Almaden Research Centre, CKS*, IBM Corporation, 1995.
- [25] H. J. Fraser, M. P. Collings, M. R. S. McCoustra and D. A. Williams, *Mon. Not. R. Astron. Soc.*, 2001, **327**, 1165.
- [26] J. D. Thrower, M. P. Collings, F. J. M. Rutten and M. R. S. McCoustra, *Mon. Not. R. Astron. Soc.*, 2009, **394**, 1510.
- [27] S. D. Green, A. S. Bolina, R. Chen, M. P. Collings, W. A. Brown and M. R. S. McCoustra, *Mon. Not. R. Astron. Soc.*, 2009, **398**, 357.
- [28] M. P. Collings, V. L. Frankland, J. Lasne, D. Marchione, A. Rosu-Finsen and M. R. S. McCoustra, *Mon. Not. R. Astron. Soc.*, 2015, **449**, 1826.

- [29] R. L. Summers, *Empirical observations on the sensitivity of hot cathode ionization type vacuum gauges*, National Aeronautics and Space Administration, Washington, D. C., 1969.
- [30] J. E. Bartmess and M. Georgiadis, R, *Vacuum*, 1983, **33**, 149.
- [31] M. Schulte, B. Schlosser and W. Seidel, *Fresenius J. Anal. Chem.*, 1994, **348**, 778.
- [32] R. S. Smith, J. Matthiesen and B. D. Kay, *J. Phys. Chem. A*, 2014, **118**, 8242.
- [33] P. A. Redhead, *Vacuum*, 1962, **12**, 203.
- [34] J. F. Counsell, D. A. Lee and J. F. Martin, *J. Chem. Soc. A*, 1971, 313.
- [35] F. G. Keyes and J. A. Beattie, *J. Am. Chem. Soc.*, 1924, **46**, 1753.
- [36] H. M. Huffman, *J. Am. Chem. Soc.*, 1926, **48**, 2788.
- [37] J. M. Meyers and S. C. Street, *Langmuir*, 1996, **12**, 1511.
- [38] G. M. A. Abdulgalil, *PhD thesis*, Heriot-Watt University, 2013.
- [39] V. L. Frankland, *PhD thesis*, Heriot-Watt University, 2011.
- [40] A. Abdulgalil, D. Marchione, J. D. Thrower, M. P. Collings, M. R. S. McCoustra, F. Islam, M. E. Palumbo, E. Congiu and F. Dulieu, *Phil. Trans. A*, 2013, **371**, 20110586.
- [41] P. Ugliengo, V. Saunders and E. Gamone, *J. Phys. Chem.*, 1994, **90**, 2260.
- [42] Y. Chen, I. Chu, Y. Wang and H. Cheng, *Phys. Rev. B*, 2011, **84**, 155444.
- [43] P. Pantalei, R. Senesi, C. Andreani, P. Sozzani, A. Comotti, S. Bracco, M. Beretta, P. E. Sokola and G. Reiter, *Phys. Chem. Chem. Phys.*, 2011, **13**, 6022.
- [44] F. C. Calaza, T. L. Chen, D. R. Mullins and S. H. Overbury, *Top. Catal.*, 2011, **54**, 56.
- [45] A. L. Smith, *The Coblenz Society Desk Book of Infrared Spectra*, Coblenz Society, 1982.
- [46] J. K. Gregory, D. C. Clary, K. Liu, M. G. Brown and R. J. Saykally, *Science*, 1997, **275**, 814.

- [47] J. Ceponkus, P. Uvdal and B. Nelander, *J. Phys. Chem. A*, 2008, **112**, 3921.
- [48] H. Marbach and H.-P. Steinrück, *Chem. Commun.*, 2014, **50**, 9034.
- [49] A. U. Nilekar, J. Greeley and M. Mavrikakis, *Angew. Chem. Int. Ed.*, 2006, **45**, 7046.

Chapter 4

Benzene on Methanol and Diethyl Ether

Contents

4.1	Introduction	148
4.2	Experimental Section	148
4.3	Benzene on Methanol	149
4.3.1	TPD of Benzene on Methanol	150
4.3.2	RAIRS of Benzene on Methanol	160
4.4	Benzene on Diethyl Ether	166
4.4.1	TPD of Benzene on Diethyl Ether	168
4.4.2	RAIRS of Benzene on Diethyl Ether	171
4.5	Computational Studies on Model Systems	173
4.6	Conclusions and Comparison with ASW	179
	Bibliography	183

4.1 Introduction

This chapter focuses on benzene (C_6H_6) adsorption on top of relatively thick “ice” layers comprising methanol (CH_3OH ; 15.2 ± 1.5 nm), or diethyl ether ($(CH_3CH_2)_2O$; 12.1 ± 1.2 nm). Benzene can be considered a prototypical polycyclic aromatic hydrocarbon (PAH) and is a convenient species for studying the interactions between aromatic molecules and different surfaces. C_6H_6 has itself been detected in the protoplanetary nebula CRL-618 [1], and it is thought to form in the ISM under single collision conditions *via* the gas phase reaction of ethynyl radicals with 1,3-butadiene [2]. Benzene is also the starting point for the generation of PAHs according to many proposed mechanisms [3, 4]. The highly vibrationally excited states of these aromatic compounds are consistent with observed spectroscopic features in the infrared [5] and UV-Visible [6] regions along many interstellar lines-of-sight. Furthermore, it is widely agreed that 10-20% of cosmic carbon is contained in PAHs and their presence in the early stages of the formation of our Solar System is strongly indicated by the extraction of PAHs from objects such as meteorites and interplanetary dust particles [7, 8]. Astrophysical implications of these observations provide the basis for the studies presented in this chapter and the following one, which could be both considered as the continuation to those results presented by Throner on thermal and non-thermal desorption of C_6H_6 on ASW [9–12].

4.2 Experimental Section

In contrast with the results presented in **Chapter 3**, the C_6H_6 experiments reported here were performed with the Beam Rig set-up; temperature programmed desorption (TPD) monitoring at $m/z = 77$, and RAIR spectra of C_6H_6 will be outlined and its analyses discussed. Simple model systems were also used for high level calculation in order to accurately describe the types of possible key interactions displayed by C_6H_6 with the molecules of these two substrates.

The polished stainless steel disk substrate was mounted on a liquid nitrogen cooled cryostat as described in the second chapter. Although initial intentions were to front-coat the metal substrate with amorphous silica (SiO_2), depositions turned out to be unsuccessful; however this favoured $(CH_3CH_2)_2O$ dosing with a sticking coefficient close to unity at the base temperature of ~ 107 K giving a clean background and higher sensitivity compared to the Ice Rig. The substrate was routinely heated up to 500 K for 15 min to remove volatile contaminants before cooling prior to conducting experiments each day. The sample position was

optimised to guarantee the best signal to the QMS or the IR detector. The average heating rate during the TPD experiments was 1.5 K s^{-1} and temperature was monitored with a precision better than 1 K. Dosing was conducted by background deposition *via* the gas manifolds collecting the vapour phase of the liquids, which were previously degassed and purified by freeze-pump thaw cycles. Exposures are expressed in Langmuir units (L) and uncorrected for the ionisation coefficient. RAIR spectra were collected using an FTIR spectrometer (Nicolet 870) with the coaddition of 1024 scans at a resolution of 2 cm^{-1} .

4.3 Benzene on Methanol

The results reported in this section were obtained by depositing different coverages of C_6H_6 on a relatively thick ice of CH_3OH (15.2 nm) on top of the substrate in the Beam Rig. Particular emphasis will be given to low coverages of C_6H_6 as most indicative of the interaction with the underlying substrate. In contrast to what is shown in the previous chapter, CH_3OH was dosed directly on the flat stainless steel disk. The multilayer spectrum at 200 L shown in **Figure 4.1** is consistent with reported values for the vibrational modes and with the data collected with the Ice Rig. However it was possible to clearly identify two additional vibrational modes undetected for the sample on the SiO_2 coated surface:

1. The methyl bend, $\delta(\text{CH}_3)$, at 1464 cm^{-1} , which might also include a minor contribution of the COH bending mode at $\sim 1510 \text{ cm}^{-1}$.
2. The CO stretching overtone at 2043 cm^{-1} .

Furthermore in the spectrum in **Figure 4.1**, the CO stretch is the most intense peak, whereas in the previous chapter the OH stretching band was reported as the highest feature. This inconsistency can be explained as the result of the combination of two elements: (i) the different RAIRS geometry of the two apparatus and (ii) the *metal surface selection rule*. In fact, the angle between the incident radiation and the metal surface normal is of $3^\circ - 6^\circ$ in the Beam Rig, while in the Ice Rig it is of 15° . Therefore, the intensity of the resulting standing wave is not the same for both the set-ups. Furthermore, even if the stainless steel disk is not perfectly flat, it is less rough than the SiO_2 surface on the copper block. Thus, the selection rule results to be more effective for the sample in the Beam Rig as explained in **Chapter 2**. Finally, the frequency of the maximum for the CO stretch is consistent with the film being mainly in the amorphous phase. TP-RAIRS spectra obtained by annealing at each temperature step for 100 seconds show crystallisation to occur 10-15 K above T_{base} (**Figure 4.2**).

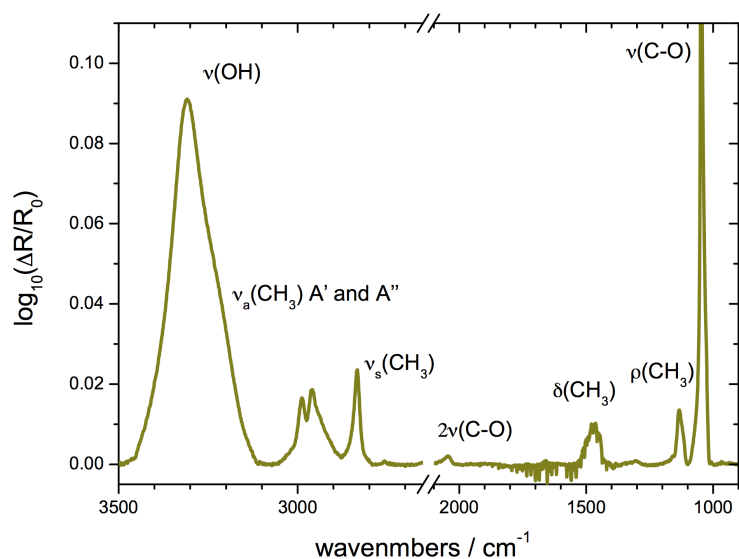


Figure 4.1: RAIR spectrum of the multilayer CH_3OH film (200 L; ~ 15.2 nm) grown on stainless steel in the Beam Rig for the C_6H_6 experiments. CH_3OH vibrations are labelled. The negative sharp features between 1800 and 1400 cm^{-1} are due to the bending modes of gaseous H_2O in the air side of the chamber, in the IR path to the detector.

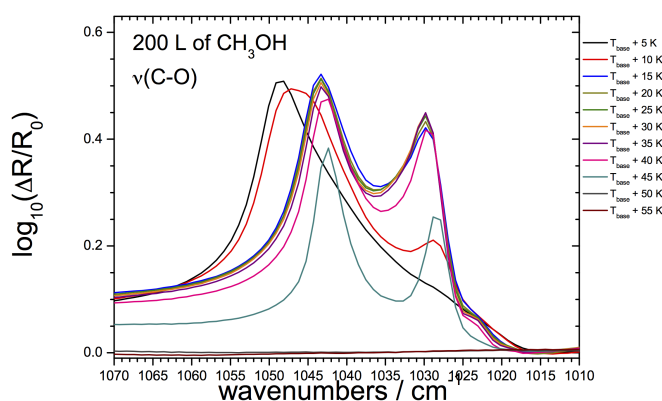


Figure 4.2: CO stretch TP-RAIR spectra when 200 L of CH_3OH is deposited at 105 K on stainless steel, then annealed at $T = 110$ K, 115 K, 120 K, 125 K, 130 K, 135 K, 140 K, 145 K, 150 K, 155 K, and 160 K for 100 seconds, and finally cooled down to base temperature. Note the transition from the amorphous to crystalline phase by the CO splitting.

4.3.1 TPD of Benzene on Methanol

Low Coverages

In **Figure 4.3** TPD traces of C_6H_6 at very low coverages on 200 L of CH_3OH exhibit little reproducibility: different desorption behaviours are observed when the same experiment is repeated multiple times. Inconsistency spans over the

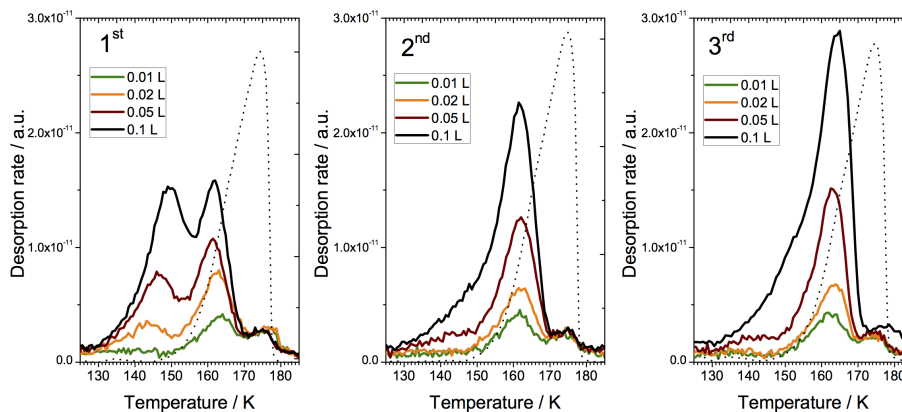


Figure 4.3: Three replications of TPD experiments of 0.01 L, 0.02 L, 0.05 L, 0.1 L of C_6H_6 deposited on thick CH_3OH film (200 L; ~ 15.2 nm). The dotted line is the scaled CH_3OH TPD trace underlying 0.05 L of C_6H_6 .

whole range of C_6H_6 exposures used (0.01 L - 500 L), with larger discrepancies at sub-monolayer level (less than 5 - 2 L^1). In the latter case, as also shown in **Figures 4.4** and **4.5**, three features can be observed in the TPD traces up to 1 L: a low temperature peak between 140 K and 155 K, another peak between 160 K and 170 K, and a small high temperature shoulder above 170 K that becomes saturated at 0.01 L. The first two peaks compete with each other and they both appear in the first data-set in **Figure 4.3**, while one clearly dominates over the other for the two remaining runs. In **Figure 4.4** this competition is displayed in four possible outcomes for the 0.1 L and 0.5 L traces: in the upper panels the two features co-exist with the slight predominance of one over the other; in the lower panels only one of the two peaks clearly emerges while the other is just a shoulder. Furthermore, the desorption kinetics is also not consistent for the same peak within the data-sets. In other words, looking at the TPD traces in **Figure 4.3**, The peak around 160 K and 170 K seem to follow a desorption kinetics that looks like second-order with a distribution of binding energies in the first run; then seem to follow a first-order kinetics in the second and third run. It should be noted that occasional variation of heating ramps in the same set of data or between different sets showed no correlations with the kinetics displayed by these two peaks.

In order to address the lack of reproducibility, one should take into account the desorption of the underlying CH_3OH ice (in dotted lines in **Figure 4.3** and **4.4**). The small shoulder that saturates at 0.01 L above 170 K displays a good match with the maximum of the CH_3OH multilayer desorption peak, therefore

¹No defined exposure can be assigned to one uniform monolayer of C_6H_6 on CH_3OH . However, as shown in the next section, the 2 - 5 L range marks the appearance of clear multilayer behaviour.

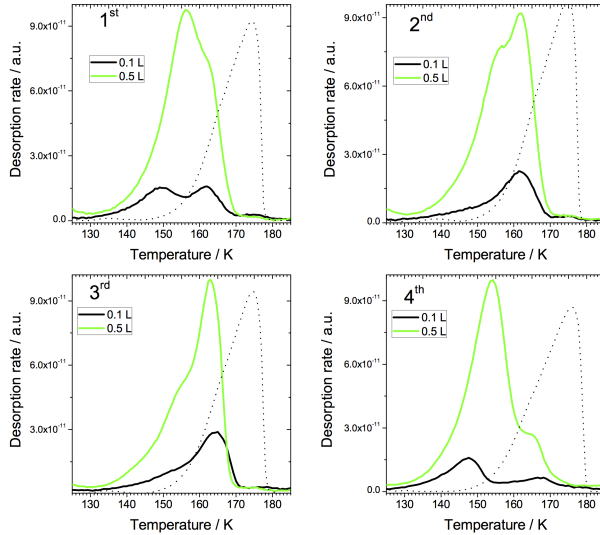


Figure 4.4: TPD traces of 0.1 L and 0.5 L of C_6H_6 deposited on thick CH_3OH film (200 L; ~ 15.2 nm). The dotted line is the scaled CH_3OH TPD trace underlying 0.05 L of C_6H_6 . The four replications show different outcomes of the experiment.

this C_6H_6 feature can only be explained as co-desorption of trapped C_6H_6 with CH_3OH . The low temperature C_6H_6 peak, that sometimes appears clearly at extremely low coverages, has almost coincident leading edges and its maximum shifts towards higher T with increasing exposure. This peak hints to a weak C_6H_6/CH_3OH interaction and could be C_6H_6 desorbing from C_6H_6 nano-islands. CH_3OH desorption is still negligible at those values of T . The higher temperature peak develops in a different scenario: CH_3OH desorption is no longer negligible and as the underlying ice sublimates, it also rearranges interacting more strongly with the C_6H_6 . However, the process that establishes better interactions between C_6H_6 and CH_3OH is limited by the diffusion of C_6H_6 into the underlayer, furthermore the mixing is in competition with both C_6H_6 and CH_3OH desorption. To summarise, competition between several processes is observed:

1. Desorption of C_6H_6 from C_6H_6 molecules as suggested by the low temperature peak growing with a kinetics close to zero-order.
2. Rearrangement of the CH_3OH underlayer as T increases leading to phase transitions and establishing stronger interactions with the C_6H_6 .
3. Desorption of bulk CH_3OH .
4. Desorption of C_6H_6 more strongly bound to the CH_3OH as suggested by the peak above 150 K following a kinetics close to first-order.
5. Co-desorption of CH_3OH and C_6H_6 .

The complexity of the C_6H_6/CH_3OH binary system is such that small changes within the experimental conditions seem to result into unpredictable outcomes. Therefore a quantitative analysis of the sub-monolayer coverages with the same

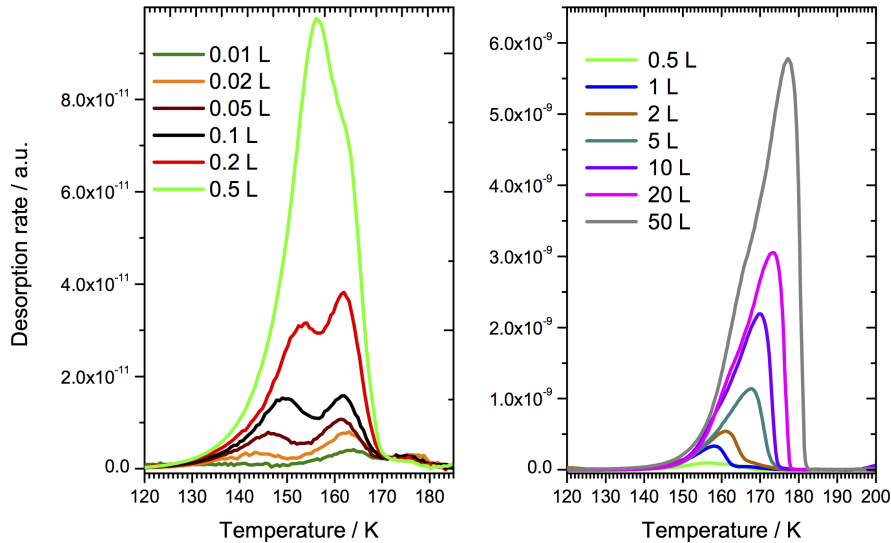


Figure 4.5: TPD traces 0.01 L - 50 L of C_6H_6 deposited on thick CH_3OH film (200 L; ~ 15.2 nm). The left panel shows sub-monolayer exposures and the right panel displays the multilayer growth.

detail seen for CH_3OH and $(CH_3CH_2)_2O$ on SiO_2 would not be reliable.

However, it is still desirable to estimate the desorption energy associated to these two peaks. The TPD traces shown in the left panel of **Figure 4.5** were chosen as most appropriate for the leading edge analysis when the coverage is increased from 0.02 L to 0.5 L. The corresponding *Arrhenius plot*, obtained by representing $\ln(r_d)$ as function of $\frac{1}{T}$, should yield a straight line with the slope containing the desorption energy E_d (**Equation 3.4**), provided that a small section of the spectrum on its leading edge is selected to approximate the coverage as constant. However, the best temperature range follows in a particular area of the TPD plot where the acquired signal is the convolution of the signal coming from the wires and the sample itself. In order to distinguish the latter from the former, the experimental points were fitted with an exponential function. This was then used to estimate the signal related to the wires (red line in **Figure 4.6**) and subtract the latter from the overall trace (black circles line in **Figure 4.6**). The resulting “cleaned” trace is a reasonable plot of the deconvoluted TPD trace specific to the substrate (blue line in **Figure 4.6**). This procedure has the drawback of forcing a mono-exponential trend for the desorption rate over a certain temperature range which overlaps in large part with the one used for the *Arrhenius plot*. Therefore the error returned by the linear fits of $\ln(r_d)$ versus $\frac{1}{T}$ cannot be considered in-

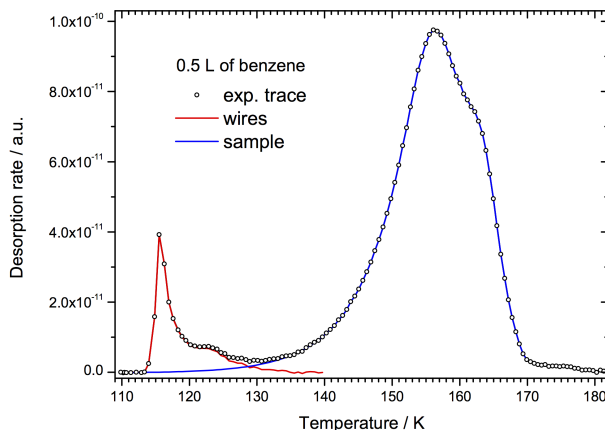


Figure 4.6: TPD traces 0.05 L of C_6H_6 deposited on thick CH_3OH film (200 L, ~ 15.2 nm), in black open circles. The contribution to the overall signal from the wires and the substrate are reported with red and blue lines respectively.

dicative of the real experimental error, which it is considerably larger. **Figure 4.7** reports the *Arrhenius plots* for C_6H_6 on CH_3OH in the low coverages regime (0.02 L, 0.05 L, 0.1 L, 0.2 L and 0.5 L). Desorption energy values obtained from

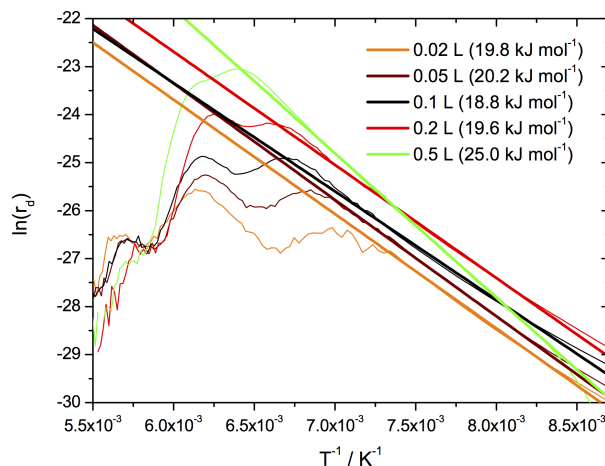


Figure 4.7: Plot of $\ln(r_d)$ against $1/T$ for the low exposures of C_6H_6 on CH_3OH . The best linear fit and the desorption energy for each coverage, is reported along the experimental traces.

the linear fits are all very close to each other with the only exception of the 0.5 L curve. Even just looking at the TPDs (**Figure 4.5**), it is noticeable that at this coverage the desorption profile changes with respect to the other traces below. This might be due to a possible contribution from the higher temperature peak and/or because of the mixing with the underlying CH_3OH . If the E_d corresponding to the 0.5 L is discarded, the average is 20 ± 2 kJ mol $^{-1}$. When the former is included the average rises to 21 ± 2 kJ mol $^{-1}$. Either way the desorption energy is the same within the error (10%). The latter was quantified as the error given by the exponential fit used for the deconvolution on the time constant, which varies

between 5% and 10%. The Redhead equation [13] used for peak B of CH₃OH on SiO₂ can be also applied in this case assuming a first-order kinetics and that activation parameters are independent of surface coverage. The peak temperature of 162.3 ± 0.8 K is obtained as an average of the experimental values found for each coverage between 0.01 L and 0.5 L and each replica of the experiments with the same heating ramp. Thus setting β equal to the experimental value of 1.47 K s⁻¹, and $\nu_0 = 10^{13}$ s⁻¹, the Redhead equation

$$E_d = RT_{max} \left[\ln \left(\frac{\nu_0 T_{max}}{\beta} \right) - 3.64 \right]$$

gives a value of 41.8 ± 0.6 kJ mol⁻¹. This value is extremely close to the desorption energy, 41 ± 0.5 kJ mol⁻¹, estimated for C₆H₆ on ASW at similar exposures [12], suggesting to a similar type of interaction where C₆H₆ has multiple hydrogen bonds with the ice surface.

Bulk Benzene and Methanol Displacement

While the low temperature peak appears to follow a zero-order desorption kinetics from low exposures, the higher temperature peak seems to grow with a first-order kinetics until 0.5 L, merges with the first peak between 2 L and 5 L, so that one multilayer peak is observed growing with a zero-order kinetics above 5 L. However, it should be noted that a different data-set (right panel in **Figure 4.5**) displays the predominance of the low temperature peak over the other above 1 L to then grow with a fractional order up to 5 L. It is not possible to define unambiguously where the monolayer completion occurs because C₆H₆ de-wets CH₃OH (low temperature peak) as on ASW, but when CH₃OH sublimates there seems to be a certain degree of interaction that breaks the islands, mixing adsorbates and underlayer. The layer-by-layer growth observed for the peak above 5 L sets a lower boundary for the multilayer regime. At any exposure below that, C₆H₆ molecules might either bind to favourable sites or group to form two-dimensional islands. However coincidence of leading edges is not observed all the way up to 50 L (right panel in **Figure 4.5**); a shoulder can be noted to appear on the left, shifting to higher temperatures as coverage is increased. Desorption behaviour assumes unconventional shapes when θ is increased from 50 L up to 500 L (**Figures 4.8** and **4.9**). The above mentioned interplay between mixing and desorption processes cannot be solely evoked to explain these observations. In fact, focusing on the CH₃OH desorption traces, it is noted that they change drastically in profile and temperature range as C₆H₆ coverage is increased. Variations among the CH₃OH TPD traces in the whole series are expected because of the inherent uncertainty

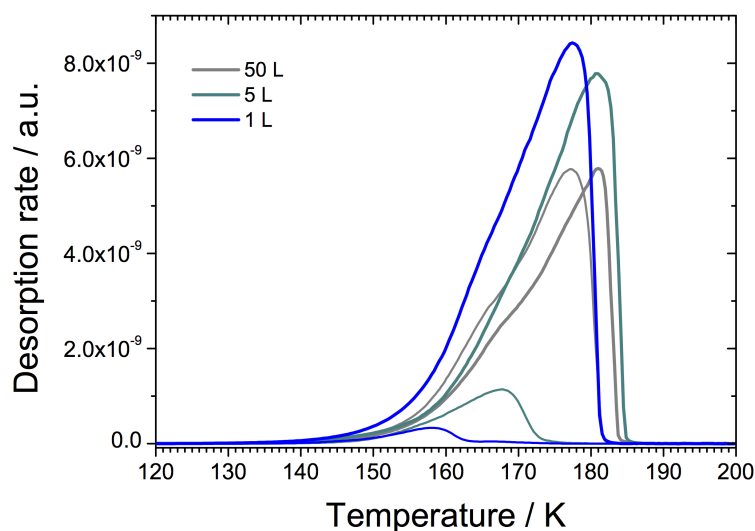


Figure 4.8: TPD traces (in thin lines) of 1 L, 5 L and 50 L of C_6H_6 deposited on CH_3OH (200 L). Scaled CH_3OH TPD traces (in thick lines) underlying 1 L, 5 L and 50 L of C_6H_6 .

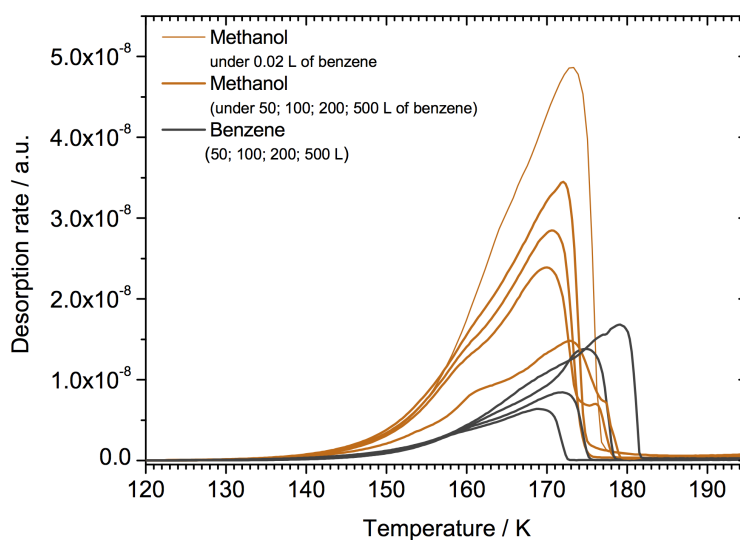


Figure 4.9: TPD traces (in grey thick lines) of 50 L, 100 L, 200 L and 500 L of C_6H_6 deposited on CH_3OH (200 L). Methanol TPD traces (in thick orange lines) underlying 50 L, 100 L, 200 L and 500 L of C_6H_6 and CH_3OH TPD trace (in thin orange lines) underlying 0.02 L of C_6H_6 .

in the methanol dose, but the displayed differences are beyond that experimental error. For instance, in **Figure 4.8** TPD traces of 1 L, 5 L and 50 L of C_6H_6 are reported along the corresponding CH_3OH curves, which were conveniently scaled by a factor of 5 in its intensity. Increasing the C_6H_6 coverage from 1 L to 5 L, and then to 50 L strongly affects the underlayer, delaying its desorption, as the shift in the traces clearly shows. Furthermore, the overall intensity is significantly decreased, meaning that CH_3OH loss occurs during C_6H_6 dosing. This is even more striking when larger C_6H_6 exposures are considered (**Figure 4.9**). In the latter plot, while C_6H_6 traces (in thick grey lines) increase in area

in the series: 50 L, 100 L, 200 L and 500 L, the relative unscaled CH₃OH curves (in thick orange lines) decrease drastically. This change is striking in the TPDs when depositing 500 L of C₆H₆ compared to a 0.02 L dose (thin orange line). Methanol displacement results in an obvious change of the thickness, likely morphology, and thus desorption kinetics, of the CH₃OH underlayer which is not the same for TPDs at different C₆H₆ exposures, especially above 1 L. Therefore the desorption profiles shift and change in shape even when coincident leading edges should be observed for multilayer growth. Under these circumstances, *LEA* could not be applied to experimentally determine the desorption order and energy of bulk C₆H₆ on CH₃OH as has been done for bulk C₆H₆ on steel, SiO₂ and ASW in previous works [12]. Nor a simple two-step *CKS* model could be used to simulate the experiments as this would be an oversimplification of the physics within the C₆H₆/CH₃OH desorption, since the kinetics of the interplay between underlayer and overlayer are yet to be fully comprehended. Throrer, using the same experimental set-up, found that the energy of bulk C₆H₆ desorption on stainless steel and SiO₂ is *ca.* 48 kJ mol⁻¹ and 45.8 kJ mol⁻¹ on compact amorphous solid water. It is sensible to look at these values as indicative of the energetics for C₆H₆ multilayer regardless the underlayer, even an hypothetical situation where CH₃OH and C₆H₆ would not mix and CH₃OH coverage would stay constant.

In order to properly quantify the loss of CH₃OH while filling the chamber with C₆H₆ for background dosing the following relationship should be considered:

$$A_{200L} : d_{200L} = A_{aL} : d_{aL} = A_{bL} : d_{bL} = \dots = A_{zL} : d_{zL} \quad (4.1)$$

$$A_{200L} : d_{200L} = \frac{1}{\kappa} A_{200L}^{Bz} : d_{200L}^{Bz} \quad (4.2)$$

where d_{200L} (as $d_{aL} \dots d_{zL}$) and A_{200L} (as $A_{aL} \dots A_{zL}$) are the area under the QMS signal for $m/z = 31$ during the dose and TPD of 200 L (a L, ... z L) CH₃OH respectively. Their ratio is the fraction of molecules that is adsorbed onto the surface during the background dosing and should be roughly constant regardless the exposure provided that the QMS signal is stable over time. The superscript *Bz* indicates that the trace was recorded prior to the C₆H₆ dose or during the TPD experiment, A_{200L}^{Bz} , d_{200L}^{Bz} . κ is a coefficient that quantifies the loss of CH₃OH. Therefore any deviation from ideality will be a number between 0 and 1 for complete loss and no loss of CH₃OH respectively. The error can be propagated by the error on the dose, $E_{d_{200L}}$ and the error on the TPD area, $E_{A_{200L}}$. They were both estimated by comparing the values of two doses and TPDs of 200 L of pure CH₃OH. Then the maximum absolute error was evaluated

for κ as follows:

$$E_{\kappa} \propto E_{d_{200L}} + E_{A_{200L}} \quad (4.3)$$

$$E_{\kappa} = E_{d_{200L}} \left(\frac{A_{200L}^{Bz}}{(A_{200L})^2} \frac{d_{200L}}{d_{200L}^{Bz}} \right) + E_{A_{200L}} \left(\frac{A_{200L}^{Bz}}{A_{200L}} \right)$$

The resulting plot of κ as a function of the C_6H_6 exposure is reported in **Figure 4.10**. The error bars are large, but it should be stressed that this is the maximum absolute error possible known *a priori*. The actual error could be less. Nevertheless, the general trend is obvious: when 500 L of C_6H_6 are dosed almost half of the CH_3OH underlayer is lost. This sets a 1 : 5 ratio as upper limit for CH_3OH displacement by C_6H_6 .

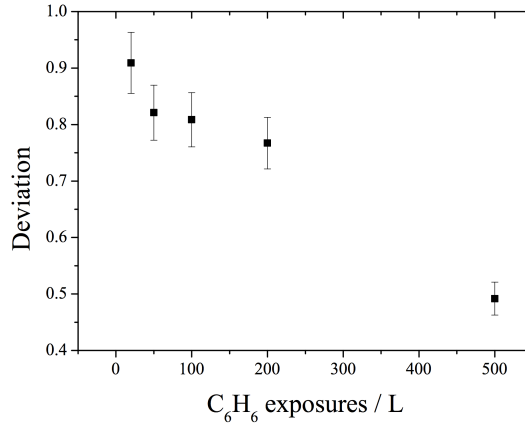


Figure 4.10: Deviation from ideality for the CH_3OH TPD traces underlying 20 L, 50 L, 100 L, 200 L and 500 L of C_6H_6 as function of C_6H_6 exposures.

Additional experiments are needed to fully comprehend the mechanism responsible of the observed CH_3OH displacement. However, it is possible to give a crude interpretation of these results. The desorption energy of bulk CH_3OH is *ca.* 42 kJ mol⁻¹ (45.4 ± 1 kJ mol⁻¹ [14]), and this needs to be balanced by another energy term. From the TPD data, C_6H_6 is found to be capable of establishing strong interactions with CH_3OH at around 41.8 ± 0.6 kJ mol⁻¹. The difference between a favourable C_6H_6 accommodation and CH_3OH displacement is around 3.6 ± 1 kJ mol⁻¹. Furthermore, it should be noted that in the experimental conditions C_6H_6 is dosed at room temperature backfilling the chamber with molecules which display a Maxwell-Boltzmann distribution of the *speed* (see **Figure 4.11**). The most probable speed, v_p and the average speed \bar{v} are:

$$v_p = \sqrt{\frac{2RT}{M}} \quad \bar{v} = \sqrt{\frac{8RT}{\pi M}} \quad (4.4)$$

where M is the molar mass and R is the gas constant. Since v_p is 79.7 m s⁻¹ and

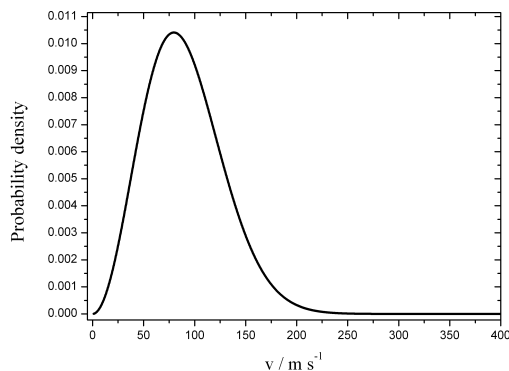


Figure 4.11: *Maxwell-Boltzmann speed distribution for C_6H_6 during background dosing.*

\bar{v} equals to 89.9 m s^{-1} , the kinetic energy, E_p and \bar{E} will be 2.5 kJ mol^{-1} and 3.2 kJ mol^{-1} respectively. The fraction of molecules that has a speed v larger than v_p is 64%, and larger than \bar{v} is 47% and could, in principle, be capable of displacing a CH_3OH molecule during the collision, momentum transfer, and after by heat release accommodating at the surface. 200 L of CH_3OH corresponds to $2.9 \times 10^{16} \text{ molecule cm}^{-2}$ and, in a similar fashion 500 L of C_6H_6 corresponds to $1.45 \times 10^{16} \text{ molecule cm}^{-2}$. Assuming a unit sticking coefficient and ionisation coefficient to be 6.0 [15], by multiplying the value found for C_6H_6 with the fractions above an upper limit for the number of C_6H_6 molecules capable of displacing CH_3OH is obtained. A 1:3 ratio is found when v_p is assumed to be the minimum speed required and a ratio between 1:4 and 1:5 is found when \bar{v} is taken into account. Both cases are bigger than what is found experimentally since the estimation above assumes that every energetic C_6H_6 colliding with CH_3OH successfully displaces it. This is not the case, since C_6H_6 is also very likely to collide with C_6H_6 itself at these exposures. Furthermore, the activation energy is generally higher than what is calculated as differences of the energy terms between the initial and final thermodynamic states. These findings should not be considered as exhaustive to the understanding of the phenomenon, which requires additional experiments to be further investigated.

4.3.2 RAIRS of Benzene on Methanol

RAIRS experiments of C_6H_6 adsorbed on CH_3OH were performed in order to gain a further insight about the C_6H_6/CH_3OH interactions. Coverage dependent spectra probe the change of the C_6H_6 binding to the chemical surrounding environment by looking at the evolution of vibrational modes going from the monolayer to the multilayer. As these data are acquired isothermally at base temperature bulk mixing of adsorbates and underlayer is not likely to occur while CH_3OH displacement during C_6H_6 dosing and change of the ice morphology does take place as for TPD experiments. The multilayer spectrum of C_6H_6 (200 L, ~ 7 nm) on

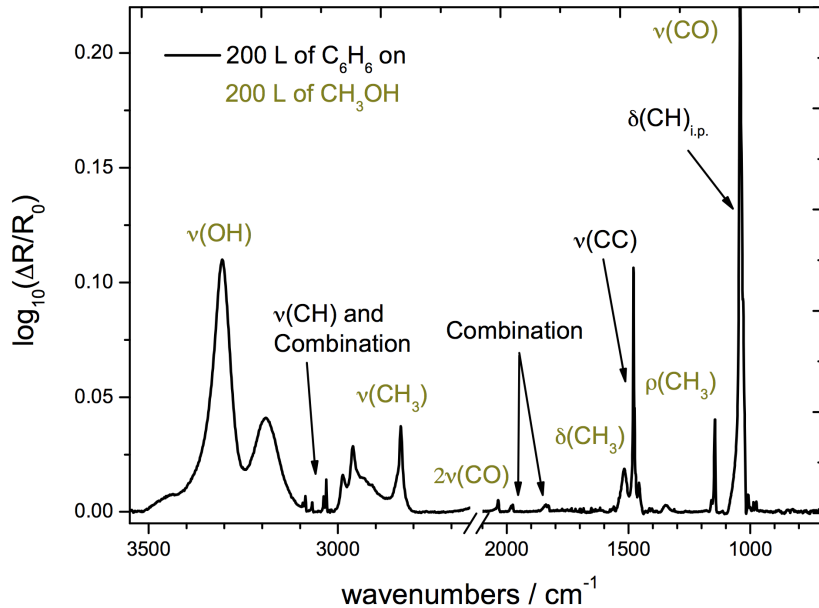


Figure 4.12: RAIR spectrum of the multilayer C_6H_6 on thick CH_3OH film (200 L; ~ 15.2 nm) at ~ 110 K. C_6H_6 vibrations are labelled in black and CH_3OH normal modes are labelled in dark yellow. Background subtraction was done using the RAIR spectrum of the substrate prior to CH_3OH deposition.

nominally 200 L of CH_3OH (**Figure 4.12**), was used as reference for the normal modes assignment as to compare band positions to existing literature values (**Table 4.1**). The agreement with previously reported values is good, with small shifts of 2 - 3 cm^{-1} , confirming that at these exposures bulk C_6H_6 is observed. These changes in the peak positions can be easily explained in terms of experimental error (resolution of 2 cm^{-1}), different film thicknesses, and techniques. For instance in the reference [12], assignment was made on 20 L of C_6H_6 on SiO_2 , thus an order of magnitude less than in this work, and transmission IR instead of RAIRS is used for the results reported in reference [16]. Additional features observed at high frequencies above 3000 cm^{-1} could arise from bulk behaviour of crystalline C_6H_6 . It is rather noticeable that there is a change in shape of the OH stretching mode along with the appearance of the CH_3OH CO stretching over-

tone around 2034 cm^{-1} . This phenomenon, as will be explained in this section, depends on CH_3OH phase change induced by C_6H_6 dosing.

Assignment	IR Frequencies / cm^{-1}			
	on CH_3OH	on SiO_2 [12]	on $\text{Si}(111)$ [16]	on Al [17]
$\delta(\text{CH})_{o.p.}$	689	690	688	678
$\delta(\text{CH})_{i.p.}$	1040 [†]	1037	1040	1038
$\nu(\text{CC})$	1479	1477	1480	1481
Combination 4	1837	1832	1836	1812
Combination 3	1977	1973	1980	1957
Combination 2	3030 3037	3027	3036	3043
Combination 1	3067	3065		3075
$\nu(\text{CH})$	3085 3092	3082	3088	3095

Table 4.1: List of vibrational modes of C_6H_6 multilayer adsorbed on amorphous CH_3OH at 110 K. The superscript [†] indicates that frequency assignment was obtained by the RAIR spectrum subtracted with the CH_3OH single beam.

It is desirable to investigate any change of the benzene modes as coverage is increased on the CH_3OH film as a reflection of the variation of the surrounding chemical environment of the C_6H_6 molecules. In order to have an idea of the average thickness of the overlayer, for each C_6H_6 exposure (**Table 4.2**), an estimate can be made in a similar fashion as done for CH_3OH and $(\text{CH}_3\text{CH}_2)_2\text{O}$ on amorphous SiO_2 : the number of adsorbed molecules per unit of surface can be calculated from the incident experimental flux multiplied by the time of dosing and assuming sticking coefficient to be unitary. Then the result is divided by the molecular density ($8.57 \times 10^{21}\text{ molecule cm}^{-3}$) of solid C_6H_6 , which was obtained by neutron powder diffraction experiments data [18]. Coverage dependent RAIR spectra are shown in **Figure 4.13**, while in **Figure 4.14** the focus is brought exclusively onto the low exposures. These spectra were subtracted with respect to the underlying CH_3OH background as to highlight the C_6H_6 vibrational modes;

Coverage / L	θ / molec. cm ⁻²	d / Å	Coverage / L	θ / molec. cm ⁻²	d / Å
0.1	2.9×10^{13}	0.03	10	2.9×10^{14}	3.5
0.2	5.8×10^{13}	0.07	20	5.8×10^{14}	7
0.5	1.4×10^{13}	0.17	50	1.4×10^{15}	17.5
1	2.9×10^{13}	0.35	100	2.9×10^{15}	35
2	5.8×10^{13}	0.7	200	5.8×10^{15}	70
5	1.4×10^{14}	1.7	500	1.4×10^{16}	175

Table 4.2: Table listing the estimated number of adsorbed C_6H_6 molecules on a thick CH_3OH ice. C_6H_6 film thickness for each exposure is also reported. Note that for the lowest coverages the monolayer is not yet complete yet and the thickness reported should be regarded as average.

in fact, being highly symmetric, C_6H_6 is significantly less IR active than H_2O , CH_3OH or $(CH_3CH_2)_2O$. In **Figure 4.13** all the assigned peaks are visible at 20 L, and grow in intensity as more molecules are dosed consistent with a gradual bulk accretion, with no shifts in maximum positions. The out-of-plane bend, combination bands and CH stretches are rather sharp suggesting the crystalline form for the deposited film. The in-plane bending mode and the CC aromatic stretch mode span over a wider range of wavenumbers with a clearly discernible low frequency shoulder. This broad distribution can be observed already within the monolayer regime and below, for exposures as low as 0.2 L - 0.5 L as displayed in **Figure 4.14**. These results are interesting because both $\nu(CC)$ and $\delta(CH)_{i.p.}$ are not just more intense than other IR C_6H_6 modes, but also particularly sensitive to any variation within the aromaticity of the ring structure. The latter is strongly perturbed when a gas phase C_6H_6 molecule binds with another molecule, therefore the broad band at low coverages RAIR spectra suggests the existence of multiple chemical environments, and hence possible interactions. The observed predominance of some frequencies and sharper features when the bulk accrues can be explained in terms of less variegated surrounding as the crystalline multilayer C_6H_6 takes form. These findings are consistent with the TPD results, where in a sub-monolayer regime, C_6H_6 seem to either bind to other C_6H_6 molecule weakly adsorbed or interacts strongly with the CH_3OH ice.

Despite background subtraction, features of underlayer CH_3OH are visible and

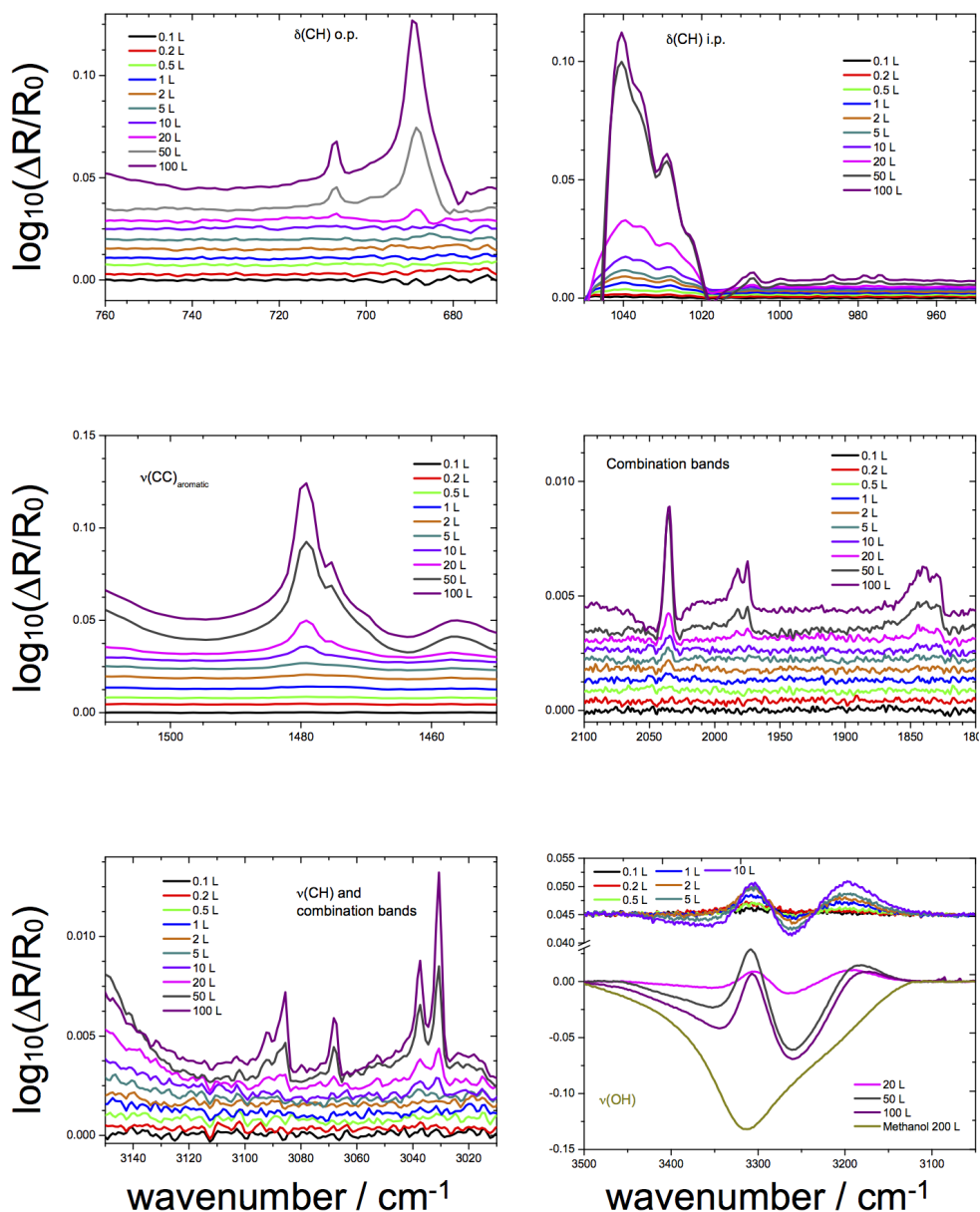


Figure 4.13: RAIR spectra of C_6H_6 on thick CH_3OH film (200 L) at increasing coverages. In the lower left panel the exposures from 0.1 L to 10 L have been offset for clarity. The reversed spectrum of pure CH_3OH in the same region is also labelled and reported in dark yellow for comparison.

evolve in intensity and shape as C_6H_6 is deposited. The CO stretch overtone appears as a sharp peak at 2034 cm^{-1} (**Figure 4.15**) around 0.5 - 1 L and gradually increases in intensity, with no shifts up to the highest exposures. From TPD data, it is clear that C_6H_6 displaces CH_3OH during background dosing, thus a negative feature would be expected, however in this case an increase is observed instead. In order to explain it, TP-RAIRS spectra of pure CH_3OH (200 L) in the frequency region of interest is reported on the left of **Figure 4.15**. The temperature was increased from base conditions at a certain temperature,

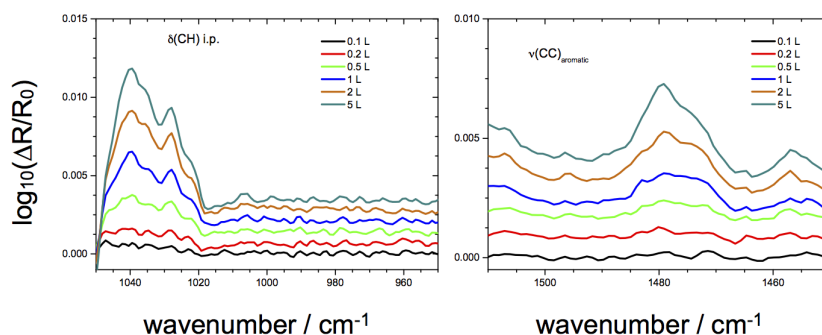


Figure 4.14: RAIR spectrum of C_6H_6 on thick CH_3OH film (200 L) at increasing coverages up to 5 L.

T_i , within a range, ΔT , of 45 K, and with a step of 5 K. The CH_3OH film was then annealed for 100 seconds and subsequently let to cool down to base, when the spectrum was acquired. This series of data display the same trend for the CO overtone observed when C_6H_6 is deposited, meaning that background dosing of C_6H_6 does not just displace CH_3OH molecules, but it also induces crystallisation within the underlayer. This conclusion is confirmed by the analysis of the OH band between $3100 - 3500 \text{ cm}^{-1}$ in **Figure 4.13**. As C_6H_6 accrues on the CH_3OH film, the OH stretching mode emerges from the background subtraction with two peaks around 3182 cm^{-1} and 3308 cm^{-1} , while it displays negative features around 3250 cm^{-1} and 3350 cm^{-1} . In **Figure 4.16**, when the RAIR spectrum of 200 L of C_6H_6 on CH_3OH (black line) subtracted to the substrate background, is compared to the plain spectrum of CH_3OH (black circles) prior to C_6H_6 exposure, the OH band area is clearly reduced and the shape changes with a similar pattern described above. The TP-RAIR spectra of pure CH_3OH (in shades of dark yellow) unambiguously assign the nature of this change as crystallisation, since the broad distribution of the OH band narrows down to two more intense peaks centred at 3306 cm^{-1} and 3203 cm^{-1} .

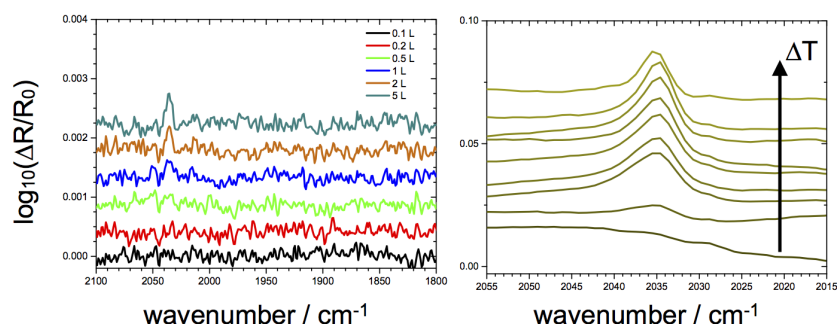


Figure 4.15: Left side: RAIR spectrum of C_6H_6 on thick CH_3OH film (200 L) at increasing coverages up to 5 L. Right side: TP-RAIR spectra of pure CH_3OH in the same frequency range, reporting spectral evolution as the film is annealed for 100 s at $T_{base} + 5 \text{ K}$, $T_{base} + 10 \text{ K}$, $T_{base} + 15 \text{ K} \dots T_{base} + 45 \text{ K}$.

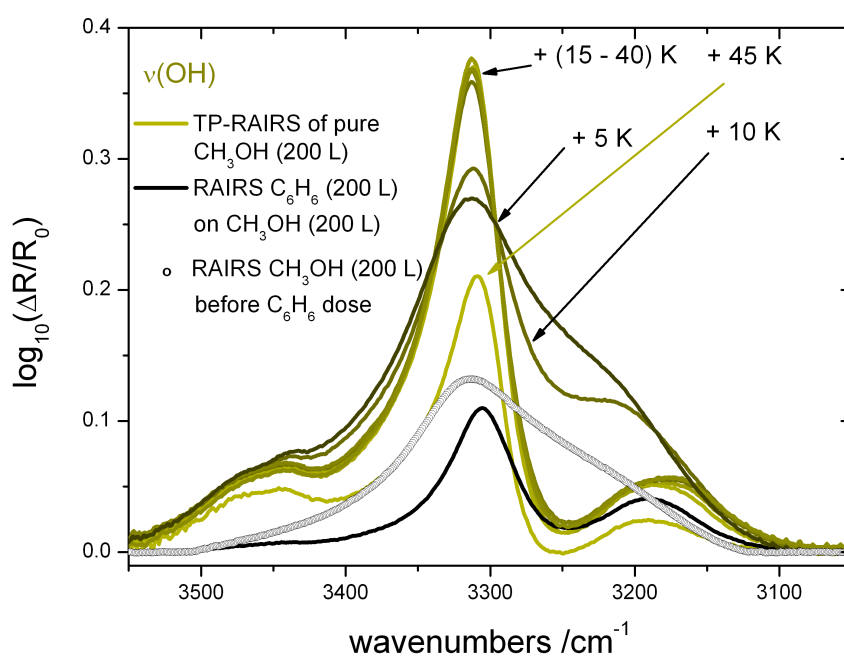


Figure 4.16: RAIR spectra of pure CH_3OH (200 L) and C_6H_6 on CH_3OH (both at 200 L) are reported in black open circles and black line respectively in the $3000 - 3500 \text{ cm}^{-1}$ region. The change in the OH band is compatible with crystallisation observed in the TP-RAIR spectra of pure CH_3OH reported with shades of dark yellow for consistency with figures 4.1 and 4.12.

4.4 Benzene on Diethyl Ether

TPD and RAIRS experiments of C_6H_6 on $(CH_3CH_2)_2O$ were performed to examine the nature of the binding between C_6H_6 and an ice with no hydrogen bonded network as reference for future irradiation experiments. The $(CH_3CH_2)_2O$ film is obtained by backfilling the chamber with $(CH_3CH_2)_2O$ at 200 L as exposure. As for CH_3OH , deposition was performed directly on steel which has the advantage of adsorbing $(CH_3CH_2)_2O$ with negligible loss during dosing at 107 K. The resulting film (**Figure 4.17**) was fully characterised by means of RAIR spectroscopy which showed it to be in the crystalline form and consistent with the results acquired with the Ice Rig. Small observed shifts, slightly larger than instrumental resolution, were attributed to a higher degree of crystallinity in thicker films at parity of exposures between the two sets. Better S/N ratio, thanks to cleaner background,

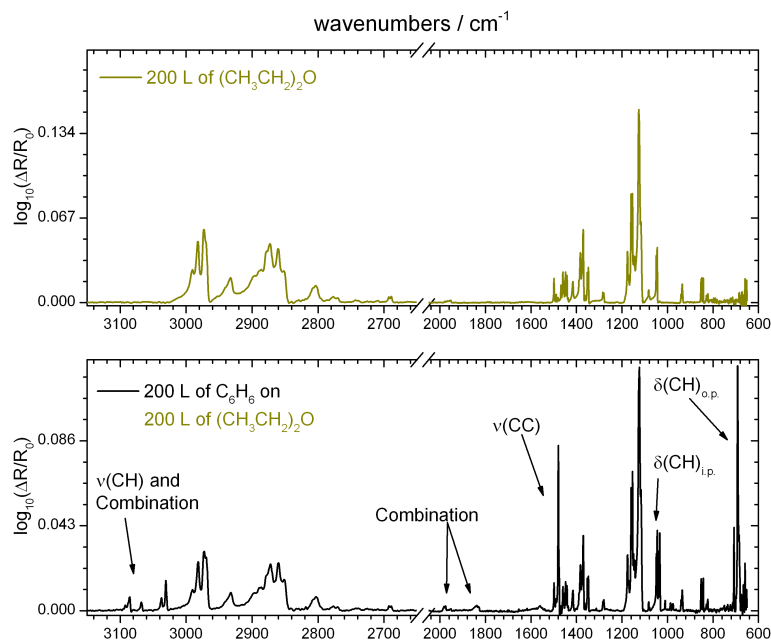


Figure 4.17: Upper panel RAIR spectrum of the multilayer $(CH_3CH_2)_2O$ film (200 L, ~ 12.1 nm) grown on stainless steel in the Beam Rig for the C_6H_6 experiments. Lower panel RAIR spectrum of 200 L of C_6H_6 deposited on 200 L of $(CH_3CH_2)_2O$. C_6H_6 vibrations are labelled in black. Note that the S/N ratio is low around 600 cm^{-1} due to the MCT detector cut-off.

has also permitted the identification of the methyl and methylene bending modes in the 1350 cm^{-1} - 1500 cm^{-1} range (**Table 4.3**). The most intense feature is the CO stretching mode at 1115 cm^{-1} , whereas in the previous chapter the CH_3 and CH_2 stretches displayed highest peak signals in the whole spectrum. This has certainly analogies with what was said about CH_3OH in the previous section: the inconsistency can be explained in terms of different experimental geometry

between the two rigs and more straightforward effect of the metal selection rule when the substrate is the stainless steel disk instead of SiO₂ on copper.

Assignment	IR Frequencies / cm ⁻¹		
	This work	Ru(0001) [19]	Cu(111) [20]
$\rho(\text{CH}_3 + \text{CH}_2)$	822	827	830
	828		
$\nu_s(\text{COC}) [\nu\text{CC}]$	843	849	848
	849		
	851		
$\nu(\text{CC} + \text{CO}) + \rho(\text{CH}_3)$	932	935	937
	940		
$2\rho(\text{CH}_3) + \nu(\text{CC})$	1045	1048	1046
	1048		
$\nu_a(\text{COC}) [\nu\text{CO}]$	1115	1120	1122
	1126		
$\rho(\text{CH}_3) + \nu(\text{CO})$	1153	1159	1159
+ $\nu(\text{CC})$ + bends	1159		
$\rho(\text{CH}_2 + \text{CH}_3)$	1170	1176	1178
	1175		
$\rho(\text{CH}_2)$ twist	1279	1283	1285
	1283		
$\delta_s(\text{CH}_3) + \delta(\text{CH}_2)_{o,p}$	1348	1346	1350
	1352		
$\delta_s(\text{CH}_3)$	1369	1370	1372
	1373		
$\delta_a(\text{CH}_3) + \delta(\text{CH}_2)_{o,p}$	1381	1382	1385
	1388		
$\delta_a(\text{CH}_3)_{o,p}$	1441	1441	1442
	1447		
$\delta_a(\text{CH}_3)_{i,p}$	1456		1459
	1459	1458	
	1468	1468	
$\delta_a(\text{CH}_2)$ scissoring	1498	1489	1491
$\nu_s(\text{CH}_3) + \nu_s(\text{CH}_2)$	2851, 2860	2856	
+ $2 \times \delta(\text{CH}_3)$	2873	2872	2875
	2886, 2896	2900	
$\nu_a(\text{CH}_2)$	2932	2932	2934
$\nu_a(\text{CH}_3)$	2972 (2803)	2970	2971
	2982 (2777)	2987	2992
	2990 (2689, 2693)		

Table 4.3: List of vibrational modes of 200 L of $(\text{CH}_3\text{CH}_2)_2\text{O}$ multilayer adsorbed on steel at 107 K.

4.4.1 TPD of Benzene on Diethyl Ether

Diethyl ether is significantly more volatile than C_6H_6 , therefore when performing TPD experiments of C_6H_6 on thick film of $(CH_3CH_2)_2O$ (200 L, 12.1 nm) it is not surprising to observe co-desorption of C_6H_6 with the underlayer ice. As the C_6H_6 exposure is increased, a new feature of C_6H_6 on steel appears. **Figure 4.18** meets these expectations. Superimposing the scaled $(CH_3CH_2)_2O$ TPD trace to

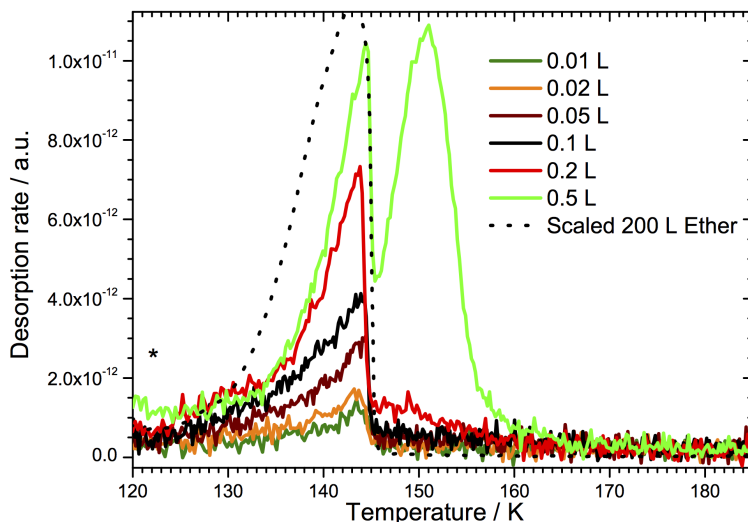


Figure 4.18: TPD traces of 0.01 L, 0.02 L, 0.05 L, 0.1 L, 0.2 L and 0.5 L of C_6H_6 deposited on a thick $(CH_3CH_2)_2O$ film (200 L; ~ 12.1 nm). The dotted line is the scaled $(CH_3CH_2)_2O$ TPD trace underlying 0.05 L of C_6H_6 .

the C_6H_6 curves allows, unambiguous assignment of the first peak in the series to co-desorption. During the heating ramp, the $(CH_3CH_2)_2O$ underlayer sublimates carrying C_6H_6 molecules with it; then, as soon as all the $(CH_3CH_2)_2O$ has been pumped away, the C_6H_6 signal suddenly drops to rise again when desorption occurs at higher temperatures and coverages. Unfortunately, these data cannot be analysed either quantitatively or semi-quantitatively because the peak shape depends entirely on the mixing of the two adsorbates during $(CH_3CH_2)_2O$ desorption and because the higher temperature peak involves solely C_6H_6 and the steel disk. However, the question whether C_6H_6 wets the $(CH_3CH_2)_2O$ surface or prefers to form islands can still be assessed by an additional set of experiments.

This consist of depositing $(CH_3CH_2)_2O$ at sub-monolayer coverages on thick icy film of C_6H_6 . If the free energy for adsorption for this experiment changes with the coverage, in the same way as $\Delta_{ads}G$ of C_6H_6 on $(CH_3CH_2)_2O$ varies with the C_6H_6 coverage, then the kinetics of an hypothetical TPD experiment of C_6H_6 adsorbed

on a non-volatile $(\text{CH}_3\text{CH}_2)_2\text{O}$ could be identified at least on a qualitative level. The left panel in **Figure 4.19** displays the raw TPD traces for $(\text{CH}_3\text{CH}_2)_2\text{O}$ (0.05 L, 0.1 L, 0.2 L, 0.5 L, and 1 L) on C_6H_6 (200 L, 7 nm). The heating ramp is of $0.8 \pm 0.04 \text{ K s}^{-1}$. The first spike is simply $(\text{CH}_3\text{CH}_2)_2\text{O}$ desorbing from the heating

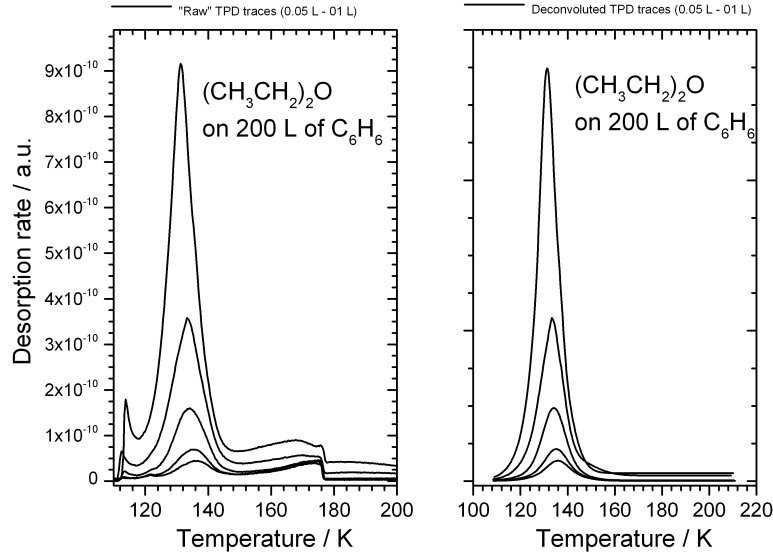


Figure 4.19: TPD traces of 0.05 L, 0.1 L, 0.2 L, 0.5 L, and 1 L of $(\text{CH}_3\text{CH}_2)_2\text{O}$ deposited on thick C_6H_6 film (200 L, ~ 7 nm). The left panel displays the raw TPD traces with $(\text{CH}_3\text{CH}_2)_2\text{O}$ desorption occurring from wires holding the sample, from the C_6H_6 ice, and co-desorption of $(\text{CH}_3\text{CH}_2)_2\text{O}$ mixed with C_6H_6 . The right panel shows the deconvoluted TPD traces of $(\text{CH}_3\text{CH}_2)_2\text{O}$ desorbing from the C_6H_6 ice. Details in the text.

wires, the second and main peak is $(\text{CH}_3\text{CH}_2)_2\text{O}$ desorbing from C_6H_6 , followed by a third complex and broad feature of $(\text{CH}_3\text{CH}_2)_2\text{O}$ co-desorbing with the underlayer ice. The latter likely arises from the two species mixing as the temperature is increased suggesting a favourable solubility of $(\text{CH}_3\text{CH}_2)_2\text{O}$ in solid C_6H_6 . The main peak below 140 K is most informative about the $(\text{CH}_3\text{CH}_2)_2\text{O}/\text{C}_6\text{H}_6$ interaction at the interface. In order to isolate this feature, each curve was subtracted from the wires contribution in the same manner as illustrated for C_6H_6 on CH_3OH . The resulting function was fitted with a convenient number of Gaussians in order to accurately reproduce the overall trace. The cumulative fitting peak reproducing the desorption of $(\text{CH}_3\text{CH}_2)_2\text{O}$ from C_6H_6 are plotted in the right panel of **Figure 4.19**. Despite the good agreement with the experimental traces, it can be inferred that such a large number of manipulations will affect any quantitative analysis. The results show desorption kinetics that look like a second-order due to a distribution of binding energies; this clearly points to $(\text{CH}_3\text{CH}_2)_2\text{O}$ wetting the C_6H_6 surface. Furthermore, the deconvoluted peaks were also used to give a semi-quantitative estimate for E_d as a function of the surface coverage using

the inversion technique previously adopted in the third chapter. The resulting curves are shown in **Figure 4.20**. The unusual behaviour at low coverages for the curves of 0.5 L and 1 L of $(\text{CH}_3\text{CH}_2)_2\text{O}$ with respect to the remaining functions can be attributed to (i) poor quality fit of the trailing edge in the TPD peaks as well as (ii) complications arising from the mixing. Likely, it was also not possible to satisfactorily reproduce the experimental curves using the desorption energy curves for the same reasons. Nevertheless, all the curves point to a plateau of *circa* $35.5 \pm 1.0 \text{ kJ mol}^{-1}$, which nicely matches the E_d values found for the second layer of $(\text{CH}_3\text{CH}_2)_2\text{O}$ on SiO_2 . It can be concluded that the C_6H_6 interface behaves as a surrogate of $(\text{CH}_3\text{CH}_2)_2\text{O}$ first layer to the adsorbate. If that is the case the energetics is similar if not identical to the second layer of C_6H_6 on $(\text{CH}_3\text{CH}_2)_2\text{O}$. All these results strongly suggest that $(\text{CH}_3\text{CH}_2)_2\text{O}$ and C_6H_6 , not surprisingly, are very much alike, thus easily mix, and the binary layered system accrues, piling up continuously and uniformly in a layer-by-layer fashion.

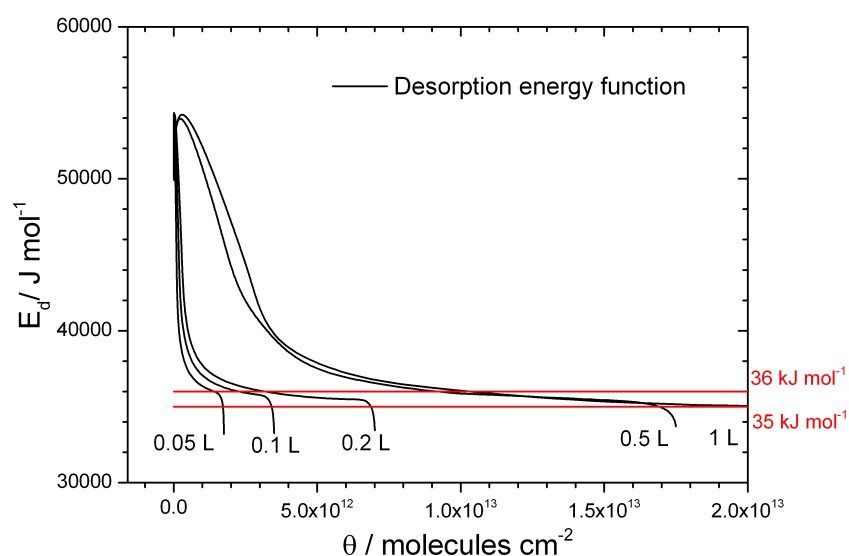


Figure 4.20: E_d as a function of surface concentration derived through inversion of the Polanyi-Wigner equation from the $(\text{CH}_3\text{CH}_2)_2\text{O}$ TPD traces on 200 L of C_6H_6 . $(\text{CH}_3\text{CH}_2)_2\text{O}$ exposures are: at 0.05 L, 0.1 L, 0.2 L, 0.5 L, and 1 L.

4.4.2 RAIRS of Benzene on Diethyl Ether

Reflection-absorption infrared spectroscopy has been used to directly probe the C_6H_6 film growth on crystalline $(CH_3CH_2)_2O$ at base temperature. The multilayer resulting from depositing 200 L of C_6H_6 on equivalent exposure of $(CH_3CH_2)_2O$ is displayed in the lower panel in **Figure 4.17**. Not surprisingly, all the maxima of peak frequencies are fully consistent with the analogous C_6H_6 film grown on CH_3OH (see **Figure 4.12** and **Table 4.1** for assignment) and any apparent deviation of 1 cm^{-1} lies within the instrumental resolution limit (2 cm^{-1}).

Figure 4.21 shows the evolution of C_6H_6 vibrational modes with increasing exposure on $(CH_3CH_2)_2O$. All IR features increase in intensity as the C_6H_6 accrues and without the slightest change in the maxima position, in perfect agreement with the gradual build up of a multilayer film. All the main bands appear between 5 L and 20 L with the only exception of the CC aromatic stretching mode that is visible at 0.5 L. It is noticeable that the latter normal mode has a narrow lineshape, within the $1473 - 1481\text{ cm}^{-1}$ range. Starting from the lowest exposures up to the highest, a sharp peak at 1479 cm^{-1} with a shoulder at 1475 cm^{-1} , clearly grows from the background from 1 L. In contrast to C_6H_6 on CH_3OH , this band spans over a wider range of wavenumbers ($1466 - 1485\text{ cm}^{-1}$) in the 0.5 - 5 L range, and only above 5 L the shape matches both the binary layered systems C_6H_6/CH_3OH and $C_6H_6/(CH_3CH_2)_2O$. This result agrees nicely with the TPD analysis in the previous paragraphs: C_6H_6 wets $(CH_3CH_2)_2O$, while islanding is observed on CH_3OH , with fewer strong interactions at lower exposures that are enhanced by the mixing of the two species during heating. Therefore, C_6H_6 grows uniformly on top of $(CH_3CH_2)_2O$, when moving from the interface at sub-monolayer level ($C_6H_6-(CH_3CH_2)_2O$) to bulk ($C_6H_6-C_6H_6$), and changes in the thermodynamics (E_d and multibody interaction) are not as marked as to lead to significant shifts observable in the series of RAIR spectra. When C_6H_6 is deposited on CH_3OH , it might accommodate in a favourable adsorption site, although island formation would be the main process. Thus, a broad range of interactions is likely to exist for the adsorbate at low coverages leading to broad IR signatures. Furthermore, even in the multilayer regime, the CH bends at 1039 and 690 cm^{-1} are sharper for $C_6H_6/(CH_3CH_2)_2O$ than for C_6H_6/CH_3OH . This might be linked to the different backgrounds. The underlayer crystalline $(CH_3CH_2)_2O$ has less intense IR features in those regions, so any change due to substrate from the displacement will, to a minor extent, affect the C_6H_6 RAIR spectra subtracted $(CH_3CH_2)_2O$ background. A more convincing explanation would also refer to the growth mechanism of the C_6H_6 film on the two ices. Is-

land formation on CH_3OH is compatible with a larger degree of heterogeneity of polycrystalline C_6H_6 , while the aromatic molecules grow as larger and more uniform crystallites on $(\text{CH}_3\text{CH}_2)_2\text{O}$, therefore displaying sharper peaks.

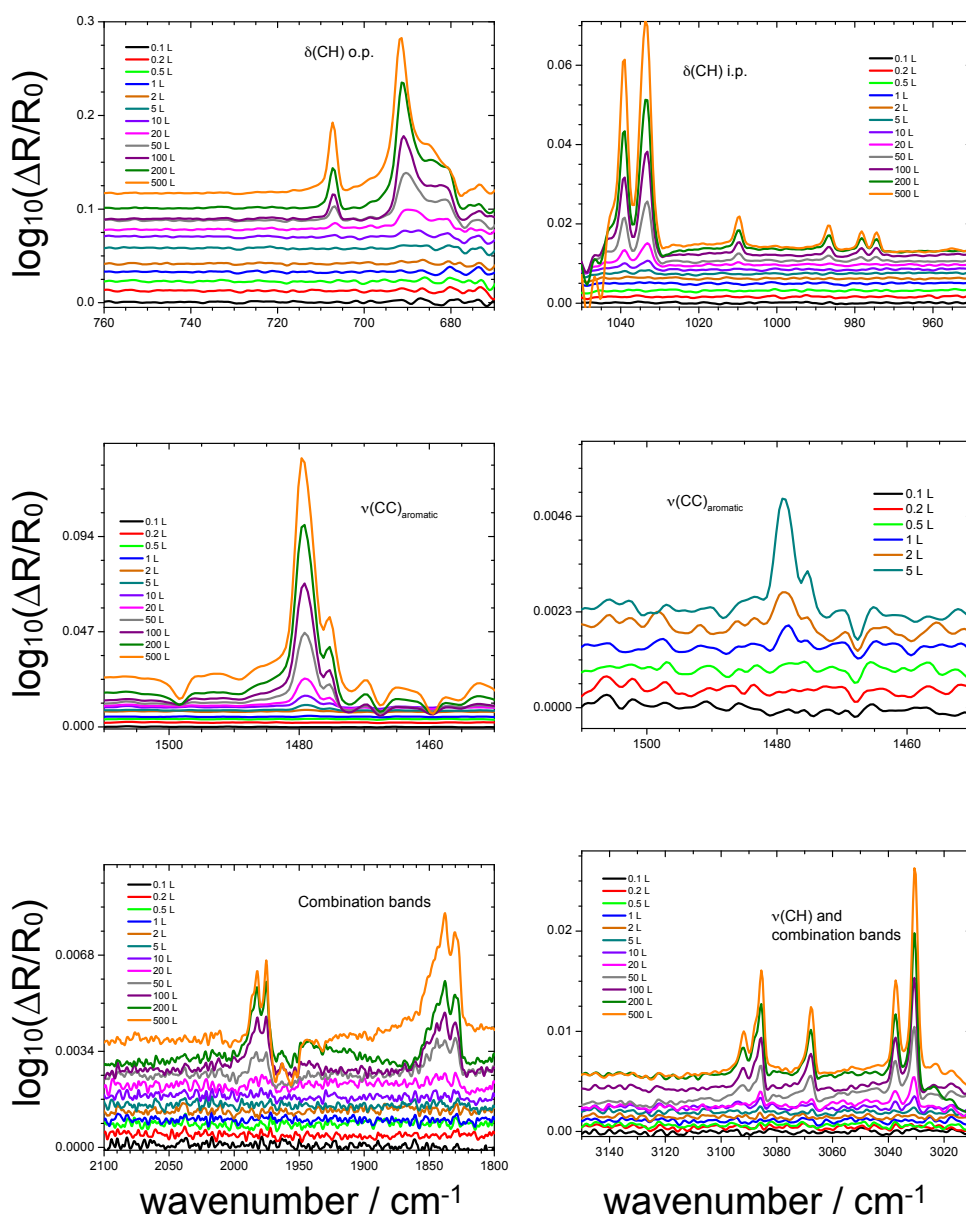


Figure 4.21: RAIR spectra of C_6H_6 on thick $(\text{CH}_3\text{CH}_2)_2\text{O}$ film (200 L) at increasing coverages. In the right central panel the lower exposures for the CC aromatic stretching mode have been highlighted for clarity.

4.5 Computational Studies on Model Systems

Model clusters of $\text{C}_6\text{H}_6\text{-H}_2\text{O}$, $\text{C}_6\text{H}_6\text{-CH}_3\text{OH}$ and $\text{C}_6\text{H}_6\text{-(CH}_3\text{CH}_2)_2\text{O}$ were investigated by means of high level QM calculations to systematically explore the fundamental interactions existing between the two species in the dimer. Previous studies have already reported the main equilibrium arrangements for C_6H_6 with n molecules of H_2O or CH_3OH [21–23]. However, the value of this analysis lies in (i) the consistency of the level of theory used for all the investigated systems, (ii) the addition of IR frequencies, not always available, and (iii) studies on C_6H_6 and $(\text{CH}_3\text{CH}_2)_2\text{O}$ clusters have not been reported so far. Furthermore, these results are the starting point and benchmark to a further ongoing study on larger clusters where C_6H_6 interacts with n molecules of H_2O , CH_3OH , or $(\text{CH}_3\text{CH}_2)_2\text{O}$. This step would more appropriately describe the binding that a single C_6H_6 molecule experiences at the interface of the different ices. Thus, the results presented in this section should not be regarded as conclusive and exhaustively complementary to the data so far reported, but rather as a consistent analysis on simple systems highlighting the dimers energetic minima and key interactions.

Computational Details

The $\text{C}_6\text{H}_6\text{-(CH}_3\text{CH}_2)_2\text{O}$ system is the most challenging dimer to describe, thus it sets the minimum level of theory that guarantees consistency, and a satisfactory accuracy to model the intermolecular interactions. The analogous dimer of C_6H_6 with the more simple dimethyl ether, CH_3OCH_3 , was successfully investigated by Amicangelo *et al.* [24] relying on geometry optimisations at MP2/aug-cc-pVDZ level, followed by a single point (SP) using an aug-cc-pVTZ basis set. Basis set superposition error (BSSE) is taken into account with a counterpoise (CP) correction in both cases. Furthermore, corrections for higher-order correlations beyond the MP2 method was considered with CCSD(T) single points. As the $\Delta\text{CCSD(T)}$ correction is somewhat insensitive to basis set size, it was approximated by the difference of the energy estimated at CCSD(T)/cc-pVDZ and MP2/cc-pVDZ levels, thus significantly reducing CPU cost. The same strategy (optimisation at MP2/aug-cc-pVDZ + single point MP2/aug-cc-pVTZ + $\Delta\text{CCSD(T)}$) was adopted in this thesis for all the dimers using Gaussian09 [25] and NSCCS resources. The harmonic IR frequencies ($\bar{\nu}$) were also calculated at MP2 level, but retaining the basis set size used for geometries would be beyond reasonable computational resources, thus a much smaller basis set, 6-31G(d,p) was used instead. This has the clear advantage of saving a lot of CPU time also allowing quick calculations on large systems, and the disadvantage that absolute frequencies of vibrational modes might differ from the experimental gas phase

values. However, a variety of chemical environments around the C_6H_6 molecule, (*e.g.* isolated C_6H_6 , C_6H_6 with CH_3OH , C_6H_6 with $(CH_3CH_2)_2O$) results in frequency shifts, $\Delta\bar{\nu}$, which should be insensitive to the basis set size and more directly relatable to experimental results so far presented.

Results and Discussion

In principle, C_6H_6 can interact with a CH_3OH molecule in several different ways: the aromatic ring can accept H-bonding from the OH end and, to a minor extent, by the methyl end; in the latter case, van der Waals forces could also play a major role; moreover the CH_3OH oxygen can accept H-bonding from the side of the C_6H_6 . Similar arrangements, exist also for the $C_6H_6-H_2O$, $C_6H_6-(CH_3CH_2)_2O$ dimers. Each of these configurations were used as starting structures for geometry optimisation. In fact, whether the aromatic ring is brought close to the methyl end of the CH_3OH molecule or when the OH hydrogen points to the centre of the aromatic ring or a carbon atom, the final optimised geometry is the same: CH_3OH hydrogen bonding to the C-C bond in the C_6H_6 ring (**Figure 4.22**). A

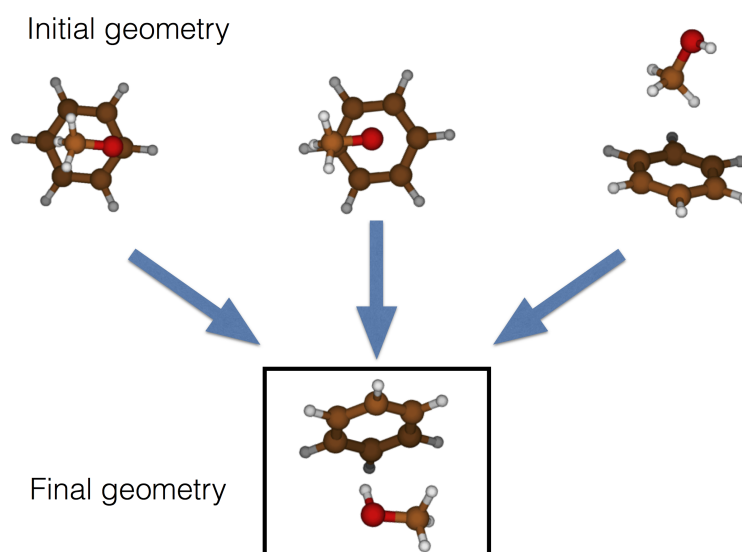


Figure 4.22: Geometry optimisation at MP2/aug-cc-pVDZ level of C_6H_6/CH_3OH dimer of different starting arrangements lead to the same minimum in the PES.

similar conclusion was found for the C_6H_6/H_2O dimer, with the difference that H_2O can orientate either one H atom to the ring edge (global minimum, 1C in **Figure 4.23**), or both the hydrogens (local minimum, 1C' in **Figure 4.23**). However, the energy difference is very small (0.2 kJ mol^{-1}) between these two structures and can be regarded as the same. In fact previous works report 1C' as the most stable [26, 27], while a detailed investigation on the change in the tilt angle, defining the directions where the two H atom points, agrees with the

results of this thesis [21]. Thus, the energy difference is so small that the H₂O molecule can in fact tilt arbitrarily as one or both of the H atoms point toward the π cloud.

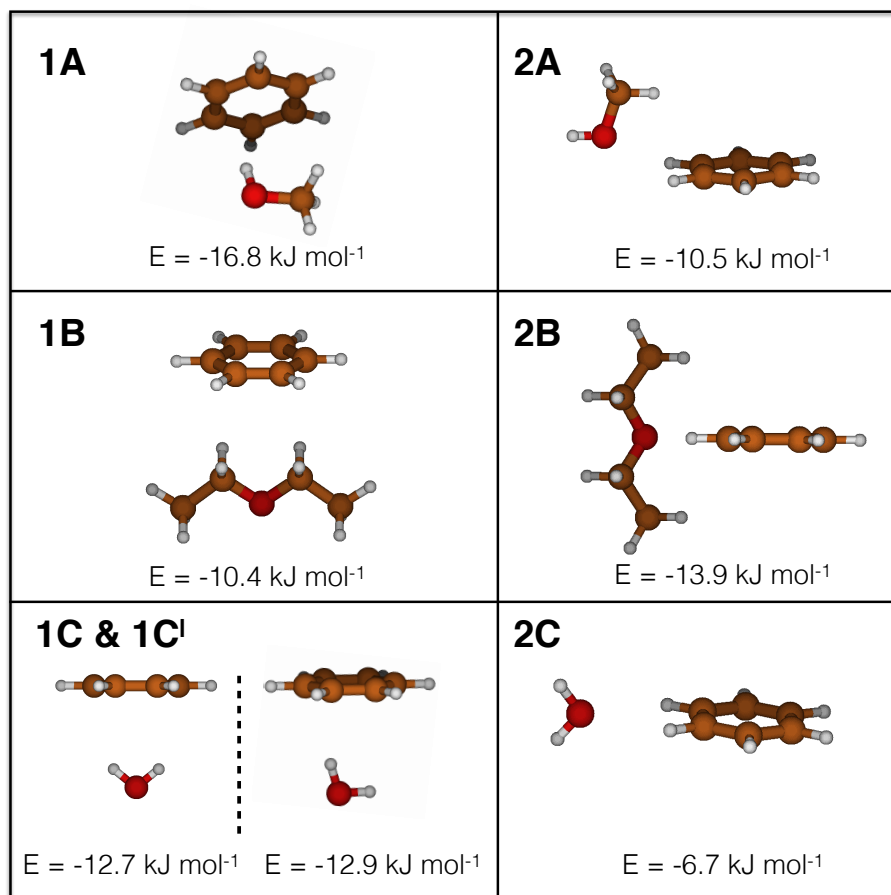


Figure 4.23: Energy minima of C_6H_6/CH_3OH and $C_6H_6/(CH_3CH_2)_2O$ dimers. Optimisations were performed at MP2/auc-cc-pVDZ level with CP corrections. The Energy reported for each dimer is estimated by a single point at MP2/aug-cc-pvTZ level and corrected using CCSD(T) calculations. Details in the text.

With the $C_6H_6-(CH_3CH_2)_2O$ dimer, it should be stressed that $(CH_3CH_2)_2O$ can lie under the C_6H_6 in two different orientations depending on the oxygen pointing away or towards the ring. Furthermore, in each of these cases the C-O bonds can align with the C-H bond of C_6H_6 (eclipsed conformer) or can be perpendicular to it (staggered). A previous work on dimethyl ether and C_6H_6 found that the difference in the binding energy between the (staggered and eclipsed orientations) is negligible, less than 0.1 kJ mol^{-1} [24]. On the other hand a drastic change is seen when the O atom is pointing away or towards the C_6H_6 , 3.6 and 9.5 kJ mol^{-1} respectively. Since $(CH_3CH_2)_2O$ is expected to interact with C_6H_6 in a similar way as its smaller analogue does, it was chosen to focus only on the more energetically stable dimer for this thesis. Two limit-cases per pair were found to be the main

minima of the potential energy surface (PES) as shown in **Figure 4.23**, while binding energy and the CC stretching values are reported in **Table 4.4** displaying a good agreement with literature. The largest difference with reported values is observed for the C₆H₆-H₂O dimer in the in-plane configuration (2C), but it can be ascribed to diversity of theoretical approaches and underestimation of DFT calculations. Nevertheless, the general trend is consistent with literature values.

Not surprisingly all these minima are stabilised by H-bond-like interactions:

- OH···π (1A, 1C, 1C'),
- CH···π (1B),
- CH···O (2A, 2B, 2C).

In the latter case, with the exception of the system containing H₂O, there might be some degree of CH-π bond and obviously London interactions as well. Therefore, the CH₃OH oxygen does not lie in the ring plane, so that the CH₃ end is brought closer to C₆H₆ ($d(\text{H}_{\text{CH}_3}\text{-C}_{\text{bz}}) = 3.0 \text{ \AA}$). This does not necessarily occur for (CH₃CH₂)₂O, where the longer aliphatic chains can reach both the two ring faces ($d(\text{H}_{\text{CH}_3}\text{-C}_{\text{bz}}) = 3.2 \text{ \AA}$). This observation is further confirmed by the fact that the O atom in the H₂O molecule (2C), even if left free to relax to the PES minimum with no symmetry constraints, retains its in-plane position with a binding energy of 6.7 kJ mol⁻¹. This value is 3.8 kJ mol⁻¹ lower than in 2A and 7.1 kJ mol⁻¹ lower than in 2B. The latter is almost twice the former difference. For comparison weak, purely dispersive interactions follow generally around 4 kJ mol⁻¹ as for dimethyl ether with the oxygen closer to the aromatic ring, suggesting that the in-plane arrangement seen for 1B and 2B, non-covalent forces further stabilise the systems. It is interesting to note that the binding energy between C₆H₆ and H₂O (1C) is almost the same as for the analogous case with (CH₃CH₂)₂O (1B), and it cannot be explained by just observing that one interaction has a stronger H-bond character than the other. If that were to be the case, then the C₆H₆/(CH₃)₂O and C₆H₆/(CH₃CH₂)₂O should have the same binding energy, but the former dimer is about 2.8 kJ mol⁻¹ less stable. Thus, dispersive forces are likely to play a role when (CH₃CH₂)₂O lies under/above the aromatic ring. More noticeable is that when CH₃OH is considered (1A), the binding energy is even higher than for the dimer with H₂O, and this hints to a combination of interactions of the type OH···π, CH···π and dispersive forces. In fact, in this case it is not just the OH to be oriented towards C₆H₆, but also the methyl end that points two H atoms towards to carbonic centres in the ring ($d(\text{H}_{\text{CH}_3}\text{-C}_{\text{bz}}) = 3.2 \text{ \AA}$) in a similar fashion as for structure 1B.

Dimer	Binding energy / kJ mol ⁻¹		E _d / kJ mol ⁻¹	Δ $\bar{\nu}_{CC}$ / cm ⁻¹		
	MP2/TZ	Corr.		Lit.	at low coverages	theory
1A	-19.18	-16.76	-18.8 [23]	(20-42) ± 2	-1.6	-2 ± 1
2A	-11.50	-10.53	-10.9 [23]		-2.6, -3.6	
1B	-12.31	-10.44		35 ± 1	-1.1	~ 0
2B	-15.52	-13.87			-3, -7.6	
1C	-14.35	-12.93	-11.58 [27], -11.97 [21]	41.0 ± 0.5	-1.4	-2 ± 1
1C'	-14.03	-12.74	-13.2 [27]		-1.3	
2C	-6.98	-6.74	-3.95 [26]		-1.6, -3.6	

Table 4.4: Binding energy calculated for the, C₆H₆/H₂O, and C₆H₆/CH₃OH and C₆H₆/(CH₃CH₂)₂O dimers at different levels of theory and vibrational shifts for the CC aromatic stretching mode with respect to the isolated C₆H₆. MP2/TZ is the BSSE corrected binding energy obtained with a single point at MP2/TZ following the optimisation with aug-cc-pVDZ basis set. Corr. is the BSSE corrected binding energy obtained adding the ΔCCSD(T) at the MP2/TZ energy. Literature values are reported when available. Experimentally determined E_d values and Δ $\bar{\nu}_{CC}$ ranges are also reported. Note that the E_d indicated for C₆H₆ on (CH₃CH₂)₂O was determined for (CH₃CH₂)₂O on C₆H₆ and does not represent the desorption energy of the inverted analogous system. It should be regarded as merely indicative. Experimental Δ $\bar{\nu}_{CC}$ were obtained by comparing the C₆H₆ bulk IR feature at ~ 1475 cm⁻¹ with the 0.1 L spectrum on CH₃OH and (CH₃CH₂)₂O in the same frequency region, and with 1 L of C₆H₆ on H₂O taken from [12].

Focusing on the IR calculations, no imaginary frequencies were found, proving that all the final geometries were not a saddle point. The CC aromatic stretching mode frequencies for each dimer were subtracted with the value calculated for the isolated C_6H_6 molecule. The results show that the largest shifts are observed for structures 2A, 2B and 2C, when the ring side interacts with the other molecule. However, no real difference emerges when moving from H_2O to $(CH_3CH_2)_2O$. In fact, in the latter case an additional peak appears with a larger bathochromic effect on the CC mode (-7.6 cm^{-1}). This is in disagreement with the experimental results where C_6H_6 displays a broader distribution of frequencies when adsorbed on CH_3OH ($1466 - 1485\text{ cm}^{-1}$) rather than on $(CH_3CH_2)_2O$ ($1473 - 1481\text{ cm}^{-1}$). **Table 4.4** presents the measured shifts in the CC aromatic stretching mode of C_6H_6 on each surface when subtracting the IR mode in multilayers of C_6H_6 to the analogous peak at low exposure (0.1 L for C_6H_6 on CH_3OH and on $(CH_3CH_2)_2O$, 1 L for C_6H_6 on H_2O [12]). The simple calculations at least confirm the shifts to be in the same direction for C_6H_6/H_2O and C_6H_6/CH_3OH as for the RAIR spectra. Although no agreement is found for the $C_6H_6/(CH_3CH_2)_2O$ structure, it could be argued that the theoretical values apply to gas phase dimers and that in the solid phase, interactions of the 1B type are preferred to those of the 2B type due to additional multi-body energy terms. Furthermore, theoretical shifts should be estimated with respect to a cluster of C_6H_6 molecules, rather than an isolated one. Further studies in this direction are ongoing.

To conclude, C_6H_6 interacts with these species with a certain degree of H bonding, with a binding energy between 16.8 and 6.7 kJ mol^{-1} which overlaps with the energies calculated for the lowest minima of the C_6H_6 dimer, 13.8 and 18.4 kJ mol^{-1} [28]. All the dimers with H_2O have a lower energy, therefore, on the basis of these model systems, that take no account of multi-body energy terms, $C_6H_6-C_6H_6$ interactions are more favourable than $H_2O-C_6H_6$ and island formation is likely to occur according to these simple systems.

The CH_3OH case is less straightforward, but there is no doubt that dimer 1A has similar energetics to the C_6H_6 dimer. The α phase of solid CH_3OH presents structure made of long chains of H-bonded CH_3OH leaving no terminal OH at the vacuum interface [29]. Therefore, a C_6H_6 molecule would initially interact in a similar fashion as for the structure 2A. In this case island formation would be the driving force during the film growth as $C_6H_6-C_6H_6$ interaction is more favourable than $C_6H_6-CH_3OH$. This is observed in the TPD traces. However, the experimental data also showed that C_6H_6 deposition is capable of displacing, and thus rearranging the underlayer ice. This would also imply a breakdown of the chain

structures in favour of equally stable interactions, such as the one indicated by 1A.

Finally, the $C_6H_6-(CH_3CH_2)_2O$ dimer (2B) has a binding energy of 13.9 kJ mol^{-1} , that is extremely close to the local minimum of $C_6H_6-C_6H_6$ (13.8 kJ mol^{-1}). Therefore, it could be inferred that C_6H_6 accrues uniformly on top of $(CH_3CH_2)_2O$ ices as TPD traces suggest.

In fact, no agreement is found between experimental desorption energies at low coverages and binding energies of dimers, neither the observed shifts in the vibrational modes are consistent with RAIR spectra (see **Table 4.4**). Of course, the energetic balance between $C_6H_6-C_6H_6$ and C_6H_6 -surface requires models with a finer level of detail, such as clusters with n molecules of CH_3OH or $(CH_3CH_2)_2O$ as to properly support or refute the experimental findings in this thesis. Nevertheless, these simple dimer-based systems were capable of outlining the key types of interactions and reproducing the experimental trend observed in the TPD for different systems. In the latter case, consistency with experimental data was obtained when comparing the dimers binding energies for C_6H_6-XOX' (where X and X' are H, CH_3 or CH_3CH_2) to the $C_6H_6-C_6H_6$ minima rather than by direct comparison with the desorption energies.

4.6 Conclusions and Comparison with ASW

In summary, C_6H_6 adsorption and accommodation on top of an icy surface comprising either CH_3OH or $(CH_3CH_2)_2O$ have been investigated. The main findings can be listed as follows:

- TPD experiments have demonstrated that C_6H_6 favours island growth on CH_3OH , with possible strong interactions of $\sim 42 \text{ kJ mol}^{-1}$ comparable to the energy of CH_3OH bulk desorption ($42 - 45 \text{ kJ mol}^{-1}$). This behaviour is likely to occur when the ordered structure of hydrogen bonded CH_3OH chains is broken. This could be the result of mixing during the temperature increase in the TPD ramp as well as subsequent C_6H_6 deposition. The latter has been observed to lead to CH_3OH displacement, as indicated by TPD data, and phase change, as shown in RAIR spectra. On the other hand, while TPD of C_6H_6 on $(CH_3CH_2)_2O$ were inconclusive, thermal desorption of $(CH_3CH_2)_2O$ from thick C_6H_6 at sub-monolayer coverages exhibited evidence of wetting of the underlayer ice. The estimated desorption energy of *ca.* 35 kJ mol^{-1} matches the E_d value found for the second layer of $(CH_3CH_2)_2O$ on SiO_2 , suggesting that C_6H_6 behaves as surrogate of the first

layer of $(\text{CH}_3\text{CH}_2)_2\text{O}$ and that the two species are very much alike. It could be inferred that C_6H_6 accrues uniformly when deposited on $(\text{CH}_3\text{CH}_2)_2\text{O}$.

- RAIR spectra have also been acquired for C_6H_6 on both CH_3OH and $(\text{CH}_3\text{CH}_2)_2\text{O}$. The multilayer data are consistent with previously reported data although a larger degree of uniformity in the crystalline phase was observed for the $\text{C}_6\text{H}_6/(\text{CH}_3\text{CH}_2)_2\text{O}$ system as result of possible layer-by-layer growth. The aromatic CC stretching mode at low coverages appears as a broader band with a lower frequency tail when the underlayer is CH_3OH rather than $(\text{CH}_3\text{CH}_2)_2\text{O}$. This might point to a wider range of interactions with the adsorbate, probably hydrogen bonds, that weaken the aromaticity and thus shift the ring modes to lower values.
- High level QM calculations on model dimers confirm the idea of weak H-bonding interactions between C_6H_6 and H_2O , C_6H_6 and CH_3OH , and C_6H_6 and $(\text{CH}_3\text{CH}_2)_2\text{O}$ in agreement with literature studies. Larger clusters of molecules have to be explored in order to provide a more appropriate comparison with experimental findings. However, these results lay a solid foundation to benchmark plane wave density functional calculations to describe realistic systems in future works.

The natural and logical conclusion of this chapter is a direct comparison of these data with the experiments of C_6H_6 on ASW and SiO_2 done by Thrower *et al.* [9–12]. The SiO_2 surface presents a wide range of binding sites for C_6H_6 which results in deviations from simple first-order kinetics for its desorption from this surface. This is consistent with our observations reported in **Chapter 3** for $(\text{CH}_3\text{CH}_2)_2\text{O}$ and CH_3OH on the same amorphous SiO_2 surface. In contrast, TPD traces of C_6H_6 on ASW exhibited island formation from the lowest exposures. However, at low coverage (≤ 0.5 L), C_6H_6 desorption kinetics deviate from ideal zeroth-order desorption with some evidence for a narrow range of desorption energies compatible with C_6H_6 π -hydrogen bonded to the SiO_2 surface. RAIR spectra for similar doses support this interpretation with evidence of small shifts in peak position of the aromatic C-C stretching mode in agreement with the data reported for C_6H_6 and CH_3OH in this thesis. **Table 4.5** summarises the growth mechanism of C_6H_6 on top of the three ices. These cases represent purely conceptual models of interstellar ices. Real astrophysical ices are far more complex given the variety of chemicals adsorbed on the dust grains. Furthermore, since the experiments were performed at a base temperature of ~ 110 K, the ices might be less porous, and hence, much more compact than they would be in colder environments, *e.g.* ~ 10 K. However, it should be stressed that this inconsistency should not be as

Ice	C ₆ H ₆ film growth	E _d / kJ mol ⁻¹ at low coverages	Main interaction at the interface
H ₂ O	Islanding	41.0 ± 0.5	H-bond
CH ₃ OH	Islanding/mixing	20 ± 2 42 ± 1	H-bond
(CH ₃ CH ₂) ₂ O	Wetting/mixing	(35 ± 1)*	weak H bond and dispersive forces

Table 4.5: Table summarising the experimentally determined film growth and energetic of C₆H₆ for the binary layered systems: C₆H₆/H₂O, C₆H₆/CH₃OH and C₆H₆/(CH₃CH₂)₂O. The E_d value indicated in brackets was determined for (CH₃CH₂)₂O on C₆H₆ and does not represent the desorption energy of the inverted analogous system. It should be regarded as merely indicative.

relevant as cosmic rays are known to process the dust mantles making them compact [30–33]. In conclusion, the results reported in this chapter might not entirely represent the complexity of hypothetical binary systems in the ISM conditions. Nevertheless, this should not be seen as a limitation because processes occurring in simpler, ideal systems will still take place in realistic scenarios. Thus, some general conclusions can still be drawn and applied to astrophysical environments.

In the outer protostellar envelope, and within the cold clouds, the composition of ices is dominated by H₂O and CO/CO₂. Abundance of C₆H₆ in astrophysical environments is not sufficient for the formation of thick ice layers, therefore interaction at the interfaces would be likely to play a significant role. Thus, C₆H₆, newly formed in circumstellar envelopes [2, 34] or coming as organic residual from protoplanetary nebulae [1], would be hydrogen bonded to the H₂O surface. A similar interaction would be retained in later stages of protostar evolution when CH₃OH accrues. Benzene molecules deposited on top would behave as on H₂O, and strong H-bonding interactions could develop within the CH₃OH matrix as CH₃OH continues to be formed.

In contrast, in the inner and middle envelope, where grain temperatures are as high as 100 K or above, CO and CO₂ have sublimated and the ice mantles will be richer in H₂O/CH₃OH and complex organic molecules, including (CH₃CH₂)₂O among many others. In this scenario, the complex mixture of chemicals will result in a heterogeneity of adsorption and desorption behaviour of C₆H₆, as well as other carbon-rich molecules, depending on the local mantle composition. Fur-

thermore, as the temperature increases mixing of C_6H_6 and CH_3OH or C_6H_6 with other aromatic or aliphatic molecules is likely to take place, depleting it from the H_2O interfaces. In other words, in the cold clouds, in the inner part of protoplanetary disks and in the outer protostellar envelope, C_6H_6 is H-bonded to H_2O or bare grains leading to delayed desorption; in the middle and outer envelopes, C_6H_6 would diffuse through the pores, de-wetting the H_2O ice and mixing with organic molecules, such as large PAHs. Moreover, if bound to volatile molecules as $(CH_3CH_2)_2O$, co-desorption is expected to take place accelerating the rate of C_6H_6 loss.

The results presented in this chapter further confirm the relevance of mixing and its competition with thermal desorption in realistic and complex ices such as in hot cores/corinos. However, these data alone cannot be used for any quantitative extrapolation to astrophysical scales, therefore future TPD experiments of C_6H_6 from within a CH_3OH ice and on H_2O/CH_3OH ice are necessary to properly assess this behaviour. In fact, mixing can either occur at the base conditions of the experiments, or exclusively during the heating ramp in the TPD. The RAIR spectra collected at ~ 110 K showed no clear evidence for the adsorbate (C_6H_6) to diffusing into the underlayer. In contrast, CH_3OH displacement and change of the ice morphology were both observed during C_6H_6 dosing at base experimental temperature. Two different strategies could shed light on the impact of operating at the threshold of the amorphous/crystalline phase transition in CH_3OH ices, and retaining ice layers on the substrate (*e.g.* $(CH_3CH_2)_2O$):

1. *Less volatile substrates for C_6H_6 could be used.* Alcohols and ethers with longer alkyl chains will result in ices that sublime at higher temperatures and thus, can be considered as more stable substrates. However, this has the drawback of a decreasing relevance of the O atom in the molecular structure as the number of carbon atoms increases. This means that the comparison with H_2O is less logically immediate and complicates the interpretation of the experiments, especially when discussing the results of **Chapter 5** which build on the TPD and RAIR spectra in **Chapter 4**.
2. *A lower base temperature.* Ideally, dosing should be done at low temperatures, such as $\sim 10 - 80$ K. Then an annealing step should follow at a convenient temperature to allow thermal relaxation of the CH_3OH or $(CH_3CH_2)_2O$ ice. Finally, the latter would be returned to base (low) temperatures. This would result into a relatively non-porous ice to be used as substrate for C_6H_6 . Given the low surface temperature (10 - 80 K), the underlayer displacement, phase change and maybe mixing that might occur

during the dosing of the adsorbate would be minimised compared to the experiments reported in this chapter ($T_{base} = 110$ K). Whereas negligible differences should be expected for TPD data between the current results and the proposed strategy.

In addition to this, TP-RAIR spectra of low exposures of C_6H_6 (*e.g.* 1 L) on top of a thick CH_3OH film might also provide additional information to assess the competition between mixing and thermal desorption.

Bibliography

- [1] J. Cernicharo, A. M. Heras, A. Tielens, J. R. Pardo, F. Herpin, M. Guélin and L. B. F. M. Waters, *Astrophys. J.*, 2001, **546**, L123.
- [2] B. M. Jones, F. Zhang, R. I. Kaiser, A. Jamal, A. M. Mebel, M. A. Cordiner and S. B. Charnley, *Proc. Natl. Acad. Sci. U. S. A.*, 2010, **108**, 452.
- [3] H. Bockhorn, F. Fitting, H. W. Wenz and B. Bunsenges, *Phys. Chem.*, 1984, **20**, 1067.
- [4] M. Frenklach, D. W. Clary, W. C. Gardiner and S. E. Stein, *Proc. Combust. Inst.*, 1984, **20**, 887.
- [5] W. W. Duley and D. A. Williams, *Mon. Not. R. Astron. Soc.*, 1981, **196**, 269.
- [6] G. H. Herbig, *Ann. Rev. Astron. Astrophys.*, 1995, **33**, 19.
- [7] P. Ehrenfreund, S. Rasmussen, J. H. Cleaves and L. Chen, *Astrobiology*, 2006, **6**, 490.
- [8] A. Lignell and M. S. Gudipati, *J. Phys. Chem. A*, 2015, **119**, 2607.
- [9] J. D. Thrower, M. P. Collings, F. J. M. Rutten and M. R. S. McCoustra, *J. Chem. Phys.*, 2009, **131**, 244711.
- [10] J. D. Thrower, A. G. M. Abdulgalil, M. P. Collings, M. R. S. McCoustra, D. J. Burke, W. A. Brown, A. Dawes, P. D. Holtom, N. J. Mason, F. Jamme, H. J. Fraser and F. J. M. Rutten, *J. Vac. Sci. Technol. A*, 2010, **28**, 799.
- [11] J. D. Thrower, M. P. Collings, F. J. M. Rutten and M. R. S. McCoustra, *Chem. Phys. Lett.*, 2011, **505**, 106.
- [12] J. D. Thrower, *PhD thesis*, Heriot-Watt University, 2009.
- [13] P. A. Redhead, *Vacuum*, 1962, **12**, 203.

- [14] S. D. Green, A. S. Bolina, R. Chen, M. P. Collings, W. A. Brown and M. R. S. McCoustra, *Mon. Not. R. Astron. Soc.*, 2009, **398**, 357.
- [15] G. D. Waddill and L. L. Kesmodel, *Phys. Rev. B*, 1985, **31**, 4940.
- [16] G. Strazzulla and G. A. Baratta, *Astron. Astrophys.*, 1991, **241**, 310.
- [17] R. Ruiterkamp, Z. Peeters, M. H. Moore, R. L. Hudson and P. Ehrenfreund, *Astron. Astrophys.*, 2005, **440**, 391.
- [18] C. J. Craven, P. D. Hatton, C. J. Howard and G. S. Pawley, *J. Chem. Phys.*, 1993, **98**, 8236.
- [19] F. C. Calaza, T. L. Chen, D. R. Mullins and S. H. Overbury, *Top. Catal.*, 2011, **54**, 56.
- [20] J. M. Meyers and S. C. Street, *Langmuir*, 1996, **12**, 1511.
- [21] S. Li, V. R. Cooper, T. Thonhauser, A. Puzder and D. C. Langreth, *J. Phys. Chem. A*, 2008, **112**, 9031.
- [22] A. Simon and F. Spiegelman, *J. Chem. Phys.*, 2013, **138**, 194309–12.
- [23] G. Matisz, A. Kelterer, W. M. F. Fabian and Kunsági-Máté, *J. Phys. Chem. A*, 2011, **115**, 10556.
- [24] J. C. Amicangelo, I. D. G. Gung, B. W. and N. C. Romano, *Phys. Chem. Chem. Phys.*, 2008, **10**, 2695.
- [25] M. J. Frisch, G. W. Trucks, H. B. Schlegel, G. E. Scuseria, M. A. Robb, J. R. Cheeseman, G. Scalmani, V. Barone, B. Mennucci, G. A. Petersson, H. Nakatsuji, M. Caricato, X. Li, H. P. Hratchian, A. F. Izmaylov, J. Bloino, G. Zheng, J. L. Sonnenberg, M. Hada, M. Ehara, K. Toyota, R. Fukuda, J. Hasegawa, M. Ishida, T. Nakajima, Y. Honda, O. Kitao, H. Nakai, T. Vreven, J. A. Montgomery, Jr., J. E. Peralta, F. Ogliaro, M. Bearpark, J. J. Heyd, E. Brothers, K. N. Kudin, V. N. Staroverov, R. Kobayashi, J. Normand, K. Raghavachari, A. Rendell, J. C. Burant, S. S. Iyengar, J. Tomasi, M. Cossi, N. Rega, J. M. Millam, M. Klene, J. E. Knox, J. B. Cross, V. Bakken, C. Adamo, J. Jaramillo, R. Gomperts, R. E. Stratmann, O. Yazyev, A. J. Austin, R. Cammi, C. Pomelli, J. W. Ochterski, R. L. Martin, K. Morokuma, V. G. Zakrzewski, G. A. Voth, P. Salvador, J. J. Dannenberg, S. Dapprich, A. D. Daniels, Á. Farkas, J. B. Foresman, J. V. Ortiz, J. Cioslowski and D. J. Fox, *Gaussian09 Revision D.01*, Gaussian Inc. Wallingford CT 2009.

- [26] M. Albertí, N. F. Lago and F. Pirani, *J. Am. Chem. Soc.*, 2000, **122**, 11450.
- [27] S. Tsuzuki, K. Honda, T. Uchimaru, M. Mikami and K. Tanabe, *J. Am. Chem. Soc.*, 2000, **122**, 11450.
- [28] J. G. Hill, J. A. Platts and H. J. Werner, *Phys. Chem. Chem. Phys.*, 2006, **8**, 4072.
- [29] O. Gálvez, B. Maté, B. Martín-Llorente, V. J. Herrero and R. Escibano, *J. Phys. Chem. A*, 2009, **113**, 3321.
- [30] M. H. Moore, *Astrophys. J.*, 1992, **401**, 353.
- [31] G. Strazzulla, G. A. Baratta, G. Leto and G. Foti, *Europhys. Lett.*, 1992, **18**, 517.
- [32] G. Leto and G. A. Baratta, *Astron. Astrophys.*, 2003, **397**, 7.
- [33] W. Zheng, D. Jewitt and R. I. Kaiser, *J. Phys. Chem. A*, 2009, **113**, 11174.
- [34] I. Cherchneff, J. R. Berker and A. G. G. M. Tielens, *Astrophys. J.*, 1992, **401**, 269.

Chapter 5

Electron Irradiation of Benzene on Water, Methanol and Diethyl Ether

Contents

5.1	Introduction	188
5.1.1	Previous Studies: Electron Induced Processes	188
5.2	Experimental Procedures	191
5.3	Electron Irradiation of Benzene Adsorbed on ASW .	192
5.3.1	Discussion	198
5.4	Irradiation of Benzene Adsorbed on Methanol and on Diethyl Ether	206
5.4.1	Results and Discussion	206
5.4.2	Electron-induced Chemistry: H ₂ Formation	211
5.4.3	EPD <i>versus</i> EIC	216
5.5	Astrophysical Implications and Conclusions	220
	Bibliography	224

5.1 Introduction

This chapter presents the experimental findings on electron irradiation (250 eV) of benzene (C_6H_6) films when deposited on different molecular ices on a polished stainless steel disc. The underlayer is a solid, made of water (H_2O) or methanol (CH_3OH) or diethyl ether ($(CH_3CH_2)_2O$), exhibiting varying degrees of hydrogen bonding within the ice itself and between the solid surface and adsorbed C_6H_6 . The principal aim of this study lies in investigating the substrate-mediated non-thermal desorption of C_6H_6 ; hence, probing the role of the hydrogen bonding network in propagating electronic excitation to the solid-vacuum (solid-adsorbate) interface. This is attempted with the series of experiments as follows:

- The first section continues from the work of Thrower on the C_6H_6 /ASW system [1, 2], by changing the H_2O ice thickness and its phase. Thus the interplay between the bulk excitation and the interface is further developed.
- Then measurements employing substrates comprised of solid CH_3OH and $(CH_3CH_2)_2O$ were performed. As discussed in **Chapter 3**, these molecules retain the intramolecular microenvironment around the oxygen atom, centre of the electronic excitation, but reduce the extent of H-bonding in the solid and between the substrate and C_6H_6 .

Furthermore competitive electron-promoted chemistry in the form of H_2 formation is also reported alongside conclusions related to the impact of these observations on the early phase of icy interstellar grain chemistry.

5.1.1 Previous Studies: Electron Induced Processes

In the literature, many experimental studies are available on exposure of astrophysically relevant ices to ionising radiation, whether it is proton bombardment [3, 4], soft X-rays [5], VUV photons [6–9] or electrons [10–13]. All of these investigations share a common goal of better understanding the processes taking place after excitation of simple molecular solids, such as water, methanol, carbon monoxide, ammonia and their mixtures. The focus is set on the chemistry in order to explain the observation of complex organic molecules (COMs) in the interstellar medium and in star and planet formation. Furthermore, although yields vary from one irradiation source to another among the key excitation mechanisms, all energetic primary ionising radiations, including X-rays, γ -rays, β and α -particles, fission fragments and fast (accelerated) heavy ions, lead to significant quantities of secondary electrons [14]. The latter are also indirectly responsible for the photoionisation occurring within the dense clouds. In fact, it is widely agreed that,

since externally sourced VUV radiation cannot penetrate into the inner layers of dark clouds, the source must be local. In contrast, cosmic rays (CR) can reach the inner areas of clouds inducing ionisation events that produce secondary electrons. These secondary electrons and the primary CR can both excite the H₂ molecules that will then relax by emitting photons in the VUV range. Thus, no matter the ionising source, the trigger is strictly linked to secondary electrons.

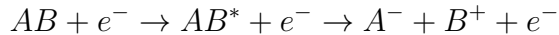
The similarity in the products in these irradiation phenomena hints to a common ground for physico-chemical processes to take place laid out by the secondary electrons. It should be stressed that this is just a fascinating hypothesis though, and that the role played by this electron chemistry is still unclear and under investigation to understand whether the observed species after irradiation are mainly produced by the primary event (photons/charged particles) or secondary electrons themselves. This concept was firmly expressed in a recent work by Mason *et al.* on 100 - 5 keV electron bombardment of thin films of O₂, CH₃OH, 1:1 mixture of CH₃OH and NH₃, mixed cluster of NF₃ and CH₃Cl [15]. Four key ideas are outlined regarding electron-induced chemistry of model interstellar ices:

1. *Dust grains as radical bomb.* The electrons produced by incident cosmic rays possess enough energy to directly dissociate molecules forming radicals, which may remain dormant at low temperature (*e.g.* 10 K). As the grain is warmed up, the thermal energy increases to allow diffusion leading to chemical reactions with other radicals and/or neutral species. The exothermicity of these reactions leads to desorption, morphology change, further chemical reactions, and diffusion of more radicals, which further enhances the energy in thermal bath and thus boosts the kinetics of the physico-chemical processes [16]. In this respect *in situ* techniques, such as IR spectroscopy are recommended in place of TPD that triggers diffusion during the heating ramp.
2. *Little energy dependence on some products yields.* Whether irradiation is conducted with 100 eV, 1 keV or 5 keV the yields, hence the branching ratios, are very similar enforcing the idea that lower energy secondary electrons are the main cause for the observed chemistry while the excess of energy is lost in thermalisation of the matrix lattice.
3. *Biochemical precursors are formed even in simple binary ices.* Formamide (HCONH₂), building block of acyclonucleosides, was observed after irradiation of ammonia-methanol films.
4. *Low energy electrons (LEE) can induce indirect and direct molecular disso-*

ciation. Dissociative electron attachment (DEA), for instance is a process that can be summarised as:



and can yield the same products of direct bond dissociation, but at energy of few meV since the electron affinity is smaller in energy than a chemical bond (units of eV). Pair formation or dipolar dissociation (DD) is another electron induced anion formation process:



and represents a direct excitation process of the target molecule which occurs at higher electron impact energies [17, 18].

The rich chemistry taking place within cold molecular clouds prior to the warm up (star formation) phase was recently reported by Kaiser and co-workers [19, 20] exposing pure CH₃OH or CH₃OH-CO mixture ices to 5 keV electrons at 5.5 K. The findings highlighted the synthetic routes of complex molecules such as methyl formate (HCOOCH₃), ketene (H₂CCO), ethylene glycol (HOCH₂CH₂OH), glycolaldehyde (HOCH₂CHO) and glycerol (CH₂OHCHOHCH₂OH) among many others at such low temperatures.

On the other hand, while a vast literature is available for small molecules like H₂O, O₂, CO, N₂, and H₂ on metal substrates (W) [21–24] or graphite [25], less has been reported concerning the astrophysical relevance of electron-promoted desorption (EPD) of interstellar ice mimics. Previous studies within this group have presented results of highly efficient desorption of isolated C₆H₆ molecules from the surface of compact amorphous solid water ice, when irradiating with 100 - 350 eV electrons [1]. The measured cross-section ranges between 10⁻¹⁶ and 10⁻¹⁵ cm² and it is at least an order of magnitude higher than the value found for the analogous experiment probing C₆H₆ adsorbed on amorphous silica or from multilayer C₆H₆. In the latter case, dehydrogenation was observed to be the dominant channel, in agreement with previous studies [26].

It is clear that efficient C₆H₆ desorption relies on the underlying H₂O ice, and likely promoted by the formation of excitons within the bulk, which migrate to the benzene *via* the interface. However many aspects of the proposed mechanism are yet to be elucidated and confirmed.

- EPD due to exciton formation and migration to the interface yet to be

confirmed.

- The dependence of C_6H_6 yield on the thickness of the compact ASW ice. If the underlayer is thick enough for long-lived excitons to form and move across several layers within the ice, a thicker perfectly flat film should have negligible change in the amount of desorbed C_6H_6 .
- Competition between chemistry (*e.g.* radiolysis products) and physics (*e.g.* non-thermal desorption).

The experiments in the next paragraphs will attempt to answer, in part, these open questions; with particular focus on the role of H-bonding in propagating the excitation to the ice-vacuum interface by studying the C_6H_6 electron-promoted desorption behaviour on multilayer films of compact amorphous solid water (ASW), crystalline solid water (CI), CH_3OH , and $(CH_3CH_2)_2O$ at 110 K.

5.2 Experimental Procedures

Electron-promoted desorption experiments were performed using the Beam Rig chamber and the same polished stainless steel disc as for the TPD and RAIR spectra in the previous chapter. The temperature was monitored by a K-type thermocouple confirming vapour deposition at 110 K. However, the thermocouple was disconnected during the irradiation and the sample grounded to avoid charging. The substrate position was initially set to be normal to the line-of-sight tube of the QMS, and at $\sim 45^\circ$ with respect to the Kimball Physics ELG-2 electron gun. Signal optimisation led to final coordinates where both the quadrupole and the sample were rotated by 10° closer to the gun, giving an angle of 30° between the latter and the normal to the disk so that the beam was incident at 60° . Electron fluxes were determined at base conditions, prior to background dosing, by measuring the current through the floating sample using a picoammeter. In order to improve the S/N ratio as much as possible, the QMS secondary electron multiplier was raised to 1700 V, higher than the 1200 V - 1400 V used for TPD experiments. Only $\frac{m}{z} = 78$ was recorded during the C_6H_6 desorption experiments since any additional channel would significantly slow down the signal integration. While $\frac{m}{z} = 2$ (or $\frac{m}{z} = 4$ for D_2O) was followed in the series of experiments focused on electron-induced chemistry. Sample cleanness was assured by annealing the substrate above 500 K before cooling down to base in the H_2O/C_6H_6 and CH_3OH/C_6H_6 experiments. While the annealing was conducted above 600 K for the $(CH_3CH_2)_2O/C_6H_6$ data.

5.3 Electron Irradiation of Benzene Adsorbed on ASW

The observations outlined in this section confirm the efficient electron-promoted desorption of C_6H_6 adsorbed on ASW at 110 K. The substrate was exposed to an electron beam of 250.0 ± 0.4 eV, focused to have a spot-size of ~ 1 mm². Despite the sample being grounded during data acquisition, preliminary tests revealed that charging might occur resulting into halving of the initial value of the current density after 700 seconds of continuous irradiation. Additional measurements at the Faraday cup on the end of the electron gun excluded beam instability larger than 10% as a source of this change. The origin of the sample charging is as yet unknown and unclear, and further investigations are needed to identify the cause of the phenomenon. Nevertheless, the change in the current density lies within the 22% in the time window of interest to probe the efficient mechanism of C_6H_6 desorption, and does not greatly affect the estimation of the EPD cross-section.

Results and Analysis

Firstly, it was important to replicate the results reported by Thrower *et al.* [1, 2] in order to (i) optimise the signal at the QMS, and (ii) verify that, despite the lack of pulse counting, it was still possible to detect EPD of C_6H_6 from H_2O ice. **Figure 5.1** displays the QMS ion signal ($\frac{m}{z} = 78$) when 1 L of C_6H_6 , previously deposited on thick (140 L, ~ 15 nm) compact amorphous solid water (c-ASW), is exposed to continuous bombardment of 250 eV electrons. As expected, the

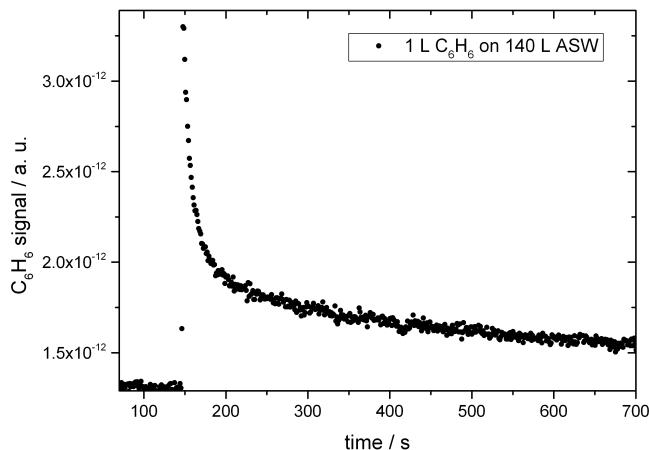


Figure 5.1: EPD C_6H_6 signal obtained for 1 L of C_6H_6 on 140 L of compact ASW. Irradiation was conducted with 250 eV electrons and beam current of 300 nA.

signal increases almost instantly as soon as irradiation begins, to quickly decay

in the first 20 seconds. After that, a slow decrease endures throughout the experiment. Since the beam spot is significantly smaller than the substrate itself, diffusion from unirradiated areas might occur at 110 K, explaining the non-zero residual. The observed trend, composed of fast and slow components, agrees well with previous results and is consistent with mainly isolated C_6H_6 molecules desorbing from H_2O . Higher exposures of C_6H_6 are expected to gradually reduce the intensity of the initial peak, while broadening its tail.

This is also observed in **Figure 5.2**, where 5 L of C_6H_6 were deposited on H_2O films of variable average thicknesses: 7.7 nm (70 L), 11 nm (100 L), 22 nm (200 L), and 55 nm (500 L) ¹. Not surprisingly, the EPD trace is independent of the film depth. Some minor variations can be observed in the decay between 50 and 100 seconds, representing the transition between the two components, but these could be ascribed to changes in the C_6H_6 exposures within the experimental error (10%). The most striking and sole difference is that for the thicker H_2O film (500 L) the signal maximum value is lower than in the other curves. This will be explained in the next section, but, for now, it will suffice to say that the change in the amplitude is linked to the roughness at the H_2O/C_6H_6 interface.

In order to quantitatively estimate the EPD cross-section for C_6H_6 on ASW it is necessary to know both (i) the time decay constant and (ii) the current density. The former can be obtained by the fit of the experimental trace; the latter from measurements of the current through the sample by a picoammeter. Assuming first-order kinetics for the EPD process, all the curves are nicely reproduced by a bi-exponential decay function that explicitly contains two desorption processes:

$$I(t) = I_1 e^{-\frac{t}{\tau_1}} + I_2 e^{-\frac{t}{\tau_2}} + I_\infty$$

$$I(t) = I_1 e^{-\sigma_1 \phi t} + I_2 e^{-\sigma_2 \phi t} + I_\infty \tag{5.1}$$

where τ_i is the time decay constant for the fast (1) and slow (2) component, I is the corresponding amplitude, while I_∞ is the residual. The desorption cross-

¹ Once again, conversion from Langmuir exposures to film depth was estimated by taking into account the ion gauge sensitivity factor for H_2O (1.1, [27]), and using **Equation 3.7** to calculate the total number of deposited molecules for surface area with the assumption that the sticking coefficient is unity. The result was then divided by the molecular density corresponding to 0.87 g cm^{-3} [28].

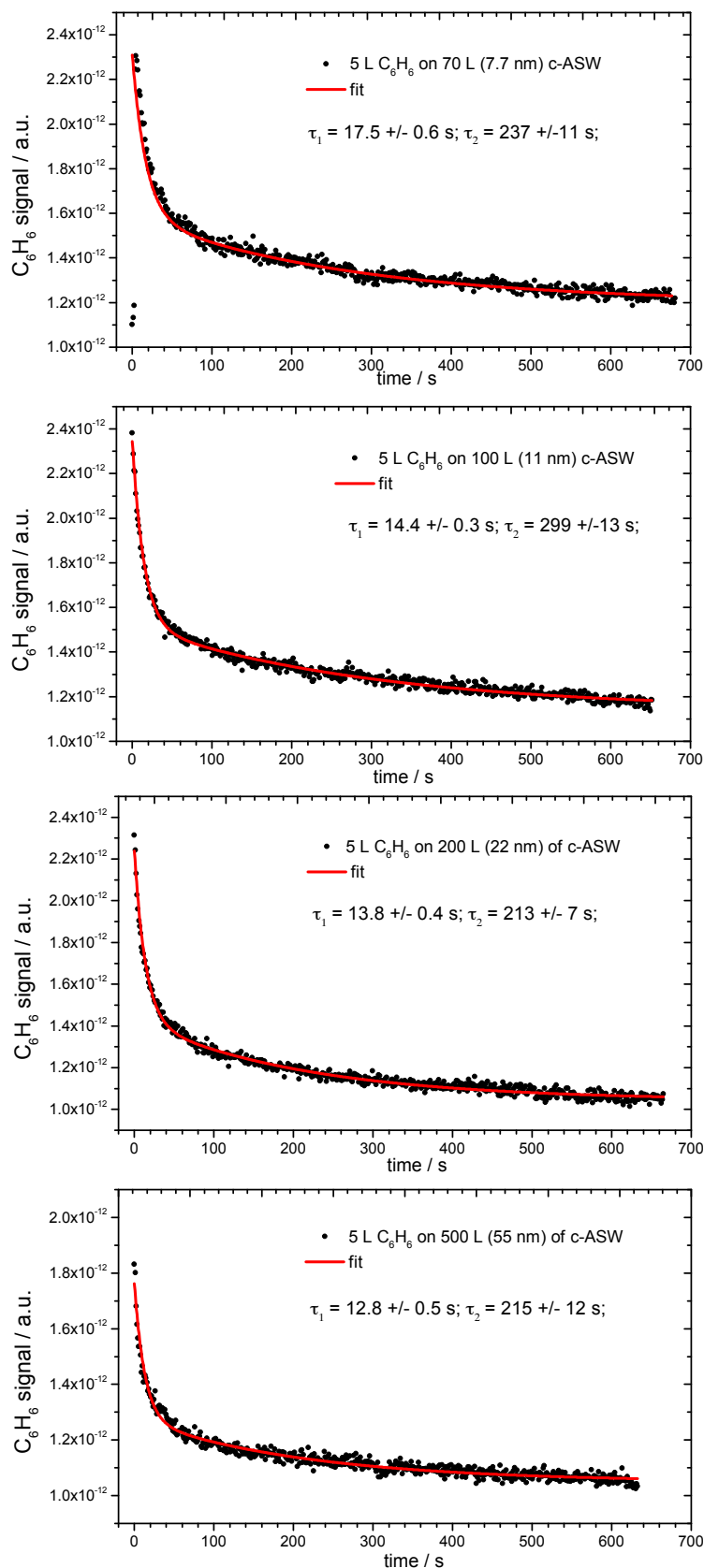


Figure 5.2: EPD C_6H_6 signal obtained for 5 L of C_6H_6 on compact ASW of different thicknesses: 7.7 nm (70 L), 11 nm (100 L), 22 nm (200 L), and 55 nm (500 L). Irradiation was conducted with 250 eV electrons and beam current of 180 nA. The experimental trace is displayed in closed black circles, the bi-exponential decay fitting function in red. Time decay constants relative to the fast (1) and slow (2) components are reported for each subplot.

section in cm^2 is σ and it is derived by the following

$$\sigma = \frac{1}{\tau\phi}$$

where ϕ is the experimental electron flux in $\text{electron cm}^{-2} \text{ s}^{-1}$. The values of the time decay constants are also reported in **Figure 5.2** in a range between 13 and 18 seconds (mean of 14.5 ± 1.7 s) and between 213 and 299 seconds (mean of 241 ± 40 s) for the fast and slow process respectively. The latter, compared to the initial sharp increase, exhibits larger uncertainty given the low S/N ratio at longer times and it is significantly more sensitive to the amount of C_6H_6 deposited on the ice. The experimental current (180 ± 40 nA) was converted into electron fluxes assuming a constant beam spot size of 1 mm^2 .

Table 5.1 summarises the observables for the first run of the experimental series. Note that due to the above mentioned charging of the substrate a lower current density was considered for the slow component (120 ± 12 nA). The second and third data-sets are consistent with the reported values, with the only difference of a lower beam current in the first two minutes of irradiation (150 ± 20 nA). This resulted into larger time decay constants (mean of 22 ± 4 s) for the fast component. However the corresponding cross-section values display a good agreement within the three sets per each H_2O film thickness.

Coverage	ϕ^{fast} ϕ^{slow}	τ_1 τ_2	σ_1 σ_2
/ L	/ $\text{electron cm}^{-2} \text{ s}^{-1}$	/ s	/ cm^2
70	$(1.1 \pm 0.2) \times 10^{14}$ $(7.5 \pm 0.7) \times 10^{13}$	17.5 ± 0.6 237 ± 11	$(5 \pm 2) \times 10^{-16}$ $(5.6 \pm 0.7) \times 10^{-17}$
100	$(1.1 \pm 0.2) \times 10^{14}$ $(7.5 \pm 0.7) \times 10^{13}$	14.4 ± 0.3 299 ± 13	$(6 \pm 2) \times 10^{-16}$ $(4.4 \pm 0.6) \times 10^{-17}$
200	$(1.1 \pm 0.2) \times 10^{14}$ $(7.5 \pm 0.7) \times 10^{13}$	13.8 ± 0.4 213 ± 12	$(6 \pm 2) \times 10^{-16}$ $(6.2 \pm 0.6) \times 10^{-17}$
500	$(1.1 \pm 0.2) \times 10^{14}$ $(7.5 \pm 0.7) \times 10^{13}$	12.8 ± 0.5 215 ± 12	$(7 \pm 2) \times 10^{-16}$ $(6.2 \pm 0.6) \times 10^{-17}$

Table 5.1: Table reporting: electron fluxes, decay constants and EPD cross-sections of C_6H_6 on ASW for each H_2O dose for the first series of experiments.

Moreover, when both the statistical and experimental errors are taken into ac-

count, the distribution of the EPD C_6H_6 cross-section as a function of the film depth of the underlayer ice is flat around a mean value of $5.5 \pm 2.0 \times 10^{-16} \text{ cm}^2$ (see **Figure 5.3** and **Table 5.2**).

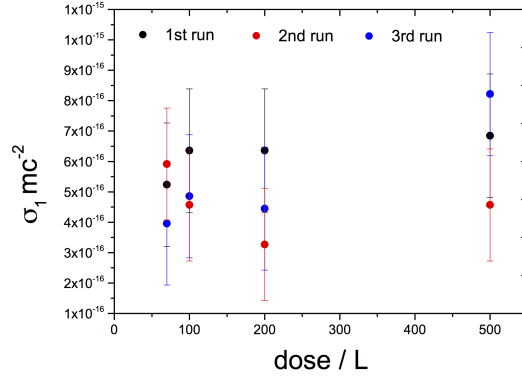


Figure 5.3: Cross-section values and error bars of the fast component in the EPD curve obtained for 5 L of C_6H_6 on compact ASW of different thicknesses: 7.7 nm (70 L), 11 nm (100 L), 22 nm (200 L), and 55 nm (500 L). Irradiation was conducted with 250 eV electrons and beam current of 180 nA (1st run) and 150 nA (2nd and 3rd run). A mean value of $(5.5 \pm 2.0) \times 10^{-16} \text{ cm}^2$ is found.

Coverage / L	data-set		
	σ_1 (1 st)	σ_1 (2 nd)	σ_1 (3 rd)
	/ 10^{-16} cm^2		
70	5 ± 2	6 ± 2	4 ± 2
100	6 ± 2	5 ± 2	5 ± 2
200	6 ± 2	4 ± 2	4 ± 2
500	7 ± 2	5 ± 2	8 ± 2

Table 5.2: Table summarising the results for the fast EPD process from all the series of experiments investigating the effect of the H_2O thickness underlying 5 L of C_6H_6 on the non-thermal desorption of the adsorbate. C_6H_6 cross-sections are reported for each H_2O dose.

This result is lower of a factor between four and five when compared to reported values of $2.6 \pm 1.0 \times 10^{-15} \text{ cm}^2$ [1, 2]. Discrepancies are expected since there are changes in the instrumental set-up such as a minor sensitivity of the QMS at the current stage (pulse counting *versus* analogue), as well as the issue of charging of the substrate. The relative orientation of the substrate, QMS and electron gun is also not the same for both the experiments reported in this thesis and in

Thrower’s work. Nevertheless, it can be concluded that the fast event that leads to the efficient electron-promoted desorption of C_6H_6 on ASW is independent from the thickness of the underlying ice and no direct effect of the metal substrate is observed. It is important to stress that 70 L of H_2O dose is the minimum exposure that guarantees the uniform coverage of the stainless disk. Accordingly, the second component was estimated to be $(5 \pm 1) \times 10^{-17} \text{ cm}^2$ for the whole series for experiments and matches the value previously found by Thrower of $8 \pm 2 \times 10^{-17} \text{ cm}^2$. However, small changes in the fit parameters revealed a large variation (50%) on the τ value, with small effect on the χ^2 . Thus a larger error on the cross-section for the second component seem to be more realistic, $(5 \pm 2) \times 10^{-17} \text{ cm}^2$.

An insightful experiment that could aid comprehending the mechanism responsible for the observed high cross-section consists of dosing a fixed amount of H_2O on the substrate at different deposition temperatures. Base conditions (110 K) are compatible with the formation of a compact amorphous film (c-ASW), while deposition at 138 K allows enough thermal relaxation to form poly-crystalline ice (poly-CI). Dosing at 153 K is likely to result into larger crystallites (crystalline ice, CI) with less degree of heterogeneity, but it has the drawback that the accommodation coefficient is no longer unity during deposition. The loss was quantified to be $\sim 36\%$ by comparing the TPD area, for a fixed exposure dosing H_2O at 110 K and 153 K. Therefore, in the latter case in order to compensate for desorption, a larger exposure was used (140 L). The plot in **Figure 5.4** displays the EPD C_6H_6 signal on c-ASW (curve in olive), on poly-CI (curve in dark yellow), and CI (curve in wine) ices. The crystalline ice has a twofold impact on the desorption trace: the fast initial event exhibits a minor rise in intensity of the (C_6H_6) signal as irradiation begins, but from ~ 50 s up to 250 s this is higher than what is displayed by the same experiment on c-ASW. Above ~ 400 s the decay is certainly accelerated. The observed trends seem to nicely correlate with the degree of crystallinity within the underlayer H_2O ice as differences among the decays are progressively more enhanced as the deposition temperature is increased. Replication of the experiment confirms these results. Any difference observed in the EPD traces at the first instants of irradiation is likely to be linked to the impact that the phase has on the H_2O/C_6H_6 interface. At longer times, ~ 50 s onwards, the effects that the electron bombardment has on the ice structure should be taken into account. Previous studies confirmed that continuous exposures of crystalline water ice to ionising sources (H^+ , VUV, especially e^-) leads to conversion into an amorphous phase [29–32]. This might be reflected by the appearance of a bump in the EPD signal around 100 s as well as the faster decay at after 400 s. On the

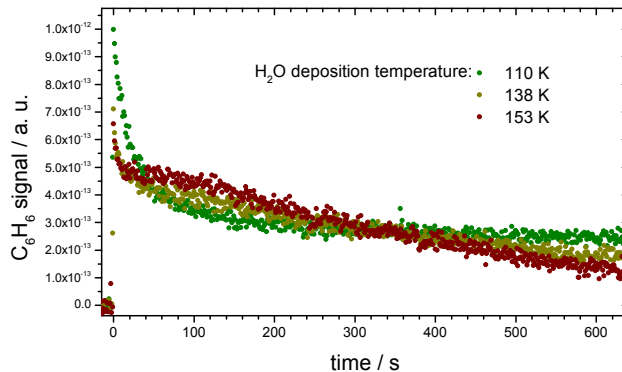


Figure 5.4: EPD C_6H_6 signal obtained for 5 L of C_6H_6 on H_2O ice. H_2O condensed at 110 K results into a compact-amorphous film (c-ASW), while higher deposition temperatures form a crystalline film (CI). Note that background dosing at 153 K leads to $\sim 36\%$ loss of H_2O , therefore the substrate was exposed to H_2O vapour for longer, as to obtain a similar film thickness of the other experiments. Irradiation was conducted with 250 eV electrons and beam current of 180 nA.

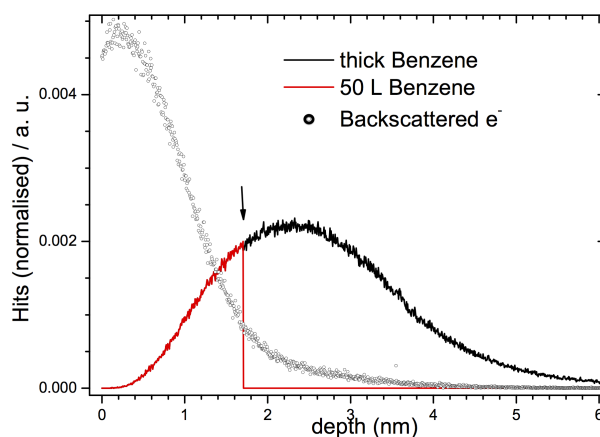
basis of these data, it is now possible to indicate the mechanism responsible for the C_6H_6 desorption on H_2O under electron irradiation.

5.3.1 Discussion

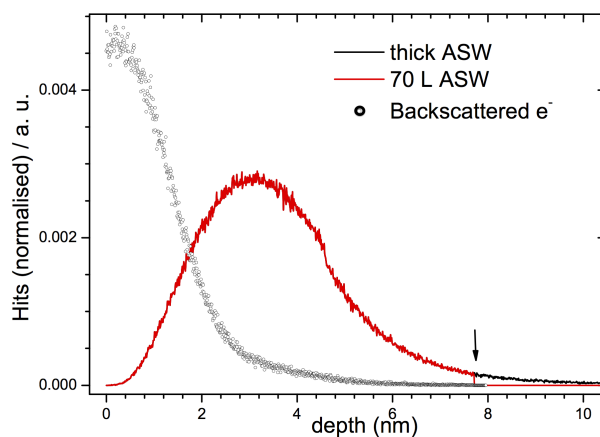
Previously reported experiments of low-energy electron (~ 100 eV) irradiation of ASW (and deuterated ASW) films [33–35] present evidence of molecular hydrogen (H_2 or D_2) formation at the interface, within the first monolayers, while no H_2 (D_2) is produced in the bulk. Nonetheless, the energy for reactions is indeed adsorbed in the bulk of the film. Therefore, some kind of excitation must be responsible for transporting the energy from the bulk to the interfaces, but its nature is still unclear. Two events take place following ionisation in the bulk: (i) H_3O^+ formation and (ii) electron-ion recombination. Hydronium (H_3O^+) displays limited mobility in ASW at 100 K, thus electron-ion pairs (excitons) are likely to be the carrier of the excitation to the interface. On this basis, it was concluded by Thrower [1, 2], that isolated adsorbed C_6H_6 molecules would desorb by accepting the energy at the ice interface released by the electron-ion recombination. In other words, depositing C_6H_6 on top of the ice at low exposures might partially quench the D_2 formation observed in pure ices in favour of the C_6H_6 EPD process. The additional experiments outlined in the paragraph above support this interpretation. If the energy used for desorption is absorbed within the ASW bulk (first 7 - 8 nm) in the first place, increasing the thickness of the underlayer ice above the maximum penetration depth of the electron beam should

result in no significant variation of the C_6H_6 EPD cross-section.

Monte Carlo simulations (CASINO) [36, 37] were performed to determine the electron penetration depth in C_6H_6 films and in ASW. The incident beam of 250 eV was set at 60° , over an area of 1 mm^2 consistent with the experimental conditions. Densities of the molecular solids were the same as the values used in the previous chapters. **Figure 5.5** displays the distributions of backscattered and incoming electrons as a function of the penetration depths in both C_6H_6 (50 L for comparison) and ASW (70 L) assuming perfectly flat surfaces. Most of the



(a)



(b)

Figure 5.5: Distribution of penetration depths (solid lines) and backscattered electrons (circles) for 250 eV in the C_6H_6 (a) and in ASW film (b) using the CASINO software. The arrow points to the estimated thickness of 50 L C_6H_6 and 70 L H_2O which are also highlighted by the superimposed red line.

backscattering events occur in the first 2 nm, bringing the same excitation in all the ASW films investigated. The beam clearly passes through the whole C_6H_6 adsorbate of 5 L (~ 0.2 nm) since the maximum penetration depth (8 nm) is larger than the film thickness, while it is completely stopped in a thicker ice *e.g.* 500 L (17.5 nm). All the electrons would be stopped in the first $\sim 3.4 - 8$ nm in a pure amorphous H_2O ice, therefore, given an exposure of 70 L, a negligible amount of electrons would directly impact the steel disk. Doses of 100 L, 200 L, and 500 L of H_2O would result in a larger spacing from the metal substrate having all thickness larger than the maximum penetration depth. The fact that the C_6H_6 EPD signal is unchanged from 70 L up to 200 L means that there is no contribution from the H_2O /disk interface. If excitons were to form within the bulk and then migrate isotropically in all the possible directions, those travelling toward the ASW/ C_6H_6 would not be affected by a larger spacing below 7-8 nm of depth.

As seen before, when comparing the desorption traces on 500 L ASW ice with the other curves for different exposures, the maximum intensity (not the cross-section) is lower in the first instants of irradiation. This can be explained in terms of available surface area at the interface. The stainless steel disk, despite having been polished, is likely to present a certain roughness that would shape the morphology of the deposited ice. A thinner H_2O film would reflect peaks and troughs of the underlying substrate, while these would be smoothed out in thicker films (see **Figure 5.6**). A minor degree of roughness means less surface

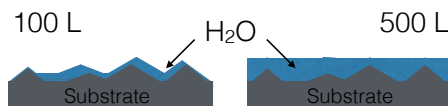


Figure 5.6: *Cartoon of ASW deposited on the metal substrate. H_2O condensed at 110 K results into a compact-amorphous film (c-ASW). The roughness of the substrate is reflected on the morphology of thinner films.*

area at the interface, resulting in less favourable sites for the adsorbates to capture the energy carried by the excitons. A consequence of this is also highlighted in the experiments on CI and c-ASW (**Figure 5.4**). It is an obvious statement to say that CI water has a much more ordered structure compared to the compact amorphous form. It is well-known that the latter phase presents larger cavities within the bulk [38]. However, these are too small to accommodate a C_6H_6 molecule, yet they might disrupt the periodicity of the microenvironments and the H-bonded framework. More importantly, the coordination number of each hydrogen-bonded O-atom in the H_2O molecule is exclusively of four in a perfect crystalline film. While amorphous phases display coordinations of two, three,

four and even five [38, 39]. This, combined with a less ordered structure, results in a larger number of H₂O/vacuum (hence H₂O/C₆H₆) interface dangling bonds for compact or porous ASW than for CI (bottom panel **Figure 5.7**).

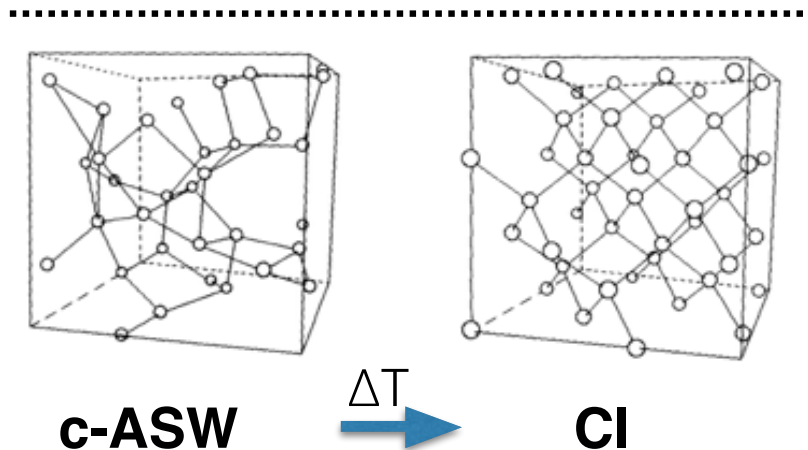
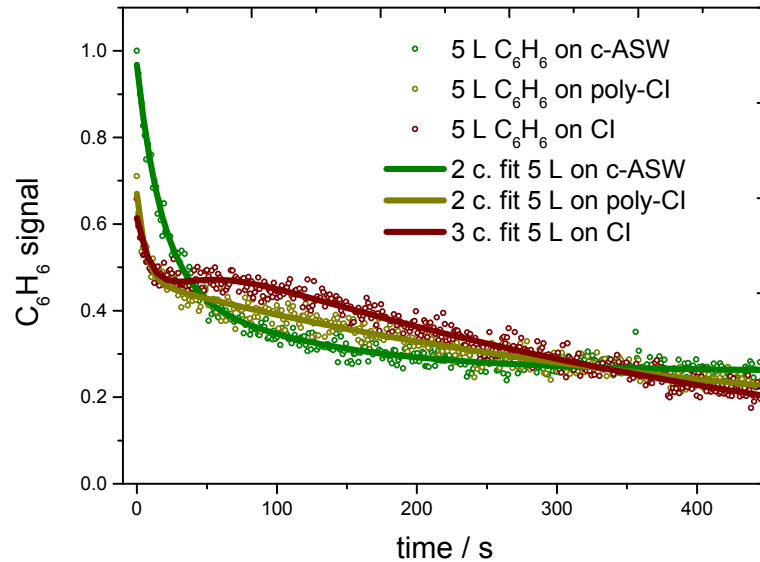


Figure 5.7: C_6H_6 EPD signal obtained for 5 L of C_6H_6 on H_2O ice. H_2O condensed at 110 K results into a compact-amorphous film (c-ASW), while higher deposition temperatures form a polycrystalline film (poly-CI) at 138 K and a crystalline film (CI) at 153 K. Note that background dosing at 153 K leads to $\sim 36\%$ loss of H_2O , therefore the substrate was exposed to H_2O vapour for longer, as to obtain a similar film thickness of the other experiments. Irradiation was conducted with 250 eV electrons and beam current of 180 nA. Multi-exponential fitting curves are displayed in full lines: 2 c. indicates a bi-exponential function, 3 c. indicates a tri-exponential function. Details in the text. Experimental points are shown in open circles. All the intensities were scaled by the maximum of the most intense trace. Lattices, adapted from [38], show the transition of c-ASW to the ordered structure of the CI when annealing. In the latter case the coordination of each O-atom in the H_2O molecules is exclusively of four whereas the amorphous phase displays coordinations of two, three, four, and even five. Furthermore the surface area at the vacuum interface decreases in the ASW to CI change.

Thus, in conclusion, the energy of the incoming beam strikes at the surface, passes through the C_6H_6 entirely, and excites the H_2O molecules in the bulk. Excitons form and migrate to the interface, where the dangling OH groups transfer the energy to the adsorbed C_6H_6 leading to the observed EPD signal. The more interface and the more dangling bonds there are (thinner amorphous films), the more C_6H_6 at the interface would desorb efficiently (fast component). The slow component was associated with desorption of C_6H_6 from C_6H_6 islands and C_6H_6 non-thermally diffusing from the edges of the islands to re-populate the H_2O interface and finally desorb. The delay in its appearance displayed in Thrower *et al.* [1, 2] could well be linked to phase changes induced by the beam itself after irradiation had started. The resemblance between the bump at ~ 100 s in **Figure 5.4** or **5.7** (crystalline to amorphous) and the delay of the second component in the literature as a bump at ~ 10 s is evident.

In order to quantitatively evaluate the effect of the H_2O ice morphology on the C_6H_6 desorption, the EPD traces were fitted with a multi-exponential function. The bi-exponential expression in **Equation 5.1** was used for the curves resulting from deposition of H_2O at 110 K and 138 K (two components fits in **Figure 5.7**). However, this function was not sufficient to describe the more complex behaviour showed by the third curve in **Figure 5.7**. Consistently with previous work [1], the phenomenological equation (three components fit) that successfully replicates the appearance of a bump peaking around 70 s is:

$$I(t) = I_1 e^{-\sigma_1 \phi t} + I_2 \left(e^{-\sigma_2 \phi t} - e^{-\frac{t}{\tau_d}} \right) + I_\infty \quad (5.2)$$

This expression is similar to **Equation 5.1**, but introduces a delay in the appearance of the second (slow) component with a time decay constant τ_d . **Table 5.3** lists the values of cross-section found for the three curves distinguishing between the fast component (σ_1), the slow component (σ_2) and its delay (σ_d) when clearly occurs. The latter is the reciprocal of ($\tau_d \phi$). The σ_1 cross-section seems to increase along the deposition temperature of the H_2O ice, reaching values of *ca.* 10^{-15} cm², which is consistent with the monotonic increase reported by Thrower for the cross-section change as a function of the electron irradiation energy between 100 and 300 eV (σ_1 varying between $(0.7 \pm 0.2) \times 10^{-15}$ cm² and $(2.2 \pm 0.5) \times 10^{-15}$ cm²) [1, 2]. The slow component, σ_2 , displays an opposite trend, although with rather modest variations, which is consistent with the qualitative description given before.

Most importantly, C_6H_6 desorption from CI follows a more complex behaviour

σ_T/cm^2	$\sigma_1/10^{-16} \text{ cm}^2$	$\sigma_2/10^{-17} \text{ cm}^2$	$\sigma_d/10^{-16} \text{ cm}^2$
$\bar{\sigma}_{110K}$	5.5 ± 2.0	5.5 ± 2.5	na
σ_{138K}	17 ± 4.0	3.2 ± 0.7	na
σ_{153K}	8.0 ± 2.0	2.9 ± 0.7	5 ± 1

Table 5.3: List of cross-section values derived from the fits of the experimental EPD traces: C_6H_6 on CI, on poly-CI H_2O film (see **Figure 5.7**) and on c-ASW. In the latter case, the values are reported as average from the experiments probing the effect of ASW film thickness, see **Figure 5.2**. The subscript under the cross-section indicates the deposition temperature of H_2O vapour.

with a delay, τ_d , in the appearance of the slow decay and having a cross-section σ_d comparable to σ_1 . It cannot be excluded that this complex kinetics also occurs for a c-ASW substrate, and only because it is undetected (in **Figures 5.2** and **5.7**) it does not necessarily imply its absence, while it is certainly enhanced for CI/ C_6H_6 . In fact, the results of Thrower have highlighted the appearance of this bump during electron irradiation of 10 L of C_6H_6 on c-ASW that was particularly enhanced at high irradiation energies (*e.g.* 300 eV). The reported value of σ_d ($\sim 10^{-16} \text{ cm}^2$) is in agreement with the result obtained for the EPD trace on CI. Irradiation dynamically changes (*roughening*) the H_2O surface and reveals additional dangling bonds that coordinate to the aromatic rings. This leads to a further increase of the desorption rate in the form of the aforementioned bump. This process can be particularly efficient, with a cross-section of $\sim 10^{-16} \text{ cm}^2$, and depends on the phase of the H_2O ice and on the energy of the impinging electrons. The exact mechanism is not yet clear, however the data presented here are consistent with the idea that the entity in which the icy surface roughens correlates with a more or less efficient rearrangement of the H_2O /vacuum interface due to amorphisation and with the disruption of the C_6H_6 islands when the electron energy is highest and the morphology changes most. Hence it follows that diffusion of the aromatic molecules from the edges of the islands themselves to available dangling OH groups determines a second increase in the EPD traces.

Two major questions concerning the mechanism responsible for the electron-induced desorption still need to be addressed:

1. What kind of excitation is primarily responsible for exciton formations?
2. How does the exciton transfer the energy?

Spectra of electronic excitations and the energy distribution of electrons from ionisation are the starting point of the search for an answer. Despite a multitude of reported studies on optical-absorption and electron-energy-loss spectroscopy (EELS) of solid and liquid water, the interpretation of experimental findings is still a matter of debate. In fact some studies support the hypothesis that plasmons are responsible for the absorption at ~ 21 eV in condensed water [40, 41], while others questioned this interpretation [42, 43]; although the evidence suggests the existence of some not well defined collective excitations [44]. Comparison of the electronic excitations of ASW, CI (cubic and hexagonal) in EEL spectra displays negligible differences between the solid phases [45]. Common features, in addition to the 21 eV peak mentioned above, are associated to electronic transitions at 8.7 eV, 10.4 eV and 14.5 eV involving the O atom in the H₂O molecule [44, 46, 47]. Similar electronic excited states can be found in the methyl derivatives of H₂O. As shown in **Figure 3.20**, any alcohol and (CH₃CH₂)₂O can be thought as derived from H₂O with one or both hydrogen atoms (H) substituted with an alkyl group (R). This would have the smallest effect on the electronic states localised around the O atom that could prompt exciton formation. **Figure 5.8** displays both the highest occupied molecular orbital (HOMO), and the lowest unoccupied molecular orbital (LUMO) for H₂O, CH₃OH and (CH₃CH₂)₂O. The semi-occupied molecular orbital (SOMO) for their analogous cations are also reported. The substitution of the H atoms with aliphatic groups does not significantly alter the electron density around the oxygen atoms in the HOMOs for the neutral species. However, this substitution introduces molecular orbitals components around the C atoms. More evidently, going from H₂O to CH₃OH and to (CH₃CH₂)₂O, the LUMOs(M) and the SOMOs(M⁺) display less and less oxygen character, opening different routes for relaxation. **Figure 5.8** reports also the HOMO-LUMO difference, ΔE_1 , which is the excitation promoting an electron to the lowest unoccupied molecular orbital, and the ionisation potential ΔE_2 for each species. Both the terms decrease as the H atoms are substituted with alkyl groups, thus, both ionisation and excitation become more energetically accessible, as the final state becomes richer in C atom character. Furthermore, the extent of hydrogen bonding is reduced in solid CH₃OH and long-range hydrogen bonding is absent in solid (CH₃CH₂)₂O. A less relevant or absent EPD fast desorption process on the reduced hydrogen-bonding (CH₃OH) and non-hydrogen bonding ((CH₃CH₂)₂O) substrates might assist in answering the aforesaid questions and present unequivocal evidence of the importance of hydrogen-bonding in supporting exciton transport.

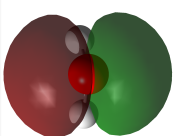
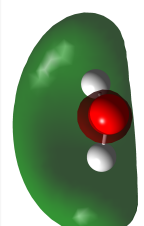
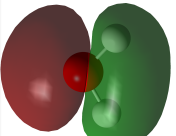
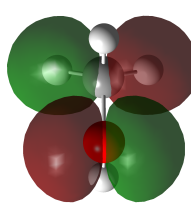
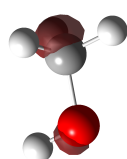
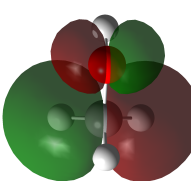
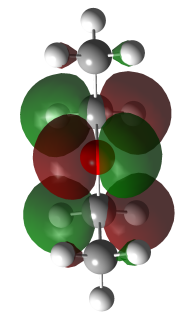
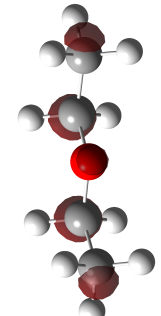
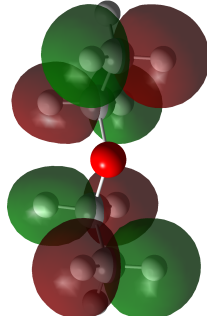
HOMO (M)	LUMO (M)	SOMO (M ⁺)	ΔE_1 / eV	ΔE_2 / eV
			14.8	12.6
			13.2	11.1
			12.4	9.9

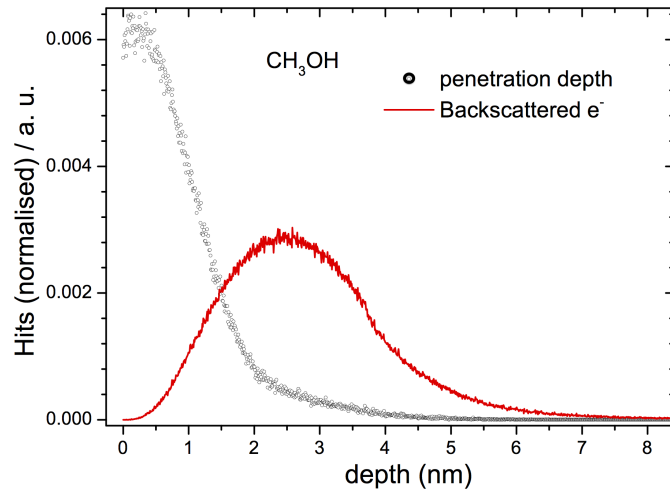
Figure 5.8: Highest occupied and lowest unoccupied molecular orbitals for H_2O , CH_3OH , and $(CH_3CH_2)_2O$ and SOMOs for the analogous ions in the ground state. Ionization value of ± 0.02 a.u. for the LUMO of the $(CH_3CH_2)_2O$, and ± 0.03 a.u. for all the others. ΔE_1 is the excitation HOMO to LUMO in eV, and ΔE_2 is the ionization potential in eV. Calculations were carried at MP2/aug-cc-pVTZ level.

5.4 Electron Irradiation of Benzene Adsorbed on Methanol and on Diethyl Ether

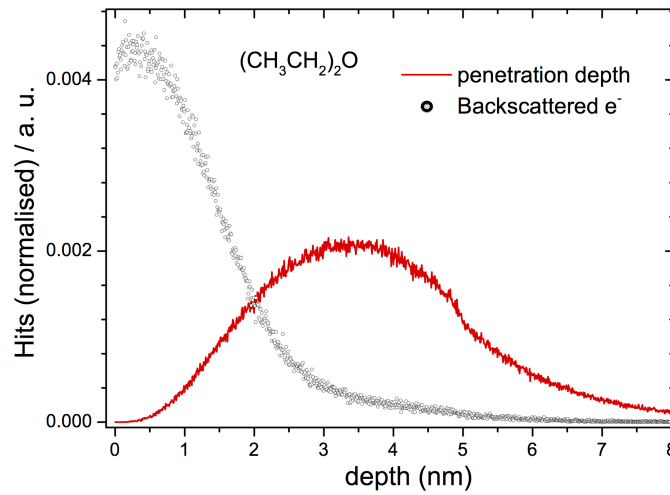
In order to probe the role of H-bonding in transporting the bulk excitation, a thick layer of CH₃OH (250 L) or (CH₃CH₂)₂O (500 L), were deposited onto the metal substrate. Preliminary experiments were performed covering the steel disk with 100 L of H₂O prior CH₃OH/(CH₃CH₂)₂O background dosing (200 L). The former was used as spacer to avoid accumulation of carbonaceous material on the steel interface. However, the penetration depth is clearly less than the average thickness estimated for 200 L of CH₃OH (15.2 nm) or (CH₃CH₂)₂O (12.1 nm) (see **Figure 5.9**), thus it is not surprising that no difference was observed between the two sets of experiments with or without ASW. Furthermore the choice of growing the ices directly on the substrate is a necessity for (CH₃CH₂)₂O since the base temperature of 110 K is not cold enough to adsorb (CH₃CH₂)₂O on ASW (as it would on CH₃OH, C₆H₆ or steel). Increasing coverages of C₆H₆ (1 L, 5 L, 10 L, 20 L and 50 L) were dosed on top of the ice and then irradiated with 250 eV electrons. The electron gun settings are kept the same as for the data outlined before.

5.4.1 Results and Discussion

Figure 5.10 shows the resulting EPD traces. The most striking aspect is the extremely low signal compared to the data-set of the C₆H₆/ASW system. There is at least one order of magnitude of difference when looking at the signal rise in the first moments of irradiation of C₆H₆ on ASW and on solid CH₃OH (**Figures 5.4 and 5.10**). Despite the S/N ratio being noticeably poorer, two distinctive desorption events can be observed: a fast desorption, and a delayed, but long-lived component that immediately follows the former. These will be referred also as the *prompt* and the *dose dependant* C₆H₆ signals in accordance with the notation proposed by Kimmel and Petrik [33]. However, it is important to make a distinction: what here is called *dose dependant* component in the C₆H₆ experiments increases with the surface coverage, while the trend is opposite for the *dose dependant* component of pure solid H₂O observed by Kimmel and co-workers. In **Figure 5.10**, the initial increase in the traces is roughly constant for all the exposures, being almost invariant with the C₆H₆ surface coverage. In contrast, the *dose dependant* signal grows in intensity and underlying area as more molecules are deposited onto the ice. However, the 50 L EPD trace seems to reverse this trend. This behaviour was proved to be reproducible, thus cannot be regarded as an artifact due to a poor quality baseline.



(a)



(b)

Figure 5.9: Distribution of penetration depths (red solid lines) and backscattered electrons (grey circles) for 250 eV in 15.2 nm thick CH₃OH ice (a) and in 12.1 nm thick (CH₃CH₂)₂O film (b) using the CASINO software.

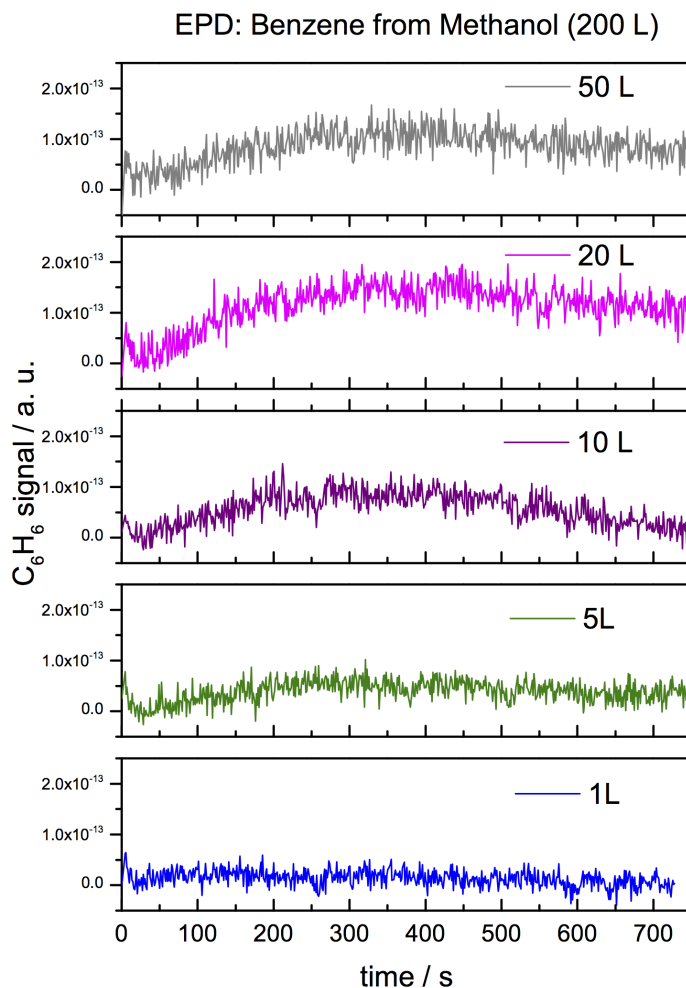


Figure 5.10: C_6H_6 EPD signal obtained for 1 L, 5 L, 10 L, 20 L, and 50 L of C_6H_6 on thick CH_3OH film (15.2 nm). Irradiation started at $t=0$ s with 250 eV electrons and beam current of 150 nA.

Similar results and considerations can be outlined for the analogous data-set for the $C_6H_6/(CH_3CH_2)_2O$ system. The quality of the signal is extremely poor in this case as well, suggesting that other processes might dominate over electron-induced desorption. In **Figure 5.11**, it is noticeable that as more C_6H_6 is dosed, the *prompt* event decreases in intensity, while the slow component increases. Although the change observed for the latter (at 10 L, 20 L and 50 L) is less marked when compared to the data in **Figure 5.10**. Furthermore, the EPD signal associated to the 20 L experiment drops suddenly at 600 s, while the decay is more gentle for 10 L and 50 L of C_6H_6 . Repeating the experiment confirmed this unusual behaviour that, hence, must be linked to an actual process occurring in the ice during the irradiation. Details of this are still unclear, but it could be related to change in the film structure due to the electron impact.

The low S/N ratio prevents a quantitative analysis of the traces to be carried

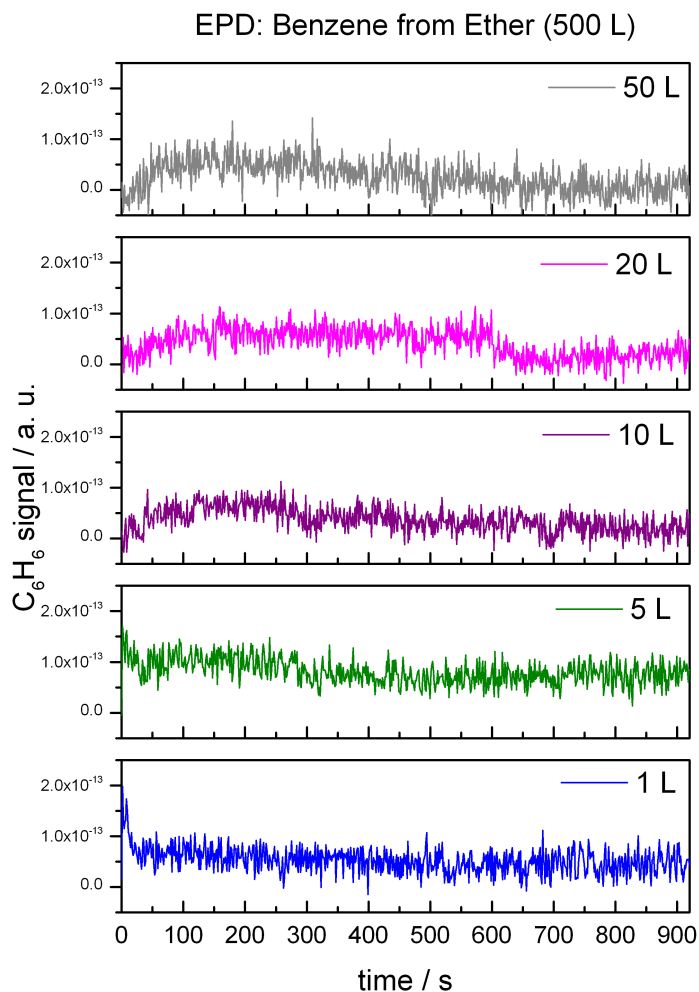


Figure 5.11: C_6H_6 EPD signal obtained for increasing C_6H_6 coverage (1 L, 5 L, 10 L, 20 L, and 50 L) on thick $(CH_3CH_2)_2O$ film (30.2 nm). Irradiation started at $t=0$ s with 250 eV electrons and beam current of 150 nA.

out as done for the series of C_6H_6 on ASW. However, these findings corroborate the mechanism proposed so far. Crystalline and especially amorphous water ices are peculiar in leading to the observation of efficient and long-lasting desorption of C_6H_6 , and perhaps other hydrogen bonded adsorbates (*e.g.* C_2H_2), with a cross-sections of 10^{-16} cm² (10^{-15} cm² [1]) and 10^{-17} cm² for the *dose dependent* and *prompt* C_6H_6 desorption respectively. Methanol film are likely to involve excitation localised around the O atom as for H_2O , but with a significantly reduced complexity of intramolecular H-bonding. Furthermore, the substitution of the H atom with a methyl (CH_3) group introduces an additional electron rich centre capable of being excited by the incident, primary and secondary, electrons. In other words, while water has electron density markedly centred at the O-atom, the C-atom in CH_3OH carries an additional spectrum of electronic excitation that

might favour other processes over desorption.

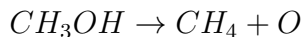
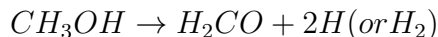
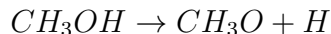
As shown by TPD data, island formation is the driving process during film growth of C_6H_6 on both H_2O and CH_3OH . The isolated molecules that are directly absorbed at the ice interface are likely to especially interact with the hydroxyl group ($OH \cdots \pi$) and with the oxygen atom ($CH \cdots O$). In addition to the former case there is also a minor contribution of the methyl end ($CH \cdots \pi$) for CH_3OH with the aromatic ring. In other words, the benzene “layer” would appear almost the same on both ASW and solid CH_3OH , the only difference is in the capability of the underlying ice to transmit the excitation from the bulk to the interface *via* H-bonding, and any possible implication arising from direct excitation of the C atom in the methyl group. These two differences are responsible for the drastic change seen in the EPD traces. The fact that the *prompt* desorption is less intense when H_2O is absent could be either linked to the difficulty of the excitons to propagate or to form in the first place. Thus, only few C_6H_6 molecules would receive the energy necessary to non-thermally desorb, and probably only from the inner layers closer to the interface. When $(CH_3CH_2)_2O$ is used as ice, the fast event is quenched entirely at 50 L of C_6H_6 . This is not observed with CH_3OH (or H_2O) and can easily be linked to the difference in the film growth. On $(CH_3CH_2)_2O$, the C_6H_6 layer forms uniformly, wetting the entire surface, hence, at even 1 L all the underlying ice would be completely covered by the adsorbate. Therefore, no isolated C_6H_6 molecules are likely to be found, whereas they might be between the islands on ASW or solid CH_3OH . At higher exposures, for instance 50 L, the outer layers would act as a cap, preventing the C_6H_6 below to desorb. This is not dissimilar from what seen by Throrer for 200 L of C_6H_6 on ASW [2], highlighting the necessity of larger doses to “fill the gaps” between the islands.

The way the C_6H_6 film grows on top of the three different substrates (H_2O , CH_3OH and $(CH_3CH_2)_2O$) could also explain why the slow component depends more strongly on the surface coverage for the C_6H_6/CH_3OH system while it seems almost insensitive to it in the $C_6H_6/(CH_3CH_2)_2O$ system. It should be kept in mind that this delayed desorption, although related to phase changes within the substrate, is assigned to multilayer C_6H_6 desorption and non-thermal diffusion from the island edges to the $H_2O/vacuum$ or $CH_3OH/vacuum$ interface. For the range of C_6H_6 exposures probed, the islands on CH_3OH would become progressively bigger. This means that the more molecules are available, the more long-lived is the EPD (*e.g.* 5 L and 20 L traces in **Figure 5.10**); hence repopulation of the “active” sites at the ice interface should in principle also be enhanced. At 50 L, in **Figure 5.10**, the gaps between the islands would be almost filled,

quenching the contribution given by the ice interface to the slow component. This would explain why on CH₃OH the 20 L trace has a more marked bump than the 50 L data. In contrast, on (CH₃CH₂)₂O, there are no gaps to fill going from 5 L to higher exposures, and mainly multilayer C₆H₆ desorption should be observed. Furthermore each (CH₃CH₂)₂O molecule has four carbon atoms, against one oxygen, capable of channelling the secondary electron energies toward other routes. Therefore, in conclusion, the electron-promoted desorption is significantly quenched by CH₃OH and (CH₃CH₂)₂O ices, mainly because secondary electrons stimulate other “excitation centres” out of the O atoms that favour chemistry over physical processes as non-thermal desorption.

5.4.2 Electron-induced Chemistry: H₂ Formation

Kaiser and co-workers have conducted extensive studies on irradiation of CH₃OH ices and mixtures of CH₃OH/CO with 5 keV electrons [19, 20, 48, 49]. Well-defined evidence for complex organic molecules forming in those films is reported. Four initial reaction pathways were identified to explain the radiation-induced decomposition of CH₃OH:



(5.3)

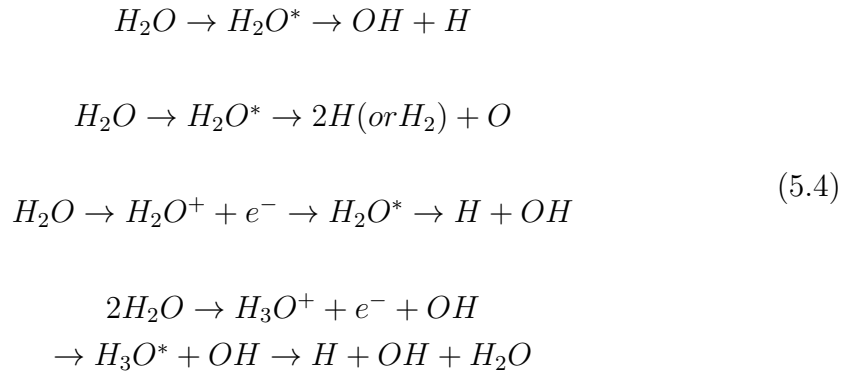
Each of these products undergo further chemical transformations to produce formaldehyde (H₂CO), glycolaldehyde (HOCH₂CHO), methyl formate (HCOOCH₃), ethylene glycol (HOCH₂CH₂OH), and many others. Some of these species were independently found by other studies [15] after irradiation with 100 eV electrons, clearly suggesting that the electron-induced chemistry is promoted by low energy secondary electrons and/or thermalised primary electrons. Therefore, there is no reason to believe that these findings would not apply to the experiments reported herein. In fact, preliminary TPD experiments (not shown), of the irradiated C₆H₆/CH₃OH films have confirmed the detection of the following values of $\frac{m}{z}$: 56, 58, 60, 62, 74 that are compatible with the COMs identified by Kaiser (see **Table 5.4**). These findings point to an obvious competition between chemistry and physics, where the former is more favoured in CH₃OH and (CH₃CH₂)₂O ices than in ASW. In other words, the energy transferred from the electrons to the

Mass / $\frac{m}{z}$	name	Compound formula
56	Propenal	CH ₂ CHCHO
58	Acetone Propanal Allyl alcohol	CH ₃ CHO CH ₂ CH ₂ CHO CH ₂ CHCHOH
60	1-Propanol 2-Propanol	CH ₃ (CH ₂) ₂ OH CH ₃ CHOHCH ₃
62	Ethylene Glycol	HOCH ₂ CH ₂ OH
74	1-Butanol 2-Butanol 2-methyl-Propanol t-Butanol	CH ₃ (CH ₂) ₃ OH CH ₂ CH ₂ CHOHCH ₃ CH ₃ CH(CH ₃)CH ₂ OH C(CH ₃) ₃ COH

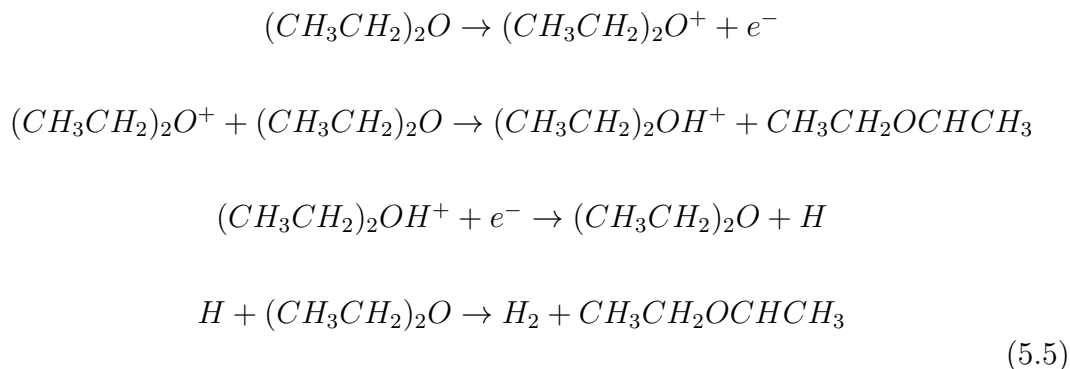
Table 5.4: Table listing the masses found by thermally desorbing 1 L C₆H₆ on 250 L of CH₃OH after exposing the ice to 250 eV electron irradiation for for ~ 700 seconds. The assignment was assumed to be the same as reported by Kaiser [20].

bulk solid is channelled to reaction pathways rather than to exciton formation and desorption of the adsorbate, maybe because of the excess of carbon atoms in the underlayer films. Further investigations need to be carried out to properly assess the decomposition mechanism for the three substrates (H₂O, CH₃OH, and (CH₃CH₂)₂O) occurring during the irradiation in these particular experiments.

Vast literature exists on the radiolysis of ASW [50], and particularly enlightening is the work of Kimmel *et al.* [34, 35, 51]. The reactions occurring between the ionising radiation and the condensed H₂O leads to a variety of channels producing oxidising and reducing species:



In contrast, no studies of electron irradiation of solid $(\text{CH}_3\text{CH}_2)_2\text{O}$ have been found to date. Nonetheless, recognising that all ionising radiation interacting with molecular solids seem to develop a common chemistry, γ -radiolysis of liquid $(\text{CH}_3\text{CH}_2)_2\text{O}$ can be regarded as a reasonable basis for the electron-induced chemistry occurring in solids as in the experiments above [52]:



In all these processes one key reaction is recurrent for all the three ices: H_2 formation. In fact, during the EPD experiments of C_6H_6 on CH_3OH or $(\text{CH}_3\text{CH}_2)_2\text{O}$, the ion gauge read an increase of five or even eight times the base pressure (10^{-10} Torr), that could not possibly be linked to C_6H_6 desorbing, but must be from different species. Thus, in order to ascertain the role of electron-induced chemistry (EIC) over EPD, experiments for 1 L of C_6H_6 on top of the three ices were repeated following $\frac{m}{z} = 2$ instead of 78. It is important to stress that the following results are just preliminary, and need to be further extended (*e.g.* effect of C_6H_6 coverage, electron energy, replica with isotopes). In addition to H_2O , CH_3OH and $(\text{CH}_3\text{CH}_2)_2\text{O}$, also an ice of D_2O was used to reduce the background noise ($\frac{m}{z} = 4$) and tentatively distinguish between the contribution to the process from the adsorbate and the substrate. **Figure 5.12** displays the H_2 (or D_2) traces for $\frac{m}{z} = 2$ ($\frac{m}{z} = 4$) during electron irradiation of the samples (EIC curves). Without a full set of the experiments with d-methanol, d-diethyl ether and d-benzene or of pure ices, it is not possible to quantify from where the contribution of the observed H_2 EIC signal comes from. There are three possibilities:

1. a physical process, such as sputtering of the ices or a consequence of the EPD process;
2. the dehydrogenation of C_6H_6 ;
3. the dehydrogenation of the underlying ice.

In principle, when C_6H_6 EPD occurs, one or more H_2O molecules could be dragged along. However, all the species considered, desorbing as whole or in clusters, have none or little contribution to the signal at $\frac{m}{z} = 2$. What is more, by simply comparing the order of magnitude of the intensities in the EPD and in

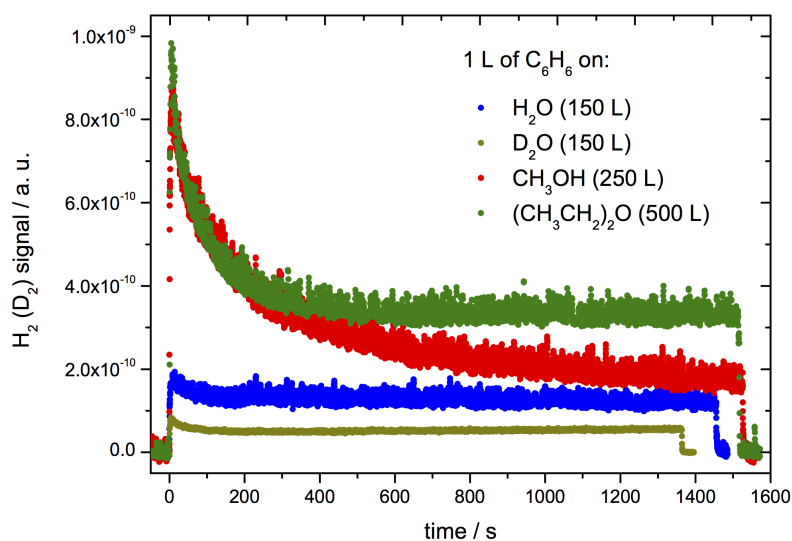


Figure 5.12: Molecular hydrogen, H_2 , formation during irradiation of 1 L of C_6H_6 on thick films of H_2O (150 L), CH_3OH (250 L), or $(CH_3CH_2)_2O$ (500 L). D_2 formation is also shown from the irradiation of 1 L of C_6H_6 on 150 L of D_2O . Irradiation was conducted with 250 eV electrons and beam current of 150 nA.

the EIC traces, the QMS ion signal carried by C_6H_6 molecules is too small and comparable to the fluctuations due to the noise in the EIC plots. Therefore, these facts exclude the first possibility and suggest that the observed curves are linked to chemical transformations.

In fact, given the striking differences between the systems for a fixed coverage of C_6H_6 (1 L), it can be argued that the observed distinct behaviours depend solely on the chemical nature of the substrates, while C_6H_6 plays a marginal role if not negligible (this still does not distinguish between the remaining two possibilities). The observed changes in the QMS signal of the curves for the three ices (**Figure 5.12**) might be too high for just 1 L of adsorbate, when taking into account that the different substrates can dehydrogenate C_6H_6 with distinct yields during irradiation. This fact poses questions about the second possibility listed above. Moreover, it was noted that the increase of the base pressure at the ion gauge, during the electron irradiation of 20 L, and 50 L of C_6H_6 on $(CH_3CH_2)_2O$ was much less (by a factor of two or three), than the same experiments with thinner C_6H_6 films. This means that either an important role of C_6H_6 dehydrogenation can be discarded or that, although in thicker films C_6H_6 dehydrogenation still occurs at the ice/ C_6H_6 interface, the overlayers might act as a cap.

Additional experiments are needed to definitively discard the second hypothesis, however, this might be feasible in the case of ASW. In the blue trace in **Fig-**

ure 5.12, the sudden increase of the H_2 forming from amorphous H_2O is in full agreement with the *prompt* signal in previous electron irradiation experiments of pure ices (thus, no C_6H_6) [33]. The similarity favours the interpretation of dehydrogenation occurring from ASW only and without involving C_6H_6 . Detection of molecular hydrogen is explained as forming at the vacuum interface (in **Figure 5.12** ASW/ C_6H_6 interface), probably from unimolecular decay of H_2O^* or H_3O^* that results from electron-ion recombination and direct excitation [53, 54]. The so-called *dose dependant* signal arises only after 500 s and it was interpreted as H_2 forming at the metal interface. This means that for the first 500 s of irradiation, the ice is thick enough that phenomena only at the C_6H_6 interface can be observed. If the QMS sensitivity is roughly the same for masses 2 and 4, and if it is assumed that the observed signal originates from the H_2O ice, then the different intensity detected in the two EIC traces for D_2O and H_2O (almost a factor of two) might be symptomatic of distinct efficiency in the exciton migration and/or energy transfer correlated to the isotopic substitution. Unfortunately, again, these data are not enough to draw a satisfactory conclusion about this matter and further investigations should be carried out in the future along a QMS calibration for masses 2 and 4.

CH_3OH and $(\text{CH}_3\text{CH}_2)_2\text{O}$ ices are, in contrast with H_2O , thick enough that only the *prompt* signal is detected, since the decay is continuous for over 20 minutes. The two curves are noticeably different between each other and in comparison with the ASW. Especially in the first moments, the increase of H_2 is considerably higher, almost an order of magnitude, for both CH_3OH and $(\text{CH}_3\text{CH}_2)_2\text{O}$ ices than it is on condensed H_2O . Then, around 200 s, the H_2 produced from CH_3OH keeps decaying gently, while that formed from $(\text{CH}_3\text{CH}_2)_2\text{O}$ reaches a steady plateau for the entire length of the experiment. This could be related both to the difference of thickness between the two solids (19 nm *vs* 30.2 nm) and to the different efficiency and nature of H_2 formation. As shown above, the process investigated consists in a unimolecular reaction in the case of CH_3OH , while it is bimolecular for $(\text{CH}_3\text{CH}_2)_2\text{O}$. Of course these considerations, do not take into account the contribution to H_2 formation from the decomposition of other species that form during the irradiation. In fact, statistically, $(\text{CH}_3\text{CH}_2)_2\text{O}$ would lead to more products bearing H atoms, especially at longer exposures to electron fluences.

5.4.3 EPD *versus* EIC

The plots in **Figure 5.12** are just a glimpse of the complex and rich chemistry taking place during the irradiation and additional experiments are needed to properly compare the EIC curves. However, it is desirable to estimate the time decay constants (and cross-section) for the global H₂ formation in the three molecular solids, capped by 1 L of C₆H₆, as to qualitatively compare these values to those associated to the C₆H₆ EPD curves. A bi-exponential function was used to fit the data starting from the maximum value, when irradiation begins, up to 600 s, to be consistent with the range considered for the C₆H₆/ASW series. The S/N ratio is too poor in the EIC trace associated with H₂O to be analysed, therefore the choice to fit the data for the D₂O ice was made. In the latter case, a smaller time scale (500 s) was adopted for the fit since the signal clearly begins to rise around 600 s (*dose dependent* signal, see bottom panel in **Figure 5.13**). The additional experiment of 1 L of C₆H₆ on 150 L of D₂O allows us to follow the D₂ kinetics during the electron irradiation by monitoring $\frac{m}{z} = 4$ instead of $\frac{m}{z} = 2$. This has the benefit of a greater signal-to-noise ratio than H₂ and it will certainly not contain any contribution arising from the possible dehydrogenations of the aromatic molecule. Values of τ and fits are shown in **Figure 5.13**, while cross-sections are summarised in **Table 5.5**. Note that the value of the σ associated with the fast component in the EIC curves is high for all the systems, and it is greatest for D₂O. It follows that it might be sensible to assume that dehydrogenation of C₆H₆ is negligible, and thus from now on, whether the ASW ice is made of H₂O or its deuterated analogous, the kinetics involved for H₂ (D₂) formations are considered to be the same². **Table 5.5** can be read in two different ways: “vertically” (or inter-system) and “horizontally” (or inter-process). The former comparison outlines how each process (H₂ EIC or C₆H₆ EPD) varies when moving from a system to the other. The latter comparison highlights the competition between chemistry and physics during electron irradiation for each binary ice. Let us consider both of them.

Looking at the fast component, the time constant is smaller for H₂O and (CH₃CH₂)₂O ices, 8 ± 2 s and 13 ± 1 s respectively, while it is larger for solid CH₃OH (27 ± 2 s). In the same order, the cross-sections are $(1.3 \pm 0.2) \times 10^{-15}$ cm², $(8 \pm 2) \times 10^{-16}$ cm² and $(3.9 \pm 0.8) \times 10^{-16}$ cm². Focusing on the slow component, it can be seen that the trend is the same, with τ being the smallest for H₂O ices, followed by (CH₃CH₂)₂O and then CH₃OH. A proper and truly reliable comparison would require similar thicknesses of the three solids, because erosion of the films

²However, this assumption is yet to be confirmed with further experiments on C₆D₆/H₂O ices and a proper calibration of the QMS for masses 2 and 4.

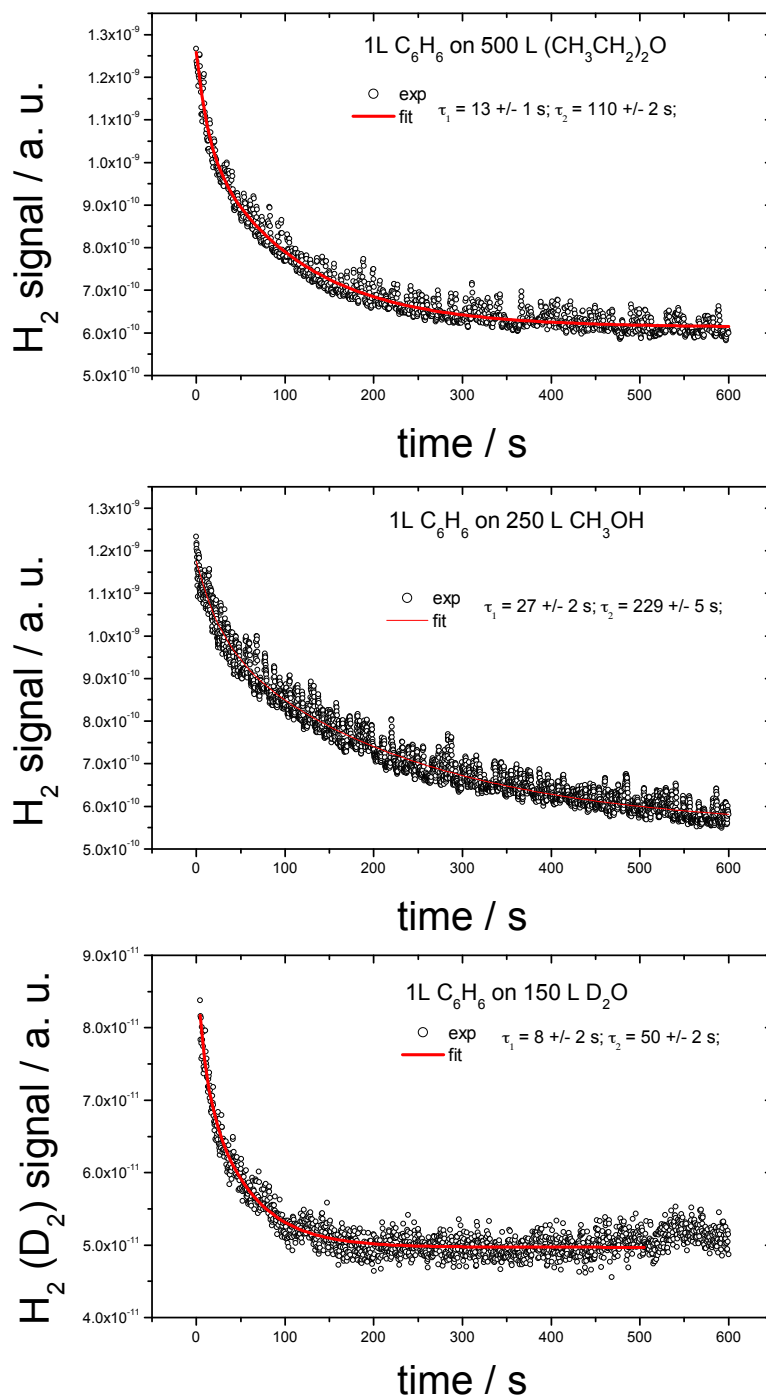


Figure 5.13: H₂ formation during irradiation of C₆H₆ (1 L) on thick film of (CH₃CH₂)₂O (500 L) or CH₃OH (250 L). D₂ formation is also shown from the irradiation of C₆H₆ (1 L) on D₂O (150 L). In the third subplot at the bottom, $\frac{m}{z} = 4$ was followed instead of $\frac{m}{z} = 2$ in order to distinguish between dehydrogenation of C₆H₆ and H₂O. Irradiation was conducted with 250 eV electrons and beam current of 150 nA.

XOX'/C ₆ H ₆	EPD		EIC
		σ_1 / cm^2	
		σ_2 / cm^2	
H ₂ O (EPD)	$(5.5 \pm 2.0) \times 10^{-16}$	$((1.3 \pm 0.1) \times 10^{-15}$ [1])	$(1.3 \pm 0.2) \times 10^{-15}$
D ₂ O (EIC)	$(5.5 \pm 2.5) \times 10^{-17}$	$((5.9 \pm 0.9) \times 10^{-17}$ [1])	$(2.7 \pm 0.5) \times 10^{-16}$
CH ₃ OH	negligible	negligible, $\sim 10^{-17}$?	$(3.9 \pm 0.8) \times 10^{-16}$ $(6 \pm 1) \times 10^{-17}$
(CH ₃ CH ₂) ₂ O	negligible	negligible, $\sim 10^{-17}$?	$(8 \pm 2) \times 10^{-16}$ $(1.2 \pm 0.2) \times 10^{-16}$

Table 5.5: Table summarising the results from all the series of electron irradiation experiments. The errors reported for the EIC values are obtained from the propagation of the error on the current and on the decay constant. Although not directly determined, the second component of the C₆H₆ EPD cross-section from CH₃OH and (CH₃CH₂)₂O can be assumed $\sim 10^{-17} \text{ cm}^2$, as estimated from electron irradiation of multilayer C₆H₆ [2]. Note that X and X' can both be: H (D) atoms or CH₃ and/or CH₃CH₂ groups. For the C₆H₆/c-ASW experiments D₂O was employed for the EIC traces, while H₂O was used for the EPD decays. In the latter case, literature values [1] are also reported.

due to the incident beam might be significant for smaller doses (*e.g.* 100 L) after $\sim 500 - 600$ s. This may also explain why there is a slow decay in the CH₃OH ices compared to the other cases. In addition to this, it should be recalled that more species are formed during the electron irradiation of (CH₃CH₂)₂O than in ASW or solid CH₃OH. These products might, in turn, dehydrogenate and should be taken into account to quantify the amount of H₂ derived from one starting molecule. Therefore, the σ values so far reported for each EIC curve should be regarded as gross indication of the overall process.

It is not possible, at this stage, to compare the C₆H₆ EPD cross-sections in the different ices, because of the poor quality signal in the traces obtained for C₆H₆/CH₃OH and C₆H₆/(CH₃CH₂)₂O. Although an indicative value of $\sim 10^{-17} \text{ cm}^2$ could be assumed from electron irradiation experiments of C₆H₆ multilayer. A direct measurement could be obtained by post-irradiation TPD traces or RAIR spectra as to estimate the C₆H₆ loss, although both the methods still require the identification of any other competitive process involved. This goes beyond the scope of this thesis, which, on the other hand, successfully proves that the efficient C₆H₆ EPD is quenched on CH₃OH and (CH₃CH₂)₂O substrates.

Returning to the previously mentioned “horizontal” comparison, electron-induced chemistry seems to be the dominating process, for all the systems investigated. However, there is a marked difference that is highlighted by the detected partial pressure at the QMS (**Figure 5.12**). In fact, irradiation of $(\text{CH}_3\text{CH}_2)_2\text{O}$ and CH_3OH ices favours chemistry over other possible processes (*e.g.* collective modes, desorption). It is not surprising that the EIC decay constants in these two cases are reminiscent of the $\sim 14.5 \pm 1.7$ s found for τ_1 in the EPD trace of 5 L of C_6H_6 on ASW, while almost no C_6H_6 desorption is observed. Thus, the cross section values for EIC of $\text{C}_6\text{H}_6/\text{CH}_3\text{OH}$ and $\text{C}_6\text{H}_6/(\text{CH}_3\text{CH}_2)_2\text{O}$ is comparable to the σ_1 of the C_6H_6 EPD from ASW³. This further suggests that reactive pathways are the dominant route for these systems to relax rather than passing the energy on to C_6H_6 . With ASW, on the other hand, EIC is still very efficient, but just as much as other processes like EPD, and it could not be otherwise since the mechanism at the base is exactly the same: excitons forming in the bulk of H_2O (D_2O), migrating to the interface to then promote both the H_2 (D_2) formation and C_6H_6 desorption.

One more fact can be highlighted concerning EPD and EIC behaviour with ASW ices: τ_2 in the EIC curve is 50 s, significantly smaller than the 240 s found for τ_2 in the EPD curves (obviously σ values have opposite trends). Therefore, although excitons might still be the primary cause of C_6H_6 desorption even at longer times, the rate determining step (in the slow component) is bound to a process that occurs on a longer time scale. In other words, if H_2 (D_2) formation also takes place with a delayed contribution around 50 s, C_6H_6 might need to diffuse over the substrate and interact favourably with the H_2O (D_2O) interface, hence additional delay, to accept the excitation.

In conclusion, electron-promoted desorption of C_6H_6 is a minor event taking place during irradiation of “organic” solids compared to ASW ices. While the data so far reported refer to the final outcome of the gross process (*e.g.* H_2 formation and/or C_6H_6 EPD), the details of the mechanisms are still unclear, especially in the first seconds of irradiation. Further work should determine what other chemical processes occur, along H_2 formation; parallel kinetics that might lead to the same products should also be identified, along with the branching ratios and yields. Therefore, it is necessary to conduct post-irradiation TPDs, collect RAIR spectra at certain times during electron bombardment, and repeat the experiments with different isotopes, but most importantly, a much faster

³This is actually more of an “oblique” rather, than an “horizontal” comparison, since the C_6H_6 EPD is negligible on both CH_3OH and $(\text{CH}_3\text{CH}_2)_2\text{O}$ ices.

detection of the desorbing species should be achieved by means of time-of-flight MS measurements.

5.5 Astrophysical Implications and Conclusions

The experiments discussed in this chapter simulate the secondary electron flux forming subsequent to ionising radiation of interstellar ices. As already said, there are several sources that could lead to ionisation and, hence, to secondary electrons: X-rays, γ -rays, cosmic rays and in some extent also energetic VUV photons. Particularly noteworthy is the case of cosmic ray protons; the differential fluxes as a function of energy that was reported by Shen *et al.* [55] is relatively flat between 1 - 100 MeV, with a maximum at 50 MeV. The integrated flux is $\sim 1 \text{ cm}^{-2} \text{ s}^{-1}$ in this energy range. The distribution of secondary electrons produced by primary ions (^1H , ^4He) in liquid water is only slightly dependent on the energy of the ions themselves (**Figure 5.14**) [14], with a mean electron energy between 38.6 eV and 65.1 eV for H^+ ions from 100 keV up to 100 MeV; while the most probable electron energy decreases from 14.0 eV to 9.1 eV. Although these distributions

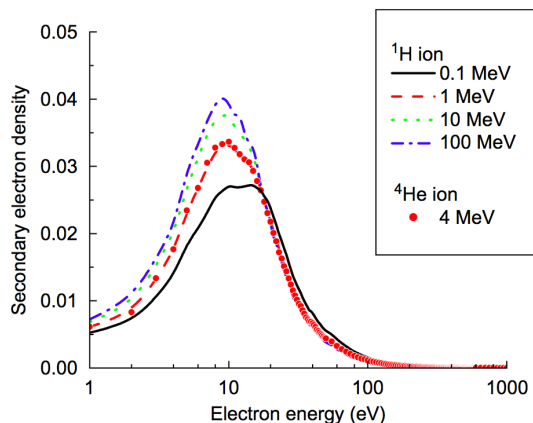


Figure 5.14: Energy distribution of secondary electrons generated in primary events in liquid water for different incident H^+ energies and for ^4He ions. Plots taken from [14]

were obtained for liquid water, they are not expected to significantly change in ASW, which has often been used in the past as model of liquid phase [50]. The curves in **Figure 5.14** match nicely with the electronic excitations of solid H_2O (8.7 eV, 10.4 eV and 14.5 eV, and 21 eV). Therefore, it can be concluded that cosmic rays impacting the icy mantles, rich in H_2O , of the interstellar dust yield a secondary electron trail within the films having energies resonant with valence electronic excitations of solid H_2O . The electron beam used in the experiments reported herein would likely be inelastically scattered and would ionise molecules forming a similar flux of electrons to that associated to cosmic rays. Therefore,

the reported results are appropriate for consideration in an astrophysical context. It should be stressed once again that the relative abundance of C_6H_6 in dense clouds is not sufficient for the formation of thick layers, however, solid H_2O is certainly the main component of the ice mantles and presents peculiarities that could favour EPD of any small molecule, including CO. While this last point needs to be proven in future investigations, it seem to be a sensible assumption. Therefore, the budget of a molecule such as carbon monoxide on the ASW would be the result of several processes:

- Adsorption from the gas phase;
- 1. Thermal desorption;
- 2. Photo-desorption induced by VUV light;
- 3. Electron-promoted desorption;
- Reduction to CH_3OH as molecular and atomic H is produced by the excitons in ASW in addition to the H impinging from the gas-phase in ISM environments.

It is clear that an additional efficient step for desorption might potentially delay the mantle enrichment in CO and hence CH_3OH formation, as well as other molecules. In order to ascertain the impact of EPD from ASW on astrophysical scale, it is desirable to quantitatively compare the relevance of electron-promoted desorption to photo-desorption (PD) of just CO on ASW at sub-monolayer, and monolayer level. Linnartz, Öberg and co-workers [56] have measured a value of 3×10^{-3} molecule photon $^{-1}$ for PD yields of CO using a VUV lamp with a flux of $\sim 6 \times 10^{13}$ photons cm $^{-2}$ s $^{-1}$. This process was shown to be independent of the thickness of the CO ice confirming that only the top few layers are directly involved. The same value of PD yield was also reported by Fillion *et al.* as $2 \pm 1 \times 10^{-3}$ molecule photon $^{-1}$ [57, 58]. In order to compare these findings with the EPD results, the CO PD rate, k_{PD}^{CO} , can be estimated under astrophysical conditions using the following equation:

$$k_{PD}^{CO} = \Phi \sigma_{abs} F_{VUV} \quad (5.6)$$

where Φ is the yield of the process (3×10^{-3}); σ_{abs} is the cross-section of CO in the VUV range between 120 nm and 160 nm (4.7×10^{-18} cm 2 [59]); and F_{VUV} is the estimated VUV flux in dense clouds. The latter, is dominated by the H_2 emission excited by cosmic rays and is typically about 5×10^3 photon cm $^{-2}$ s $^{-1}$ [60, 61]. Therefore a value of 7.0×10^{-17} s $^{-1}$ is obtained. The estimate of EPD rate for CO on ASW is less straightforward and requires few assumptions to be made:

- The cross-section is assumed to be the same as for C₆H₆ ($5 \times 10^{-16} \text{ cm}^2 - 10^{-15} \text{ cm}^2$);
- Hydrogenation of CO from ASW is not considered at this stage. Further experiments are needed to evaluate the EPD/EIC branching ratio.
- Only the fast component will be considered as this relates to isolated molecules on the ASW surface and it might be more relevant to astrophysical irradiation times;
- The yield of secondary electrons produced by cosmic rays in 5 nm of c-ASW (0.87 g cm^{-3}) will be estimated using SRIM [62, 63] for a flux of $1 \text{ cm}^{-2} \text{ s}^{-1}$ 1 MeV H⁺ ions;
- The energy deposited per ionisation event is assumed to be twice the ionisation potential of the target molecule being ionised (11.0 eV) [64, 65]
- No direct effect of the incoming ions will be considered on CO, which will be assumed to be “transparent”.

As **Figure 5.15** clearly displays, for an incident H⁺ flux with energy ranging from 10 keV to 100 MeV all the energy is lost in scattering with the electron density within the target molecular solid, while the scattering due to the nuclei is several orders of magnitude lower. The energy deposited in the film associated with all inelastic electronic events in $1 \mu\text{m}$ is $20 \text{ keV } \mu\text{m}^{-1}$, divided by the amount of energy transferred per ionisation event and taking into account a penetration depth of 5 nm, gives the secondary electron yield (4.5 electrons). This yields a secondary electron flux (F_{e^-}) in c-ASW of $4.5 \text{ electrons cm}^{-2} \text{ s}^{-1}$ for $1 \text{ cm}^{-2} \text{ s}^{-1}$ 1 MeV H⁺ incident ions. The EPD rate constant, k_{EPD}^{CO} , is defined as:

$$k_{EPD}^{CO} = \sigma F_{e^-} \quad (5.7)$$

and its value is found in the range $(2.5 - 4.5) \times 10^{-15} \text{ s}^{-1}$ depending on the cross-section value. The ratio between the two non-thermal desorption rates is

$$\frac{k_{EPD}^{CO}}{k_{PD}^{CO}} = 64 - 36$$

In conclusion, provided that all the assumptions made above are proven to be sensible, the electron-promoted desorption for an adsorbate on ASW, such as CO, cannot be ignored and should be taken into account in more evolved astrochemical models as much as other non-thermal processes. In contrast, once a CH₃OH film grows, all the electron-promoted processes from the ASW ice (molecular oxygen, hydrogen, and water desorption yields) are quenched by CH₃OH, while the

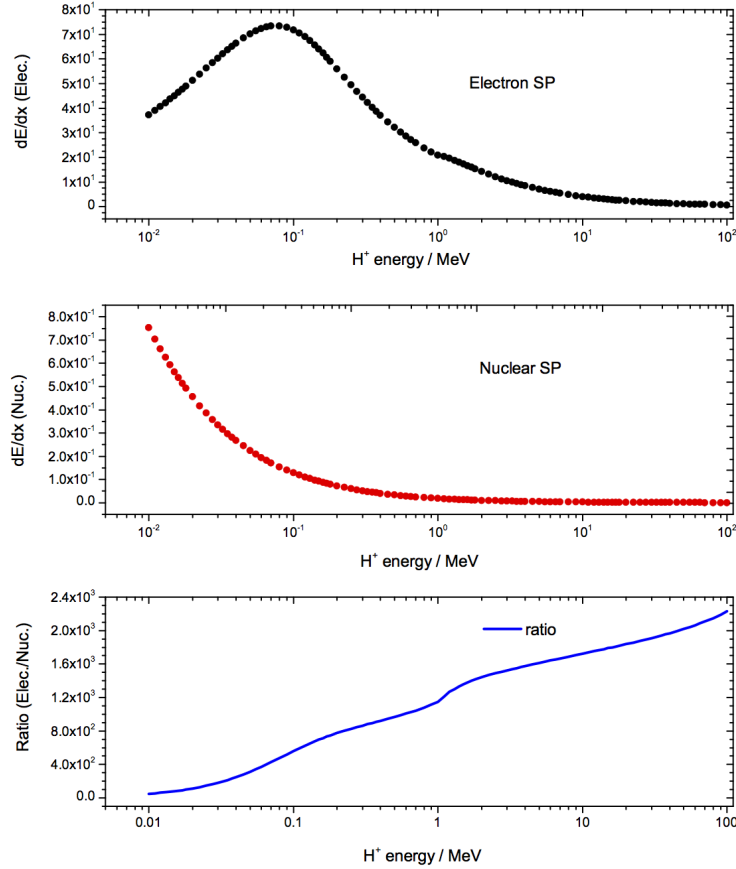


Figure 5.15: Energy deposited in *c*-ASW by electron and nuclear scattering per μm^{-1} and per H^+ ion having energy between 10 keV and 100 MeV using the SRIM software. The plot at the bottom displays the ratio between the energy deposited in the ice by the two inelastic scattering events displaying the predominance of electron scattering in the energy range of interest.

CH_3OH EPD yield increases proportionally to the CH_3OH coverage [51]. Once a multilayer of CH_3OH is formed, the results presented in this chapter point to a significant reduction of the EPD yields of C_6H_6 -like molecules and probably other species including CO, in favour of an active chemical reactivity that accelerates the accretion of the icy mantle and its enrichment with larger and more complex molecules.

It is important to stress that experiments of electron irradiation of ASW gave evidence for a common underlying mechanism to both H_2 formation and C_6H_6 desorption. The cartoon in **Figure 5.16** summarises the findings reported so far for H_2O ices, and highlights the competition between physical processes, EPD, and chemistry, EIC in form of H_2 or reduction of adsorbates (*e.g.* HCO and CH_3OH forming from CO). Therefore, the validity of the model previously proposed for CO is limited by two unknowns: (i) the explicit CO EPD cross-section, (ii) and the relevance of CO reactivity at the interface during electron irradiation.

tion. ASW/CO/ASW ices have been investigated by Kimmel and co-workers [35] proving both oxidation and reduction of CO to occur within the solid H₂O film. However, the competition of EPD and EIC for CO at the ASW interface is yet to be determined, and future works will address this matter.

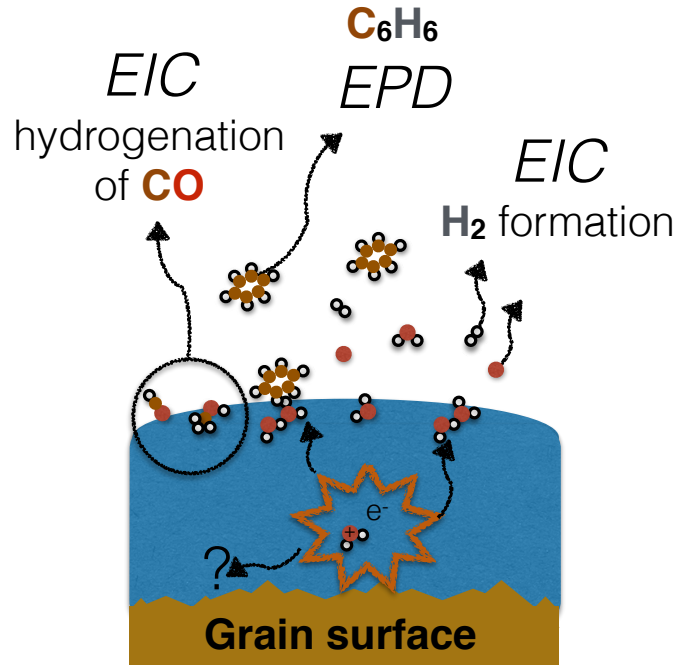


Figure 5.16: Cartoon representing exciton formation in the solid H₂O bulk during electron irradiation and their migration to the vacuum interface leading to three main possible outcomes: C₆H₆ desorption, H₂ formation, reactions at the ASW interface such as hydrogenation of CO. The question mark indicates unknown processes at the SiO₂/H₂O interface.

Bibliography

- [1] J. D. Thrower, M. P. Collings, F. J. M. Rutten and M. R. S. McCoustra, *Chem. Phys. Lett.*, 2011, **505**, 106.
- [2] J. D. Thrower, *PhD thesis*, Heriot-Watt University, 2009.
- [3] P. Modica and M. E. Palumbo, *Astron. Astrophys.*, 2010, **519**, 22.
- [4] P. Modica, M. E. Palumbo and G. Strazzulla, *Planet. Space Sci.*, 2012, **73**, 425.
- [5] Y. J. Chen, A. Chiaravella, G. M. M. Caro, C. Cecchi-Pestellini, A. Jimenez-Escobar, K. J. Juang and T. S. Yih, *Astrophys. J.*, 2013, **778**, 162.
- [6] G. M. Muñoz Caro, U. J. Meierhenrich, W. A. Schutte, B. Barbier, A. Arcones Segovia, H. Rosenbauer, W. H.-P. Thiemann, A. Brack and J. M. Greenberg, *Nature*, 2002, **416**, 403.
- [7] C. Lee, J. Kim, E. Moon, Y. C. Minh and H. Kang, *Astrophys. J.*, 2009, **697**, 428.
- [8] S. H. Cuylle, D. Zhao, , G. Strazzullai and H. Linnartz, *Astron. Astrophys.*, 2014, **570**, A83.
- [9] S. H. Cuylle, *PhD thesis*, Leiden University, 2015.
- [10] S. Jheeta, A. Domaracka, S. Ptasinska, B. Sivaraman and N. Mason, *Chem. Phys. Lett.*, 2013, **556**, 359.
- [11] P. Maksyutenko, L. G. Muzangwa, B. M. Jones and R. F. Kaiser, *Phys. Chem. Chem. Phys.*, 2015, **17**, 7514.
- [12] B. Maté, I. Tanarro, M. A. Moreno, M. Jimenez-Redondo, R. Escribano and V. J. Herrero, *Faraday Discuss.*, 2014, **168**, 267.
- [13] M. D. Boamah, K. K. Sullivan, K. E. Shulenberger, C. M. Soe, L. M. Jacob, F. C. Yhee, K. E. Atkinson, M. C. Boyer, D. R. Haines and C. R. Arumainayagam, *Faraday Discuss.*, 2014, **168**, 249.

- [14] S. Pimblott and J. Verne, *Rad. Phys. and Chem.*, 2007, **423**, 1244.
- [15] N. J. Mason, B. Nair, S. Jheeta and E. Szymanska, *Faraday Discuss.*, 2014, **168**, 235.
- [16] T. Lamberts, X. de Vries and H. M. Cuppen, *Faraday Discuss.*, 2014, **168**, 327.
- [17] E. Szymanska, I. Cadez, E. Krishnakumar and N. J. Mason, *Phys. Chem. Chem. Phys.*, 2014, **16**, 3425.
- [18] E. Szymanska, N. J. Mason, E. Krishnakumar, C. Matias, C. Mauracher, P. Scheier and S. Denifl, *Int. J. Mass Spectrom.*, 2014, **365-366**, 356.
- [19] S. Maity, R. I. Kaiser and B. M. Jones, *Faraday Discuss.*, 2014, **168**, 485.
- [20] S. Maity, R. I. Kaiser and B. M. Jones, *Phys. Chem. Chem. Phys.*, 2015, **17**, 3081.
- [21] D. Menzel and R. Gomer, *J. Chem. Phys.*, 1964, **41**, 3311.
- [22] D. Menzel and R. Gomer, *J. Chem. Phys.*, 1964, **41**, 3329.
- [23] N. Nishijima and F. M. Propst, *Phys. Rev.*, 1970, **B2**, 2368.
- [24] T. E. Madey and J. T. Jates, *J. Vac. Sci. Technol.*, 1971, **8**, 525.
- [25] M. I. Datsiev, I. Belyakov and Z. Tekhn, *Sov. Phys. Tech. Phys.*, 1968, **13**, 554.
- [26] J. E. Whitten and R. Gomer, *Surf. Sci.*, 1996, **347**, 280.
- [27] R. L. Summers, *Empirical observations on the sensitivity of hot cathode ionization type vacuum gauges*, National Aeronautics and Space Administration, Washington, D. C., 1969.
- [28] G. A. Kimmel, Z. Dohnálek, K. P. Stevenson, R. S. Smith and B. D. Kay, *J. Chem. Phys.*, 2001, **114**, 5295.
- [29] M. H. Moore, *Astrophys. J.*, 1992, **401**, 353.
- [30] G. Strazzulla, G. A. Baratta, G. Leto and G. Foti, *Europhys. Lett.*, 1992, **18**, 517.
- [31] G. Leto and G. A. Baratta, *Astron. Astrophys.*, 2003, **397**, 7.
- [32] W. Zheng, D. Jewitt and R. I. Kaiser, *J. Phys. Chem. A*, 2009, **113**, 11174.

- [33] N. G. Petrik and G. A. Kimmel, *Phys. Rev. Lett.*, 2003, **90**, 166102–1.
- [34] N. G. Petrik and G. A. Kimmel, *J. Chem. Phys.*, 2005, **123**, 054702.
- [35] N. G. Petrik, R. J. Monckton, S. P. K. Koehler and G. A. Kimmel, *J. Chem. Phys.*, 2014, **140**, 204710.
- [36] *Theory of Condensed Matter Group Cambridge, CASINO V 2.13*, <http://www.gel.usherbrooke.ca/casino/What.html>, 2014.
- [37] P. Hovington, D. Drouin and R. Gauvin, *Scanning*, 1997, **19**, 1.
- [38] P. Jenniskens, D. F. Blake, M. A. Wilson and A. Pohorille, *Astrophys. J.*, 1995, **455**, 389.
- [39] J. A. Noble, C. Martin, H. J. Fraser, P. Roubin and S. Coussan, *J. Phys. Chem. C*, 2014, **118**, 20488.
- [40] A. Otto, M. J. Lynch and J. Aust, *Phys.*, 1970, **23**, 609.
- [41] M. Heller, R. N. Hamm, R. D. Birkhoff and L. R. Painter, *J. Chem. Phys.*, 1974, **60**, 3483.
- [42] J. Daniels, *Opt. Commun.*, 1971, **3**, 240.
- [43] J. A. LaVerne and A. Mozumder, *Radiat. Res.*, 1993, **133**, 282.
- [44] C. D. Wilson, C. A. Dukes and R. A. Baragiola, *Phys. Rev. B*, 2001, **63**, 121101.
- [45] R. D. Leapman and S. Sun, *Ultramicroscopy*, 1995, **59**, 71.
- [46] K. Kobayashi, *J. Phys. Chem.*, 1983, **87**, 4317.
- [47] G. A. Kimmel, T. M. Orlando, C. Vézina and L. Sanche, *J. Chem. Phys.*, 1994, **101**, 3282.
- [48] C. J. Bennett, S. H. Chen, B. J. Sun, A. H. Chang and R. I. Kaiser, *Astrophys. J.*, 2007, **660**, 1588.
- [49] C. J. Bennett and R. I. Kaiser, *Astrophys. J.*, 2007, **661**, 899.
- [50] B. C. Garrett, D. A. Dixon, D. M. Camaioni, D. M. Chipman, M. A. Johnson, C. D. Jonah, G. A. Kimmel, J. H. Miller, T. N. Rescigno, P. J. Rossky, S. S. Xantheas, S. D. Colson, A. H. Laufer, D. Ray, P. F. Barbara, D. M. Bartels, K. H. Becker, K. H. Bowen, S. E. Bradforth, I. Carmichael, J. V. Coe, L. R. Corrales, J. P. Cowin, M. Dupuis, K. B. Eisenthal, J. A. Franz,

- M. S. Gutowski, K. D. Jordan, B. D. Kay, J. A. LaVerne, S. V. Lymar, T. E. Madey, C. W. McCurdy, D. Meisel, S. Mukamel, A. R. Nilsson, T. M. Orlando, N. G. Petrik, S. M. Pimblott, J. R. Rustad, G. K. Schenter, S. J. Singer, A. Tokmakoff, L.-S. Wang and T. S. Zwier, *Chem. Rev.*, 2005, **105**, 355–390.
- [51] C. A. Minta, N. G. Petrik and G. A. Kimmel, *J. Chem. Phys.*, 2009, **130**, 104710.
- [52] M. K. M. Ng and G. R. Freeman, *J. Am. Chem. Soc.*, 1965, **87**, 1635.
- [53] B. R. Rowe, F. Vallee, J. L. Queffelec, J. C. Gomet and M. Morlais, *J. Chem. Phys.*, 1988, **88**, 845.
- [54] N. G. Adams, C. R. Herd, M. Geoghegan, D. Smith, A. Canosa, J. C. Gomet, B. R. Rowe, J. L. Queffelec and M. Morlais, *J. Chem. Phys.*, 1991, **94**, 4852.
- [55] C. J. Shen, J. M. Greenberg, W. A. Schutte and E. F. van Dishoeck, *Astron. Astrophys.*, 2004, **415**, 203.
- [56] K. I. Öberg, G. W. Fuchs, Z. Awad, H. J. Fraser, S. Schlemmer, E. F. van Dishoeck and H. Linnartz, *Astrophys. J.*, 2007, **662**, L23.
- [57] J.-H. Fillion, E. C. Fayolle, X. Michaut, M. Doronin, L. Philippe, J. Rakovsky, C. Romanzin, N. Champion, K. I. Oberg, H. Linnartz and M. Bertin, *Faraday Discuss.*, 2014, **168**, 533.
- [58] N. J. Mason, A. Dawes, P. D. Holtom, R. J. Mukerji, M. P. Davis, B. Sivaraman, R. I. Kaiser, S. V. Hoffmann and D. A. Shaw, *Faraday Discuss.*, 2006, **133**, 311.
- [59] G. A. Cruz-Diaz, G. M. M. Caro and T. S. Chen, Y. J. and Yih, *Astron. Astrophys.*, 2014, **562**, A119.
- [60] C. J. Shen, J. M. Greenberg, W. A. Schutte and E. F. van Dishoeck, *Astron. Astrophys.*, 2004, **415**, 203.
- [61] J. . Mathis, . G. Mezger and N. Panagia, *Astron. Astrophys.*, 1983, **128**, 212.
- [62] J. F. Ziegler, *SRIM/TRIM*, <http://www.srim.org>, 2013.
- [63] J. F. Ziegler, J. P. Biersack and M. D. Ziegler, *The Stopping and Range of Ions in Solids*, Pergamon Press, New York, 2008.
- [64] W. F. Schmidt and E. Illenberger, *Nukleonika*, 2003, **48**, 75.

- [65] M. Vinodkumar, K. N. Joshipura, C. G. Limbachiya, and B. K. Antony,
Nucl. Instrum. Methods Phys. Res. B, 2003, **212**, 63.

Chapter 6

Conclusions and Outlook

Contents

6.1	Introduction	231
6.2	Overall Conclusions and Future Work	231
	Bibliography	241

6.1 Introduction

This brief chapter summarises the key findings reported in the thesis with an emphasis on how the intermolecular interactions affect both the growth mechanism and desorption behaviour of the ices. On this basis, some of the possible strategies for future developments are then illustrated.

6.2 Overall Conclusions and Future Work

Chapters 3, 4 and 5 can be schematically summarised as follows in terms of main results and outlook.

Chapter 3

Pure ices of H₂O, CH₃OH and (CH₃CH₂)₂O adsorbed on amorphous SiO₂ at 20 K and 110 K were investigated by means of TPD and RAIRS. Multilayer data are consistent with literature values and bulk behaviour. At low coverages, marked variations are observed in how the three species adsorb on the same substrate. These results can be interpreted in terms of the different strengths of intermolecular forces. H₂O de-wets the SiO₂ surface as soon as it becomes mobile, overcoming a diffusive barrier of $\sim 10 - 15 \text{ kJ mol}^{-1}$, to form two dimensional islands. The multiple hydrogen-bonds established with other H₂O molecules are the driving force that leads to this thermodynamically stable state, which is more favoured than any other interaction with the SiO₂ interface. In contrast, the interaction of (CH₃CH₂)₂O with SiO₂ is significantly stronger than the dispersive forces acting in the bulk (CH₃CH₂)₂O. Thus homogeneous covering of the substrate is observed to occur with a distribution of desorption energies that hints to a non-negligible degree of chemisorption. CH₃OH, not surprisingly, exhibits an intermediate behaviour between these two limiting-cases, because bulk interactions are as stabilising as binding to the terminal silanol groups of the SiO₂ surface. Thus, CH₃OH wets the SiO₂ surface exclusively at low coverage, while islands formation is most favoured at larger exposures. TP-RAIR spectra seem to indicate a diffusive barrier of 5 - 10 kJ mol⁻¹ for CH₃OH over SiO₂, which is significantly lower than what is estimated for H₂O. However, no direct and conclusive evidence was found to identify molecular diffusion by looking at the C-H normal modes for both (CH₃CH₂)₂O and CH₃OH for several reasons: the broadness of these IR signatures, the smaller dynamic dipole moments compared to H₂O (hence less intense peaks), and the fact that any change in the molecular electronic cloud due to van der Waals interactions is extremely challenging to

observe in the condensed phase.

These findings are of fundamental interest in physical chemistry and help to understand the interactions of key components of interstellar ices, such as H₂O and CH₃OH, in different cooling environments. Desorption energies can be implemented in astrochemical models to the Arrhenius equations describing the rates for thermal desorption and mobility of these species on a bare SiO₂ grain surface. This applies particularly to the activation energies for diffusion reported in this thesis. Grains accrue their mantles in a cooling environment as going from diffuse clouds, where the average temperature is 100 K, to dense clouds, where temperature drops down to 10 K (**Figure 6.1**). Ballistic deposition, reactive accretion and limited diffusion of H₂O would form porous ices only in the latter case (stages III and IV in **Figure 6.1**), while island growth of c-ASW might follow reactive accretion of H₂O on bare grains in more diffuse (warmer) environments (stages I and II). This means that even at later stages, bare SiO₂ grain surface might be exposed to adsorb molecules such as CO or N₂, which would not be only embedded in the ice or on top of it [1].

Outlook

In order to improve estimation of the diffusive barrier of H₂O over the SiO₂ surface, a strategy based on the synergy of experimental surface science and computational chemistry is proposed below. In the last 10 years, non-linear techniques, such as sum-frequency vibrational spectroscopy, have stimulated a new era for surface-specific spectroscopy shedding light on the H₂O structure at the interfaces [2]. Vibrational spectra generally exhibit in the OH stretch region a so called “liquidlike” peak at $\sim 3400\text{ cm}^{-1}$ and an “icelike” peak at $\sim 3200\text{ cm}^{-1}$, associated with disordered and ordered structures respectively. The interpretation is still object of debate [3, 4]. Nonetheless recent studies [5, 6] report results compatible with the TP-RAIR data presented in this thesis, assigning strong H-bonds between the terminal silanol groups and H₂O molecules to the lower wavenumbers feature, while the higher energy peak is identified as resulting from the bulk or from a second population of H₂O molecules adsorbed at the quartz surface, but less strongly bound. Combining non-linear optical techniques to UHV and surface science at cryogenic temperatures might, therefore, bring conclusive and independent evidence of the relatively high diffusive barrier found for H₂O on SiO₂ as well as extending the investigation to CH₃OH and (CH₃CH₂)₂O. A further insight on the matter could be gained by computational chemistry tools. The first would consider two model silicate clusters with and without the OH group and

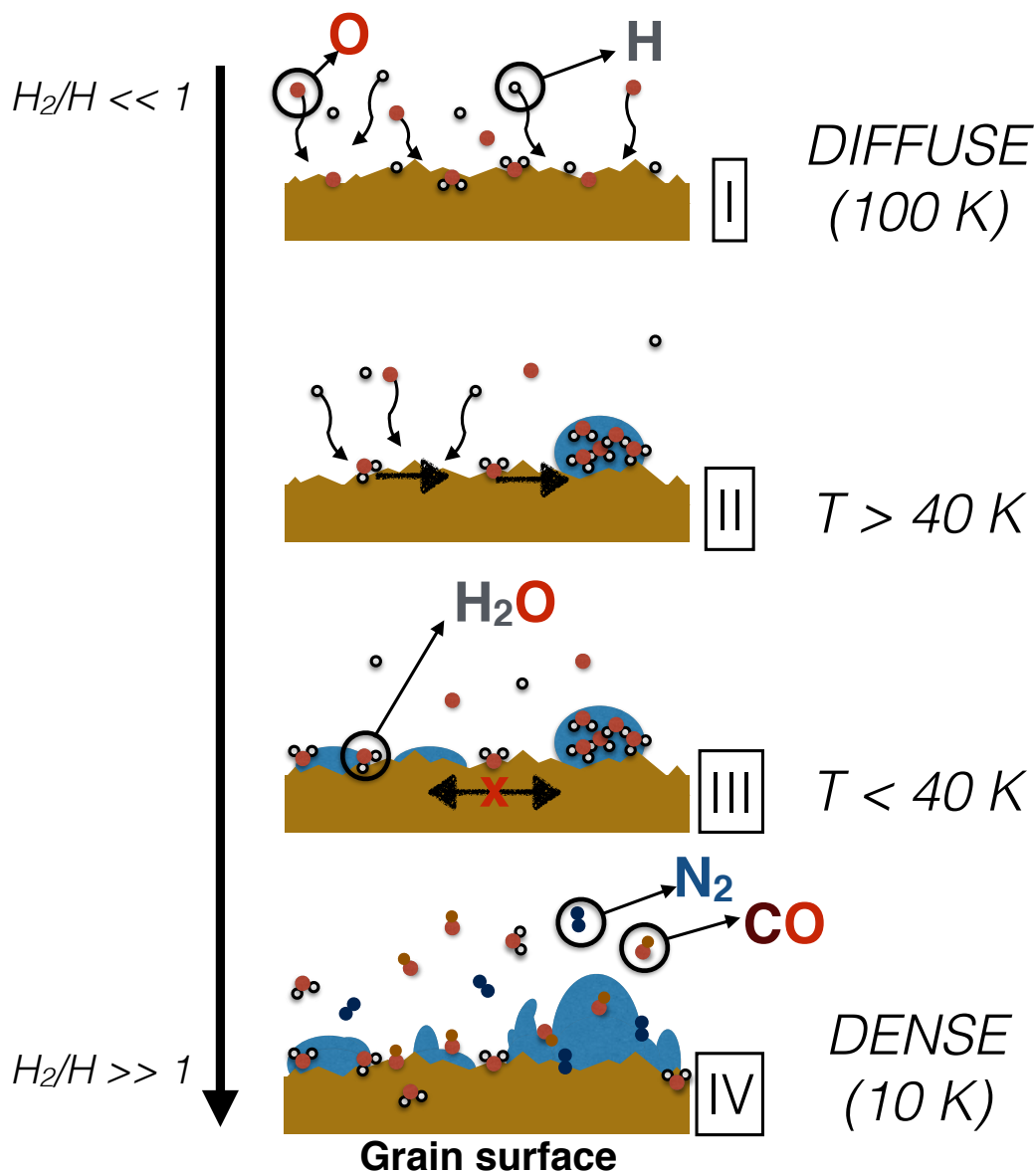


Figure 6.1: Cartoon representing the H_2O -rich mantle on bare SiO_2 grain: (I) by reactive accretion, (II) diffusion and H_2O island formation, (III) ballistic deposition and (IV) enrichment of other species on bare grain, in the solid H_2O pores, on the H_2O surface. Time evolution is illustrated in terms of molecular and atomic hydrogen abundance ratio. This is less than one in diffuse clouds, and larger than one in dark clouds.

determine the interaction with a molecule of H_2O , CH_3OH or $(\text{CH}_3\text{CH}_2)_2\text{O}$. An example is given in **Figure 6.2**, where the H_2O accepts hydrogen-bonding from the terminal silanol and at the same time interacts with a bridge oxygen (Si-O-Si) atom. The binding energy at MP2/aug-cc-pVTZ is 34.0 kJ mol^{-1} , consistent with both the schematic in **Figure 3.21** and similar calculation for SiO_2/NH_3 (38.3 kJ mol^{-1}) [7]. Obviously, in order to calculate the diffusion barrier, local and global minima of the PES are not enough, and saddle points need to be considered to detail a clear picture for the initial, final and transition states.

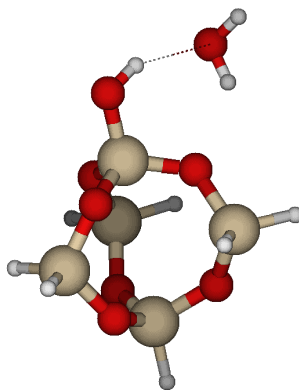


Figure 6.2: Cluster model of terminal silanol groups at the SiO_2 surface interacting with a H_2O molecule. Geometry optimisation was performed at MP2/aug-cc-pVDZ level followed by a single point at MP2/aug-cc-pVTZ to estimate the binding energy (34.0 kJ mol^{-1}).

Moreover, it would be interesting to probe the effect of more realistic grain mimics, which contain heavy atoms such as Mg and/or Fe (*e.g.* olivine or forsterite substrates) on the adsorption behaviour of the same molecules considered in **Chapter 3** with the addition of apolar ones, such as methane. TPD of H_2O performed on lunar analogs are particularly enlightening in this respect, displaying high temperature tails depending on the relative composition [8].

Chapter 4

This chapter describes the film growth of binary layered ices of $\text{C}_6\text{H}_6/\text{CH}_3\text{OH}$ or $\text{C}_6\text{H}_6/(\text{CH}_3\text{CH}_2)_2\text{O}$. TPD experiments and RAIR spectra displayed similarities for C_6H_6 adsorbing on CH_3OH to its behaviour on ASW, despite the results being complicated by other processes, such as crystallisation and mixing. Furthermore, displacement and phase change of the underlayer were also observed during C_6H_6 dosing and explained in terms of simple gas kinetics. These findings question the reproducibility of some experiments and invite a careful analysis of the data to be conducted keeping in mind the actual experimental conditions.

TPD of C_6H_6 on $(\text{CH}_3\text{CH}_2)_2\text{O}$ displayed co-desorption of the overlayer along with its more volatile substrate providing little information on how the C_6H_6 film grows. Therefore, TPD of the reversed system were analysed revealing wetting behaviour, and hence, reciprocal affinity between the two species. This interpretation was also supported by RAIRS data, where the aromatic CC stretching mode of C_6H_6 on top of a thick ice of $(\text{CH}_3\text{CH}_2)_2\text{O}$ remains unchanged as moving from low to higher coverages.

High level QM calculations on model dimers shed light on how C_6H_6 might bind

at the interface of solid H_2O , CH_3OH , or $(\text{CH}_3\text{CH}_2)_2\text{O}$. Three main key interactions of H-bonds were identified: $\text{OH}\cdots\pi$, $\text{CH}\cdots\pi$, and $\text{CH}\cdots\text{O}$. These findings while more of a fundamental interest are important to **Chapter 5**, but of limited astrophysical relevance. Nevertheless, they confirm a scenario, in the inner and middle envelope during star formation, where thermal desorption behaviour of organic molecules is accelerated or delayed depending on the local ice mantle composition, and where processes like mixing should not be ignored in the overall kinetics.

Outlook

Despite this chapter being almost self-conclusive, two aspects could benefit from future developments. First of all, and most obvious, the QM calculations should be extended to larger systems, such as the one in **Figure 6.3**, where one molecule of C_6H_6 interacts with a cluster of molecules of H_2O , CH_3OH or $(\text{CH}_3\text{CH}_2)_2\text{O}$. Furthermore, the C_6H_6 trimer could also be considered in order to properly in-

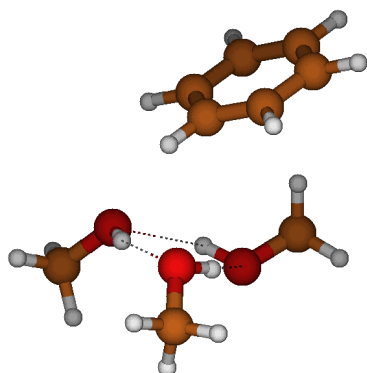


Figure 6.3: One of the possible structures for C_6H_6 interacting with three CH_3OH molecules. Geometry optimisation was performed at MP2/aug-cc-pVDZ level.

terpret the observed shifts in the IR frequencies. A good starting point would be to look at the cyclic structure in **Figure 6.4** for two reasons: (i) it is the global minimum and (ii) it contains the main types of interlayer and intralayer interactions in the crystal structure [9]. All these clusters are best representative

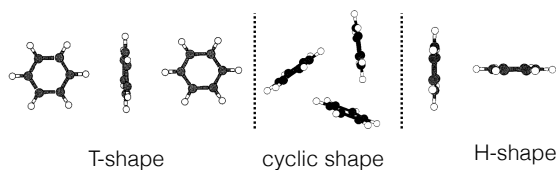


Figure 6.4: Energy minima of C_6H_6 trimer structure. Figure adapted from [10].

of gas-phase systems, while it is not currently practical performing calculations

of large systems that closer resemble the experimentally studied surfaces using wavefunction based correlation methods such as MP2 combined with Coupled-cluster single points [11] (as seen in **Chapter 4**). The non-linear increase of the computational cost (N^x , where $x = 2, 3, 4, \dots, 9$) makes these high level calculations prohibitive, especially when the Counterpoise (CP) correction is taken into account. However, if the models proposed above of three to four molecules, are treated consistently at the same level of theory (MP2/aug-cc-pVTZ), a reliable benchmark would be provided for plane wave density functional calculations on even larger systems. Alternatively, as described in **Chapter 2**, the RI-MP2 method could be extended to surfaces (of hundreds of atoms). But it should be stressed that such calculations are only feasible by introducing additional approximations, such as resolution-of-the-identity (RI) for the four-index electron repulsion integrals (ERIs) with optimised auxiliary basis sets. Furthermore the basis set superposition error (BSSE), and hence the CP correction, might likely require significant reduction in the size of the system in order to make the computation cost-effective.

Furthermore, experimentally, the TPD of C_6H_6 on $(CH_3CH_2)_2O$ suggests that when molecules are bonded to more volatile substrates, co-desorption might take place accelerating the loss rate of the adsorbate. Therefore, coronene on ASW could be an excellent system to investigate given that $C_{24}H_{12}$ would otherwise desorb only after all the H_2O had sublimated. Finally, the TPD data of C_6H_6 adsorbed on CH_3OH or $(CH_3CH_2)_2O$ highlighted some issues of operating at ~ 110 K using the current experimental set-up (Beam Rig). Therefore, it was proposed that a lower base temperature should minimise the observed phase change in the ice and its displacement during the C_6H_6 dose. In order to be consistent with the non-thermal desorption experiments presented in **Chapter 5** for the same binary layered ices, it would be preferable to modify the cryogenic system in the Beam Rig, rather than repeating the TPD in the Ice Rig ($T_{base} \sim 20$ K). Cooling by liquid nitrogen (N_2) down to the 80 - 90 K range would be feasible if a continuous flow N_2 cryostat were to be implemented instead of a static reservoir. For instance, a relatively cheap option would be to change the long re-entrant, that is used as Dewar and support of the substrate, with a stainless steel coil of comparable overall diameter size and having the inlet and outlet in the airside of the chamber. The same design which is currently used for the thermal contact to the sample mounting *via* a welded copper rod might be kept.

Chapter 5

This chapter has considered the irradiation with 250 eV electrons of C_6H_6 adsorbed on H_2O , CH_3OH , or $(CH_3CH_2)_2O$ at 110 K. When the underlayer is made of solid H_2O , both enhanced electron-promoted desorption of C_6H_6 and electron-induced chemistry in the form of H_2 formation from the substrate itself are observed. Consistent with literature data, both the phenomena seem to share a common mechanism as suggested by similar value of cross-sections and time decay constants. The incident electrons pass through the entire C_6H_6 film, penetrating into the bulk of H_2O , where long-lived excitons form as a consequence of inelastic scattering from H_2O excited in the 8-20 eV range. These excitons then migrate to the ASW/ C_6H_6 interface, where H_2O both produces H_2 (EIC) and transfers the excitation to the aromatic ring, allowing it to desorb (EPD). The process seems to take place within an ice depth of ≤ 8 nm, and any further increase of the underlayer thickness is ineffective for C_6H_6 desorption.

A decreased intensity in the EPD traces during the first instants of irradiation is observed when the experiment is performed on crystalline H_2O . This hints to a dependence of the process on the absolute number of dangling OH bonds at the interface, hence, suggesting that the excitation is transferred by the hydrogen-bond to the π cloud of the aromatic ring.

In order to understand the role of H-bonding in also supporting exciton transport, EPD of C_6H_6 was also investigated from CH_3OH or $(CH_3CH_2)_2O$ ices. These molecules have comparable electronic transitions to H_2O and similar shape of the molecular orbitals around the O atom. However, the extent of hydrogen bonding is reduced in solid CH_3OH compared to solid H_2O , and is absent in solid $(CH_3CH_2)_2O$. Furthermore, the presence of carbon atoms, introduces new possible excitations compared to H_2O along with new possible outcomes following scattering with low-energy electrons. Thus, it is not surprising that EPD of C_6H_6 on CH_3OH or $(CH_3CH_2)_2O$ is negligible, while EIC occurring in the ice itself is undoubtedly dominant, leading to significant H_2 formation.

These experiments mimic the effect of the secondary electrons produced in interstellar icy mantles by energetic ions, such as cosmic rays. The high abundances of solid H_2O on top of the grains and its peculiarity in transporting the excitation to promote non-thermal desorption both should encourage to have EPD included in astrochemical models to explain observations. As described in **Chapter 1**, non-thermal desorption has only been implemented recently in the astrochemical

models. Photon-stimulated desorption has traditionally been implemented into the models as a non-selective mechanism with uniform yields for all species, and only in the last years molecule-specific yields were considered [12–14]. The effect of the interaction between the ISM dust grains and cosmic rays is treated as a local impulsive heating (up to 70 K) inside the icy mantles, which ignores non-adiabatic processes such as EPD. In fact, the latter could more efficiently lead to the desorption of species adsorbed on the H₂O-rich mantel (hence a higher rate) compared to thermal desorption. Furthermore, EPD might take into account the loss of heavier molecules¹, such as C₆H₆, that would not desorb because of the increase in the surface temperature to 70 K. Tentatively, in order to ascertain the impact of this process on astrophysical scale, it is assumed that the estimated EPD cross-section for C₆H₆ from ASW is the same as that for other simple molecules, such as CO. Thus, the photo-desorption and the electron-promoted desorption rate constant were compared giving a ratio between 64 and 36 in favour of the latter. From this, it can be inferred that CO accretion and ultimately, CH₃OH formation, might be delayed in H₂O-rich mantles during the cooled-down phase of pre-stellar core.

Outlook

These experiments confirm the importance of hydrogen bonding in supporting exciton transport. The microscopic mechanism of exciton transport is still unclear; it could be explained as Förster resonant energy transfer (FRET) [15, 16] and/or excited state proton transfer (ESPT), which might be considered akin to Dexter electronic excitation transport (DEET) [17]. Both lead to the same outcome as shown in the **Figure 6.5**, and both can be derived by the Fermi golden rule for non-radiative transitions. However, depending on what term manifests, the Columbic integral or the the exchange integral, the Förster or Dexter mechanism is observed respectively. The two processes differ from each other in their nature, and hence selection rules and range. The Förster mechanism occurs *via* dipole-dipole coupling, therefore it obeys the Wigner rule (spin conservation) and it is most effective at intermolecular distances, R , between donor (D) and acceptor (A), less or equal to the so called Förster distance, R_0 , where the rate for the excitation transfer, k_{ET} , is:

$$k_{ET} = \frac{1}{\tau_D} \left(\frac{R_0}{R} \right)^6 \quad (6.1)$$

¹However, their surface concentration should be negligible in the early stages of the ice mantle growth, when EPD would be most efficient.

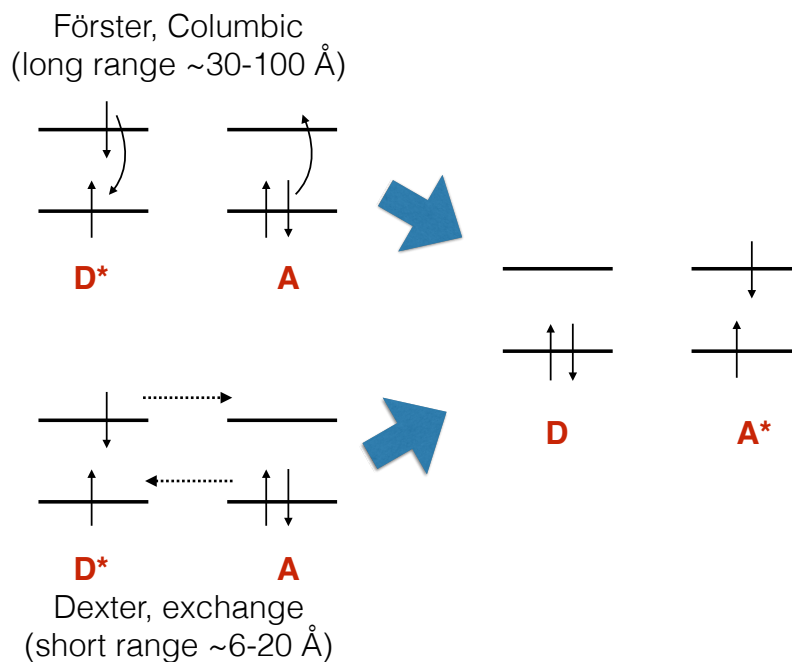


Figure 6.5: Schematic of Förster (dipole-dipole coupling) and Dexter (molecular orbitals overlapping) mechanisms for excitation transfer. *A* is the acceptor molecule that is excited (*A*^{*}) and *D*^{*} is the excited donor molecule that relaxes to ground state (*D*).

where τ_D is the overall time decay of the excited donor molecule. Conversely, Dexter ET proceeds *via* molecular orbitals overlapping, and the rate constant has the form of:

$$k_{ET} \propto e^{-\frac{2R}{L}} J \quad (6.2)$$

where L is the sum of the Van der Waals radii, and J is the overlap integral between the “emission” of the donor and the “absorption” of the acceptor. The exchange mechanism decays exponentially with R , thus acts in a shorter range compared to the Columbic ET. However, in ASW it is not straightforward to distinguish between the two mechanisms, since the excitation is transferred among molecules of the same species in solid phase, where intermolecular distances are compatible for both Dexter and Förster ET. On the other hand, excited state proton transfer might favour formation of protonated C_6H_6 , or $C_6H_6-H_2O$ clusters, providing a distinctive mark for this process. Therefore, future work could rely on time-of-flight MS measurements of the desorbing species, to guarantee a fast detection and definitively identify their nature (neutrals, positive and negative ions) and study their translational energies.

Furthermore, additional detailed information on the desorption kinetics can also be obtained by well-known techniques such as Laser Induced Fluorescence (LIF)

or Resonance Enhanced Multiphoton Ionisation (REMPI), which are often used to determine the velocity or vibrational distributions in a selected rotational level of the scattered molecules from the surface [18–20]. For instance, a recent study [21] applied UV-UV double resonance spectroscopy to measure desorption rates of CO from Pt(111). A CO pulsed molecular beam is used to dose on the surface, then, the molecules desorbing are tagged by a pump laser into a metastable state. These are finally detected by a (1+1) REMPI transition. The delay between the two laser pulses, defines the velocity of the molecules being detected. The results showed a bi-exponential kinetics for CO desorption with a fast component assigned to CO leaving the (111) terraces, and the slow component was assigned to sequential diffusion from steps to terraces followed by desorption. This technique and approach could be applied to non-thermal desorption as well, providing an additional and independent tool from MS measurements to look at the EPD traces (*e.g.* CO from H₂O ices).

The investigation carried out for C₆H₆ on ASW could also be extended to bigger aromatic molecules, such as PAHs, and smaller molecules, such as C₂H₂ or CO, eventually confirming the hypothesis of a general rationalisation for the observed EPD, which is specific only to the H₂O ice, and not to C₆H₆. It would also be interesting to investigate the effect of the surface temperature on the EPD cross-section. Although the exciton-based mechanism proposed in this thesis might not be affected by performing the experiments at 10 K, the structure of the H₂O film (porous ASW) and the accommodation of the adsorbate on the ice at 10 K will be different from the same system at 110 K. Moreover, in order to verify the postulated invariance of the excitation transfer on the ice temperature², the EPD experiment of C₆H₆ on c-ASW could be repeated by dosing at 110 K and irradiating at 10 K.

Finally, electron irradiation experiments could be probed by means of RAIRS, which could reveal additional information about the induced chemistry. This approach was extensively used by Kaiser and co-workers [22, 23] for CH₃OH ices and mixtures of CO/CH₃OH at 5 K and the results are consistent with other similar experiments [24]. Collecting IR spectra during the electron bombardment of C₆H₆/CH₃OH and C₆H₆/(CH₃CH₂)₂O could aid and support the results reported in this thesis, especially providing complementary investigation to the EPD and EIC curves outlined in **Chapter 5**. In fact, by looking at the evolution of the vibrational modes, such as the CC aromatic stretch, as a function of the

²The mechanism for the excitation transfer is fundamentally independent of the temperature because it is based on the Fermi golden rule for non-radiative transitions

irradiation time, data consistent with the EPD traces can be obtained, while the appearance of new bands and their change with time might help to identify newly formed species. The C_6H_6/H_2O ice was already fully characterised by the work of Thrower [25] and two limits to this approach could be highlighted.

1. C_6H_6 is highly symmetric and hence, does not display intense IR bands at low coverages. Furthermore, the metal surface selection rule reduces the numbers of the detected molecules. Even rastering the electron beam over the surface, the observed changes in the intensity or band area for a given vibration are small and are enhanced only at very long irradiation times. Thus, the ice needs to be exposed to the electron irradiation up to 2000 seconds, compared to the analogous experiment using the QMS, where 500 seconds are usually more than enough. Another consequence of this is that RAIRS lacks of the speed necessary to resolve the fast desorption of C_6H_6 from c-ASW, and only the slow component can be measured.
2. No irradiation products were detected for low and intermediate coverages of C_6H_6 (up to 20 L) on c-ASW.

A follow-up on these experiments, using the same equipment as Thrower, was done for the irradiation of plain c-ASW [26], but RAIRS alone is not capable of discriminating between the H_2O loss due to the chemistry and the non-thermal desorption. However, for the CH_3OH and $(CH_3CH_2)_2O$ ices, it is feasible to detect new bands which would be exclusively linked to the EIC, and using isotopes will help to assess the relevant channels responsible for the observed H_2 formation.

Bibliography

- [1] M. P. Collings, V. L. Frankland, J. Lasne, D. Marchione, A. Rosu-Finsen and M. R. S. McCoustra, *Mon. Not. R. Astron. Soc.*, 2015, **449**, 1826.
- [2] H. C. Allen, N. N. Casillas-Ituarte, M. R. Sierra-Hernandez, X. Chen and C. Y. Tang, *Phys. Chem. Chem. Phys.*, 2009, **11**, 5538.
- [3] G. L. Richmond, *Chem. Rev.*, 2002, **102**, 2693.
- [4] M. C. Gurau, G. Kim, S.-M. Lim, F. Albertorio, H. C. Fleisher and P. S. Cremer, *Chem. Phys. Chem.*, 2003, **4**, 21231.
- [5] V. Ostroverkhov, G. A. Waychunas and R. Y. Shen, *Phys. Rev. Lett.*, 2005, **94**, 046102.
- [6] M. Sulpizi, M.-P. Gaigeot and M. Sprik, *J. Chem. Theory Comput.*, 2012, **8**, 1037.
- [7] B. Civalleri and P. Ugliengo, *J. Phys. Chem. B*, 2000, **104**, 9491.
- [8] A. J. DeSimone, *PhD thesis*, Georgia Institute of Technology, 2013.
- [9] G. J. Kearley, M. R. Johnson and J. Tomkinson, *J. Chem. Phys.*, 2006, **124**, 044514–9.
- [10] O. Engkvist, P. Hobza, H. L. Selzle and E. W. Schlag, *J. Chem. Phys.*, 2005, **110**, 5758.
- [11] M. G. Zaleśny, R. Papadopoulos, P. G. Mezey and L. J., *Linear-Scaling Techniques in Computational Chemistry and Physics*, Springer, 2011, vol. 13.
- [12] J. F. Roberts, J. M. C. Rawlings, S. Viti and D. A. Williams, *Mon. Not. R. Astron. Soc.*, 2007, **382**, 733.
- [13] K. Öberg, H. Linnartz, R. Visser and E. F. van Dishoeck, *Astron. Astrophys.*, 2009, **693**, 1209.

- [14] K. Öberg, E. F. van Dishoeck and H. Linnartz, *Astron. Astrophys.*, 2009, **496**, 281.
- [15] T. Förster, *Annalen. Phys.*, 1948, **2**, 55.
- [16] G. D. Scholes, *Ann. Rev. Phys. Chem.*, 2003, **54**, 57.
- [17] D. L. Dexter, *J. Chem. Phys.*, 1953, **21**, 836.
- [18] G. Scoles, *Atomic and molecular beam methods*, Oxford University Press, New York, 1988.
- [19] N. Bartels, B. C. Krüger, D. J. Auerbach, A. M. Wodtke and T. Schäfer, *Angew. Chem. Int. Ed.*, 2014, **53**, 13690.
- [20] M. A. Tesa-Serrate, K. L. King, G. Paterson, M. L. Costen and K. G. Mc Kendrick, *Phys. Chem. Chem. Phys.*, 2014, **16**, 173.
- [21] K. Golibrzuch, P. R. Shirhatti, J. Geweke, J. Werdecker, A. Kandratsenka, D. J. Auerbach, A. M. Wodtke and C. Bartels, *J. Am. Chem. Soc.*, 2015, **137**, 1465.
- [22] S. Maity, R. I. Kaiser and B. M. Jones, *Faraday Discuss.*, 2014, **168**, 485.
- [23] S. Maity, R. I. Kaiser and B. M. Jones, *Phys. Chem. Chem. Phys.*, 2015, **17**, 3081.
- [24] N. J. Mason, B. Nair, S. Jheeta and E. Szymanska, *Faraday Discuss.*, 2014, **168**, 235.
- [25] J. D. Thrower, *PhD thesis*, Heriot-Watt University, 2009.
- [26] G. M. A. Abdulgalil, *PhD thesis*, Heriot-Watt University, 2013.